FIRST INTERNATIONAL CONFERENCE ON LOW-DIMENSIONAL ADVANCED MATERIALS

ICLODAM-24

FEBRUARY 18-19 , 2024 SAMARKAND,
FEBRUARY 21-22, 2024 TASHKENT,
UZBEKISTAN

BOOK OF ABSTRACTS

Organizing committee

Prof. Ashurov Kh.B., Arifov Institute of Ion-Plazma and Laser Technologies - chair

Prof. Utamuradova Sh.B., Institute of Semiconductor Physics and Microelectronics - co-chair

Prof. Olimov Kh.K., Physical-Technical Institute   - co-chair

Prof. Gulamov K.G., Uzbekistan Physics Council – member

Dr. Parpiev O.R., Institute of Material Sciences – member

Prof. Kurbanov M.Sh., Arifov Institute of Ion-Plazma and Laser Technologies – member

Prof. Razykov T.M., Physical-Technical Institute   - member

Prof. Usmanov D.T., Arifov Institute of Ion-Plazma and Laser Technologies – member

Prof. Khushvaktov H. Samarkand State University -member

Dr. Ergashev B.E., Physical-Technical Institute   – member

Dr. Kuchkarov K.M., Physical-Technical Institute   -member

Scientific committee

Prof. Zakhidov A., The University of Texas at Dallas -chair

Prof. Hong S., Sejong University -co-chair

Prof. Khalmuradov R.I. Samarkand State University -member

Prof. Abdullaev F.Kh., Physical-Technical Institute   - member

Prof. Alessandro R., University of Verona - member

Prof. Goswami Y., Clean Energy Research Center, USF - member

Dr. Nikiforov A.I., Rzhanov Institute of Semiconductor Physics – member

Prof. Utamuradova Sh. B., Institute of Semiconductor Physics and Microelectronics -member

Prof. Kurbanov M.Sh., Arifov Institute of Ion-Plazma and Laser Technologies – member

Prof. Lebedev A.A., Ioffe Institute -member

Prof. Karazhanov S, IFE, Norway -member

First International Conference on Low-Dimensional Advanced Materials ICLODAM-24 // Book of Abstracts. Tashkent, 2024, p.140.

The technical program of the conference included presentations by invited international speakers and local speakers, including young scientists. The conference was organized by the Ministry of Higher Education, Science, and Innovations of the Republic of Uzbekistan; the Uzbekistan Academy of Sciences; the Council of Uzbekistan Physicists; the Korean Physical Society; Samarkand State University; the Arifov Institute of Ion-Plasma and Laser Technologies of the Uzbekistan Academy of Sciences; the Physical-Technical Institute of the Uzbekistan Academy of Sciences; the Institute of Material Sciences of the Uzbekistan Academy of Sciences; the Institute of Semiconductor Physics and Microelectronics at the National University of Uzbekistan; and GRI-TPC IRC @ Sejong University.

The conference aimed to create collaborative networks among researchers and young scientists from Uzbekistan and other countries in the field.

Results on solid-state low-dimensional and advanced functional materials, device development, innovative applications, as well as adjacent field topics, were presented.

DILUTED MAGNETIC SEMICONDUCTORS FOR SPINTRONICS APPLICATIONS

Sh. Yuldashev[1,2,], K. Mukimov[1], G. Eshonkulov[2], A.Arslanov[2], J. Xudoykulov[2]*

[1]Center of Nanotechnologies Development, National University of Uzbekistan
[2]Department of Physics, National University of Uzbekistan, Tashkent, Uzbekistan

Diluted magnetic semiconductors (DMSs) are new functional materials created by doping magnetic ions in non-magnetic semiconductors. The exchange effect between magnetic ions and carriers in semiconductors gives DMSs novel magneto-electric and magneto-optical properties. As a candidate material for spintronics, it has attracted increasing attention in last 20 years [1].   In addition, DMSs take advantage of both the charge and spin properties of electrons, making them potentially widely useful in spin field effect transistors (spin-FETs), high-density nonvolatile memory and spin qubits for quantum computers [2]. There are two main factors that limit the practical application of DMSs in equipment. The first is that the Curie temperature of DMS material is lower than room temperature, and the second is whether the ferromagnetism in DMS material is intrinsic, that is, mediated by free carriers, or purely from the local secondary phase of magnetic dopants, such as clusters or precipitates. If ferromagnetism is not mediated by free carriers, spin polarization cannot be carried by them. Therefore, it is generally not suitable for spintronic devices. At present, there is only GaMnAs confirmed ferromagnetic semiconductor with high Curie temperature. However, the highest Curie temperature is about 200K by using nanostructure engineering and it is far below room temperature [3]. In the seminal paper by T. Dietl et al. [4] it was theoretically predicted a room temperature ferromagnetism (RTFM) in 5 at.% Mn-doped p-type GaN and ZnO, with free holes concentration about 10^{20}cm^{-3}. ZnO suffer from a low concentration of free holes and isovalent anion alloying can improve this problem. ZnO and ZnS alloy exhibits a very strong valence band (VB) offset bowing as a function of sulfur content. The VB-bowing can be utilized to enhance p-type doping with lower formation energy and shallower acceptor state in the ZnO-ZnS alloy

In this work, structural, optical and magnetic properties of $Zn_{1-x}Mn_xO_{1-y}S_y$, additionally doped with nitrogen, thin films grown by ultrasonic spray pyrolysis system are reported. This films of $Zn_{1-x}Mn_xO_{1-y}S_y$ thin films were synthesized by ultrasonic spray pyrolysis (USP) method on Si (1 0 0) and quartz substrates. Zinc acetate, manganese acetate, ammonia acetate and thiourea were used as the zinc, manganese, nitrogen and sulfur sources, respectively. Figure 1 shows the SEM images of the nitrogen doped $Zn_{0.95}Mn_{0.05}O_{0.85}S_{0.15}$ thin film grown by using ultrasonic spray pyrolysis.
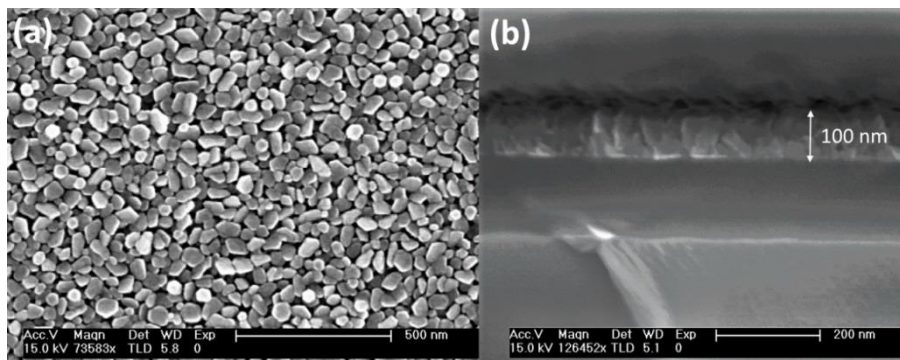

Fig.1. SEM images of the nitrogen doped $Zn_{0.95}Mn_{0.05}O_{0.85}S_{0.15}$ thin film: (a) top view and (b) cross-section view, respectively.

It is seen from Fig.1 that the $Zn_{0.95}Mn_{0.05}O_{0.95}S_{0.15}$ film consists of hexagonal shaped nanoflakes whose lateral size was estimated to be between 100 ~ 200 nm with the layer thickness of around 100 nm as shown in the cross-section image.

In order to study the magnetic properties of the diluted magnetic semiconductors based on $Zn_{1-x}Mn_xO_{1-y}S_y$ thin films, the magnetization dependencies on the magnetic field and temperature were measured by using a SQUID (superconducting quantum interference device) magnetometer. Figure 2 shows the magnetization dependencies on: a) magnetic field, measured at T = 10K and b) temperature for the $Zn_{0.95}Mn_{0.05}O_{0.95}S_{0.15}$ thin film.
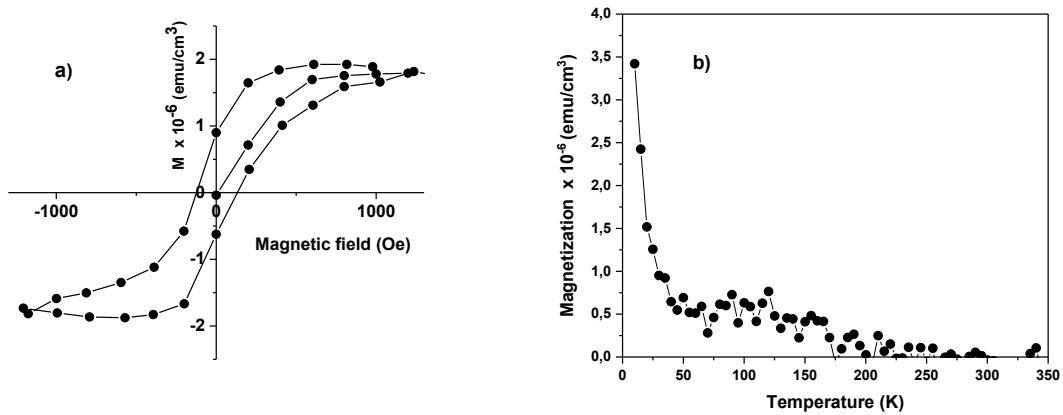

Fig. 2. The magnetization dependencies on: a) magnetic field and b) temperature, for the $Zn_{0.95}Mn_{0.05}O_{0.95}S_{0.15}$ thin film.

It is seen from Fig.2a that the magnetization dependence on magnetic field for the $Zn_{0.95}Mn_{0.05}O_{0.95}S_{0.15}$ film demonstrates the hysteresis loop at T =10 K, which shows the existence of ferromagnetism in the material at this temperature. The temperature dependence of the magnetization presented in Fig. 2b shows that the magnetization is going to zero at temperature between 250K and 300K, which is much higher than it was observed for GaMnAs material.

In conclusion, the effect of the sulfur concentration on the magnetic properties of the $Zn_{0.95}Mn_{0.05}O_{1-y}S_y$ thin films doped by nitrogen semiconductors grown by ultrasonic spray pyrolysis method was studied. The obtained films exhibit a polycrystalline hexagonal wurtzite structure with (002) preferred orientation. The results of XRD and optical transmission measurements demonstrates a successful incorporation of the sulfur ions into ZnMnO crystal lattice. The SQUID measurements demonstrate the ferromagnetism in the sulfur doped ZnMnO thin films with the Curie temperature close to room temperature. In order to increase the Curie temperature father the hole concentration should be increased in this material. The problem with obtaining of p-type ZnO with a high concentration of free holes is still waiting its solution.

References

[1] S. A. Wolf, et al., Science 294 (2001) 1488-1495.
[2] S. J. Pearton, et al., Journal of Applied Physics 93 (2003) 1-13.
[3] Lin Chen, et al., Nano Letters 11 (2011) 2584–2589.
[4] T. Dietl, et al., Science 287 (2000) 1019-1022.

THE THREE-, TWO- AND ONE-DIMENSIONAL ASPECTS OF CELL BIOPHYSICS

Ravshan Z. Sabirov

Institute of Biophysics and Biochemistry, National University of Uzbekistan, Tashkent 100174, Uzbekistan

The living cells have various sizes and shape. The red blood cells (RBCs) are one of the smallest cells in human body. Their diameter is about 8 µm, and they have a shape of donuts-like biconcave disc. Most immune cells, such as T- and B-lymphocytes are a bit larger (~10 µm) and spherical. Isolated cardiac myocytes are roughly rectangular, 100–200 µm long and 30–50 µm wide, have striation. Skeletal muscle myocytes are much larger with a length of about 2–3 cm and diameter of ~100 µm. These cells have multiple nuclei as a result of fusion of mononucleated myoblasts during fiber formation. Brain cells have most peculiar shapes. Neurons have relatively small body (soma) of 10–50 µm in diameter. Numerous extensions of 50-100 µm and longer (dendrites) receive input signals, whereas the longest extension called axon transduces the action potential generated by neurons to the distance as long as ~1 meter (when reaching from the base of the spine to the toes). The Schwann cells wrap the axons to insolate them, whereas the astrocytes (star-shaped cells) protect the neurons and feed them by taking up the nutrients from blood capillaries and passing glucose and lactate to the nerve cells. Although it is clear that, overall, the cells are **3D**-constructions made up of the cytoskeleton wrapped by the plasma membrane with a variety of organelles (nucleus, mitochondria, endoplasmic reticulum, Golgi apparatus, etc.), it is still not clear how the information written in the genome is translated to the particular cellular shape.

Whatever the shape, the cells are separated from the extracellular space by a lipid bilayer membrane permeable to water and small ions; thus, they behave like osmometers and obey the Vant-Hoff's low. However, many intracellular osmolytes (proteins and metabolites, such as ATP) are membrane-impermeable. Therefore, left unopposed, the oncotic gradient would cause the osmotic catastrophe and cell lysis. The stable basal cellular volume is adequately described within the framework of the Donnan equilibrium and the pump-leak mechanism (PLM) developed by Tosteson and Hoffman. However, great osmotic stress and respective swelling (or shrinkage) often occur during normal life (e.g. in lung epithelium during intensive breezing, in the epithelium of the gastro-intestinal tract upon drinking, in kidney epithelium upon salt stress, etc.) and in pathological conditions, such as ischemia/reperfusion in heart and brain, trauma and stroke. In order to maintain the volume within the range compatible with life, the cells activate a number of ion transporting pathways in the cellular plasma membrane, which is essentially a **two-dimensional** structures and is described regardless of the 3D-aspects of the cell biophysics. Thus, the mechanical stress caused by the cellular swelling activates the plasma membrane Ca^{2+}-permeable ion channels (such as recently discovered Piezo-channels). Calcium influx, in turn, activates the K^+-channels to employ the potassium gradient as a driving force for the regulatory volume decrease (RVD) mechanism that counteracts the excessive cellular swelling to keep the volume close to the normal level.

The net K^+ efflux cannot occur without the parallel movement of an equivalent amount of anions as required by the principle of electroneutrality. This is accomplished by activation of the volume-activated anion channels (VAACs). At normal metabolic state with high intracellular ATP, the major anionic pathway is the volume-sensitive outwardly rectifying (VSOR) Cl-channel of intermediate conductance (~30-70 pS) (Okada et al. *Pharmacol. Rev.* 2019; 71: 49-88). However, when ATP is depleted (e.g. under ischemia/hypoxia), the Maxi-Cl channel with very large conductance of ~300-400 pS becomes active (Sabirov et al. *Life (Basel).* 2021, 11: 509). The human VSOR Cl-channel was recently identified as a hexameric complex of the leucine-rich repeat containing family 8 (LRRC8) protein A (obligatory) and C, D and E (second necessary) proteins of

the same family. We have demonstrated that the mouse counterpart is also composed of the same orthologs (Okada et al. *Channels* 2017; 11(2): 109-120).

The Maxi-Cl channel was shown to be a complex of the core pore component made of the SLCO2A1 protein (Sabirov et al. *EMBO J.* 2017, 36: 3309-3324) and two auxiliary regulatory components: annexin 2A (ANXA2) provides dephosphorylation-dependent activation by removing phosphate from Tyr23, and S100A10 (also known as p11) that is a Ca^{2+}-binding protein and provides activation upon rise in the intracellular calcium (Islam et al. *Cell Physiol. Biochem.* 2020, 54: 538-555).

Small molecules which are capable to bind specifically to these ion channels and modulate their function (activate or inhibit) would open a way to make cells, organs and the whole organisms healthier. However, pharmacology of these two channels is relatively poor. Thus far, the most selective inhibitor of the VSOR Cl-channel is 4-[(2-butyl-6,7-dichloro-2-cyclopentyl-2,3-dihydro-1-oxo-1H-inden-5-yl)oxy]butanoic acid (DCPIB). We have recently shown that some flavonoids (especially, lavandulyl-containing), tannins and polyphenol compound, gossypol, are able to inhibit the RVD process in acutely isolated rat thymocytes and suppress the activity of VSOR Cl-channel in cultured cells (Rustamova et al. *Pharmacol. Rep.* 2019, 71: 1079-1087; Tsiferova et al. *Eur. Pharm. J.* 2019, 66(2): 37-44; Chorieva et al. *Clin. Exp. Pharmacol. Physiol.* 2021, 48(2): 227-237). The Maxi-Cl channel is sensitive to the extracellular Gd^{3+}, which distinguishes it from other chloride channels, but also affects some cationic channels and, thus, cannot be considered as a selective pharmacological tool. Since the channel's core component, SLCO2A1, is known to function as a prostaglandin transporter (PGT) in an inactivated state, the Maxi-Cl channel was found to be sensitive to the PGT inhibitor, bromosulfophtalein. No natural selective inhibitor for this channel is found thus far.

The transport of ions through the ion channels occurs in **one dimension**: from one side of the membrane to the other. Therefore, it is described as a one-dimensional movement of permeating ion species along the channel pore by falling into the energy wells and overcoming the energetic barriers formed by protein backbone and/or by the side chains of the amino acids along the pore one-dimensional axis.

REVOLUTIONARY NOVEL AND LOW-COST CHEMICAL MOLECULAR BEAM DEPOSITION METHOD FOR FABRICATION OF CHALCOGENIDE COMPOUNDS FILMS FOR LOW DIMENSIONAL STRUCTURES AND SOLAR CELLS

T.M. Razykov, B.A. Ergashev, Sh.M. Bobomuradov

Physical-Technical Institute, Chingiz Aytmatov Street 2B, Tashkent 100084, Uzbekistan
*bobur_7007@yahoo.com

The physical properties of semiconductor films depend on both the thermodynamic conditions of synthesis and the method of fabrication. Each method has its own limitations and is therefore applicable to solving specific tasks. There are several methods for producing A2B6 compound films. Earlier, in [1,2], the basic principles, advantages, and disadvantages of existing methods were considered. In recent years, their range has expanded, and new methods have emerged.

Unlike existing methods, the fabrication of thin films developed in our laboratory is an economical method of chemical molecular-beam deposition (CMBD), as shown in Fig. 1. The fundamental difference between CMBD and molecular beam epitaxy (MBE) is that in the former, the synthesis process is conducted in a hydrogen or inert gas environment at atmospheric pressure, whereas in the latter, it is performed in a vacuum of no less than 10^{-7} Torr.
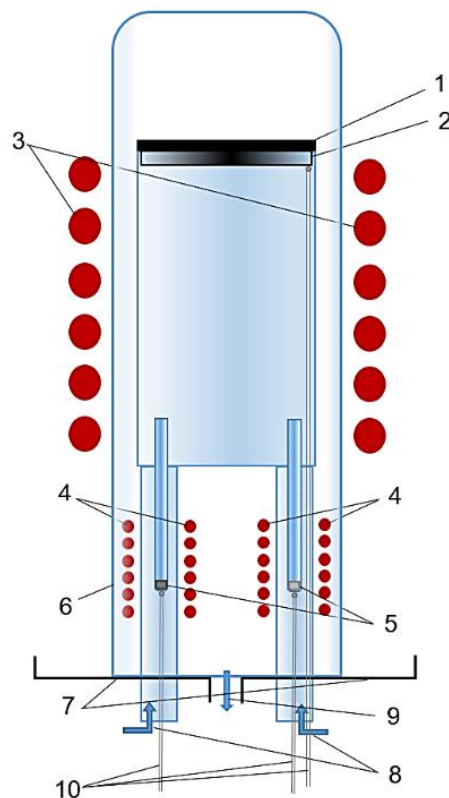

Fig.1. Schematic representation of the CMBD method for obtaining thin films.

1, 2 – substrate and holder, 3 – substrate heater, 4 – source heaters, 5 – crucibles of evaporated components, 6 – reactor cap, 7 – flange, 8 – gas inlet, 9 – gas outlet, 10 – thermocouples.

As demonstrated in [3,4], the novel and economical CMBD method offers several advantages, such as:

1. Deposition is carried out using a gas flow at atmospheric pressure, eliminating the need for expensive vacuum equipment, making this method cost-effective.
2. Deposition processes are controlled at the molecular level (10^{10} - 10^{14} cm^{-2}), enabling precise control of film composition.
3. Deposition rates can be varied over a wide range (10-10^4 Å/s).
4. Films can be deposited over a large area (50 cm^2) using existing equipment.
5. Doping of films is performed during the growth process.
6. Non-toxic gases are utilized.

Due to the merits of this method, particularly the discrete placement of component sources with independent heating and gas carrier supply through each of them, it is feasible to easily obtain films of a specified composition, thus enabling control over their properties, including conductivity type and concentration of intrinsic point defects (IPDs) in the grown films.

References
[1] Hartmut Frey, Hamid R. Khan. Handbook of Thin Film Technology. Springer-Verlag Berlin Heidelberg 2015.
[2] Zexian Cao. Thin Film Growth: Physics, Materials Science and Applications. Woodhead Publishing. 2011.
[3] T.M.Razykov. Chemical molecular beam deposition of II-VI binary and ternary compound films in gas flow // Applied Surface Science, -1991, v.48/49, N1, pp.89-92.
[4] T.M. Razykov, J.Bekmirzoev, A. Bosio, B.A. Ergashev,* and etc. Structural and optical properties of Sb_xSe_y thin films obtained by chemical molecular beam deposition method from Sb and Se precursors. Solar Energy, Volume 254, April 2023, Pages 67-72.

PROPAGATION OF ELECTROMAGNETIC WAVES IN THE ARRAY OF NONLINEAR OPTICAL WAVEGUIDES WITH MANAGED PT-SYMMETRY

F.Kh. Abdullaev[1], S.Sh. Tadjimuratov[2]

[1]Physical-Technical Institute of the Uzbekistan Academy of Sciences;
*[2]National University of Uzbekistan.*

The propagation of electromagnetic beams in the array of 2N tunnel coupled nonlinear optical waveguides with managed PT-symmetry is investigated. The conditions of stationary propagation of EM waves in such optical crystals are found. The criterion of the breaking of the PT-symmetry is derived. The analytical results are confirmed by the direct numerical simulations of the extended discrete nonlinear Schrodinger equation.

UNDERSTANDING SELECTIVE SYNTHESIS PUZZLES USING COMPUTATIONAL MATERIALS SCIENCE

Umedjon Khalilov

Arifov Institute of Ion-Plasma and Laser Technologies, The Academy of Sciences of the Republic of Uzbekistan
University of Antwerp, Belgium

As Moore's Law encounters limitations, carbon nanotechnology emerges as a potential alternative to silicon, focusing on materials such as fullerene, carbon nanotubes (CNTs), graphene, and more. This presentation illustrates the crucial role of computational materials science (CMS) in significantly aiding the investigation of selectively synthesizing carbon nanostructures (CNS) in contemporary experiments. Specifically, in the growth of CNTs through catalyzed chemical vapor deposition (CVD), our simulations explore parameters such as feedstock composition, temperature, and the k-coefficient. These simulations reveal the potential for tailoring CNT diameters and achieving chirality control. Furthermore, we examine plasma-enhanced CVD (PECVD) for selective CNT etching, emphasizing the importance of curvature, metallicity, and the angle (γ) between ortho-hydrogen pairs and the chirality vector. Additionally, endohedral synthesis, encompassing carbon peapods and graphene nanoribbon (GNR) synthesis, sheds light on the catalyst-feedstock interplay in determining nanostructure outcomes. Subsequently, our research outcomes provide insights into carbyne stability, controllable electronic properties, and the potential for current amplification in functionalized samples.
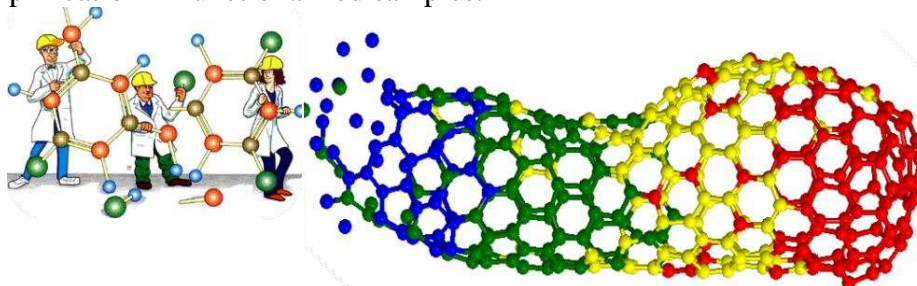
Overall, CMS bridges the gap between theory and experiment, interpreting key observations in CNS synthesis. The synergy between CMS and experimentation not only enhances our understanding of fundamental principles but also drives the development of new carbon materials and technologies with transformative potential in various industries.

References
Khalilov, U., Bogaerts, A., & Neyts, E. C. (2015) Nature Communications, 6(1), 10306.
Khalilov, U., Bogaerts, A., Xu, B., Kato, T., Kaneko, T., & Neyts, E. C. (2017) Nanoscale, 9(4), 1653.
Khalilov, U., Bogaerts, A., Hussain, S., Kovacevic, E., Brault, P., Boulmer-Leborgne, C., & Neyts, E. C. (2017) Journal of Physics D: Applied Physics, 50(18), 184001.
Khalilov, U., Vets, C., & Neyts, E. C. (2019) Nanoscale Horizons, 4(3), 674.
Khalilov, U., Vets, C., & Neyts, E. C. (2019) Carbon, 153, 1.
Khalilov, U., & Neyts, E. C. (2021) Carbon, 171, 72.

EXTRACTION OF RHENIUM IN POWDER

*A.S. Khasanov[1], Sh.A. Ashirova[2], K.Zh. Khakimov[3], Kh.B. Ashurov[4]*

[1] - Almalyk Mining and Metallurgical Complex Joint Stock Company
[2] - Higher School of Business and Entrepreneurship
[3] - Termez Engineering and Technology Institute
[4] - Institute of Ion-Plasma and Laser Technologies of the Uzbek Academy of Sciences

Rhenium (named after the Rhineland in Germany) Re is a metal of group VII of the periodic table; atomic number 75, atomic mass 186.207; belongs to the group of rare trace elements. Two isotopes of rhenium are found in nature: stable 185Re (37.07%) and radioactive 187Re (62.93%). The most common artificial radioactive isotopes of rhenium with wt. numbers 182, 183, 184, 186, 188, 189, 190, 192. Electronic configuration is $1s^2 2s^2 2p^6 3s^2 3p^6 4s^2 3d^{10} 4p^6\ 5s^2 4d^{10} 5p^6 6s^2 4f^{14} 5d^5$. It was discovered in 1925 by German chemists and spouses Walter and Ida Noddack. Its own minerals are very rare; it isomorphically replaces Mo in molybdenite and Cu in chalcopyrite. The rhenium minerals dzhezkazganite $Cu(ReMo)S_4$ and Columbite - $Fe(Nb,Re)_2O_6$ were found.
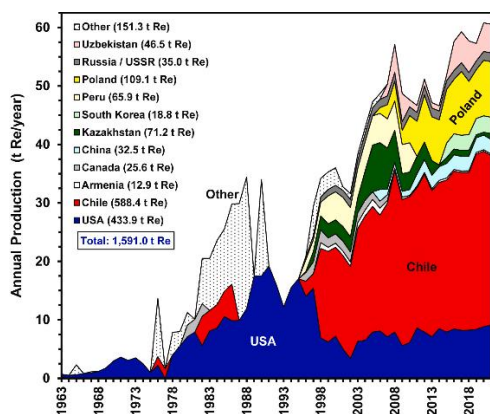
World reserves of rhenium

In practical terms, the most important raw materials for producing primary rhenium on an industrial scale are molybdenum and copper sulfide ores. In the overall balance of production, the production of primary rhenium on an industrial scale in the world accounts for about 80%. The rest comes from secondary raw materials. Confirmed reserves of rhenium, according to USGS estimates, are 10-15 thousand tons. The total "recoverable" reserves of rhenium (i.e., the extraction of which is profitable at current prices) are estimated at only 1.5 thousand tons, of which 0.59 thousand tons are in Chile, which accounts for 39% of world reserves.

The second largest reserves volume is the USA, with a share of 29%. Russia's share in rhenium reserves is 3%. Kazakhstan ranks fourth in global reserves with a share of 6%. There are also rhenium reserves in Armenia, Peru and Canada. Chile is also the leader in terms of annual production. Uzbekistan accounts for about 2 tons per year.

Production

The largest rhenium producing country is Chile, which provides 53% of the world's rhenium production. Notable producers are the USA - 16%, Poland - 16%, Uzbekistan - 10%. Russia's share in rhenium production is less than 1%. The volume of rhenium production in the world in 2014 decreased by 0.3% to 48.8 tons. The price for 1 gram of rhenium is US$ 3-5.

Rhenium consumption in the world in 2014 amounted to 59.7 tons, of which 45.4 tons were in the USA, and 15.2 tons in other countries.

The extraction of rhenium from molybdenum intermediate product (MPM) of the copper concentration plant (COP) of the Almalyk MMC has been carried out in the rare metals production shop (CPRM) for more than 20 years. During this time, the technology was improved and the hardware and technological scheme was developed to increase rhenium extraction and improve the quality of rhenium products. The indicators achieved in 2005-2010 are characterized by the end-to-end extraction of rhenium from PPM into ammonium rhenium (AR) at the level of 70% and the production of AP-0 grade products.

To further improve the technological scheme, an urgent need is to perform a systematic analysis of the operational indicators of rhenium extraction. Obtaining the results of the analysis

will allow us to develop recommendations for further improvement of the technology and improvement of technical and economic indicators.

To increase the efficiency of the technological process and reduce the consumption of electricity and hydrogen, a new technology has been developed for producing rhenium metal powders from ammonium perrhenate using plasma.

To test the new technology, an enlarged laboratory plant (ELP) for the production of rhenium was also developed and manufactured. The basis of the enlarged laboratory is a vacuum chamber with a hemispherical body and an elongated cylindrical part. The chamber is equipped with many flanges that allow the installation of viewing windows, current leads, as well as the input of plasma-forming gas and pressure sensors. The chamber opens as wide as possible, thanks to the presence of a seal with a Viton or silicone gasket. The chamber is double-walled and allows to keep the wall temperatures low due to cooling with water. A large viewing window provides visual observation of ongoing plasma-chemical processes. Plasma processions are carried out at low pressures. The vacuum is provided by a mechanical pump. A condenser is installed between the reaction chamber and the vacuum pump, which retains the reduction reaction products such as water and ammonia. The condenser is made in the form of a spiral from a copper tube with a diameter of 10 mm and is cooled to a temperature of -30°C using a refrigeration unit. The plasma generator is an HF generator at a frequency of 50 kHz. The source of hydrogen is a hydrogen generator with a capacity of 25 l/h and a purity of 99.9995%. It can provide pressure up to 6 atm.

Chemical analysis of rhenium metal

Elements	Ag	Al	Li	S	P	Si	Mg	Na	K	Ca	Ti	V	Cr	Mn	Fe	Co	Ni	Cu	Zn	AS	Se	Pb	Au	Pt	Rb
%.mass	0,0010753	0,0005177	0,0000069	0,0004402	0,0001005	0,0002478	0,0000006	0,0000213	0,0003462	0,000012	0,00100336	0,0000063	0,0000561	0,0000102	0,0010705	0,0001311	0,0013156	0,0009627	0,0021269	0,0005025	0,0007884	0,0006338	0,0010719	0,0008334	0,0003469

Elements	Pd	La	Ce	Pr	Nd	Sm	Eu	Gd	Ho	Yb	Zr	Tl	Tm	W	Sn	Sr	Te	Sb	Sc	Mo	Er	Cd	Bi	B	Re
%. mass	0,0001362	0,0005525	0,0002679	0,0001099	0,000603	0,0002682	0,0000006	0,0000045	0,0000597	0,0000024	0,0000222	0,0003519	0,000003	0,0002898	0,000618	0,0000006	0,0019773	0,0056136	0,0020198	0,0041341	0,0000558	0,0001923	0,0022809	0,0004098	99,967731

Studies have been carried out on the processes of converting ammonium perrhenate into rhenium metal using samples of ammonium perrhenate at different loading layer thicknesses. The elemental composition of the obtained samples was determined by X-ray diffraction and inductively coupled plasma optical emission spectrometry. The optimal conditions for the conversion of ammonium perrhenate into rhenium metal have been determined. The purity of the obtained metallic rhenium ammonium perrhenate grade AR-00 was over 99.9%. When using special purity grade hydrogen as a reducing agent, the product yield from the stoichiometric composition AP-00 was more than 93%. At the same time, compared to traditional technology, the process temperature was reduced by more than half, and hydrogen consumption by up to 10 times.

References
1. Tim T. Werner, Gavin M. Mudd, Simon M. Jowitt, David Huston, Rhenium mineral resources: A global assessment, Resources Policy, Volume 82, 2023, 103441, ISSN 0301-4207, https://doi.org/10.1016/j.resourpol.2023.103441.

STUDY OF RADIATION DEFECT FORMATION PROCESSES IN SILICON CARBIDE

A.A. Lebedev, V.V.Kozlovski, M.E.Levinshtein, A.M.Strelchuk

Ioffe Institute, Politekhnicheskaya street 26, St.Petersburg 194021, Russian Federation

Increasing the reliability of the operation of nuclear power plants, space technology devices and already designed thermonuclear installations requires the use of electronics that are radiation-resistant to various ionizing converters: electron, proton, neutron, alpha, beta and gamma. This determined the relevance of the study.

As is known, radiation-resistant materials include semiconductors with high binding energy - diamond, boron nitride, GaN, SiC. The Physicotechnical Institute has been conducting research in the field of creating silicon carbide electronics for many years. The goal was set - using the accumulated reserves, to move towards the development of radiation-resistant electronics based on it. Its achievement also required solving problems of studying the processes of radiation defect formation in SiC. During the work, the following main results were obtained:

1. The parameters of the main radiation defects (RD) in the 4H- and 6H-SiC polytypes and the rate of their introduction were determined depending on the dose and type of irradiation [1,2].
2. The participation of the resulting RDs in the processes of radiative and non-radiative recombination has been established [3].
3. It has been shown that the main mechanism of radiation compensation of silicon carbide is the formation in the lower half of the band gap of RDs of an acceptor nature, which capture electrons from the conduction band, turning into negatively charged centers [4].
4. Prototypes of SiC-based nuclear particle detectors have been developed and manufactured [5].
5. The rates of carrier removal in epitaxial layers of SiC and in devices based on it (rectifier diodes, Schottky diodes, JBS, MOSFET) were determined [6,7].
6. It has been established that the main reason for radiation degradation of SiC devices is an increase in the resistance of lightly doped layers [8].
7. It is shown that the role of irradiation temperature is reduced to changing the conditions of secondary defect formation and the formation of the corresponding spectrum of defects. It was found that the radiation resistance of devices does not deteriorate with increasing temperature of their operation, but significantly improves [8,9].
8. The statistics of electron filling of RDs in SiC was studied, which made it possible to explain the observed significant discrepancy in the values of carrier removal rates obtained by different experimental methods, especially at high degrees of material compensation [9].

References
1.A.M.Strel'chuk, A. A. Lebedev, V.V. Kozlovski, N.S. Savkina, D.V. Davydov, V.V.Soloviev, M.G. Rastegaeva, Doping of 6H-SiC pn structures by proton irradiation, **Nuclear Instruments and Methods in Physics Research B 147 (1999) p 74-78**
2.Lebedev A.A., Veinger A.I., Strel'chuk A.M., Savkina N.S., V.V.Kozlovskii, Davydov D.V., *"Doping of n-type 6H-SiC and 4H-SiC with defects created with proton beam",* **J.of Applied Physics**, **88**, N11, 6265-6271 (2000).
3. Lebedev A.A., B.Ya. Ber, N.V.Seredova, D.Yu Kazantsev, V.V.Kozlovski, *Radiation-stimulated photoluminescence in electron irradiated 4H-SiC*, **Journal of Physics D: Applied Physics, 48, 485106 (2015)**

4. V.V.Kozlovski, A.A.Lebedev, E.V.Bogdanova, *Model for conductivity compensation of moderately doped n- and p-4H-SiC by high-energy electron bombardment*, **J. Appl.Phys., 117, 155702 (2015)**

5. N. B. Strokan, A. M. Ivanov, N. S. Savkina, A. M. Strelchuk, A. A. Lebedev, M. Syväjärvi, and R. Yakimova *." Detection of strongly and weakly ionizing radiation by triode structure based on SiC films"* **J. Appl. Phys. 93, 5714-5719 (2003).**

6. V.V.Kozlovski, V.V.Emtsev, A.M.Ivanov, A.A,Lebedev, G.A.Oganesyan, D.S.Poloskin, N.B.Strokan, *Charge carrier removal rates in n-type silicon and silicon carbide subjected to electron and proton irradiation.* **Physica B, 404, (2009) 4752-4754.**

7. A.A. Lebedev, V.V. Kozlovski, M.E. Levinshtein, A.E. Ivanov, A.M. Strel'chuk, A.V. Zubov, Leonid Fursin, *Impact of 0.9 MeV electron irradiation on main properties of high voltage vertical power 4H-SiC MOSFETs*, **Radiation Physics and Chemistry 177 (2020) 109200**

8.V.V.Kozlovski, A.A.Lebedev, V.V.Emtsev, G.A.Oganesyan, *Effect of the Energy of Recoil Atoms on Conductivity Compensation in Moderately Doped n-Si and n-SiC under Irradiation with MeV Electrons and Protons,* **Nuclear Instruments and Methods in Physics Research Section B 384 (2016) 100-105.**

9.V.V.Kozlovski, A.A.Lebedev, M.E.Levinshtein, S.L.Rumyantsev, J.W.Palmour, *Electrical and noise properties of proton irradiated 4H-SiC Schottky diodes,* **JAP, 123, 024502, 2018**

10. A.A. Lebedev, V.V. Kozlovski, K.S.Davydovskaya, R.A. Kuzmin, M.E. Levinshtein, A.M. Strel'chuk, *Features of the Carrier Concentration Determination during Irradiation of Wide-Gap Semiconductors: The Case Study of Silicon Carbide,* **Materials 2022 15, 8637.**

SPIN DYNAMICS IN INDIRECT BAND GAP QUANTUM DOTS

T.S. Shamirzaev[1], D.S.Smirnov[2], D. R. Yakovlev[2,3] and M. Bayer[3]

[1]Rzhanov Institute of Semiconductor Physics of SB RAS, 13 pr.Lavrentieva, Novosibirsk 630090, Russia
[2]Ioffe Institute, Russian Academy of Sciences, 194021 St. Petersburg, Russia
[3]Experimentelle Physik 2, Technische Universität Dortmund, 44221 Dortmund, Germany
e-mail: tim@isp.nsc.ru

Abstract. A new spin orientation mechanism for localized electrons: dynamic electron spin polarization provided by nuclear spin fluctuations has been revealed. The detrimental effect of nuclear spin fluctuations can be harnessed and employed to provide angular momentum for the electrons via the hyperfine interaction in a weak magnetic field. For this, the sample is illuminated by an unpolarized light, which directly polarizes neither the electrons nor the nuclei. The proof of principle experiment is performed on momentum-indirect excitons in (In,Al)As/AlAs quantum dots, where in a magnetic field of 17 mT the electron spin polarization of 30% is measured.

1. Introduction

Generation of electron and hole spin polarization can be achieved in several ways. The main approaches to spin orientation are: optical spin orientation [1] and thermal spin polarization in a magnetic field [2]. The first one is based on the transfer of the angular momentum from circularly polarized photons to electrons through the spin-orbit interaction. The second approach requires a lowering of the lattice temperature, so that the thermal energy becomes smaller than the electron Zeeman splitting. It can be enhanced in nonequilibrium conditions. We have suggested another approach to spin polarization: the dynamic electron spin polarization [3]. In contrast to the optical spin orientation, the proposed mechanism does not require circular polarization of the optical excitation. In contrast to the thermal spin polarization, we consider weak magnetic fields, for which the electron Zeeman splitting is much smaller than the thermal energy. This mechanism was approved experimentally for (In,Al)As/AlAs quantum dots (QDs) [3].

2. Experiment

The studied self-assembled (In,Al)As QDs embedded in an AlAs matrix were grown by molecular-beam epitaxy on a semi-insulating (001)-oriented GaAs substrate with a 400-nm-thick GaAs buffer layer. The structure contains one QD layer sandwiched between two 70-nm-thick AlAs layers. The nominal amount of deposited InAs is about 2.5 monolayers. The QDs were formed at the temperature 520°C with a growth interruption time of 20 s. The top AlAs barrier is protected from oxidation by a 20-nm-thick GaAs cap layer. From the growth conditions and model calculations, we conclude that the average QD composition is $In_{0.75}Al_{0.25}As$ [14]. The size and density of the lens-shaped QDs were measured by transmission electron microscopy, yielding an average diameter of 12 nm and a density of about 2×10^{10} dots per cm^2. The relatively low QD density prevents carrier redistribution between the QDs. The sample was placed in a liquid helium bath cryostat. The temperature for all experiments was fixed at T=1.8 K. Low magnetic fields in the millitesla range were generated by an electromagnet. The photoluminescence (PL) was excited nonresonantly with the laser photon energy exceeding the direct band gap of the AlAs matrix, which is equal to 3.099 eV. We used the third harmonic of a Q-switched Nd:YVO$_4$ pulsed laser with a photon energy of 3.49 eV, a pulse duration of 5 ns, and a repetition rate of 1 kHz. The time delay between the pump pulse and the start of PL recording, t_d, was varied from zero up to 1 ms. The duration of PL recording, i.e., the gate window t_g was varied from 1 ns to 1 ms. The signal intensity and the time resolution of the setup depend on t_d and t_g.

3. Results and discussions

An exciton localized in a QD, which consists of an electron with spin projection on the growth z axis $S_z=\pm1/2$ and the heavy hole with spin $J_z=\pm3/2$. Therefore, four exciton states with spin $F_z=\pm1$ and ±2 are formed. The exchange interaction splits these exciton states by δ_0 into two upper bright states with the total spin $F_z=\pm1$ and the lower dark ones with $F_z=\pm2$. The bright excitons can radiatively recombine and have the lifetime τ_b, while the radiative recombination of the dark excitons is spin forbidden. The dark excitons can recombine via mixing with bright one, so they radiative recombination taken place at the transitions from dark to bright states. Due to these optical selection rules, the dark exciton states are preferentially populated.

In zero magnetic field the splittings between the dark and bright states with $F_z=+1$ and $+2$ or $F_z=-1$ and -2, are equal. However, in the longitudinal magnetic field B_z, the splittings between the dark and bright states with the total angular momenta begins different, so the transitions from the dark to bright states go with different rates. As a result population of bright states with $F_z=+1$ and -1 begins not equal. Since they are accompanied by the electron-nuclear spin flips in opposite directions, the angular momentum is extracted from nuclei to exciton. Our theoretical calculation yields the polarization degree of electron-in-exciton [3]:

$$P_e = \frac{-2B_z B_{exch}}{B_{exch}^2 + \Delta_B^2 + B_z^2} \qquad (1)$$

where B_{exch} is proportional to the electron-hole exchange strength and Δ_B is the typical Overhauser field of randomly oriented nuclear spins.

The proof of principle experiments were performed with momentum-indirect excitons in (In,Al)As/AlAs QDs of the type-I. We performed polarization and time resolved photoluminescence (PL) measurements after nonresonant and unpolarized pulsed optical excitation.

To dynamically polarize electron spins, we apply the longitudinal magnetic field of 17 mT (Faraday geometry). In Fig. 1(a) we show the PL circular polarization as a function of time, detected at the energy of 1.70 eV. The degree of circular polarization is defined as $P_c = (I^+ - I^-)/(I^+ + I^-)$, where $I^{+/-}$ are the intensities of $\sigma^{+/-}$ polarized emission. The polarization appears with a delay of 15 μs after the pump pulse and saturates after 100 μs. It is in line with model prediction that the dynamic polarization appears only after recombination of the bright excitons. It is noteworthy that the PL stays polarized up to 1 ms.
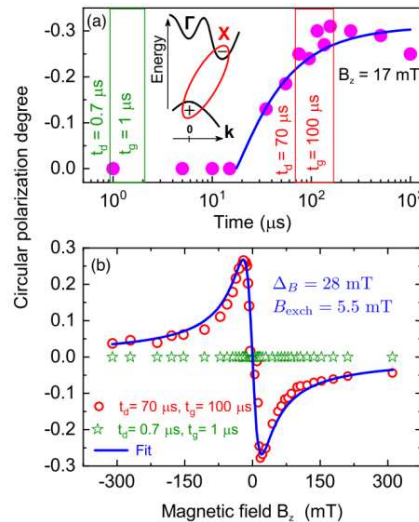
Fig. 1. *(a) Dynamics of PL circular polarization degree measured at $B_z=17$ mT and T=2 K; the integration time is 5 μs. Vertical lines show time-integration windows for (b). (Inset) The band diagram of the momentum-indirect (In,Al)As/AlAs QDs. (b) Magnetic field dependencies of the polarization degree measured at $t_d=0.7$ (green stars) and $t_d=70$ μs (red circles) with the integration*

windows of $t_g=1$ and $t_g=100$ μs, respectively. Blue line is a fit after Eq.1 with $\Delta_B=28$ and $B_{exch}=5.5$ mT.

The magnetic field dependence of the dynamic polarization integrated for two time windows is shown in Fig.1(b). This is the main experimental result. The absolute value of $P_c(B_z)$ increases in weak fields, reaches maximum of about 0.3 at $B_Z=17$ mT, and then monotonously decreases tending to zero in high fields. Fitting this dependence with Eq.1 we find two parameters: $\Delta_B=28$ and $B_{exch}=5.5$ mT. The strength of the hyperfine interaction is in good agreement with measurements of optical spin orientation in transverse and longitudinal magnetic fields in a similar sample [4], which supports our interpretation. Using the electron g factor $g_e=2$, we find the splitting between bright and dark states $\delta_0=0.6$ μeV.

4. Conclusions
A new spin orientation mechanism for localized electrons: dynamic electron spin polarization provided by nuclear spin fluctuations has been revealed. The dynamic electron spin polarization has the following advantages: (i) It requires weak magnetic fields, which can be easily modulated. (ii) It uses nonresonant and unpolarized optical excitation. (iii) It is temperature independent, as long as the spin relaxation is dominated by the hyperfine interaction. (iv) 100% electron spin polarization is feasible. All that makes dynamic spin polarization very attractive for the spin orientation in nanodevices for quantum information processing.

References
Optical Orientation, edited by F. Meier and B. P. Zakharchenja (North-Holland, Amsterdam, 1984).
E. L. Ivchenko, Magnetic circular polarization of exciton photoluminescence, Phys. Solid State **60**, (2018) 1514.
D. S. Smirnov, T. S. Shamirzaev, D. R. Yakovlev, and M. Bayer, Phys. Rev. Lett. **125**, (2020) 156801.
J. Rautert, T. S. Shamirzaev, S. V. Nekrasov, D. R. Yakovlev, P. Klenovský, Yu. G. Kusrayev, and M. Bayer, Phys. Rev. B **99**, (2019) 195411.

THIN FILM MATERIALS FOR PHOTOVOLTAICS: STATE OF THE ART AND NEW PERSPECTIVES

A.Romeo, E. Artegiani, N. Torabi, S.Olavil Karaiy, I. Anefnaf, M. Mukhtar
University of Verona, Italy

Binary alloys like CdTe, Sb_2Se_3 or Sb_2S_3 as well as quaternary compounds such as CuInGaSe2 - CIGS-and Cu2SnZn(S,Se)4 -CZTS-can be deposited on different substrates (glass, polymers, ultra-thin glass) and deliver high-efficiency flexible devices. With a band gap that ranges from 1.2 to 1.7 eV and with an exceptionally high absorption coefficient, they have optimal photovoltaic characteristics. In particular, CdTe has reached an efficiency of 22.4% and has demonstrated a remarkable robustness that allows mass-scale production. On the other hand, Sb_2Se_3 has a unique ability for 1-D conduction along a ribbon-like structure whose orientation strongly affects electronic transport and a champion absorption coefficient that allows for sub-micrometer thick absorbers. On the other hand, more complex compounds assure high efficiencies (CIGS) or good performance with non-vacuum techniques (CZTS).
In this work, we will present all the latest developments for the production of these materials, together with their based window layers and contacts. In particular, we will show the fine engineering of $CdSe_xTe_{1-x}$ graded band gap for CdTe which brings to an efficiency of about 16% for a 2 micrometer thin CdTe layer, a new CdSe buffer layer for Sb_2Se_3, and a novel spraying technique for CZTS.

SYNTHESIS, STRUCTURE AND PROPERTIES OF THE $Ag_{1-x}Cu_xGaSe_2$ SOLID SOLUTIONS – NEW SEMICONDUCTOR MATERIALS FOR PHOTOCATHODES IN DIRECT ELECTROCHEMICAL DECOMPOSITION OF WATER

RakitinV.V.[1], _Gapanovich M.V._[1,2], _Rabenok E.V._[1], _Stanchik A.V._[3], _Gremenok V.F._[3], _Kobyliatski A.V._[3]

[1]_Federal Research Center of Problems of Chemical Physics and Medicinal Chemistry RAS, Chernogolovka, Russian Federation_
[2]_Faculty of Fundamental Physical and Chemical Engineering, M.V. Lomonosov Moscow State University, Moscow, Russia_
[3]_Scientific-Practical Materials Research Centre, National Academy of Sciences of Belarus, Minsk, Belarus_
tel: +7(49652) 2-17-93, e-mail: domi-tyan@yandex.ru

Currently, there is a great interest in development of photoelectrochemical cells that can be used as fuel production sources, in particular for the direct water decomposition under light radiation in order to produce pure hydrogen. To carry out this process in a photoelectrochemical cell, it is necessary that the band gap of photocathode semiconductor be within the optimal value of $E_g \sim 1.7$ eV [1]. At the same time, thin (1-2 μm) films of compounds of the I-III-VI group with chalcopyrite structure (E_g in the range from 1 to 2.4 eV) can act as an alternative to expensive and sufficiently effective photocathodes based on semiconductors of the III-V group. The $CuGaSe_2$ ($E_g = 1.68$ eV) and $AgGaSe_2$ ($E_g = 1.6–1.8$ eV) compounds, as well as the $Ag_{1-x}Cu_xGaSe_2$ solid solutions are of particular interest [1, 2]. At the same time, it was found that photocathodes in which ~6% of copper is replaced by silver demonstrate a significantly higher photocurrent compared to analogues based on $CuGaSe_2$ [3].

In this work, a wide range of materials of the $Ag_{1-x}Cu_xGaSe_2$ (0≤x≤1) solid solutions was synthesized for the first time by solid-phase ampoule synthesis. To study structure and composition of the samples, a combination of XRD (PANalitical Aeris, Cu-K_α) and Raman spectroscopy (Bruker Senterra micro-Raman system (radiation 532 nm)) methods was used. Fig. 1 (*a*) shows the XRD data for synthesized compounds. One can see that a shift of the main lines is observed during the transition from $CuGaSe_2$ to $AgGaSe_2$. At the same time, a type of crystal lattice remains tetragonal (s.g. *I*-42d) for all samples. The lattice parameters change from *a*=5.6142(15) Å, *c*=10.997(8) Å and *V*=346.62(22) Å^3 for $CuGaSe_2$ to *a*=5.9895(10) Å, *c*=10.878(5) Å, *V*=390.25(13) Å^3 for $AgGaSe_2$. Fig. 1 (*b*) shows the Raman spectra. One can see that the maximum position of the main line shifts from 184 cm^{-1} for $CuGaSe_2$ to 177 cm^{-1} for $AgGaSe_2$.
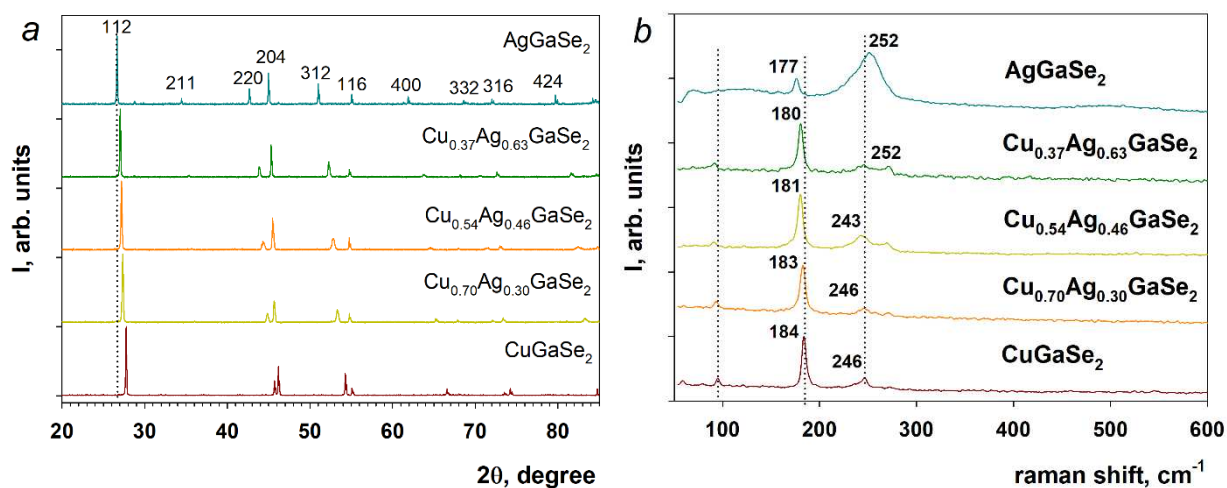
Fig. 1. XRD data (*a*) and Raman spectra (*b*) of the $Ag_{1-x}Cu_xGaSe_2$ ($0 \leq x \leq 1$) solid solutions

The lifetime of current carriers have measured by time-resolved microwave photoconductivity (universal research facility «Unit for determining the lifetime of photogenerated current carriers by measuring microwave photoconductivity in the frequency range of 36 GHz») in wide temperature range. The time resolution of the electric circuit was ~5 ns. Photoconductivity was excited with an LGI 505 nitrogen laser (wavelength $\lambda = 337$ nm, pulse duration 8 ns, $I_{max} = 10^{16}$ photons/cm^2 per pulse). This study has shown that the lifetimes of current carriers vary depending on the composition [4].

1. Yubin Chen, Xiaoyang Feng, Maochang Liu et al. // Nanophotonics. 2016. V. 5. № 4. P. 524.
2. Valderrama R.C., Sebastian P.J., Enriquez J.P. et al. **//** Sol. Energy Mater. Sol. Cells. 2005. V. 88. P. 145.
3. Li Zhang, Tsutomu Minegishi, Jun Kubota, Kazunari Domen **//** Phys. Chem. Chem. Phys. 2014. V. 16. P. 6167.
4. Rabenok E.V. and Gapanovich M.V. // High Energy Chem. 2023. V. 57. № 2. P. 214.

SURFACE MODIFICATION OF CARBON NANOTUBES FOR BIOMEDICAL APPLICATIONS

Khaydarov R.R. [1], *Gapurova O.U.*[1], *Praveen Thaggikuppe Krishnamurthy*[2]

[a]Institute of Nuclear Physics, Tashkent, Uzbekistan
[b]Department of Pharmacology, JSS College of Pharmacy (JSS Academy of Higher Education & Research), Tamil Nadu, India
renat@inp.uz

In 2021-2023, the Uzbek-Indian joint project No. UZB-Ind-2021-77 "CD133 mAbs surface modified carbon nanotubes loaded with survivin siRNA and Paclitaxel for the treatment of non-small cell lung cancer" has been executed in the Institute of Nuclear Physics of the Academy of Sciences of the Republic of Uzbekistan. This project is devoted to creating nanocarriers for target delivery of medications that allows to increase their concentration in certain places and prevent/restrict their accumulation in healthy sites. The targeted transport also allows to increase action time and efficiency of drugs, to decrease their side effects. As a part of the mentioned project, methods of surface modification of carbon nanotubes have been developed. They allow to produce nanocomposites with the following modifications: 1) Nanocarbon-Polyethyleneimine; 2) Carbon nanotube - Paclitaxel, 3) Carbon nanotubes conjugated with CD133 monoclonal antibody; 4) CD133 mAb and Survivin siRNA surface functionalized SWCNT internally loaded Paclitaxel (cf. Fig 1.)
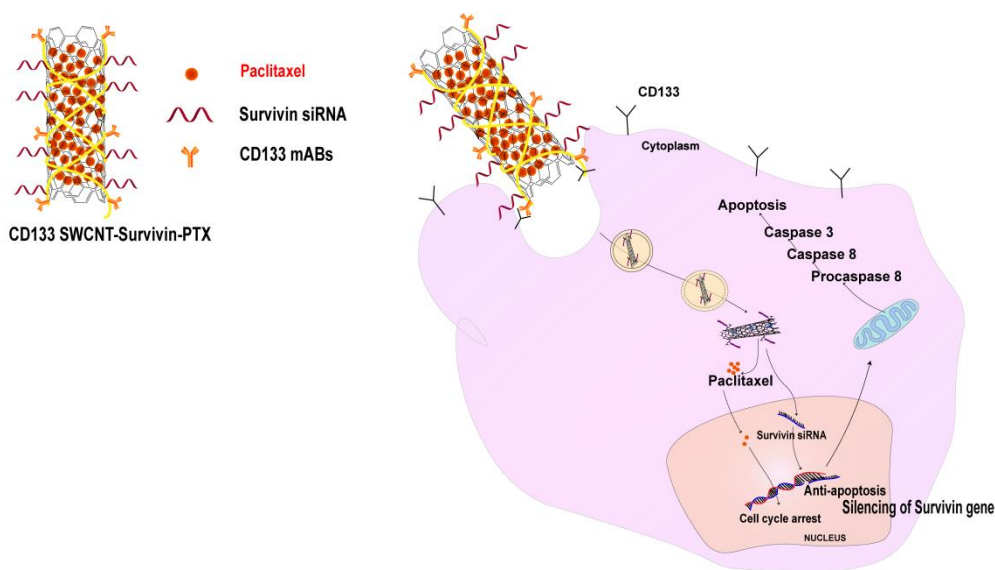
Figure 1. Targeted delivery of CD133-SWCNT-Survivin-PTX formulation (CD133 mAb and Survivin siRNA surface functionalized SWCNT internally loaded Paclitaxel)

MATERIALS SCIENCE APPROACHES TO RECHARGEABLE BATTERY DEVELOPMENT

I.Ashurov, U.Choriev, A. Avvalboyev, Sh.Iskandarov, T.Turdaliev, Kh.Ashurov, M.Kurbanov

Arifov Institute of Ion–Plasma and Laser Technologies, Academy of Sciences of the Republic of Uzbekistan,
Tashkent, 100125 Uzbekistan

The imperative to transition from non-renewable fossil fuels to sustainable alternatives in electricity production has intensified the focus on various energy storage systems. Vanadium redox flow batteries (VRFBs) emerge as a promising solution for large-scale energy storage, offering advantages such as enhanced charging and discharging rates, environmental sustainability, and extended service life. In response to challenges associated with the specific energy density (~25 Wh/L) of VRFBs, this study pioneers an innovative approach by integrating recycled vanadium pentoxide. The incorporation of recycled material not only holds the potential to enhance the specific energy density but also offers promising prospects for improving economic viability and ecological sustainability in the context of VRFB technology.

In the realm of lithium-ion batteries (LIBs), traditional anodes commonly utilize graphite or carbon-based materials due to their stable structure and favorable electrical conductivity. Our investigation intricately explores contemporary trends, challenges, and prospects associated with silicon (Si) and its oxides (SiO, SiO_2) as potential LIB anode materials. Despite their superior theoretical capacities (Si-4200, SiO – 2600, SiO_2 – 1965 mAh g^{-1}) compared to graphite (372 mAh g^{-1}), the integration of Si and its oxides poses challenges, particularly concerning volumetric expansion during charge-discharge cycles. SiO_2, derived from metallurgical industry waste, emerges as a promising alternative due to its commendable attributes, including moderate volume expansion and cost-effectiveness.

The transition to aluminum batteries gains momentum due to their lightweight nature, cost-effectiveness, and impressive theoretical specific capacities. However, the selection of cathode materials for aluminum batteries presents scientific challenges. Graphene, a two-dimensional material with exceptional electronic and structural properties, is identified as an ideal candidate. Research involving commercially available graphene paper treated with $AlCl_3$-EmimCl electrolyte solutions reveals a crucial correlation between electrolyte ratios and electrochemical performance.

Through the application of a material science framework, our research systematically propels the evolution of three distinct battery categories, intricately exploring the details of battery technology. This methodological approach not only facilitates substantial contributions to the field but also places a pronounced emphasis on enhancing sustainability, efficiency, and economic viability across a diverse spectrum of energy storage systems.

X-RAY ANALYSIS OF MANGANESE-DOPED SINGLE CRYSTAL SILICON AND EPR SPECTRA OF SAMPLES WITH VARIOUS DEGREES OF COMPENSATION

Sh. B. Utamuradova, A. Sh. Mavlyanov, Kh. J. Matchonov

Institute of Semiconductor Physics and Microelectronics, Tashkent, 100057, Uzbekistan
e-mail: husniddin94_04@bk.ru

The aim of the present research was to investigate the behavior of manganese atoms in the silicon crystal lattice by implementing X-ray diffraction analysis and thus, the phase states of manganese atoms in silicon have been studied using this technique.

For study of structural and phase states of silicon samples doped with manganese impurity atoms the authors used for the experiment the Empyrean Malvern X-ray diffractometer. IN order to determine peak maximums OriginPro2019 program was implemented. X-ray diffraction measurements were carried out in Bragg-Brentano $2\theta_Б$ beam geometry in the range from 10° to 90° continuously at a scanning step of 0.33 deg/min and an angular step of 0.0200 (deg).

The experimental results obtained using the X-ray diffraction method for sample of n-Si<Mn> are shown on Fig.1.
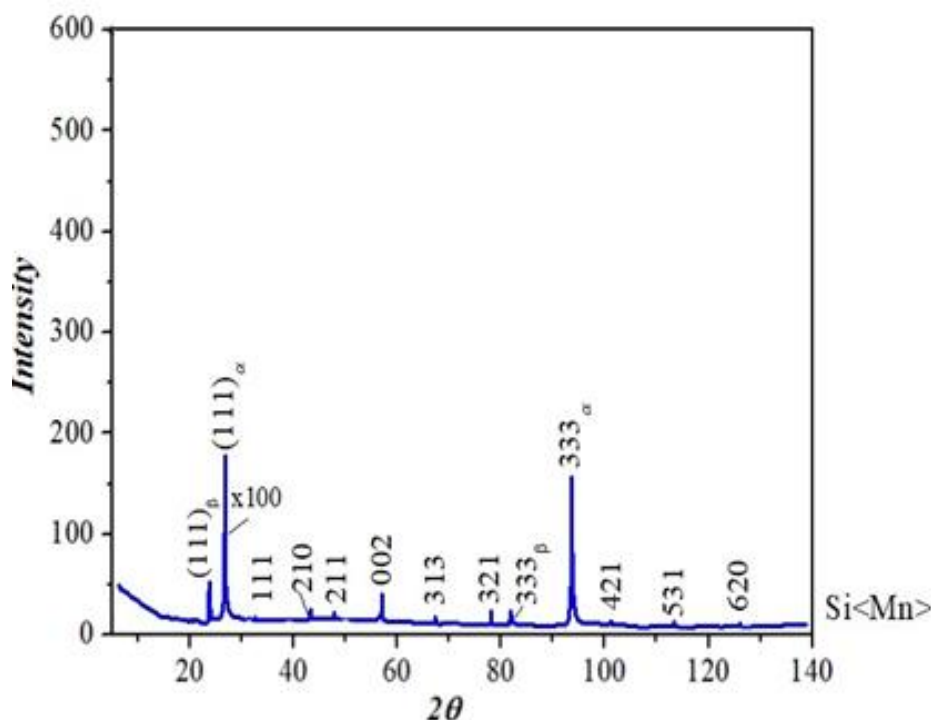
Fig. 1. Diffractogram of *n-Si<Mn>* single crystals.

It's worth noting that the diffraction pattern of the studied sample differs from the diffraction pattern of n-Si<Mn> sample with a SiO_2 layer and there is no diffuse reflection at $2\theta \approx 17.4°$ on X-ray diffraction pattern and we witness a decrease in the intensity of structural reflection $(111)_\alpha$ by 2.5 times, the intensity of the third reflection $(333)_\alpha$ by 1.7 times, respectively [1].

The intensity of the structural reflection (002) reduces, while the intensities of reflections (313), (513) and (620) do increase slightly significantly and they ensure diffraction shift in the spectra of the diffraction pattern of the n-Si<Mn> sample towards smaller angles. Dimensions of crystallites and the lattice parameter have been determined from half-width of the (111) structural line for n-Si<Mn> and had 58 nm and a_{Si}=0.5419 nm, respectively. It's important to take into

24

consideration that lattice parameter of the sample proved to be slightly less than the lattice parameter (a_{Si}=0.5426 nm) of *n-Si‹Mn›* sample with SiO_2 surface layer. However, this has possibly ensured a shift of structural reflections in the *n-Si‹Mn›* diffraction pattern towards smaller scattering angles.

At the same time a thorough study of EPR spectra of samples with various degrees of compensation were performed.

The results of studies in overcompensated *n - Si‹Mn›* samples with a resistivity $\rho \leq 2 \cdot 10^2$ Ω·cm at 3.8 K have revealed that a spectrum was observed that consists of six ultrathin lines, due to interaction of d - electrons with their own core Mn^{55} (I = 5 /2). The measured parameters of the spectrum had the values g = 2.362 ± 0.003, A = (58.0 ± 0.2) G. The spectrum had a strong temperature dependence and completely disappeared at T=8 K [2].

Spectral parameters correspond to neutral centers of manganese intercalation - $Mn^0(3d^7)$. As $\rho > 5 \cdot 10^2$ Ω·cm have increased, this center was ionized. It should be noted that the spectra of ionized $Mn^+(3d^6)$ and $Mn^{++}(3d^5)$ centers were observed only in newly prepared Si‹Mn› samples. In times of long-term storage of these samples at room temperature, the spectra of ionized manganese centers tended to disappear.

Besides that, in all overcompensated *Si‹B,Mn›* samples with ρ>5·10^2 Ω·cm at low temperatures (~ 4 K) in virtually absent outer magnetic field, the spectrum consisting of a large number of lines, the position and intensity of which changed from sample to sample, had occurred [2].

Thus, based on the analysis of the above experimental results one can make the following conclusions:

- the value of the lattice parameter of the sample *n-Si‹Mn›* is 0.5419 nm and caused a shift of structural reflections in *n-Si‹Mn›* diffraction pattern towards smaller scattering angles;

Having analyzed the above experimental data we can conclude that the diffraction patterns of n-Si<Mn> on the surface exhibit several selective structural reflections with different intensities. It is shown that the lattice parameter of Si<Mn> samples is slightly less than the lattice parameter of Si<Mn> samples with a SiO_2 film on the surface, and this leads to a shift of structural reflections in the Si<Mn> diffraction pattern towards smaller scattering angles.

REFERENCES

1. Utamuradova, Sh.B., Matchonov, Kh.J., Khamdamov, J.J., & Utemuratova, Kh.Y. (2023). X-ray diffraction study of the phase state of silicon single crystals doped with manganese. *New Materials, Compounds and Applications*, *7*(2), 93-99.

2. Sh. Askarov, B. Sharipov, A. Mavlyanov, Sh. Saliyeva, D. Shukurova, A. Mavlonov. Paramagnetic and ferromagnetic centers of manganese in silicon // International symposium on magnetism, Samarkand, 2023, July 2-6, Pp.120.

AMPLIFIED SPONTANEOUS EMISSION IN ZnO MICRORODS

R.R. Jalolov[1,2], B.N. Rustamova[1], Z.Sh. Shaymardonov[1,2], Sh.Z. Urolov[1,3]

[1]Arifov Institute of Ion-Plasma and Laser Technologies, Tashkent 100125, Uzbekistan
[2]The National University of Uzbekistan, Tashkent 100174, Uzbekistan
[3]Tashkent Institute of Irrigation and Agricultural Mechanization Engineers, Tashkent 100000, Uzbekistan
rr_jalolov@iplt.uz

The development of miniaturization in the field of electronics and the production of various optoelectronic devices requires a new generation of low-cost, energy-efficient, nano- or micro-sized semiconductor lasers. Zinc oxide (ZnO) based microrods and nanowire lasers are considered as possible candidates for employment in the Ultraviolet (UV) range. Moreover, various ZnO nanostructures (thin films, nanorods, etc.) are also suitable for fabricating UV optoelectronic devices and light sources. ZnO is a material with large exciton binding energy (~60 meV) and a direct wide band gap (E_g ~ 3.37 eV) [1,2]. Nowadays, these nanostructures are a subject of intense research. However, in nano-sized semiconductor lasers, due to the small size of the material and the relatively high probability of spontaneous emission, the lower limit of generation is greater than in other lasers [3-4]. Another important fact is that if the light waves propagating inside the nanorods are greater than or equal to the size of the nanorods, the forced amplification of light does not occur as a result of light scattering or diffraction. Therefore, there is a lower limit to the size of nanorods in obtaining nanoscale lasers operating in the UV region.

Typically, a photoluminescence (PL) spectrum of ZnO nanostructures consists of two parts: a near band edge (NBE) emission centered at around 380 nm and defect related emission bands in the visible range [1]. The photoluminescence characteristics of ZnO nanostructures strongly depend on their crystalline quality, which in turn is determined by growing conditions and methods and post-grown treatment history. The defect related emission bands can appear in violet–blue (390–460 nm) or/and green (500–520 nm) or/and yellow–orange (560–600 nm) or/and red (650 nm) ranges. The NBE emission, in addition to the emission of free exciton recombination, can also contain bands caused by transitions to or from the defect related levels which are located near conducting or valence bands.

The photoluminescence characteristics of ZnO nanostructures also depend on excitation intensity. An increase in excitation intensity gives rise to the appearance of new emission bands. Their intensity may increase stronger and as a result, they suppress or overlap some bands presented at low excitation intensities. For example, under high intensity excitation, the PL spectrum from ZnO nanostructures is dominated by a band located at around 389 nm. Usually, this so-called P-band appears with an increase in excitation intensity and it has been attributed to exciton–exciton or exciton–optical phonon scattering collisions [3-6]. Many studies have been devoted to investigate the lasing properties of the P-band. However, most investigations have proved only an amplified spontaneous emission (ASE) behavior of the band. It should be noted that ASE has some features similar to laser action. A bandwidth of ASE decreases with an increase in the excitation intensity and ASE has directionality and shows threshold behavior. Nevertheless, ASE only precedes laser action. A stable laser generation requires also presence of a resonator and round-trip, coherent amplification of light.

In the studies, the influence of the excitation light intensity on the nature of the emission bands observed in the PL spectrum of ZnO mircorods synthesized by vapor phase transport method at high temperatures was studied. The pulses of the N_2 laser (λ= 337.1 nm, P= 10 kW, repetition rate 100 Hz) were used as the photoluminescence excitation source. PL spectra excited on ZnO mircorods were recorded using a device that integrates gate signals with a gate width of 40 ns - a boxcar integrator. In the study of the dependence of the PL properties on the intensity of the excitation light, the position where the PL spectrum recording axis was parallel to the growth

direction of the mircorods was selected, and the intensity of the excitation light was changed using neutral filters. Using a long-focus UV lens, the excitation laser beam was focused on the sample in the form of a circle with a diameter of 400 μm, and the angle between the excitation beam and the PL spectrum recording axis was kept constant at ~25°. All experimental studies were carried out at room temperature.
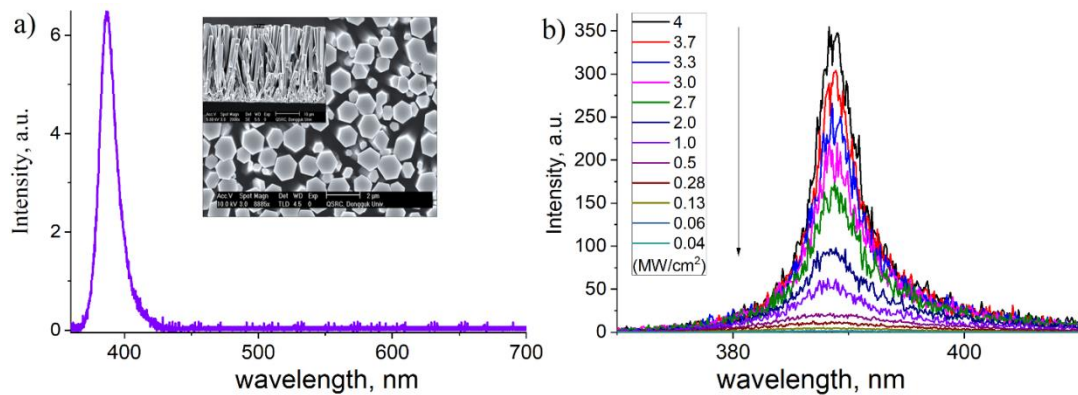

Figure 1. a) PL spectrum of ZnO mircorods and their SEM images; b) PL spectra of ZnO mircorods recorded at different values of excitation light intensity

The as-synthesized ZnO mircorods were hexagonal in shape, highly ordered on the substrate surface, and grew in a perpendicular direction to the substrate. The base and side surfaces of the mircorods were smooth and flat, exhibiting excellent crystallinity. The length of the mircorods is ~30 mm, and the diameter is about 0.5-1.5 mm (inset of Fig. 1a). According to the results of the research, the spectrum of emission generated by ZnO mircorods excited by high-power nitrogen laser pulses consists of a high-intensity, narrow emission band in the UV region with a maximum at a wavelength of ~387 nm (Fig. 1b). The effects of the excitation light intensity on the PL properties of ZnO mircorods were studied in the studies. It was found that a narrow emission band with a high intensity, located at a maximum wavelength of 387 nm, is observed in ZnO mircorods under the influence of UV light. As the intensity of the excitation light increased, the PL intensity also increased, and the maximum of the emission band was redshifted to 389 nm (Fig. 1b). It was also observed that the half-width of the emission band narrowed simultaneously with the increase in the intensity of the emission band. As the excitation light intensity increased from 0.06 to 4 MW/cm^2, the full width half maximum of the emission band decreased from ~15 nm to ~4 nm. The narrowing of the emission band occurred almost symmetrically. As the power density of the excitation light increases, the narrowing of the spectrum indicates the normal spontaneous emission enhancement process.

In conclusion, it can be said that these results obtained on the enhancement of spontaneous emission in ZnO mircorods serve to create fundamental foundations for the creation of a new generation of nanolasers operating in the ultraviolet field.

References

1. Ü. Özgür, Ya. I. Alivov, C. Liu, A. Teke, M. A. Reshchikov, S. Doğan, V. Avrutin, S.-J. Cho, and H. Morkoç, J. Appl. Phys. **98** (2005) 041301.
2. T. W. Kang, Sh. Yuldashev and G. N. Panin, in *Handbook of Semiconductor Nanostructures and Nanodevices*, Edited by A. A. Balandin and K. L. Wang (American Scientific Publishers, Los Angeles, 2005).
3. A. E. Siegman, Lasers. University Science Books, Sausalito, CA, 1986.
4. Lee W. Casperson. Threshold characteristics of multimode laser oscillators. // Journal of Applied Physics. 1975. 46. 5194.

IMPACT OF VACUUM TEMPERATURE-DESORPTION ON DEFECTS OF LASER-INDUCED GRAPHENE

G.S. Boltaev,[1,2,3] B.G. Atabaev,[4] Sh.R. Kamalov,[4] A.I. Kamardin,[5] V.M. Rotshteyn,[4] B.R. Sobirov,[4] and B.X. Eshchanov[3]

[1] Department of Physics, American University of Sharjah, Sharjah 26666, UAE
[2] Institute of Fundamental and Applied Research, TIIAME National Research University, Kori Niyoziy 39, Tashkent 100000, Uzbekistan
[3] Department of Physics, Faculty of Physics and Chemistry, Chirchik State Pedagogical University, 104 Amir Temur, Chirchik 111700, Uzbekistan
[4] Institute of Ion-Plasma and Laser Technology, Durmon yuli 33, Tashkent 100125, Uzbekistan
[5] Scientific Production and Design Centre Academpribor, Uzbekistan Academy of Sciences, Durmon yuli 33, Tashkent 100125, Uzbekistan

Correspondence: gboltaev1985@gmail.com

Laser-induced graphene (LIG) is a process that involves using a laser to create a graphene-like material on various substrates such as polymers, paper, or even food [1]. This process has gained significant attention due to its simplicity, low cost, and potential applications of LIG materials in various fields such as flexible electronics, sensors, energy storage devices, and even water purification [2,3]. Some of the key advantages of LIG include its ability to be easily patterned, its high electrical conductivity, and its compatibility with flexible substrates. Research on laser-induced graphene is ongoing, with efforts focused on improving the quality and properties of the material, as well as exploring new applications [4,5]. While there are still challenges to overcome, such as scalability, reproducibility and defects, the actuality of laser-induced graphene as a promising material for various applications is clear.

The most important defects are structural defects such as vacancies, grain boundaries, and edge defects that can form in the graphene structure during the laser-induced conversion process. These defects can affect the electrical, mechanical, and thermal properties of LIG. Addressing these defects in LIG is crucial for enhancing its performance and enabling widespread application in various fields. Research efforts are focused on developing techniques to minimize defects, improve the quality of LIG, and optimize its properties for specific applications.

One of the techniques to reduce such structural defects of LIG is a vacuum temperature-desorption of chemically bonded atoms or molecules from multilayer graphene, which can vary depending on the specific experimental conditions and the nature of the multilayer graphene. However, in general, the desorption temperature for carbon from multilayer graphene is typically in the range of 600 °C to 900 °C under high vacuum conditions. This temperature range is often required to effectively remove adsorbed species and contaminants from the surface of multilayer graphene. It's important to note that the exact desorption temperature may need to be determined through experimentation and optimization for the specific application and the particular characteristics of the multilayer graphene being used.

Here we textured porous 3D-LIG on the surface of polyimide (PI) by using ultrafast femtosecond laser pulses in normal conditions The 3D porous LIG containing a few layers of graphene and structural defects was created by applying a continuous scan regime of the ultrafast laser ablation process. The continuous laser scanning options led to a decrease in the electric resistance of the LIG formed on the surface of PI. We applied a vacuum temperature-desorption method to study the correlation between temperature and intensity of the defects in the Raman spectra of LIG in vacuum conditions. Raman spectra showed that, despite the high temperature of femtosecond laser plasma of 5000 K, a polyimide temperature of several hundred degrees is not enough to form low-defect graphene layers. To anneal furnace defects and pores, vacuum annealing of graphene has been proposed to clean polyimide impurities from adsorbed oxygen and stimulate the coalescence of

vacancies and diffusion of carbon in the graphene lattice due to hydrogen desorption. A new method was developed: graphene was vacuum annealed at 500°C for 45 minutes with liquid nitrogen vapour injected before depressurizing the chamber to prevent the adsorption of oxygen impurities. Comparative Raman analysis of the D/G peak ratio spectra showed that vacuum annealing of D defects and restoration of graphene layers occurs with an increased 2D peak.

References

1. D. Wei et al. "Laser-Induced Graphene", Science, 2015.
2. S. Pei et al. "Scalable production of graphene via wet chemistry: progress and challenges" Chemical Society Reviews, 2018.
3. J. Lin et al. "Laser-Induced Graphene as a Versatile Platform for Advanced Electronics and Energy Storage" Advanced Materials, 2019.
4. C. Zhang et al. "Recent advances in laser-induced graphene for electrochemical applications" Chemical Society Reviews, 2020.
5. Y. Huang et al. "Laser-Induced Graphene-Based Electrodes for Flexible Energy Storage Devices" Advanced Materials Technologies, 2021.
6. Zhang et al. "Laser-Induced Graphene for Flexible and Integrated Energy Storage Devices" by W. Nano Energy, 2018

FROM UNUSUAL PRECESSION OF MAGNETIC MOMENTS TO NONTRIVIAL ULTRAFAST SPIN DYNAMICS IN MAGNETICS

M.R. Jumaev

Bukhara Engineering-Technological Institute, Bukhara, Uzbekistan
e-mail: mrjumaev2011@mail.ru

In the first part of work the precession of the magnetization vector in nano-sized magnets is induced by a femtosecond laser pulse, the frequency of which lies in the transparency region of the magnet material. It is shown that an alternating magnetic field applied to the XOY plane generates the magnetic equilibrium position vectors and elliptical precession occurs if a constant magnetic field acts along the Z axis. In this case the precession angle changes periodically in time and the precession frequency is determined by the amplitude of the total magnetic field.

Recently, one of the intensively developed areas of femtomagnetism is the control of the magnetization of nano-sized magnets, and also the speed of ultrafast laser-induced spin precession with spin-orbit interaction [1-2].

Previously, we considered the nontrivial dynamics of magnetization when two mutually perpendicular constant magnetic fields applied to the XOZ plane act on it.

The following results were obtained in the work:

1. System of coupled equations of motion of the components of the magnetic moment vector with periodically changing coupling coefficients.

2. Equation of motion of magnetization in a rotated coordinate system.

3. Solutions of shortened equations of motion for the magnetic moment are found.

The results of the research can be used to control the precession of magnetic moments and spins when their motion is induced by an ultrashort laser field.

The system of coupled equations of motion for the components of magnetic moments with periodically changing coefficients was obtained by us for the first time.

The second part of paper proposes a resonant-dissipative model of ultrafast spin dynamics, which takes into account the effects of both an external magnetic field and spin-orbit coupling. It is shown that under the combined action of these factors it is possible to control the polarizability of ferromagnets, which determines the permittivity and refractive index of the systems under study.

At present, one of the widely used methods for ultrafast magnetization control is laser-induced changes in magnetic anisotropy and ultrafast spin dynamics. There are a number of important experimental and theoretical works in which the mechanisms of ultrafast spin dynamics, as well as its theoretical foundations, are investigated [3].

Below we propose a resonant-dissipative model of ultrafast spin dynamics, which is a certain generalization of the known, so-called oscillatory models [4-5]. In contrast to them, we have taken into account the effects of an external magnetic field and damping of oscillations. The latter is due, as is known, to the fact that relaxation processes in electron and spin systems occur as a result of the absorption of femtosecond optical (or laser) pulses in ferromagnets or nanosized metamaterials.

Based on the proposed resonant-dissipative model of ultrafast spin dynamics, the following results are obtained, which have both scientific and applied significance:

1. It has been shown for the first time that, under the action of an external magnetic field, it is possible to create, as well as eliminate off-diagonal susceptibility components.

2. The so-called critical frequency of the electromagnetic field is found, which separates the regions of positive and negative real susceptibility.

3. The extreme frequency of the laser pulse is determined at which the imaginary part of the susceptibility will be the largest.

We can conclude that the results obtained should be generalized for anisotropic magnetic crystals, for which it is necessary to study the off-diagonal susceptibility components not considered here.

References:
1. Jumaev M, Sharipov M, Rizoqulov M and Ergasheva N 2021 *Journal of Physics: Conference Series* **1889** 022073
2. Zhumaev Mustakim R, Sharipov Mirzo Z and Rizoqulov M N 2022 *J. Phys.: Conf. Ser.* **2388** 012005
3. Zhumaev M R, Sharipov M Z, Shavrov V G, Koledov V V, Shcheglov V I and Rizokulov M N 2023 *Journal of Radio Electronics* **4** 1-11
4. Battiato M *et al*. 2012 *Phys.Rev. B* **86** 024404
5. Xinwei Li *et al*. 2022

THE CONCEPT OF VARIZONACITY IN THE PROBLEMS OF HELIO MATERIALS SCIENCE

Suleymanov S. Kh.[1], Oksengendler B.L.[1], Kulagina N.A.[1]

[1]*Institute of Materials Science of the Academy of Sciences of Uzbekistan*
2B, Chingiz Aytmatov str., Tashkent, 100084, Uzbekistan
E-mail: sultan.suleimanov@gmail.com

Long-term studies of solid surfaces (including interfaces) have convinced us of their deep fundamental reason - dimensions (topological and fractal D_T; D_F), for which the following relations are valid: $2 \leq (D_T; D_F) \leq 3$ [1]. This class of properties also includes homovariation of the electronic structure in the near-surface regions of the crystal, which fully applies to interfaces. Below we briefly describe a number of phenomena in this area.

Surface states in ionic crystals in the variable band gap

Recently, in a series of our works [2-4] it has been shown that the exit of the variable zone to the surface leads to a completely new situation radically different from all previous works. «Figure 1» demonstrates how varizonicity creates potential pits of a special type (namely Airy pits) in which a whole group of local near-surface states can be localized.

$$E_n = \left[\frac{F^2\hbar^2}{m}\right]\alpha_{n+1} \quad (n = 0, 1, 2, \ldots \ldots)$$

$$\alpha_{n+1} = \alpha_{n+1}^0 + f[U_1, U_2]$$

where α_{n+1}^0 are the roots of the equation for the Airy function (2.7; 4.09; 5.52…….);

As can be seen in Figure 1, a number of local levels are placed in the Airy well, the width of which depends on the temperature (!). Thus, the crystal actually becomes layered, and the location of the Fermi level (E_S) can be controlled by the filling of this well with electrons. This leads to two cases:

1. At filled levels, the resulting structure represents a selective window that reflects electromagnetic waves well and transmits short waves;

2. When the upper well is empty, the possibility of electronic transitions (zone-zone) opens up, which is less than the total band gap. The application of both cases will be shown later.

Figure 1. Electronic structure in the near-surface region of the graded-gap design

The role of the varizonicity of metal film plates in the superconducting sandwich structure

In the broad problems of superconductivity, a special role is devoted to the search for recipes for both materials and principles (mechanisms) to increase the critical temperature of the high temperature of superconductivity (T_c) [5].

Among the proposed principles, such as a fundamental concept for the topological and fractal dimensions of an object undoubtedly plays a special role, and in this regard it is necessary to note the intuition of V.L.Ginzburg «Figure 2». Our innovation is the use of graded-gap semiconductor plates («Figure 3»).

As our calculations show (in the same $\varepsilon(k, \omega)$ - formalism), this replacement actually modifies all components required for the calculation of T_c. In particular, even in a very rough approximation, using polarization mechanisms, varizonicity leads to important relationship between the critical temperatures of superconductivity in variable zone and the planar one:

$$T_c^{var}/T_c^{pl} \cong (\tilde{\Omega}/\Omega)\sqrt{(\mathring{\varepsilon}_0 + 1)/(\varepsilon_\circ + 1)} > 1. \quad \varepsilon_\circ = \varepsilon_1\frac{\varepsilon_1+\varepsilon_2}{\varepsilon_1-\varepsilon_2}; \quad \mathring{\varepsilon}_\circ = \varepsilon_1\frac{\varepsilon_1+\mathring{\varepsilon}_2}{\varepsilon_1-\mathring{\varepsilon}_2}; \quad \mathring{\varepsilon}_2 > \varepsilon_2; \quad \tilde{\Omega} > \Omega$$

In all these equalities, the values of ε_i and Ω imply a fractional averaging.
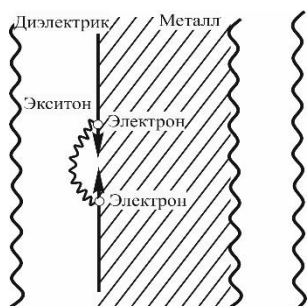
Figure 2. Sandwich structure and exciton mechanism
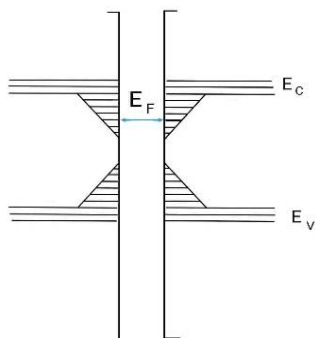
Figure 3. Sandwich structure with variable forbidden zone and Airy pits

The role of varizonicity in the efficiency of the carbothermic method of hydrogen production

The approach to solving the outlined problem, designated as "hydrogen energy", contains all the signs of complexity [6] (due to its multi-step nature) and is quite optimistic.

Phenomenological analysis. The scheme we have adopted contains two stages of the thermochemical cycle with the involvement of factors of influence of a Big Solar Furnace (BSF):

$$ZnO + C \rightarrow Zn + CO (\Delta H1 = 350 \text{ kJ/mol})$$
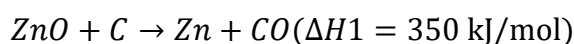
Zinc is needed in the form of nanopowder and everything happens in the presence of concentrated solar energy. $Zn + H_2O \rightarrow ZnO + H_2 (\Delta H2 = -62 \text{ kJ/mol})$

The reaction takes place on the surface of zinc nanoparticles, the ZnO product returns to the reactor, completing the thermochemical cycle.

Due to the multifactorial nature of BSF radiation, the Born-Haber energy cycle is completely satisfied, which corresponds to the law of conservation of energy, without disturbing the entire cycle. However, it is necessary to check the issue of coupling flows at interfaces where energy is transformed (satisfaction of the Umov-Pointing principle).

In general, the coupling of flows according to the Umov-Pointing principle looks like this

$$\vec{j_1} = \rho_1 \vec{v_1} = \rho_2 \vec{v_2} + (\vec{q_{12}})$$

Here ρ_i and v_i are the energy density and the velocity of the energy carrier on both sides of the interface; $\vec{q_{12}}$ - is the heat outflow vector. With an ideal pairing, when $j_1 < j_2$, there is no degradation of the interface but under the condition $j_1 > j_2$, i.e. $q > 0$ degradation is possible. In the latter case, for the scheme we are discussing, it means that the case of degradation corresponds to the recrystallization of zinc nanoparticle powders with a sharp decrease in the catalytic activity of the zinc surface and inhibition of the process.

In the light of the problem of varizonality discussed here, the presence of local levels in potential Airy pits at the interface can serve as a certain drain of the heat released. At the same time, the electrons in these potential wells, which serve as a certain type of hub, are excited by taking the excess energy on themselves. The movement of these electrons along the surfaces of the powders will result in the outflow of excess energy, which, in principle, will suppress the degradation.

Literature:
[1] Dash J. Physics Today 1985. December, p.26.
[2] Kutlimurotov B., Oksengendler B., Suleymanov S. et.al. 2022. Uzb Phys Journal **24(4)** p.254-262.
[3] Karimov Z., Oksengendler B., Suleymanov S et.al. 2022. J Phys Conf Series **2388(1)**:012003
[4] Suleymanov S., Oksengendler B.L., Kulagina N., Sattarova D., 2023. Synthesis of materials on a Large Solar furnace in Uzbekistan (Tashkent: Ideal press) p. 5-27.
[5] Problems of high-temperature superconductivity ed. Ginzburg V.L. 1977 (Moscow: Nauka) p. 400.
[6] Oksengendler B.L. at al. "Interaction of Radiation with Hierarchical Structures", J. Surf. Investig. 2023. vol. 17(1), pp. 31–42.

GROWING OF $(Si_2)_{1-x}(GaP)_x$ SOLID SOLUTIONS WITH NANOCRYSTALS ON Si SUBSTRATES

Saidov A.S., Saparov D.V., Usmonov Sh.N., Turgunov O.Z.

Physical-technical Institute of the Academy of Sciences of the Republic of Uzbekistan, Tashkent st. Ch. Aitmatova 2B. e-mail: dada@uzsci.net

The growth of solid solutions (SS) of various semiconductors is of undoubted interest for the development of modern semiconductor materials science, since a solid solution synthesized from several semiconductors can combine the advantages of each component. By smoothly changing the composition of the solid solution, it is possible to control the fundamental parameters of the material, such as the band gap, the region of spectral photosensitivity, and the lattice parameter. For example, if a solid solution consisting of silicon and gallium phosphide is synthesized, then this solid solution combines the spectral regions of photosensitivity of silicon and gallium phosphide and has a wider spectral region of photosensitivity than silicon and gallium phosphide [1]. Expanding the spectral range of a device's photosensitivity is important for creating efficient solar cells and photodetectors.

To form a solid solution between silicon and gallium phosphide, it is necessary to create conditions for molecular substitution, that is, gallium phosphide molecules must be replaced by silicon molecules. These conditions were created based on the model of A.S. Saidov. According to this model, semiconductor compounds III-V, II-VI and elementary semiconductors, such as silicon and germanium, when dissolved in metal solvents at temperatures significantly lower than the melting point of these compounds are mainly in the form of molecules.

Epitaxial films $(Si_2)_{1-x}(GaP)_x$ were grown on Si (111) substrates from the liquid phase of a tin solution-melt (Sn-Si-GaP) using the technology described in [2]. The initial and final crystallization temperatures were 980 and 830 °C, respectively, and the cooling rate was 1 degree/minute. The composition of the melt solution: Sn - 100 g, Si - 1.8 g, GaP - 2.5 g, was determined from the state diagram of the Sn–Si binary alloy, taking into account the solubility of GaP in tin.

The grown epitaxial films $(Si_2)_{1-x}(GaP)_x$ had *n*-type conductivity, and their thickness, depending on the gap between the substrates, varied in the range of 15-30 μm. The surface relief of the grown epitaxial films was studied using a scanning atomic force microscope (AFM) (Fig. 1). On the surface of $(Si_2)_{1-x}(GaP)_x$ SS, wells with a depth of 8-10 nm and a diameter of 35-45 nm are observed (Fig. 2).
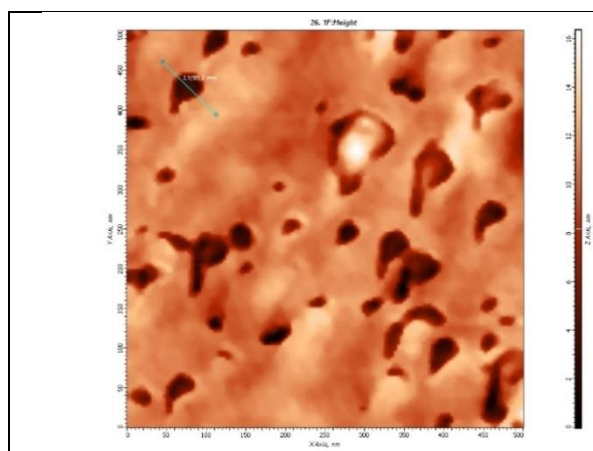
Figure 1. AFM image of the surface of $(Si_2)_{1-x}(GaP)_x$ solid solution films	Fig.2. Profile of a well on the surface of $(Si_2)_{1-x}(GaP)_x$ solid solution films.
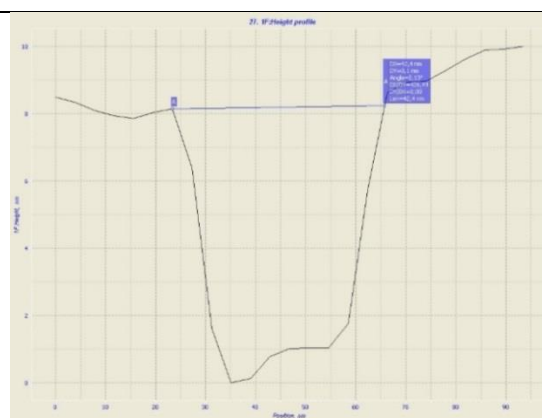
Depth – 8.2 nm, width – 42.4 nm.

A study of the chemical composition of epitaxial films showed that the composition of the solid solution changes smoothly from pure Si to GaP (3). The epitaxial film is graded-gap. In the near-surface region of the films, the content of silicon atoms is no more than one mole percent. The potential of Si atoms is lower than that of GaP. The nanosized wells observed in the AFM image (Fig. 1) appear to be caused by nanocrystallites created by silicon atoms.

Figure 3 shows the spectral photosensitivities of pSi- n(Si$_2$)$_{1-x}$(GaP)$_x$ and pSi-nSi structures. As can be seen from Figure 3, the pSi- n(Si$_2$)$_{1-x}$(GaP)$_x$ ($0 \leq x \leq 1$) structure has a wider range of spectral sensitivity, mainly in the short wavelength region, than the pSi-nSi structure and can be used for expanding the range of spectral sensitivity of silicon photodetectors and photocells. The increase in the photosensitivity of the studied structure in the short-wave region is due to the graded-gap nature of the structure, as well as the influence of molecules of the wide-gap component of the solid solution - GaP. The complex nature of the dependence of the photosensitivity of the structure on the photon energy is associated with the inhomogeneity of the SS across the thickness of the epitaxial layer. Covalent bonds between silicon atoms and gallium phosphides, as well as their nanocrystallites present in the solid solution, contribute to the formation of photosensitivity of the structure.

Figure 4 shows the photoluminescence spectrum of the (Si$_2$)$_{1-x}$(GaP)$_x$ epitaxial film, measured at 5 K. The spectrum has a peak at 525 nm, which corresponds to the GaP band gap of 2.28 eV. In addition, in the long-wavelength region of the spectrum, a peak is observed at 840 nm, which corresponds to a photon energy of 1.47 eV. Photoluminescent radiation is formed by the surface layer of the solid solution, where the content of silicon atoms is no more than 1 mol.%. The peak at a photon energy of 1.47 eV apparently belongs to the atoms of Si$_2$ molecules. Atoms of Si$_2$ molecules in the (Si$_2$)$_{1-x}$(GaP)$_x$ ($x < 0.01$) solid solution form energy levels located in the band gap 1.47 eV below the bottom of the conduction band of the SS.

Fig.3. Dependences of the photosensitivity of pSi–n(Si$_2$)$_{1-x}$(GaP)$_x$ and control pSi–nSi structures on photon energy.	Fig.4. Photoluminescence spectrum of the (Si$_2$)$_{1-x}$(GaP)$_x$ solid solution measured at 5 K
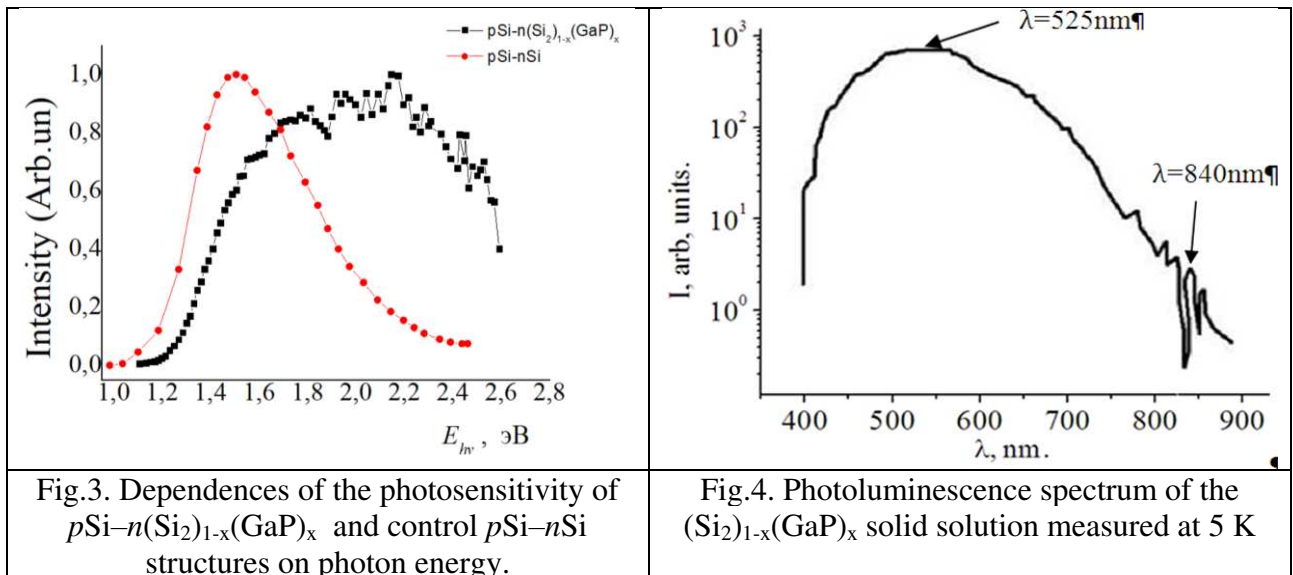
1. D. V. Saparov, M. S. Saidov, and A. S. Saidov. *Applied Solar Energy*, 2016, Vol. 52, No. 3, pp. 236–237.
2. A. S. Saidov, M. S. Saidov, Sh. N. Usmonov, et.al. *Physics of the Solid State*, 2011, Vol. 53, No. 10, pp. 2012–2021.
3. A. S. Saidov, D. V. Saparov, Sh.N. Usmonov, et.al. *Advances in Condensed Matter Physics* Volume 2021, Article ID 3472487, 8 pages.

THE PROCESSES OF DEFECT FORMATION IN SILICON, DOPED WITH TRANSITION ELEMENTS

Sh.B. Utamuradova[1], K.M.Fayzullaev[1], D.A. Rakhmanov[1], Sh.A. Yusupova[2]

[1]*Institute of Semiconductor Physics and Microelectronics at the National University of Uzbekistan, 20 Yangi Almazar st., Tashkent, 100057, Uzbekistan*
[2]*Physical-Technical Institute named after. A.F. Ioffe, 1940021 St. Petersburg, Russia*
e-mail: sh-utamuradova@yandex.ru

It is known that the processes of complex formation in semiconductors are determined by the concentration ratios of certain defects, their charge state and the defect structure of the crystal as a whole. The parameters of semiconductor devices, such as speed, forward voltage and reverse currents, the quantum yield of LEDs and the gain of transistors strongly depend on the presence of impurities with deep levels (DL) [1].

The properties of silicon doped with transition elements have been studied by a number of authors [2-3] using various methods. These studies showed that transition elements form efficient recombination centers and can be used to optimize the lifetime of nonequilibrium current carriers in devices. Silicon, compensated by platinum and manganese, has high photosensitivity in the impurity region of the spectrum. All this encourages continued research into platinum-manganese levels in silicon.

The purpose of this work is to study the interaction of impurities that create deep levels in the band gap of silicon: the influence of the diffusion of platinum atoms on the energy spectrum of deep centers and on the concentration distribution of manganese impurities in silicon.

We present experimental data obtained using capacitive spectroscopy of deep centers and radioactive techniques in silicon pre-doped with manganese and then with an impurity of platinum.

The studies used n-Si samples grown by the Czochralski method with a resistivity $\rho = 5$ Ohm $\cdot$ cm. The dimensions of the samples were 13x6x1 mm^3. Manganese was introduced into these samples by diffusion from a layer of manganese chloride containing the radioactive isotope ^{54}Mn deposited on one side of the sample. Diffusion annealing was carried out in air at 1200 °C for two hours. After annealing, the end planes were ground down to 200 μm and the samples were washed in HF and also in aqua regia to remove non-diffused manganese.
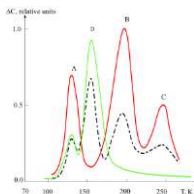
Fig.1. Typical DLTS spectra of n-Si<Mn> (red curve), n-Si<Pt> (green curve) and n-Si<Mn, Pt> (black curve) samples.
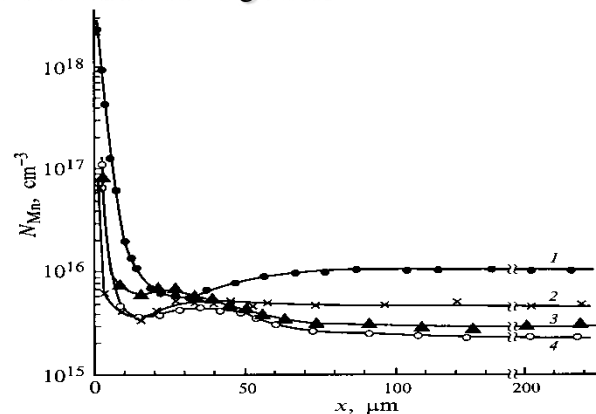
Fig.2. Concentration distributions of ^{54}Mn in silicon: 1-Initial sample after manganese diffusion; 2-control sample; 3- with an Au layer on the

To determine the energy spectrum of deep levels using deep level transient spectroscopy (DLTS), Schottky barriers were fabricated.Then, the nickel concentration profile was determined in several samples by sequential removal of layers and their radiometry.

In Fig.1 shows the DLTS spectra of n-Si<Mn>, n-Si<Pt> and n-Si<Mn, Pt> samples. Analysis of the results obtained shows that the introduction of a manganese impurity into silicon leads to the formation of three deep levels with ionization energies Ec-0.22 eV, Ec-0.42 eV and Ec-0.54 eV. Additional sequential introduction of platinum impurity into these samples leads to transformation of the DLTS spectrum of the n-Si<Mn> sample and the appearance of a level associated with platinum impurity. At the same time, the concentrations of levels associated with manganese and platinum decrease significantly.

As experiments showed, the concentration distribution of manganese, similar in nature to the diffusion distributions of impurities of other transition elements in silicon, consisted of two sections (Fig. 2): a near-surface with a sharply falling impurity concentration (to a depth of ~ 50 - 100 μm) and a volumetric one with a uniformly distributed impurity[4].

Next, a layer of non-radioactive Pt impurity was sprayed onto one of the large surfaces of the sample saturated with radioactive manganese. Repeated diffusion annealing of the samples was carried out under conditions corresponding to the regime of introduction of radioactive ^{54}Mn. Control samples (without sputtering of a non-radioactive diffusant) were also annealed at the same time.

The results obtained by layer-by-layer radiometry of samples indicate that the total concentration of manganese N_{Mn} in the volume of samples annealed with a metal layer decreases by more than half an order of magnitude compared to control samples (see figure.2).

Thus, platinum deposited on the Si(^{54}Mn) surface acts as a getter for Mn in Si. The diffusion introduction of Pt from a layer on the surface into silicon doped with manganese leads to its purification from impurities due to the gettering of manganese atoms by the surface and near-surface layers. The gettering mechanism, in our opinion, is associated with the formation of complex silicide compounds, which, along with metals, may also include oxygen, which is always contained in silicon.

References
1. Utamuradova Sh. B., Rakhmanov D.A(2022). Physics AUC, vol. 32, Pp.132-136.
2. Utamuradova Sh.B., Daliev Kh.S., Daliev Sh.Kh., Fayzullaev K.M.(2019). Applied Physics. 6. P. 90.
3. Utamuradova Sh. B., Muzafarova S. A., AbdugafurovA. M., Fayzullaev K. M., NaurzalievaE. M., RakhmanovD. A.(2021). Applied Physics. №4. P. 90.
4. Kulikov G.S., Yusupova Sh.A(2000). Semiconductors, vol.34, issue.2. P.168.

RAMAN AND PL SPECTROSCOPY OF TWO-DIMENSIONAL TRANSITION METAL DICHALCOGENIDES $Mo_xW_{1-x}Se_2$

E.A. Kolesov[1], M.S. Tivanov[1], O.V. Korolik[1]

[1]Belarusian State University, Nezavisimosti av. 4, 220030 Minsk, Belarus
Corresponding author: E.A. Kolesov (kolesov.bsu@gmail.com)

Abstract

Photoluminescence and Raman spectroscopy studies were carried out on two-dimensional solid solutions of transition metal dichalcogenides $Mo_xW_{1-x}Se_2$ of various stoichiometric compositions (x values – 0, 0.1, 0.3, 0.4, 0.8, 1) with the number of layers from 1 to 3. The following dependencies were found: photoluminescence band position on x for monolayer solutions, the E^1_{2g} Raman peak position on x for three-layer solutions, A_{1g} Raman peak position and intensity on x and number of layers. The dependency of A_{1g} intensity on x was found to change its shape qualitatively depending on the number of layers: at $x = 0$ and $x = 0.1$, the intensity of the A_{1g} peak was maximum in the case of two-layer solutions; at $x = 0.3$ and $x = 0.4$ it decreased with increasing number of layers; at $x = 0.8$ and $x = 1.0$ it increased with increasing number of layers. The results are useful for estimating bandgap, structural and phonon properties of $Mo_xW_{1-x}Se_2$ when designing opto- and nanoelectronic devices.

VIBRATION PROPERTIES OF Sb_xSe_{1-x} THIN FILMS IN THE FAR-INFRARED RANGE: EXPERIMENTAL AND THEORETICAL STUDIES

Bohdan Andriyevsky [1], Leszek Bychto [1], Aleksy Patryn [1], Takhir Razykov [2], Bobur Ergashev [2],*
Kudratulia Kouchkarov [2], Ramozan Khurramov [2], Diyorbek Isakov [2], Mukhammad Pirimmatov [2],
Ulrich Schade [3], Ljiljana Puskar [3], Alexander Veber [3,4], Andrii I. Kashuba [5]

[1] *Koszalin University of Technology, Koszalin, Poland, bohdan.andriyevskyy@tu.koszalin.pl*
[2] *Physical-Technical Institute of Uzbekistan Academy of Sciences, Tashkent, Uzbekistan*
[3] *Helmholtz-Zentrum Berlin für Materialien und Energie GmbH, Berlin, Germany*
[4] *Humboldt Universität zu Berlin, Berlin, Germany*
[5] *Lviv Polytechnic National University, Lviv, Ukraine*

The antimony selenide (Sb_2Se_3) possesses a number of useful properties for photovoltaic application, such as binary stoichiometry, an optimal band gap (1.2−1.3 eV), a large absorption coefficient, and a quasi-one-dimensional crystal structure [1, 2]. The aim of the present study is to reveal features of the experimental phonon spectra of Sb_xSe_{1-x} films for different compound indices x by their comparison with the theoretically calculated ones for Sb_2Se_3 crystals taken at the orthorhombic space group of symmetry.

The Sb_xSe_γ thin films were fabricated through chemical molecular beam deposition (CMBD). Utilizing 99.999% high-purity Sb and Se beads, soda-lime glass (SLG) served as the substrate.

The reflectance at normal incidence and transmission spectra of semiconductors Sb_xSe_{1-x} were measured in the spectral range of 20 – 8000 cm^{-1}. Measurements were performed at quasi-normal light beam incidence with a gold film as reference using the Fourier-transform infrared (FTIR) Bruker Vertex 70/v spectrometer and synchrotron radiation of BESSY II storage ring of HZB (Berlin) [3]. Spectra were recorded with (a) Cryogen free THz bolometer in the spectral range between 700 and 8000 cm^{-1} and (b) mechanically cooled transition edge superconducting bolometer (QMC) in the spectral range between 20 and 500 cm^{-1} with the resolution of 4 cm^{-1}.

For all samples measured clear reflectance spectra extrema were observed in the wavenumbers range of 20 – 220 cm^{-1} corresponding to the phonon excitations. Simultaneously, the free electron excitations in Sn_xSe_{1-x} layers are expected, in this range, to be in the form of the monotonous decrease of the reflectance spectrum $R(\lambda^{-1})$.

Analysis of Sb_xSe_{1-x} reflectance spectra $R(\lambda^{-1})$ shows a presence of the interference fringes in the wavenumber range of $\lambda^{-1} > 1200$ cm^{-1} for several Sb_xSe_{1-x} compounds (Fig. 1). The phonon reflectance bands are presented in all Sb_xSe_{1-x} compounds studied in the wavenumber range of $\lambda^{-1} < 220$ cm^{-1} (Fig. 2). No clear interference fringes are observed for several Sb_xSe_{1-x} compounds studied in the wavenumber range $\lambda^{-1} > 1200$ cm^{-1} (Fig. 1), that may be caused by the relatively high coefficient of optical absorption here, caused by the quasi-free electrons.
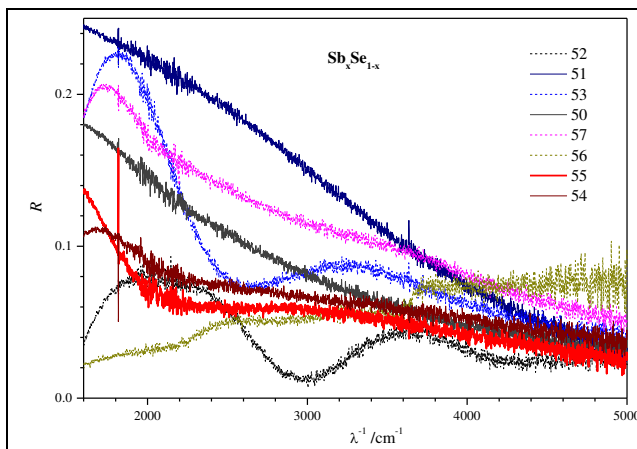
Fig. 1. Reflectance spectra $R(\lambda^{-1})$ of Sb_xSe_{1-x} films on soda lime glass substrates measured at room temperature (296 K) and presented for the wavenumber scale 1600-5000 cm^{-1} using globar as a source of radiation. The red thick line corresponds to the compound index $x = 2/3$

The largest reflectance coefficients take place for the compound index $x^{(51)} = 0.212$, $x^{(50)} = 0.283$, and $x^{(54)} = 0.441$ (Table 1). The compound indices $x^{(51)}$ and $x^{(50)}$ correspond to the increased amount of selenium in comparison to the stoichiometric compound Sb_2Se_3 with the compound index $x^{(55)} = 0.4$ (Sb_xSe_{1-x}). The relatively large reflectance coefficients R of materials in the far-infrared range associated

with their quasi-monotonous decrease in the frequency/wavenumber scale may be caused by the increased quasi-free electron or hole concentration. In turn, the increased quasi-free electron or hole concentration causes the increased optical absorption. The latter eliminates the interference fringes in the reflectance and transmittance spectra. This really takes place for Sb_xSe_{1-x} samples with the compound indices $x^{(51)} = 0.212$, $x^{(50)} = 0.283$, and $x^{(54)} = 0.441$ (Fig. 1).
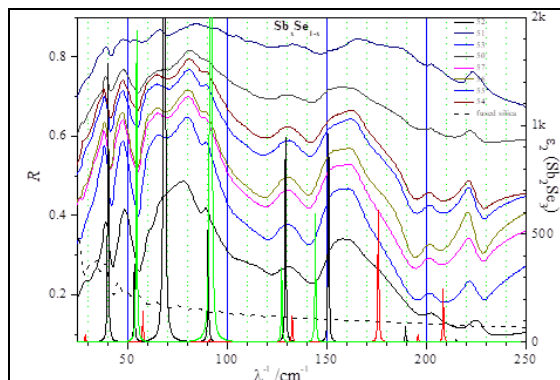
Fig. 2. Experimental reflectance spectra $R(\lambda^{-1})$ of Sb_xSe_{1-x} films and theoretical spectra of imaginary part of dielectric permittivity $\varepsilon_2(\lambda^{-1})$ of Sb_2Se_3 crystal at the space group of symmetry *Pnma*. Here, narrow black, red and green peaks correspond to *x*-, *y*-, and *z*-polarizations of $\varepsilon_2(\lambda^{-1})$
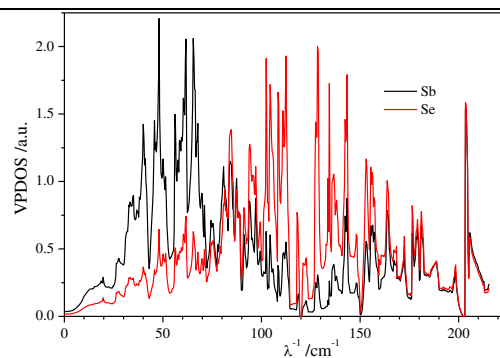
Fig. 3. Vibration partial density of states VPDOS of Sb2Se3 for Sb and Se calculated using GGA-PE exchange-and-correlation functionals

The calculated static dielectric permittivities $\varepsilon^{(e)}$ (electronic contribution) and $\varepsilon^{(i)}$ (ionic contribution) of Sb_2Se_3 crystal (Table 1) are in semi-quantitative agreement with the experimentally presented in the Ref. [4].

Table 1. Macroscopic static dielectric permittivities $\varepsilon^{(e)}$ (electronic contribution) and $\varepsilon^{(i)}$ (ionic contribution) of Sb_2Se_3 crystal at space group of symmetry *Pnma* (no. 62) calculated for PE and PS exchange-and-correlation functionals

Dielectric permittivity Exch.-and-corr. functional	$\varepsilon^{(e)}_x$	$\varepsilon^{(e)}_y$	$\varepsilon^{(e)}_z$	$\varepsilon^{(i)}_x$	$\varepsilon^{(i)}_y$	$\varepsilon^{(i)}_z$
PE	9.7078	18.7331	18.3270	3.2709	63.4419	80.8120
PS	14.9948	24.4771	25.7605	5.0581	68.9774	101.2156

The calculated vibration partial density of states (VPDOS) of Sb_2Se_3 crystal (Fig. 3) is characterized by a large number of maxima, which corresponds to the large number of the calculated phonon energy bands.

The features of the experimental spectra of Sb_xSe_{1-x} films for the different compound indices *x* are similar. This confirms the stoichiometry of the compound Sb_2Se_3 in Sb_xSe_{1-x} films. Besides, the positions of maxima in the phonon reflectance spectra obtained for the samples Sb_xSe_{1-x} are in a quantitative agreement with the positions of maxima of the imaginary part of dielectric permittivity $\varepsilon_2(\lambda^{-1})$ obtained from the DFT-based calculations of Sb_2Se_3 crystal.

The relatively large number of separate phonon energy bands in Sb_2Se_3 crystal indicates the quasi-local character of the corresponding vibration states. This may be caused by the relatively large coulomb-like charge screening in the crystal due to the relatively large dielectric permittivity.

References

[1]. I. Caño et al, *ACS Appl. Mater. Interfaces* **14** (2022) 11222−11234
[2]. C. Chen, et al, , *Appl. Phys. Lett.* **107** (2015) No. 043905
[3]. U. Schade, M. Ortolani, J. Lee, , *Synchrotron Radiation News* **20** (2007) 17-24
[4]. J. Petzelt, J. Grigas, *Ferroelectrics* **5** (1973) 59 - 68

LATERAL PHOTOELECTRIC EFFECT IN THE PEROVSKITE-SILICON-BASED HYBRID STRUCTURES

Anvar A. Zakhidov[1], Eshkuvat U. Arzikulov[2], Alisher D.Nurimov[2], Norboyev Qodirbek[2], Canan Varlikli[3], Hakan Bozkurt[3]

[1]*The University of Texas at Dallas, USA. zakhidov@utdallas.edu*
[2]*Samarkand State University, Uzbekistan. nurimov-alisher.samdu.uz*
[3]*Izmir Institute of Technology, Turkey. cananvarlikli@iyte.edu.tr*

Abstract. In this paper, we demonstrate experimental results on the technology of obtaining perovskite-silicon-based hybrid structures, the lateral photoelectric effect (LPE) observed in these hybrid structures and its advantages over the iron-silicon hybrid structure, the adhesion of the perovskite layer of the PEDOT: PSS polymer layer to the silicon enhancement and its effect on LPE, dependence of LPE on the laser wavelength of illumination, etc. According to the research results, perovskite-silicon-based hybrid structures can be used to make position-sensitive detectors.

1. Introduction.

In general, it is well-known and famous that when a semiconductor junction is illuminated, a photovoltage is generated on both sides (transverse) of the junction. This paper discusses the mechanism of generation of transition-parallel lateral photovoltage (LPV) as a result of nonuniform illumination and a structure with extraordinarily high LPV. The lateral photoelectric effect occurs as a result of the separation of the electron-hole pair formed as a result of nonuniform illumination along the upper layer and the base, due to the potential gradient of the space-charge layer. It is used in creating position-sensitive detectors from the voltage that changes from positive to negative maximum due to the lateral photoelectric effect, that is, the shift of the light spot [1]. Highly sensitive lateral photo effect (LPE) has been observed in many semiconductor structures such as superlattices, heterostructures, two-dimensional electronic systems and silicon Schottky barrier structures [2]. Efforts to develop such new LPE-based semiconductor materials at the demand level are still ongoing.

2. Results and discussions.

PbI_2 and MAI were dissolved in 2 mL of DMSO each in separate vials in a molar ratio of 1:1. The solutions were stirred at room temperature for 12 h using a magnetic stirrer. After the precursors were completely dissolved, solutions of PbI_2 in DMSO and MAI in DMSO with a concentration of 0.1 M were prepared. p-Si<B> was chosen as the base, and three stages of cleaning were carried out to eliminate impurities and oils originally present on the base. Thus, Si substrates, on which a thin layer can be formed, were prepared, and PEDOT:PSS polymer and the above-mentioned perovskite precursors were deposited on it in a nitrogen environment using a spin-coater. Two different types of hybrid structure(HS)s were formed: $Si<B>/SiO_2/MAPbI_3$ and $Si<B>/SiO_2/PEDOT:PSS/MAPbI_3$. It should be noted here that the purpose of depositing the PEDOT:PSS polymer before the perovskite layer on the second sample is to improve the adhesion of the perovskite layer to the Si substrate.

Two ohmic contacts were formed on the $MAPbI_3$ perovskite layer of the obtained samples as shown in Figure 1, the diameter of the contacts is ~0.5 mm, the distance between the contacts is ~2 mm, the size and power of the 532 nm laser light spot are ~0.5 mm and 20 mW, respectively.

a)

b)
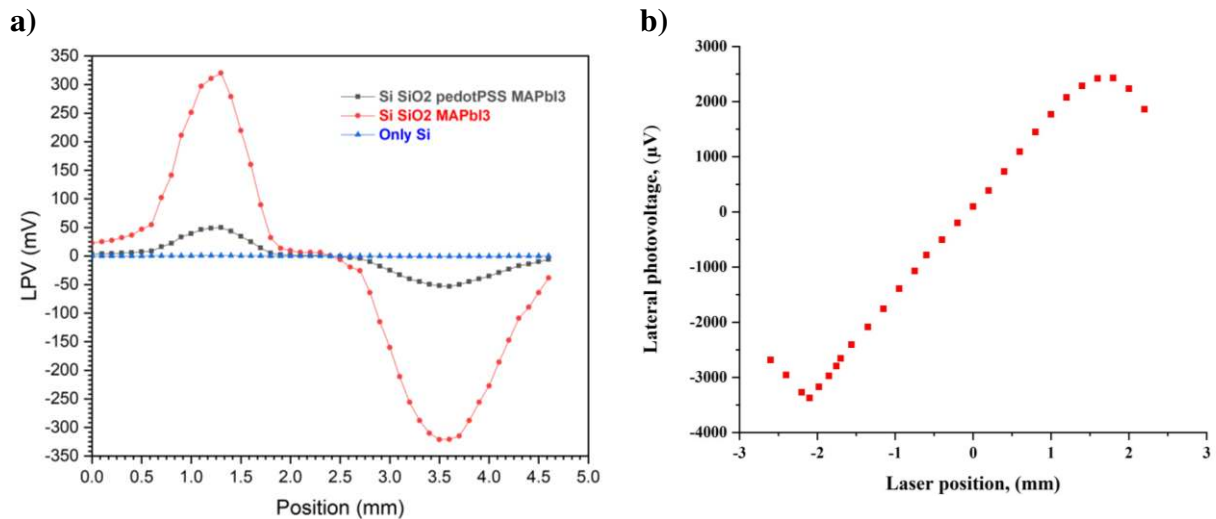
Figure 1. (a) LPV measurement in different HSs based on perovskite. (b) LPV measurement in Si<B>/SiO₂/Fe HS.

Figure 1b shows the results of the LPE effect observed in Fe/SiO$_2$/p-Si<B> HS, which makes it possible to compare with our previous research [3], it can be seen that the maximum value of PLV in this MOS structure does not exceed 3 mV. The reason why the maximum value of LPV is small compared to perovskite-based HS is that the conductivity of the metal layer is very high. This nonlinearity between the two contacts leads to an increase in the lateral diffusion of photogenerated electrons that occur when illuminated. As a result, the energy potentials between the contacts are closer to each other, so LPV is high won't be. In the perovskite layer, the excited electrons do not change the energy levels in the non-illuminated contact area, which leads to a high potential difference between the high contacts.

3. Conclusion

In this work, we have demonstrated that perovskite-based HSs on a silicon substrate will have high LPV and high sensitivity. In this, we made two perovskite-based HSs. From the obtained results, it can be concluded that Si/SiO$_2$/MAPbI$_3$ HSs have higher LPV and higher sensitivity compared to Si/SiO$_2$/Fe and Si/SiO$_2$/PEDOT:PSS/MAPbI$_3$ HSs. However, the adhesion of the perovskite layer to the Si substrate is much higher in the Si/SiO$_2$/PEDOT:PSS/MAPbI$_3$ structure than in the Si/SiO$_2$/MAPbI$_3$ structure, although the PEDOT:PSS LPE reduces the effect. LPE depends on the wavelength of the light being illuminated, and in our studies, the 632 nm laser showed higher LPV and higher sensitivity than the 532 nm laser. In short, perovskite-based HSs have the possibility to create PSDs with high sensitivity.

REFERENCES

1. J. Henry, J. Livingstone. Improved position-sensitive detectors using high resistivity substrates. *J. Phys. D: Appl. Phys*. **2008**, *41*, 165106. https://doi.org/10.1088/0022-3727/41/16/165106
2. S.Q. Xiao, H. Wang, Z.C. Zhao, Y.Z. Gu, Y.X. Xia, Z.H. Wang. The Co-film-thickness dependent lateral photoeffect in Co-SiO$_2$-Si metal-oxide-semiconductor structures. *Opt. Express.* **2008**, *16*, 3798-3806. https://doi.org/10.1364/OE.16.003798
3. E.U. Arzikulov, A.D. Nurimov, F.A. Salakhitdinov, U.A. Ashirov, T.S. Sharafova, A. Sh. Khujanov, R.M. Usanov. Lateral photoelectric effect in iron-silicon dioxide-compensated silicon hybrid structures. East European Journal of Physics 2023, 4, 159-166. https://doi.org/10.26565/2312-4334-2023-4-17

STABLE NANOSILICA HYDROSOL AS NANOADDITIVE FOR CONCRETE PLASTICITY INCREASE

B.A. Allaev, S.Z. Mirzaev, O.V. Trunilina, Sh.E. Kurbanbaev, K.B. Egamberdiev

Academy of Sciences of Uzbekistan, Institute of Ion-Plazma & Lazer Technologies Named after U.A.Arifov, Durmon Yuli str.33, Tashkent 100125, Uzbekistan, bahtiyor.74.74@mail.ru

A main feature of earthquake-resistant concrete is its multicomponence with a variety of dispersed compounds and complex nanoadditives. Along with traditional methods of regulating the structure of concrete, its modification with low dimensional nanoscale particles is also promising, when introduced into the mineral matrix of the binder, its structuring occurs. The main problem of creating nanomodified concretes is the uniform distribution of nanomaterial in the volume of the cement matrix, which is especially important in cases of adding a modifier in small quantities. To solve this problem, an additional medium is needed, forming a continuous phase in the composite. This function can be performed by a liquid dispersed phase, which is the mixing water. The optimal combination of modifier nanoadditives and other organic and mineral materials allows you to control the rheological properties of concrete mixtures and modify the structure of cement stone so as to give concrete properties that ensure high operational reliability of structures. The obtained properties of concrete are the result of complex physical processes affecting the phase composition, porosity and strength of cement stone. Such modified concretes with high flexibility and plasticity are characterized by high strength, low permeability and exothermy, increased corrosion resistance and durability, and improved deformation characteristics measured in accordance with Hooke's laws. At the same time, the effect on the hardening process and structuring of concrete-cement stone occurs through modification of the mixing water, which leads to a change in its ionic composition, indicators of hydrogen ion activity, structuring of hydrogen bonds when water acquires high chemical and hydration activity, resulting in the possibility of directional regulation of the technological properties of concrete systems. The experimental samples were prepared with a water-cement ratio (W/C) of 0,4. Nanosilica with the particle size and concentration (shown in the table 1) was used as a nanoadditive [1,2]. Plasticity was determined by the blurring of the cone according to GOST 310.4-81 for samples with and without anionic surfactant. As shown experimental results in table 1, nanoparticle size and concentration, also surfactant using influence to concrete plasticity and increase it.

Table 1. Anionic surfactant influence to concrete plasticity with silica nanoadditive using

Nanoparticle size, nm	Nanoparticle concentration, wt.%	Water, l	W/C	Blurring of the cone, mm	
				-Surfactant	+Surfactant
100	1	0,2	0,4	111	129
100	3	0,2	0,4	127	132
100	10	0,2	0,4	129	135
7	1	0,2	0,4	116	135
7	3	0,2	0,4	134	139

The scientific research carried out contributes to the development of methods for the multifunctional modification of concrete-cement mixtures with nanomodifiers in combination with surfactants based on diphilic molecules, which reduces aggregate consumption and optimizes the cost of earthquake-resistant construction with improved plasticity characteristics.

References

1. Yokubov, U., Egamberdiev, K., Allaev, B., Trunilina, O., Telyaev,S., _Journal of Chemical Technology and Metallurgy_, (2023), 58(5), p. 932–936

2. M.Sh. Kurbanov, L.S. Andriyko, J.A. Panjiev, S.A. Tulaganov, V.M. Gun'ko, A.I. Marynin, S. Pikus. *Journal of Nanoparticle Research*. 25, 202 (2023), doi.org/10.1007/s11051-023-05852-w.

DETECTION OF SPECIAL ORIENTATIONS IN PbMoO$_4$ CRYSTALS FOR ACOUSTO-OPTICAL DEVICES

M.I.Elboeva[1], F.R.Akhmedzhanov[1]

[1]Institute of Ion-Plasma and Laser Technoligies, 33 Durmon yuli str., 100125 Tashkent, Uzbekistan
e-mail: elboyevamoxinur1990@gmail.com

PbMoO$_4$ (lead molybdate) crystals are known for their unique optical and acousto-optic properties and are used in a variety of applications including acousto-optical devices. When using PbMoO$_4$ crystals, it is important to know the directions along which pure longitudinal acoustic waves propagate.

To determine such directions in PbMoO$_4$ crystals, the dependence of the polarization angle of the acoustic wave ψ, the components of the energy flux density vector Ai, and the angle of deviation of the energy flux ξ on the direction of the wave vector of the acoustic wave φ in the (010) plane was revealed. The results obtained were used to calculate the phase and group velocities of quasi-longitudinal waves in PbMoO$_4$ crystals.

The components of the energy flow density vector in an elastic wave are determined from expression (1).

$$A_i = C_{ijkl}\gamma_j\gamma_l\kappa_k \tag{1}$$

Here C_{ijkl} are the components of the elasticity tensor, γ_j and κ_k are the components of the polarization and displacement vector of the acoustic wave, respectively.As a result, this vector **A**determines the magnitude and direction of the energy transfer velocity [1-2].
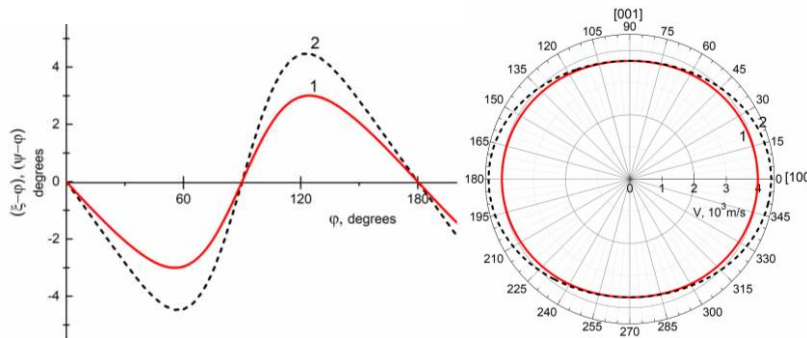
Fig. 1. Deviation of energy flux density (1) and polarization (2) of acoustic wave propagated in the (010) plane in PbMoO$_4$ crystals

Fig. 2. Anisotropy of phase (1) and group (2) velocity of quasi-longitudinal acoustic waves in the (010) plane in PbMoO$_4$ crystals

It can be seen (Fig.1) that along the directions [100] and [001] are propagated pure at the same time ordinary longitudinal acoustic waves.At that time the maximumdeviation the energy flux density vector from wave vector is 4.5^0. Fig. 2 shows that the phase velocity of longitudinal acoustic wave is weakly changed and the group velocity along the [001]axis is equal to the phase velocity. The value of the phase velocity along the [100] axis (3.99 km/s) differs from the group velocity (4.4 km/s) by 10%.The obtained results will be usefullat the development of acousto-optical deviceson PbMoO$_4$ crystals.

References

1. E. Dieulesaint, D. Royer, Elastic Waves in Solids.(1980) 511 pp
2. J.W.Jaeken, S. Cottenier, Solving the Christoffel equation: Phase and group velocities, Computer Physics Communications, 207(2016) 445–451.

EXCESS REFRACTIVE INDICES WATER AND ETHANOL SOLUTIONS

Dilbar Bozorova[1,2], Shukur Gofurov[2], Oksana. Ismailova[2,3,4]*

[1]Institute of Ion-plasma and laser technologies, 100125, 33 Durmon yuli street, Uzbekistan
[2]Turin Polytechnic University in Tashkent, 100195, Almazar district, 17 Kichik Khalka yuli street, Uzbekistan
[3]Uzbekistan-Japan Innovation Center of Youth, 100195, 2B Universtiteskaya street, Uzbekistan
[4]National University of Uzbekistan named after Mirzo Ulugbek, Tashkent 100174, Uzbekistan.
email: bozorova191@gmail.com

Ethanol (C_2H_5OH) and water solutions have been the most interesting and relevant topic for researchers. It is linked the widespread use of ethanol and water in the fields of pharmaceuticals, chemistry and physics. Alcohols, being polar and self-organizing systems, depending on the solvent, can exhibit various types of interactions. Refractometric, volumetric, viscometric properties are widely used to identify structural changes and effects in organic compounds. Among them, refractometry is also suitable to get the informations of molecular interactions in solutions. Many studies have been done on ethanol – water solutions by various methods [1-2]. The present work presents the excess refractive indices of ethanol and water solutions. Ethanol (99.9 %, Sigma-Aldrich, USA) and double-distilled water with pH=7.02 were used in the experiments. Refractive indices were measured at room temperature and atmospheric pressure for the whole range of composition (0-1.0 mole). The data obtained by using a high – sensitivity PAL – RI digital refractometer (ATAGO, Japan). The instrument measures refractive indices in the range of 1.3306 – 1.5284, the measurement error n is <0.0001. Each mixture corresponding to a specific concentration was recorded three times at a fixed temperature of 25 ± 0.05 °C and the average

Figure 1. Excess refractive index for binary solutions of ethanol+water.

value was calculated. The experimental data are used to calculate excess refractive indices (n^E), deviations in refractive index. The positive n^E arises due to dominance of the following factors. They are chemical interaction between component molecules such as heteromolecular association and clusters through the formation of hydrogen bonds and molecular geometry of the components are fitted to each other.

Graphical variations of calculated n^E and the curves representing in Figure 1, respectively. For water and ethanol system the excess refractive indices are positive throughout the whole range of composition with maxima ~ 0.3 mole fractions of ethanol. The results showed that essential structural changes occur in ethanol – water solutions at this peak. This fact indicates that at low concentrations, ethanol molecules interact strongly with water molecules and heteromolecular structures formed by hydrogen bonds.

[1] M. Pozar, B. Lovricevic, M. Primorac, B. Zoranic, L. Zoranic, T. Primorac, F. Sokolic, A. Perera. Phys. Chem. Chem. Phys., 18, (2016) 23971.
[2] 6. Sh. Gofurov, O. Ismailova, U. Makhmanov, A. Kokhkharov. Int. J. Chem.Mol. Eng. 11, N 4 (2017) 320.

UNDERSTANDING THE INITIAL STAGES OF ORGANIC NANOCRYSTAL FORMATION THROUGH MOLECULAR DYNAMICS SIMULATIONS

D. Husanova[1], J. Ochilov[2] and U. Khalilov[1,3]

[1] Institute of Ion-Plasma and Laser Technologies, Tashkent, 100125, Uzbekistan
[2] Denau Institute of Entrepreneurship and Pedagogy, Denau, 190507, Uzbekistan
[3] University of Antwerp, Antwerp, 2610, Belgium

This study investigates the stages of how prenucleation clusters form, with a focus on the very early steps before the actual perylene-based organic crystal formation begins. Using computer simulations, we examine how flat perylene molecules come together in a vacuum. Our findings show that these molecules cluster together due to forces between them, like π-π stacking and van der Waals forces, without the influence of solvents or external factors [1]. Also, we observed the Ostwald ripening process, where larger particles grow at the expense of smaller ones: clusters initially form but can break down into individual molecules, which then rejoin larger clusters. The presence of oxygen atoms in perylene molecules plays a crucial role by promoting clustering through hydrogen bonding. This interaction speeds up the formation of large clusters. We identified specific clusters, tetramer1 and tetramer2, which have unique arrangements. Interestingly, these preferred clusters do not match the typical crystal structures of α or β perylene crystals [2]. This discovery enhances our understanding of how organic crystals form in a vacuum, emphasizing the importance of unconventional pathways in explaining the origin of perylene-based organic crystals.
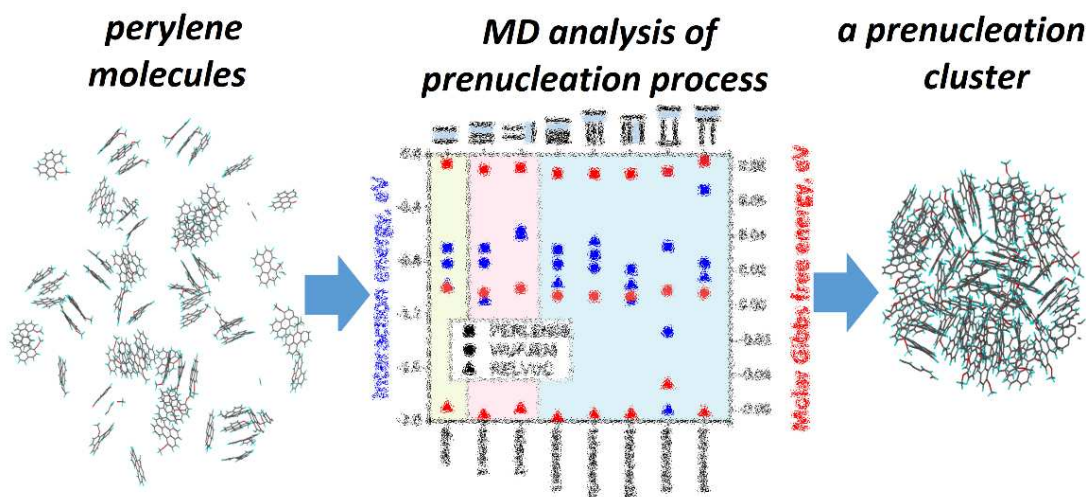
Fig.1. Interaction energy of a monomer (molecule) with a cluster and the molar Gibbs free energy of the resulting perylene cluster.

References

1. U. Khalilov et al. Uzbek Journal of Physics 23.3 (2021) 7-11.
2. D.Husanova et al. Chemical Physics 579 (2024) 112191

FIRST STEPS IN THE AGGREGATION OF SUB-10 NM DIAMETER SiO$_2$ Nanoclusters

D. Husanova[1], A. Ergasheva[1], F. Safarov[1], K. Egamberdiyev[1] and U. Khalilov[1,2]

[1] Institute of Ion-Plasma and Laser Technologies, Tashkent, 100125, Uzbekistan
[2] University of Antwerp, Antwerp, 2610, Belgium

The aggregation of sub-10 nm SiO$_2$ (silica) nanoclusters is influenced by synthesis factors and surfactant choice, impacting stability and preventing agglomeration [1,2]. While researchers optimize these parameters, the initial steps of aggregation for such nanoparticles remain elusive, posing a challenge to a complete understanding of their aggregation process. SiO$_2$ nanoparticle clustering processes (Fig. 1a) with sub-10 nm diameter were simulated using the reactive MD method with the ReaxFF potential [3]. Simulations involved 1, 2, and 5 nm SiO$_2$ clusters, with periodic boundary conditions, running for 1 ns and repeated five times for each case. The results demonstrated that the positive surface energy and negative volume free energy determine nanoparticle aggregation stability [2], with smaller clusters becoming increasingly unstable and decreasing in size over time in a vacuum [1] (Fig. 1b). The formation of initial aggregates accelerates the growth of larger clusters, indicating a tendency for small SiO$_2$ nanoparticles to transform into larger ones in a vacuum (Fig. 1a).
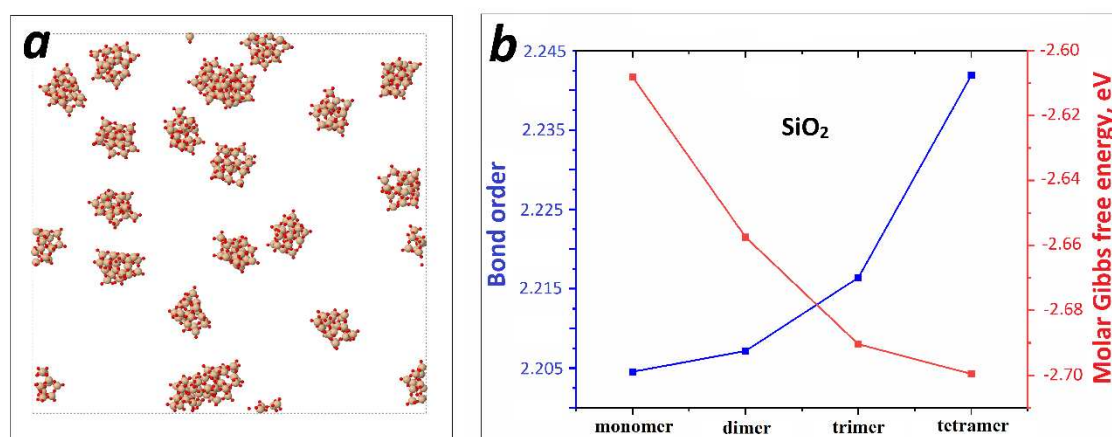
Fig.1.   (a) Aggregation process of silica nanoclusters. (b) Bond order and stability of the resulting nanoaggregates.

References

1. J.G. Croissant et al., Nature Reviews Materials, 5, 886 (2020).
2. N.T.K. Thanh et al., Chem. Rev., 114, 7610 (2014).
3. U. Khalilov et al., Carbon 171, 72-78 (2021)

STUDY OF SPUTTERING OF NIOBIUM-ZIRCONIUM POLYCRYSTAL UNDER BOMBARDING WITH LOW ENERGY ATOMIC IONS

Kakhramonova P.G., Mavlanov R.R., Nazarov M.M., Sh.J. Akhunov*, D.T. Usmanov**

Institute of Ion-Plasma and Laser Technologies, Uzbekistan Academy of Sciences, Durmon Yoli street 33, 100125, Tashkent Uzbekistan
*e-mail: a.shovkatjon@mail.ru, **e-mail: usmanov@iplt.uz

The emission of clusters during bombardment by atomic ions during sputtering of solids is currently the object of intensive research. The relevance of such work is determined, on the one hand, by the need to obtain fundamental knowledge about atomic sputtering processes, and on the other hand, by the prospect of multifaceted practical use of clusters. Occupying an intermediate position between individual atoms and condensed matter, clusters are a promising object for scientific research and for the development of new approaches in materials science, technology (nanoscale materials, cluster beam deposition), and analytical methods (SIMS). When light atomic ions interact with a solid in a small area of the surface, the local energy release increases significantly, which leads to the development of high-density nonlinear cascades. In this case, the observed increase in the sputtering coefficients and the yield of secondary cluster ions is proportional to the energy of the bombarding atoms [1,2].

The experiments were carried out in an experimental setup containing a source of atomic cesium ions, a sputtered polycrystalline niobium-zirconium (NbZr) target and a magnetic analyzer of secondary ions based on the MI 1201 mass spectrometer. The setup was significantly modernized for studying sputtering processes.

In this work, the emission of atomic and cluster ions sputtered from a niobium-zirconium (NbZr) target by atomic cesium ions in the energy range $E_0 = 2-5$ keV was studied, and experimental results were obtained. The energy dependence of the yields of sputtered secondary particles upon bombardment with atomic ions has been studied. In the mass spectra of the secondary ion emission of the NbZr target, molecular and atomic niobium ions predominated. This circumstance is associated with the low ionization potentials of niobium atoms and, accordingly, the high ionization efficiency during sputtering. The yield of secondary ions of impurities constituting the target, measured during bombardment of an NbZr target with atomic cesium ions, shows a decrease in the growth of the yield of secondary impurity ions with increasing energy of the bombarding atoms. This indicates that an increase in energy will cleanse the surface of the target and enable the release of molecular ions of the target.

Reference

1. S.N.Morozov, U.Kh. Rasulev, Izv. RAS. Ser. physical 2002. T. 66. No. 4. P. 522.
2. Sh. Akhunov, S.N. Morozov, U.Kh. Rasulev, Nucl. Instr. And Meth. B. 203 (2003) 146.

INVESTIGATION OF ELECTRON FLUENCE EFFECTS ON (TiHfTa)CN NANOCOMPOSITE NANOCRYSTALLITES

Yuldashova I.I. Tashmetov M.Yu.

Institute of Nuclear Physics, Academy of Sciences of Uzbekistan, Tashkent, Uzbekistan,
e-mail: *iroda@inp.uz*

It is known that changes in structures lead to changes in structural-mechanical properties [1]. Irradiation can create defects by changing the structure or remove existing defects as a result of "radiation damage annealing" [2]. Therefore, it is important to study the structural changes as well as the defects, for example, the density of dislocations, which may occur at different fluences as a result of irradiation. In addition, the study of the size of crystallites and microstrain allows to determine the laws of changes that can occur in multi-component nanocoatings [3].

The (TiHfTa)CN nanocoated sample from such high-entropy ceramics was selected as the object of this work, and its morphological and structural structure was analyzed, and the change of the above characteristic values when it was exposed to electrons of different fluences with energy of 2 MeV was studied. In order to determine whether the nanocomposites are evenly distributed on the surface of the sample, more than 35 points were scanned in a scanning electron microscope (SEM EVO MA 10) (CARL ZEISS). According to the results, the nanocomposites are evenly distributed on the sample surface and the coating is as follows: Ti – 41,7 (0,2) %, Hf – 29.4 (0.2) %, N – 13.9 (0.3) %, Ta – 8.0 (0.2) % C – 3.0 (0.1) % and Fe – 0.4 (0.1) % was found to be. SEM analysis shows that Fe is the base material element. The topography of the surface was also studied with the help of SEM, and it was shown two-dimensional nucleus growth that appeared on the surfaces after irradiation is related to the screw movement dislocations towards the surface [4].

Structural analyzes were performed before and after irradiation on a modern diffractometer of the Malvern Pananalytical company, type Empyrean 3, which works based on X-ray scattering. The results of the diffractogram were processed in the FullProf program using the Rietveld method, and the Miller indexes, lattice parameters and space groups were determined. The coating exhibited a two-phase nanostructure: phase 1 (TiHfTa)CN (phase.gr. $Fm\bar{3}m$), phase 2 Fe (phase.gr. $Im\bar{3}m$). The appearance of Fe reflexes is due to its use as a substrate.

The size of nanocrystallites was determined by drawing the Williamson-Hall plot from the (111), (200), (220), (311) and (420) reflections of (TiHfTa)CN phase. The density of dislocations is inversely proportional to the nanocrystallite size D [3], which is a measure of defects in crystalline solids. These values were determined for non-irradiated and irradiated samples and are listed in Table 1.

Table 1. Nanocrystallite size (D), microstrain (ε) and dislocations values (δ) of (TiHfTa)CN nanocomposite.

Flyuence, e/cm^2	D, nm	ε, $\times 10^{-3}$	$\delta \times 10^{12}$, cm^{-2}
0	7,30±0,03	5,38±0,06	1,883±0,08
0.2×10^{17}	12,24±0,04	3,87±0,08	1,024±0,05
1.5×10^{17}	20,69±0,03	1,31±0,09	0,234±0,06
2.5×10^{17}	23,73±0,03	1,30±0,07	0,178±0,07
3.5×10^{17}	24,23±0,03	1,29±0,05	0,170±0,06
4.5×10^{17}	27,34±0,02	1,20±0,05	0,134±0,04

Based on the obtained results, the dependence function of the (TiHfTa)CN nanocrystallite size on the electron fluence was determined (1) and plotted (Fig. 1):

$$D = D_0 + \rho e^{-\Phi/t} \tag{1}$$

here, D_0 is the initial nanocrystallite size, ρ is a constant size (-18.4 ± 1.8), Φ is fluence, t is 1.35 ± 0.42.

The increase of nanocrystallites is related to the reduction of their grain boundaries. As the fluence increases, we can see that the amorphous phase disappears at a small angle and a new peak is formed at the fluence of 4.5×10^{17} e/cm^2. This clearly indicates that crystallization has occurred (Fig.3). This can be determined by the ratio of the integral intensity of the nanocrystallite reflection in the nanocoating to the integral intensity of the amorphous state at small angles. This value changes from 2.04 to 9.83 in (TiHfTa)CN after 4.5×10^{17} e/cm^2 radiation fluence. This shows that crystallization occurs after irradiation in accordance with the obtained results (Fig. 2).
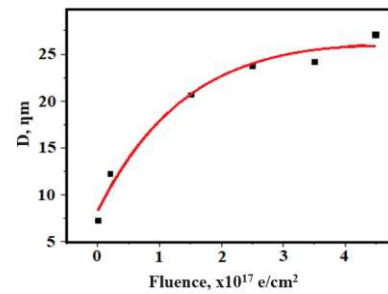
Fig.1. Dependence of the nanocrystallite size of (TiHfTa)CN nanocomposite on the electron fluence: black dots are the results obtained in the experiment; The red solid line is the proposed rule (Eq.1).
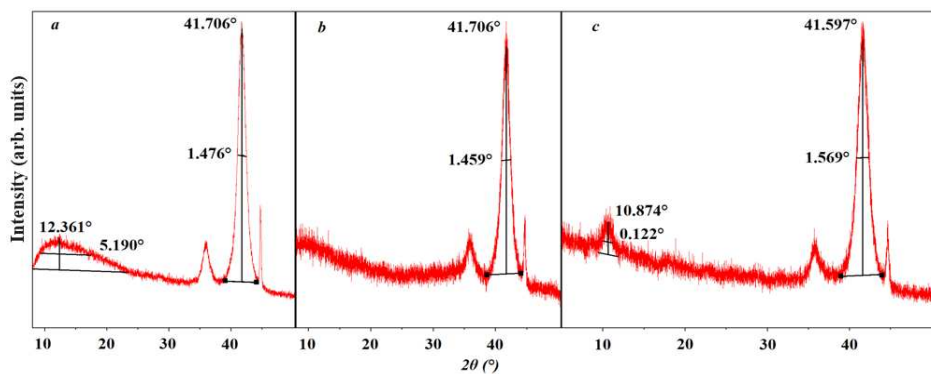
Fig.2. Diffractograms of the (TiHfTa)CN non-irradiated (a), and irradiated at fluences of 2.5×10^{17} e/cm^2 (b) and 4.5×10^{17} e/cm^2 (c) in the range of 2θ=8-50°.

The obtained results show that when the (TiHfTa)CN nanocoating was exposed to high-energy electrons, the size of the nanocrystallites increased, the density of dislocations decreased, the amorphous phase disappeared, and the crystallization increased due to the decrease in microstrain.

References:

1. Adda, Y., Beyeler, M., & Brebec, G. Radiation effects on solid state diffusion // Thin Solid Films. –Elsevier (Netherlands), 1975. –Vol.25. –No.1. –P.107–156.
2. A.D. Pogrebnjak, I.V. Yakushchenko, O.V. Bondar, O.V. Sobol', V.M. Beresnev, et al. Influence of implantation of Au- ions on the microstructure and mechanical properties of the nanostructured multielement (TiZrHfVNbTa)N coating. Phys. Solid State. 57 (2015), 1559-1564.
3. Tashmetov M.Yu., Yuldashova I.I., Ismatov N.B. Surface structure, nanocrystallite and defects in (ZrTi)CN nanocomposite irradiated by electron beam. International Journal of Modern Physics B, Vol. 35, No. 08, 2150111 (2021).
4. Yuldashova I.I. (2023). Structure and sizes of nanocrystallites of carbon nanotubes and carbon-based (ZrTi)CN, (TiHfTa)CN nanocoatings, irradiated by electrons (PhD dissertation, Institute of Nuclear Pysics). Information Resource Centre of the Institute of Nuclear Physics. https://inp.uz/storage/Dissertatsiyalar/Disser_Yuldashova_I.I.pdf

PERSPECTIVES OF APPLICATION BIOLOGICALLY IMPROVED PROPERTIES OF ADDITIVES IN MODERN MATERIALS

Turakhodjaeva F.

Arifov Institute of Ion-Plasma and Laser Technologies
E-mail: bioinnovation97@iplt.uz

In recent years, there has been a notable surge in research and innovation focused on biologically enhanced properties of additives in advanced materials. This trend reflects the growing recognition of the potential benefits that can be derived from incorporating biological principles into material science [1]. Biologically enhanced properties of additives refer to the integration of biological components or principles into materials to enhance their performance. This approach often draws inspiration from nature to develop materials with improved characteristics, such as increased strength, durability, or biocompatibility [2]. Here are some promising biologically enhanced properties of additives in materials:

Biodegradability: Incorporating biodegradable additives derived from natural sources can make materials more environmentally friendly. These additives can enhance the biodegradation of the material, reducing its environmental impact.

Self-healing: Taking inspiration from biological systems, self-healing materials can be designed by incorporating additives that can repair damage automatically. This property is particularly useful in applications where maintenance or repair is challenging, such as in aerospace or medical devices [3].

Biocompatibility: Adding bioactive components to materials can enhance their compatibility with biological systems [4]. This is crucial for medical implants, drug delivery systems, and other applications where the material interacts with living tissues.

Antibacterial properties: Integrating antibacterial or antimicrobial additives derived from natural sources can make materials resistant to microbial growth. This is beneficial in applications where maintaining a sterile environment is essential, such as in medical devices or food packaging.

Strengthening and reinforcement: Some biological materials, like cellulose or chitin, possess excellent mechanical properties. Incorporating these materials into composites can enhance the strength and toughness of the resulting material, making it suitable for various applications in industries such as construction or automotive [5].

Sustainability: Utilizing additives from renewable sources can contribute to the overall sustainability of materials. For example, incorporating plant-based additives can reduce reliance on fossil fuels and decrease the environmental impact of material production.

Adaptive and responsive behavior: Biomimicry can inspire the development of materials that exhibit adaptive or responsive behavior. For instance, materials that can change their properties in response to environmental conditions, mimicking the behavior of certain biological tissues or organisms.

Improved thermal and electrical conductivity: Some biological materials, such as certain proteins, exhibit unique thermal or electrical conductivity properties. Incorporating these elements into materials can enhance their performance in specific applications, like in electronic devices or thermal management systems [6].

Researchers and engineers continue to explore the vast potential of biologically enhanced additives to create innovative materials with improved properties and reduced environmental impact [7]. This interdisciplinary approach, often at the intersection of biology and materials science, holds promise for developing advanced materials for a wide range of applications. As experimental data from young researchers at the Arifov Institute of Ion Plasma and Laser Technologies have shown, the biological method of improving the mechanical properties of concrete can increase of strength about 20-25%. Using suspension of microorganisms as additive to compound of concrete dramatically increases the seismic resistance of concrete structures, significantly remove rebuilding

concrete construction in a period of earthquake. The field of biologically improved materials is dynamic, and ongoing research continues to explore innovative applications. As technology advances, the integration of biological principles into material design is likely to lead to breakthroughs in diverse areas, ranging from consumer products to healthcare and sustainable infrastructure.

In conclusion, the perspectives on the application of biologically improved properties of additives in modern materials are diverse and offer exciting possibilities for creating advanced materials with enhanced performance, sustainability, and functionality. Ongoing research and innovation in this field are likely to yield further breakthroughs in the development of novel materials for various applications.

REFERENCES

1. André R Studart. Additive manufacturing of biologically-inspired materials // Chemical Society Reviews 45(2). January 2016. DOI:10.1039/c5cs00836k
2. S. Pradhan, A.K. Brooks, V.K. Yadavalli. Nature-derived materials for the fabrication of functional biodevices // Materials Today Bio. Volume 7, June 2020. https://doi.org/10.1016/j.mtbio.2020.100065.
3. https://en.wikipedia.org/wiki/Self-healing_material
4. J.M. Anderson. Biocompatibility // Polymer Science: A Comprehensive Reference. Volume 9, 2012, Pages 363-383. https://doi.org/10.1016/B978-0-444-53349-4.00229-6.
5. Seena K. Thomas, Jyotishkumar Parameswaranpillai, Senthilkumar Krishnasamy, P.M. Sabura Begum, Debabrata Nandi, Suchart Siengchin, Jinu Jacob George, Nishar Hameed, Nisa.V. Salim, Natalia Sienkiewicz. A comprehensive review on cellulose, chitin, and starch as fillers in natural rubber biocomposites // Carbohydrate Polymer Technologies and Applications. Volume 2, 25 December 2021. https://doi.org/10.1016/j.carpta.2021.100095.
6. Ye Xue, Samuel Lofland, Xiao Hu. Protein-based flexible thermal conductive materials with continuous network structure: Fabrication, properties, and theoretical modeling // Composites Part B: Engineering. Volume 201, 15 November 2020. https://doi.org/10.1016/j.compositesb.2020.108377.
7. Turakhodjaeva F. Methods of improving the mechanical properties of biomass // Talented youth of New Uzbekistan, Republic best collection of articles, Uzbekistan, February 2020. ISSN: 978-9943-368-05-7

INVESTIGATION THE SCATTERING Ne IONS FROM CdTe(001)

U.O.Kutliev, Sh.R.Sadullaev

Urgench State University,Urgench, Uzbekistan
e-mail: uchkunk@mail.ru

The interaction of ions with a solid is one of the independent branches of fundamental physics. This interaction can result in changes in the physical properties of solids and the creation of materials with desired properties. At the beginning of studies of the scattering of ions by the surfaces of solids, the path to the conclusion about the paired interaction of the scattering ion with the atoms of the solid was quite difficult. The reflection of primary ions incident on the surface of a solid is the result of their interaction with lattice atoms. In the region of low and medium energies, the trajectories of colliding particles are determined to a first approximation by the forces of elastic interaction of atoms. These forces arise from the Coulomb forces of interaction between nuclei and electron atoms and, therefore, act at any distance between the interacting particles. Consequently, to calculate the trajectory of an incident ion, it is necessary to consider its interaction in the crystal lattice with all atoms simultaneously, which is very difficult. However, at not very low energies, ion-atom collisions can be considered as isolated pair collisions of particles. To further develop mathematical modeling of the process of scattering of medium and low energy ions in a wide range of angles of incidence and scattering, we used the laws of the collision of two heavy particles. So, we will consider the scattering of an ion beam from the surface of a single-crystal sample based on the model of paired single-, double-, etc. multiple impacts[1-2].

In the present work the scattering processes of Ne$^+$ ions with the initial energy 5keV on the CdTe(001) surface under grazing ion bombardment have been investigated by computer simulation by using the binary collision approximation. In the pair collision approximation, two basic programs are based, with the help of which a wide range of processes caused by the bombardment of solid bodies by accelerated particles are simulated - the MARLOWE program and the TRIM program. Both programs are based on almost the same formalism. The difference between these programs is that the first one initially operates with crystalline targets, while the second one operates with amorphous ones. In the MARLOWE program, the scattering angle is determined by numerical calculation of the classical scattering integral or using pre-calculated and tabulated values of these integrals for the Molière potential.The ion refocusing effect by surface semichannels which manifests in a growth of intensity of the scattered flux at certain grazing angles of incidence have been carefully studied. The analitical expression for calculation of the refocusing energy was found. The computational results show that in the energy spectrum the characteristic peaks corresponding to scattering of ions by the surface atomic chains and semichannels are observed. The situation and intensity of these peaks depend on the geometrical shape of the surface semichannels. The computer simulation allowed an investigation of the effect of the atomic steps on the single crystal surfaces upon the trajectory features of the ions being scattered along the ridge of the atomic chains and undergoing the surface hyperchanneling and semichanneling. This technique can be useful for investigations of semiconductor structures.

Reference

1. Parilis E.S., Turaev N.Yu., Umarov F.F., Nizhnaya S.L. Theory of scattering of medium-energy atoms by the surface of a solid body.-Tashkent, 1987.212 p.

2. Parilis E.S., Kosshinevsky L.M., Turaev N.Yu.et al. Atomic collisions on solid surfaces. Amsterdam: North-Holland, 1993.664p.

"ARCHIMEDES' FORCE" IN SUPERIONIC CONDUCTORS WITH DIFFERENT SURFACE TOPOGRAPHY

F.R. Akhmedzhanov[1], G.S. Nuzhdov[1], B.L. Oksengendler[2]

[1]Institute of Ion-Plasma and Laser Technologies
named after U.A. Arifov of the Academy of Sciences of the Republic of Uzbekistan
[2] Institute of Materials Science of the Academy of Sciences of the Republic of Uzbekistan
nujdov_g@mail.ru

The surface of a solid body is a low-dimensional object, combining the chemical properties of the gas phase and the physical properties of a solid body [1]. In this case, the surface topography plays a significant role, enhancing the influence of one or another phase. In the case of regular repetition of fragments of such a relief, fractal methods of analysis are applicable, which leads to the concept of nanofractality - one of the most important concepts in the process of synthesizing new materials with specified properties [2].

As an example, a crystal of lanthanum trifluoride (LaF3) was selected as an object of study using the modeling method, in the hexagonal cell of which twelve fluorine ions, denoted F1, are located between the base anion-cation planes [2]. These ions are shifted from the vertical plane passing through the lanthanum cations by 0.042 nm. Four fluorine ions, called F_2, are displaced from the basal planes containing the lanthanum cations by a distance of ± 0.046 nm. These F_2 ions are located on adjacent third-order symmetry axes on opposite sides of the base planes. The remaining two fluorine ions, called F_3, lie in these base planes. The most mobile ions are the F_1 type. In superionic crystals of lanthanum trifluoride, the transition to a highly conductive state has the character of a diffuse phase transition and is observed at room temperature. The formation of vacancies occurs according to the Frenkel mechanism. In this case, such a vacancy can move inside the crystal and on its surface in the XY plane over macroscopic distances [3]. The intensity of its movement on the surface is 2-3 orders of magnitude higher than in the volume. At the same time, the question of the movement of a vacancy to the surface (along the Z axis) is practically not described.

The simulation was carried out using the PM7 method [4]. 3 crystal lattice models with linear dimensions of 3.5×2.0×2.2 nm were specified. The first model had an ideal surface in the XY plane, the second and third have a protrusion and a notch, respectively, with linear dimensions of 7 angstroms.

At the zero stage, a Frenkel defect of the node-internode type was created. In this case, the node fluoride ion F_1 moved to some distant interstitial site formed by a pair of F_2 ions. Then the total energy of the crystal lattice was calculated. Next, a fluorine ion F_2 located near this vacancy was moved to the vacancy site, after which the lattice energy was again calculated. Then the F_2 ion moved to its place, being on the same Z axis, but located closer to the surface. As a result, the vacancy overcomes the cation plane. After this, the vacancy was occupied either by the nearest F_1 ion or moved higher, closer to the surface, occupying the position of the F_2 fluorine ion. This process was repeated until the vacancy came to the surface. Thus, the step-by-step change in the energy of the crystal lattice was calculated. The results are presented in Figure 1. The graph shows the formation energy E_a of a vacancy during its rise to the surface. Curve 1 corresponds to the path of a vacancy to a flat surface, curve 2 to a notch, and curve 3 to a protrusion.
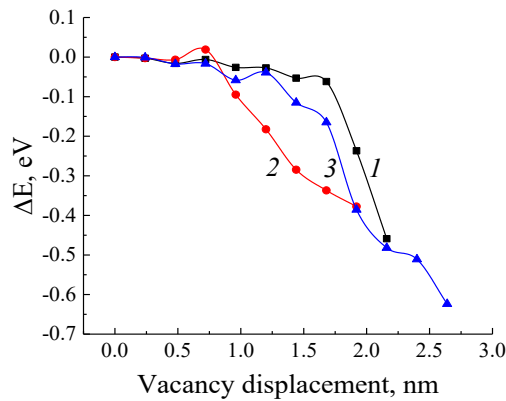
Figure 1. Change in potential energy of the LaF₃ crystal lattice

It is clearly seen that the release of a vacancy to the surface is energetically favorable, which allows us to speak of an analogue of the Archimedes force in the surface layer of the crystal. It is important to note the fact that due to the heterogeneity of the surface, in the case of a notch, such a force comes into action earlier than in the case of a flat surface and protrusion. Thus, if in the case of a flat surface the movement of a vacancy along the X axis is invariant, then in the case of a fractal surface this movement is no longer invariant. This statement is shown in Figure 2 and can be represented as formula (1).
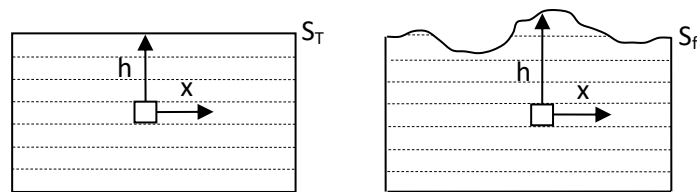
Figure 2. Effect of surface dimension on the movement of a fluorine ion vacancy (S_T - ideal surface, S_f - fractal surface, h - distance from the vacancy to the surface).

$$\left. \frac{\partial h}{\partial x} \right|_{x=\text{var}} = 0 \qquad\qquad \left. \frac{\partial h}{\partial x} \right|_{x=x_i(\,fractal)} = 0 \qquad (1)$$

In the first case, the distance from the vacancy to the surface (h) is the same for any step along the X axis. In the second case, only for a fractal step.

It is also clear that the movement of a vacancy to the surface of the protrusion is most likely for the crystal lattice, since the energy of its formation is E_a=-0.6 eV. A position on a flat surface is less likely (E_a =-0.46 eV), and a position in a notch is even less likely in terms of formation energy (E_a=-0.37 eV). Moreover, this effect is nanosized in nature and can significantly affect the concentration of vacancies, which is of great importance in an applied sense (surface conductivity and chemical reactivity).

References.

1) Volkenshtein F.F. Electrons and crystals. M. Nauka. 1983, 127 p.

2) Oksengendler B.L., Turaeva N.N., Ashurov Kh. B. et al. // HWPh, 2019, vol. 298, pp. 1-36. ISBN: 978-1-53614-795-7

3) Rhandour, A., Reau, J.M., Matar, S.F., et al. // MRB, 1985, vol. 20, pp. 1309–1327. **DOI:** 10.1016/0025-5408(85)90125-4

4) Axmedjanov F. R., Mirzaev S. Z., Nuzhdov G. S., Maxarov, N. M.// UJPh, 2021. vol. 23, №3, С. 33–37. **DOI:** 10.52304/.v23i3.261

5) Stewart JJ. // JMM. 2013, vol. 19, №1, pp 1-32. **DOI**: 10.1007/s00894-012-1667-x.

IMPORTANCE OF THERMAL HEATING METHOD IN IMPROVING THE STABILITY OF PEROVSKITE SOLAR CELLS

[1]Otakulova N.F., [1]Ibragimova H.F. [1,2]Saparbayev A.A.

[1]*National University of Uzbekistan named after Mirzo Ulugbek,*
[2] *Institute of Ion Plasma and Laser Technologies named after U.A. Arifov*
Email: otaqulovanilufar98@gmail.com

Perovskite solar cells (PSCs) are attracting great interest among world scientists due to high power conversion efficiency (PCE), low production costs, high absorption coefficient, and the possibility of preparation at low temperatures[1-2]. After fourteen years of intensive development, 28% PCE of organic-inorganic hybrid perovskite solar cells [5]. However, PSCs still face a number of challenges in implementing potential commercialization programs. One of the main problems in PSCs research is stability, i.e. lifetime. Although perovskite solar cells have achieved high PCE, due to their sensitivity to the environment in a very short time, perovskites decompose very quickly under the influence of oxygen and moisture in atmospheric conditions and become unsuitable for receiving energy from sunlight[6-7]. Currently, many methods are used to solve these problems, such as adding additives to the perovskite synthesis solution, perovskite synthesis at high temperature, thermal heating of the perovskite active layer, washing the surface of the perovskite active layer with liquid[2-4]. In this work, we used a glass/FTO substrate heating method during the deposition of the perovskite active layer to improve the quality of the inorganic perovskite active layer. Figure 1 shown a schematic diagram of $CsPbIBr_2$ perovskite active layers prepared by heating the glass/FTO substrate and at room temperature. The fabrication method of PSC in two different conditions is carried out in the following as. First, the glass/FTO substrates were cleaned in an ultrasonic bath, acetone, deionized (DI) water, and isopropyl alcohol (IPA) for 13 min each, and then dried using high purity nitrogen gas. Subsequently, the glass/FTO substrates were cleaned by treatment for 6 min in an oxygen plasma cleaner. After the glass/FTO surface was prepared, TiO_2 was deposited using the spin coating method at 4000 rpm for 20 seconds and heated in an oven at 110°C for 10 minutes under atmospheric conditions.
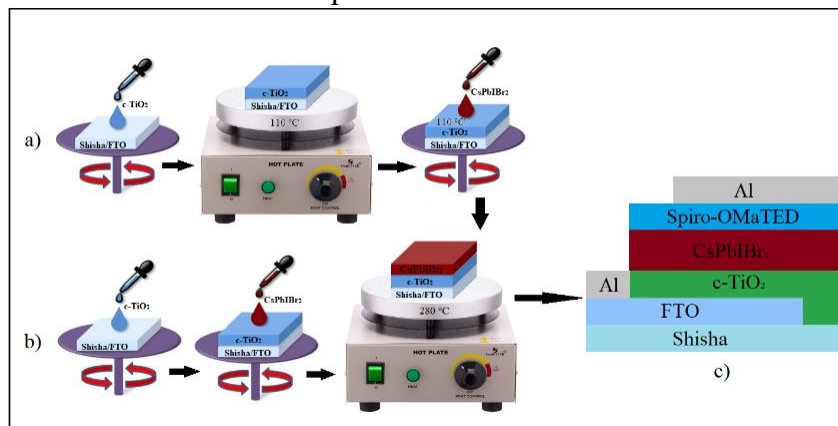
Figure 1. Schematic diagram of the method of preparing PSCs

Then, the heated glass/FTO/TiO_2 and quickly 25-30 μL of $CsPbIBr_2$ solution was dropped and deposited by the spin-coating method at a speed of 3500 rpm for 20 s (Fig. 1a). Then, perovskite solution deposited on Glass/FTO/TiO_2 cooled to room temperature (Fig. 1b). $CsPbIBr_2$ perovskite active layers prepared under without glass/FTO substrate preheating method and by glass/FTO substrate preheating method, then both perovskite active layers termal annealed at 280°C for 10 minutes. Then, Spiro-OMeTAD solution was dropped on the surface of the cooled active layer and it was coated using the spin-coating method at a speed of 4000 rpm for 20 s. When the whole structure was ready, Al (aluminum) with a thickness of 100 nm was deposited as a cathode by thermal evaporation under vacuum conditions of under a pressure of 5×10^{-4} Pa (Fig. 1c). Analyzing

the photovoltaic results, increased the short current circuit density value from 7,26 to 11.32 mA/cm^2 and the open circuit voltage value from 0.80 to 0.90 V and PCE increased from 4.1% to 6.9% via heating the glass/FTO substrate at 110 °C. In figure 2 compares the stability of CsPbIBr$_2$ PSCs prepared without heating the glass/FTO substrate and by heating the glass/FTO substrate. We can see in figure 2 results, increased not only the photovoltaic parameters of the PSCs prepared by heating the glass/FTO substrate, but also their stability significantly increased and better than PSCs prepared without heating the glass/FTO substrate.

The PCE of PSCs prepared by the conventional method was almost zero within 24 days, on the contrary, the PCE of PSCs prepared by heating the glass/FTO substrate remained around 1% even after 30 days. In conclusion, using glass/FTO substrate heating to prepare perovskite active layers improves their structure by effectively reducing defects in the active layer

Figure 2. Stability of PSCs prepared under different conditions.

and increase the size of crystal particles. In addition, using this method, the thickness of the active layer increased and their charge recombination decreased significantly. Significantly increased stability and photovoltaic parameters of the PSC prepared by this method.
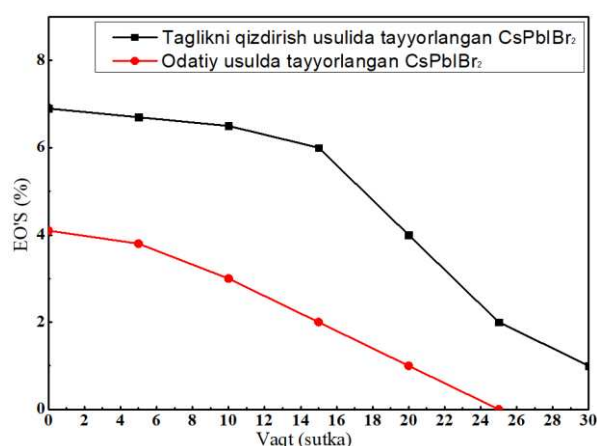
References

1. Qidong Tai, Kai-Chi Tang, Feng Yan, "Recent progress of inorganic perovskite solar cells" . 7th June 2019.
2. Kim, Minjin, et al. "Conformal quantum dot–SnO$_2$ layers as electron transporters for efficient perovskite solar cells." Science 375.6578 (2022): 302-306.
3. Eswaramoorthy, Nandhakumar. "Fabrication and Manufacturing Process of Perovskite Solar Cell." Green Energy: Solar Energy, Photovoltaics, and Smart Cities (2020): 6
4. Kojima A, Teshima K, Shirai Y, et al. Organometal halide perovskites as visible-light sensitizers for photovoltaic cells. Journal of the American Chemical Society: 2009, 131 (17): 6050-6051.
5. Oxford PV perovskite solar cell achieves 28% efficiency. Oxford PV: 2019.
6. CHEN P-Y, QI J, KLUG MT, et al. Environmentally responsible fabrication of efficient perovskite solar cells from recycled car batteries. Energy & Environmental Science: 2014, 7 (11): 3659-3665.
7. Lu L, Zheng T, Wu Q, et al. Recent advances in bulk heterojunction polymer solar cells. Chemical reviews: 2015, 115 (23): 12666-12731.

ELECTRON ENERGY IN A RECTANGULAR FINITE POTENTIAL WELL BASED ON NARROW BAND-GAP SEMICONDUCTORS

A. Davlatov[*], *A. Abdukarimov, A. Botirjonov, R. Mukhiddinov*

Namangan State University, 316 Uychi Street, Namangan 716019, Uzbekistan.
*Corresponding author: litsey111213@gmail.com

Annotation

It is known that we can encounter transcendent equation when determining the energy levels in a finite deep potential well and this is inconvenient. By using Nelson's formula for the effective mass in right-angled finite deep potential well medium based on narrow band-gap semiconductors, we calculated electronic energy levels using Gareetti's formula and obtained analytical expression

The main part

Nowadays, the research of small-scale quantum wire, quantum dots and quantum layers is considered essential in the world. The study of heterostructures with semiconductor potential has been an important problem of quantum mechanics. Because lasers, light-emitting diodes, field-effect transistors, photodetectors and solar cells are being developed based on semiconductor potential wells. Understanding, manufacturing, and their control depend, to a large extent, on the precise knowledge of the energy of electrons, holes, etc. moving in these devices.

The fact that $\psi(x)$ is nonzero at the walls increases the de Broglie wavelength in the well (compared with that in the infinite well), and this in turn lowers the energy and momentum of the particle.

[1] offers an interesting expression for the finite potential well problem. He recommends viewing a finite-dimensional potential well L as $L \to L + 2\delta$ an infinitely deep potential well. Let's repeat these relations taking the nonparabolicity into account for the potential well in narrow band gap semiconductors. Then, δ will be equal to the following:

$$\delta = \frac{\hbar}{\sqrt{2m^*_{InAs(0)}(V - E_0(n))}} \tag{1}$$

The energy $E_0(n)$ is equal to:

$$E_0(n) = \frac{1}{2\alpha_{InAs}}\left[\sqrt{1 + 2\alpha_{InAs}\frac{\hbar^2\pi^2 n^2}{m^*_{InAs(0)}L^2}} - 1\right]. \tag{2}$$

If we insert the denotation $E_0 = \dfrac{\pi^2\hbar^2 n^2}{2m^*_{InAs(0)}L^2}$, the expression (2) takes the following form.

$$E_0(n) = \frac{1}{2\alpha_{InAs}}\left[\sqrt{1 + 4\alpha_{InAs}E_0} - 1\right] \tag{3}$$

Taking the above relations into account, it is possible to express the n-level in a finite potential well.

$$E(n) = \frac{\pi^2\hbar^2 n^2}{2m^*_{InAs}(L + 2\delta)^2} = \frac{\pi^2\hbar^2 n^2}{2m^*_{InAs(0)}(1 + \alpha_{InAs}E(n))\left(L + \dfrac{2\hbar}{\sqrt{2m^*_{InAs(0)}(V - E_0(n))}}\right)^2} \tag{4}$$

Table 1 lists the band parameters of InP and InAs semiconductors. The Garrett's approximation for the potential well with InP/InAs/InP heterostructure gives good results at the first level. But deviations at the second and higher levels will be very rude. The reason for this is that the denominator in equation (1) strives for zero. From equations (1) and (2) it is clear that

$$V_0 \gg \frac{1}{2\alpha_{InAs}}\left[\sqrt{1+2\alpha_{InAs}\frac{\hbar^2\pi^2 n^2}{m^*_{InAs(0)}L_k^2}}-1\right] \quad \Rightarrow \quad L_k \gg \sqrt{\frac{\hbar^2\pi^2 n^2}{2V_0\left(1+V_0\alpha_{InAs}\right)m^*_{InAs(0)}}} \qquad (5)$$

when the relationship above is applicable, the use of approximation gives results close to exact values. The (4) equation given by us is convenient for determining energy levels in a finite deep potential well.

Table 1. Band parameters for InAs and InP semiconductors samples [2].

Material parameters	$E_g,(eV)$	$m^*_{(0)}/m_0$	$\alpha,(1/eV)$
InAs	0.36	0.023	2.65
InP	1.35	0.077	0.63
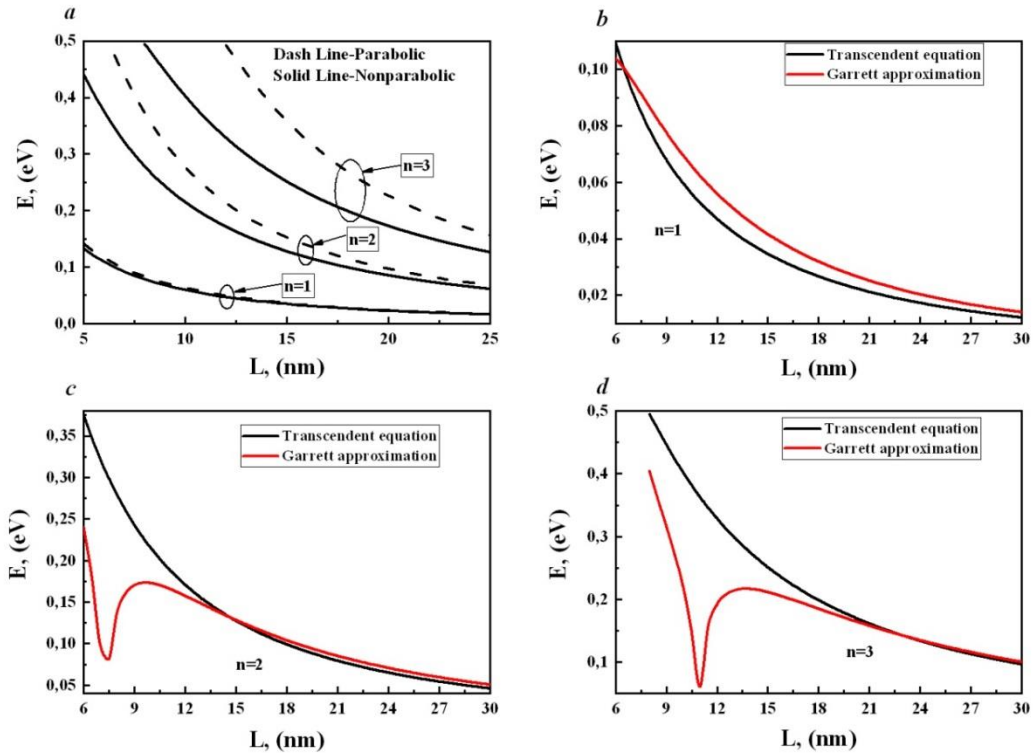
Figure 1. Dependence of electron energy levels in InP/InAs/InP heterostructural potential well on the width. a) Levels 1, 2 and 3 for non-parabolic and parabolic dispersion, b) for level 1, c) for level 2, d) for level 3.

References

1. Garrett, S. (1979). Bound state energies of a particle in a finite square well: A simple approximation. American Journal of Physics, 47(2), 195–195. doi:10.1119/1.11875

2. Gulyamov G., Gulyamov A.G., Davlatov A.B., Juraev Kh.N. Energy levels in nanowires and nanorods with a finite potential well. Advances in Condensed Matter Physics. 2020. 4945080, 12 p. (2020).

STRUCTURE OF ESSENTIAL SPECTRA AND DISCRETE SPECTRUM OF THE ENERGY OPERATOR OF FOUR-ELECTRON SYSTEMS IN THE IMPURITY HEISENBERG MODEL IN ONE-DIMENSIONAL LATTICE. THIRD TRIPLET STATE

S.M.Tashpulatov, R.T. Parmanova

Institute of Nuclear Physics of the Academy of Science of Republic of Uzbekistan, Tashkent, Uzbekistan, sadullatashpulatov@yandex.com

The spectrum of the energy operator of system of four-electrons in a crystal described by the Hubbard Hamiltonian in the triplet state was studied in [1]. In the four-electron systems are exists quintet state, and three type triplet states, and two type singlet states. The spectrum of the energy operator of four-electron systems in the Hubbard model in the quintet, and singlet states were studied in [2]. In this work We consider of the energy operator of four-electron systems in the impurity Hubbard model in the one-dimensional lattice, and investigated the structure of essential spectra and discrete spectrum of the system for the third triplet state. Hamiltonian of the considering system has the form
$H = A \sum_{m,\gamma} a_{m,\gamma}^+ a_{m,\gamma} + B \sum_{m,\tau,\gamma} a_{m,\gamma}^+ a_{m+\tau,\gamma} + U \sum_m a_{m,\uparrow}^+ a_{m,\uparrow} a_{m,\downarrow}^+ a_{m,\downarrow} + (A_0 - A) \sum_\gamma a_{0,\gamma}^+ a_{0,\gamma} + (B_0 - B) \sum_{\tau,\gamma} (a_{0,\gamma}^+ a_{\tau,\gamma} + a_{\tau,\gamma}^+ a_{0,\gamma}) + (U_0 - U) a_{0,\uparrow}^+ a_{0,\uparrow} a_{0,\downarrow}^+ a_{0,\downarrow}$. Here A (A_0) is the electron energy at a regular (impurity) lattice site; $B > 0$ ($B_0 > 0$) is the transfer integral between electrons (between electron and impurity) in a neighboring sites, $\tau = \pm e_j, j = 1,2,\dots,\nu$, where e_j are unit mutually orthogonal vectors, which means that summation is taken over the nearest neighbors, U (U_0) is the parameter of the on-site Coulomb interaction of two electrons, correspondingly in the regular (impurity) lattice site; γ is the spin index, $\gamma = \uparrow$ or $\gamma = \downarrow$, $\uparrow$ and $\downarrow$ denote the spin values $\frac{1}{2}$ and $-\frac{1}{2}$, and $a_{m,\gamma}^+$ and $a_{m,\gamma}$ are the respective electron creation and annihilation operators at a site $m \in Z^\nu$. The third triplet state corresponds four-electron states (or anti bound states) to the basis functions: ${}^3t_{p,q,r,k \in Z^\nu}^1 = a_{p,\uparrow}^+ a_{q,\uparrow}^+ a_{r,\uparrow}^+ a_{k,\uparrow}^+$. The subspace ${}^3\widetilde{\mathcal{H}}_t^1$, corresponding to the third triplet state is the set of all vectors of the form ${}^3\psi_t^1 = \sum_{p,q,r,k \leq Z^\nu} f(p,q,r,k) \, {}^3t_{p,q,r,k \in Z^\nu}^1, f \in l_2^{as}$, where l_2^{as} is the subspace of antisymmetric functions in $l_2((Z^\nu)^4)$. In this case, the Hamiltonian H acts in the antisymmetric Fock space ${}^3\widetilde{\mathcal{H}}_t^1$. Let ${}^3\widetilde{H}_t^1$ be the restriction H to the subspace ${}^3\widetilde{\mathcal{H}}_t^1$. The third triplet state corresponds the free motions of four-electrons in the lattice and their interactions. Let $\varepsilon_1 = A_0 - A$, $\varepsilon_2 = B_0 - B$, and $\varepsilon_2 = U_0 - U$. The energy of the system depends on its total spin S. The Hamiltonian H acts in the antisymmetric Fock space $\mathcal{H}_{as}$. Let φ_0 be the vacuum vector in the space $\mathcal{H}_{as}$.

Theorem 1. The subspace ${}^3\widetilde{\mathcal{H}}_t^1$ is invariant under the operator H, the restriction ${}^3\widetilde{H}_t^1$ of operator H to the subspace ${}^3\widetilde{\mathcal{H}}_t^1$ is a bounded self-adjoint operator. It generated a bounded self-adjoint operator ${}^3\overline{H}_t^1$ acting in the space l_2^{as} as: $({}^3\overline{H}_t^1 f)(p,q,r,k) = 4Af(p,q,r,k) + B \sum_\tau [f(p + \tau, q, r, k) + f(p, q + \tau, r, k) + f(p, q, r + \tau, k) + f(p, q, r, k + \tau)] + U[\delta_{p,q} + \delta_{q,r} + \delta_{q,k}] + \varepsilon_1[\delta_{p,0} + \delta_{q,0} + \delta_{r,0} + \delta_{k,0}]f(p,q,r,k) + \varepsilon_2 \sum_\tau [\delta_{p,0} f(\tau, q, r, k) + \delta_{q,0} f(p, \tau, r, k) + \delta_{r,0} f(p, q, \tau, k) + \delta_{k,0} f(p, q, t, \tau) + \delta_{p,\tau} f(0, q, r, k) + \delta_{q,\tau} f(p, 0, r, k) + \delta_{r,\tau} f(p, q, 0, k) + \delta_{k,\tau} f(p, q, r, 0)] + \varepsilon_3[\delta_{p,0} \delta_{q,0} + \delta_{q,0} \delta_{r,0} + \delta_{q,0} \delta_{k,0}]f(p,q,r,k).$ (1)

The operator ${}^3H_t^1$ acts on a vector ${}^3\psi_t^1 \in {}^3\widetilde{\mathcal{H}}_t^1$ as
$${}^3H_t^1 \, {}^3\psi_t^1 = \sum_{p,q,r,k \in Z^\nu} ({}^3\overline{H}_t^1 f)(p,q,r,k) \, {}^3t_{p,q,r,k \in Z^\nu}^1. \qquad (2)$$

Lemma 1. The spectra of the operators ${}^3H_t^1$ and ${}^3\overline{H}_t^1$ coincide.

The spectral properties of four-electron systems in the impurity Hubbard model in the third triplet state are closely related to those of its two-particle subsystems consisting of one-electron and

impurities. Therefore we first study the spectrum and localized impurity states of one-electron impurity systems. In the work [3] were investigated the structure of essential spectra and discrete spectrum of two-electron systems in the impurity Hubbard model in the singlet state. The energy spectrum of one-electron systems in the impurity Hubbard model is also studied there. We will use from the results of the works [3]. From obtaining results is obviously, that the spectrum of the energy operator one-electron systems in the impurity Hubbard model $\widetilde{H}_1$ is consists from continuous spectrum and no more two eigenvalues.

Theorem 2. Let $\nu = 1$. Then

1). If $\varepsilon_2 = -B$ and $\varepsilon_1 < -2B$ (respectively, $\varepsilon_2 = -B$ and $\varepsilon_1 > 2B$), then the essential spectrum of the operator ${}^3\widetilde{H}_t^1$ is consists of the union of eight segments: $\sigma_{ess}\left({}^3\widetilde{H}_t^1\right) = [4A - 8B, 4A + 8B] \cup [3A - 6B + z, 3A + 6B + z] \cup [2A - 4B + 2z, 2A + 4B + 2z] \cup [A - 2B + 3z, A + 2B + 3z] \cup [2A - 4B + z_3, 2A + 4B + z_3] \cup [A - 2B + z + z_3, A + 2B + z + z_3] \cup [2A - 4B z_4, 2A - 4B + z_4] \cup [A + 2B + z + z_4, A + 2B + z + z_4]$, and discrete spectrum of the operator ${}^3\widetilde{H}_t^1$ is consists of three eigenvalues: $\sigma_{disc}\left({}^3\widetilde{H}_t^1\right) = \{4z, 2z + z_3, 2z + z_4\}$, $z = A + \varepsilon_1$, and z_3, z_4 are same concrete numbers.

2). If $\varepsilon_2 = -2B$ or $\varepsilon_2 = 0$ and $\varepsilon_1 < 0$ (respectively, $\varepsilon_2 = -2B$ or $\varepsilon_2 = 0$ and $\varepsilon_1 > 0$), then the essential spectrum of the operator ${}^3\widetilde{H}_t^1$ is consists of the union of eight segments: $\sigma_{ess}\left({}^3\widetilde{H}_t^1\right) = [4A - 8B, 4A + 8B] \cup [3A - 6B + z, 3A + 6B + z] \cup [2A - 4B + 2z, 2A + 4B + 2z] \cup [A - 2B + 3z, A + 2B + 3z] \cup [2A - 4B + z_3, 2A + 4B + z_3] \cup [A - 2B + z + z_3, A + 2B + z + z_3] \cup [2A - 4B + z_4, 2A - 4B + z_4] \cup [A + 2B + z + z_4, A + 2B + z + z_4]$, and discrete spectrum of the operator ${}^3\widetilde{H}_t^1$ is consists of three eigenvalues: $\sigma_{disc}\left({}^3\widetilde{H}_t^1\right) = \{4z, 2z + z_3, 2z + z_4\}$, $z = A - \sqrt{4B^2 + \varepsilon_1^2}$ (respectively, $z = A + \sqrt{4B^2 + \varepsilon_1^2}$).

3). If $\varepsilon_1 = 0$ and $\varepsilon_2 > 0$ or $\varepsilon_1 = 0$ and $\varepsilon_2 < -2B$, then the essential spectrum of the operator ${}^3\widetilde{H}_t^1$ is consists of the union of sixteen segments: $\sigma_{ess}\left({}^3\widetilde{H}_t^1\right) = [4A - 8B, 4A + 8B] \cup [3A - 6B + z_1, 3A + 6B + z_1] \cup [3A - 6B + z_2, 3A + 6B + z_2] \cup [2A - 4B + 2z_1, 2A + 4B + 2z_1] \cup [2A - 4B + 2z_2, 2A + 4B + 2z_2] \cup [2A - 4B + z_1 + z_2, 2A + 4B + z_1 + z_2] \cup [A - 2B + 3z_1, A + 2B + 3z_1] \cup [A - 2B + 3z_2, A + 2B + 3z_2] \cup [A - 2B + z_1 + 2z_2, A + 2B + z_1 + 2z_2] \cup [A - 2B + 2z_1 + z_2, A + 2B + 2z_1 + z_2] \cup [2A - 4B + z_3, 2A + 4B + z_3] \cup [A - 2B + z_1 + z_3, A + 2B + z_1 + z_3] \cup [2A - 4B + z_4, 2A - 4B + z_4] \cup [A + 2B + z_1 + z_4, A + 2B + z_1 + z_4] \cup [A - 2B + z_2 + z_3, A + 2B + z_2 + z_3] \cup [A - 2B + z_2 + z_4, A + 2B + z_2 + z_4]$, and discrete spectrum of the operator ${}^3\widetilde{H}_t^1$ is consists of eleven eigenvalues: $\sigma_{disc}\left({}^3\widetilde{H}_t^1\right) = \{4z_1, 3z_1 + z_2, 4z_2, 2z_1 + 2z_2, z_1 + 3z_2, 2z_1 + z_3, z_1 + z_2 + z_3, 2z_2 + z_3, 2z_1 + z_4, z_1 + z_2 + z_4, 2z_2 + z_4\}$, where $z_1 = A - \frac{2BE}{\sqrt{E^2 - 1}}$, $z_2 = A + \frac{2BE}{\sqrt{E^2 - 1}}$ and $E = \frac{(B + \varepsilon_2)^2}{\varepsilon_2^2 + 2B\varepsilon_2}$.

REFERENCES

1. Tashpulatov S. M. Spectra of the energy operator of four-electron systems in the triplet state in the Hubbard Model. Journal Phys. Conf. Ser. 2016:697: 012025, 1-25.
2. Tashpulatov S. M. The structure of essential spectra and discrete spectrum of four-electron systems in the Hubbard model in a singlet state. Lobachevskii Journal of Mathematics. 2017: 38: No 3: 5303541.
3. Tashpulatov S.M. Spectra of the Energy Operator of Two-Electron System in the Impurity Hubbard Model. Journal of Applied Mathematics and Physics. 2022: 10: No 9: 274332779.

STEPS OF DOUBLE-WALLED CARBON NANOTUBE NUCLEATION

F. Safarov[1,2], H. Soatova[2], A. Dustmatov[2] and U. Khalilov[1,2,3]

[1] *Arifov Institute of Ion-Plasma and Laser Technologies, Tashkent, 100125, Uzbekistan*
[2] *Denau Institute of Entrepreneurship and Pedagogy, Denau, 190507, Uzbekistan*
[3] *University of Antwerp, Antwerp, 2610, Belgium*
fakhmsafarov@gmail.com

In contrast to single-walled carbon nanotubes (SWNTs), double-walled carbon nanotubes (DWNTs) exhibit superior mechanical strength and thermal stability. However, the widespread adoption of DWNTs faces obstacles due to difficulties in selectively growing them [1]. Understanding the nucleation step is critical for precisely controlling CNT growth [2]. This study investigates the nucleation of DWNTs using molecular dynamics (MD) simulations. Growth is accomplished by allowing methane species [3] to impinge on a Ni_{91} nanocluster. During the simulations, the system temperature was maintained at 2000 K, regulated by a canonical Bussy thermostat. Simultaneously, the cluster was physisorbed onto a virtual Al surface. Based on the preliminary results, the process can be divided into two stages: 1) The steps leading to the catalyst reaching the supersaturation point and the subsequent development of graphene networks on it closely mirror the SWNT nucleation process [4] (Figs. 1*a* and 1*b*); 2) As the initial cap-shaped structure expands and rises from the nanocluster's surface, carbon atoms disperse within the nanocluster, giving rise to fresh carbon chains on its surface. These chains ultimately contribute to the creation of initial carbon rings, culminating in the eventual development of a second cap. (Figs. 1*c* and 1*d*)

(a)   *(b)*   *(c)*   *(d)*
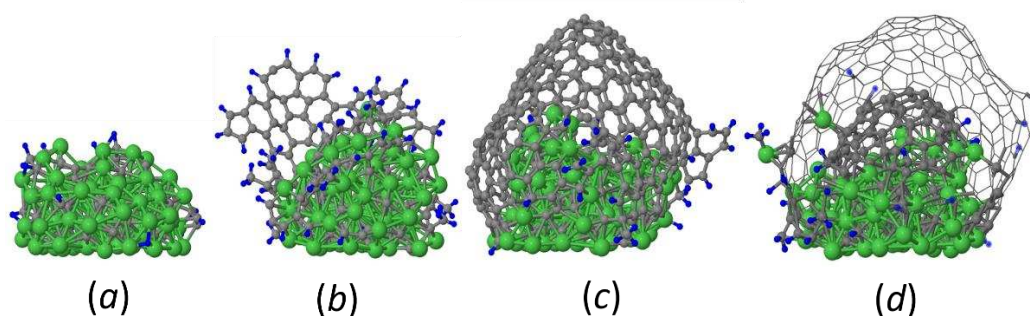
Fig.1. Nucleation steps of the DWNT: (a) super-saturation point; (b) graphene network formation; (c) first cap formation; (d) second cap formation. Ni, C, and H atoms are shown in green, gray, and blue, respectively.

References

1. Shen C. et al., Nanoscale 3, 503-518 (2011).
2. Khalilov U. et al., Nature Communications 6, 10306 (2015).
3. Hash D. B. et al., Journal of Applied Physics 93, 750-752 (2003).
4. Khalilov U. et al., Nanoscale 6, 9206-9214 (2014).

DEVIATION OF DISPLACEMENT VECTOR AND ENERGY FLOW FROM THE WAVE VECTOR OF ACOUSTIC WAVES IN NaCl$_{0.7}$Br$_{0.3}$ CRYSTALS

F.R. Akhmedzhanov, [*] _F.B. Tugalov, V.N. Avdievich_

Institute of Ion-Plasma and Laser Technologies of the Academy of Sciences of Uzbekistan,
str. Durmon Yuli 33, 100125 Tashkent, Uzbekistan
*Corresponding author: akhmedzhanov.f@gmail.com

As it is known the direction of energy flow is essential when setting up experiments with acoustic waves and especially when measuring the velocity and attenuation of acoustic waves. In this work, the dependence of the polarization vector and energy flow density on the longitudinal and transverse waves in NaCl$_{0.7}$Br$_{0.3}$ crystals and their dependence on the wave vector was investigated for the first time. The studied samples have the form of parallelepiped, the long side of which was oriented along the main cubic directions [100] and [110]. The orientation of the samples was carried out along the cleavage planes during grinding and polishing of the crystals. The studies were carried out at the room temperature in the frequency range 0.3-1.6 GHz. Acoustic waves were excited using piezoelectric transducers made of quartz or lithium niobate by 50-100 microns thick.

The acoustic properties of crystals were studied using the Gren-Christiffel system of equations. In general, the direction of the polarization vector **η** and the energy flow density vector do not correspond to the direction of the acoustic wave vector **q**. In particular, for quasi-longitudinal and quasi-transverse waves in the (001) plane, when the direction of the wave vector is changed by an angle φ, the deviation of the polarization vector from axis [100] ψ is determined as follows [1]:

$$\Psi = arctg\left(\frac{\Gamma_{12}}{\rho V^2 - \Gamma_{22}}\right) \qquad (1)$$

where V-acoustic wave velocity, ρ -crystal density, Γ_{12} and Γ_{22} are the real components of the Gren-Christoffel tensor. The angle of deviation of the energy flow density vector ξ is defined as follows:

$$\xi = arctg\left(\frac{A_2}{A_1}\right) \qquad (2)$$

where A$_1$ and A$_2$ are the components of the energy flux density tensor.
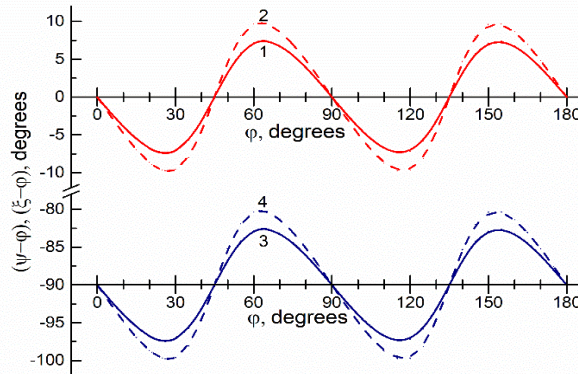
Fig. 1. Deviation of direction of polarization (1,3) and energy flux density (2,4) on the direction of the wave vector of quasi-longitudinal (1, 2) and quasi-transverse waves (3, 4) in the (001) plane in NaCl$_{0.7}$Br$_{0.3}$ crystals

As can be seen from Figure 1, there are three special directions [100], [110] and [010] in this plane, along which purely longitudinal and purely transverse waves propagate. The angle of maximum deviation of the polarization vector from the wave vector is 7.4 degree. It was determined that the angle of deviation of the energy flow density vector from the wave vector is equal to 9.8 degree.

References

[1]. Dieulesain E., Royer D. Elastic waves in solids. Application for treatment of signals.1982. M. Nauka,342 p.

ANISOTROPY OF ATTENUATION OF HIGH FREQUENCY ACOUSTIC WAVES IN MgO CRYSTALS

F.R. Akhmedzhanov, <u>N.M. Makharov</u>, J.O. Kurbanov

Institute of Ion-plasma and Laser Technologies of the Academy of Sciences of Uzbekistan

In [1], a new approach was proposed to describe the anisotropy of acoustic waves in crystals using effective real and imaginary elasticity constants. In this work, such an approach is developed to establish a connection between the effective Grüneisen constant, which characterizes the nonlinearity of interatomic interaction forces, and the anisotropy of the attenuation of acoustic waves in MgO crystals. The MgO samples had the shape of parallelepipeds and were oriented along the [100], 110] and [111] axes with an accuracy of 10. Acoustic waves were excited by X- and Y-cut quartz transducers. The studies were carried out at room temperature using the ultrasonic method [2]. The accuracy of determining the speed and attenuation of acoustic waves was 0.2% and 10%, respectively.

The measurement results and calculated values of the real and imaginary effective elastic constants c'_{eff} and c''_{eff} for the [100], [110] and [111] directions are given in Table 1.

Table 1. Velocity and attenuation (1 GHz) of acoustic waves, effective real and imaginary elastic constants, and Grüneisen parameter in MgO crystals

q	η	V, 10^3 m·s^{-1}	c'_{eff}, 10^{10} N·m^{-2}	α, cm^{-1}	c''_{eff}, 10^7 N·m^{-2}	$\gamma_{эфф}$
[100]	[100]	8.94	28.6	0.56	4.56	2.58
	[001]	6.43	14.8	0.11	0.33	0.69
[110]	[110]	9.67	33.4	0.23	2.33	1,69
	[110]	5.27	9.95	1.53	2.56	1.77
	[001]	6.43	14.8	0.11	0.33	0.63
[111]	[111]	9.89	35.06	0.14	1.59	1.38
	[110]	5.68	11.56	0.87	1.81	1.48

Three independent components of the real and imaginary parts of the elasticity tensor for MgO crystals, which are necessary to find the effective elastic constants, were determined by us from the values of the velocity and attenuation coefficient of longitudinal and transverse waves along the [100] and [110] directions. As a result, the values of the real and imaginary components of the complex elasticity tensor were obtained:

$$c'_{11} = 28.6 \cdot 10^{10} \text{ N·m}^{-2}; \ c'_{12} = 8.7 \cdot 10^{10} \text{ N·m}^{-2}, \ c'_{44} = 14.8 \cdot 10^{10} \text{ N·m}^{-2}$$

$$c''_{11} = 4.56 \cdot 10^{7} \text{ N·m}^{-2}, \ c''_{12} = -0.550 \cdot 10^{7} \text{ N·m}^{-2}, \ c''_{44} = 0.326 \cdot 10^{7} \text{ N·m}^{-2}.$$

The obtained values of the constants make it possible to calculate the attenuation of acoustic waves according to the Akhiezer mechanism [2] along any direction of propagation of acoustic waves in MgO crystals, using the expression [3]:

$$\alpha = \frac{1}{2} \omega \frac{c''_{эфф}}{c'_{эфф}} \qquad (1)$$

Here the real and imaginary effective elastic constants are determined through the real c'_{ijkl} and imaginary c''_{ijkl} components of the complex elasticity tensor:

$$c'_{эфф} = c'_{ijkl} \kappa_j \kappa_l \eta_i \eta_k \qquad (2)$$

$$c''_{эфф} = c''_{ijkl} \kappa_j \kappa_l \eta_i \eta_k \qquad (3)$$

where κ_j and η_I are the components of the unit wave normal vector κ and the polarization vector η. Calculations using the Christoffel equations showed that in this plane the maximum deviation of the polarization vector from the wave vector is 11.5 angular degrees. The anisotropy of the attenuation

coefficient of acoustic waves with a frequency of 1 GHz propagating in the crystallographic plane (110), calculated on the basis of experimental data and expressions (1), (2) and (3) is shown in Figure 1.
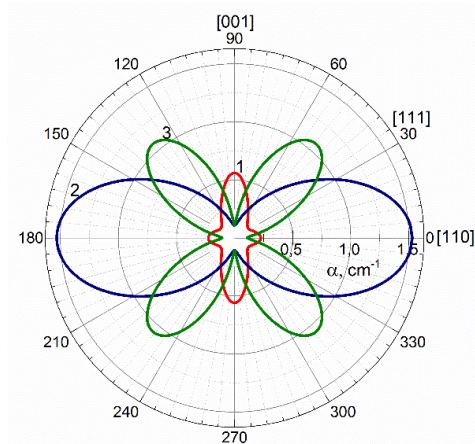
Figure 1. Section of the attenuation surfaces of quasi-longitudinal (1), quasi-transverse (2) and pure transverse (3) acoustic waves in MgO crystals by the (110) plane.

According to [2, 3], the expression for the attenuation of acoustic waves according to the Akhiezer mechanism can be written in the following form:

$$\alpha = \gamma_{эфф}^2 \frac{\lambda T \omega^2}{2\rho V^2 V_D^2} \tag{4}$$

where T is the temperature, λ is the thermal conductivity coefficient, γ is the effective Grüneisen constant, V_D is the average Debye velocity [3].

Using the experimental results on acoustic attenuation and expression (4), the effective Grüneisen constants for longitudinal and transverse waves along various directions were determined, which are also given in Table 1. The values of the effective Grüneisen constants were determined through the relation:

$$\gamma_{эфф} = \left(\frac{c''_{эфф} \cdot V_D^2}{2 \cdot \lambda \cdot T \cdot \omega} \right)^{1/2} \tag{5}$$

The table shows that the spatial dispersion of the Grüneisen constants leads to a strong anisotropy of the attenuation of both longitudinal and transverse acoustic waves. The results also showed that the strongest anisotropy of the attenuation coefficient is observed for transverse acoustic waves, for which this value changes by an order of magnitude with a change in the direction of propagation. The proposed approach to determining the effective Grüneisen constants can be used to study the nonlinear elastic and thermal properties of other cubic crystals.

References

F.R. Akhmedzhanov, V.V. Lemanov, A. Nasyrov. Acoustic attenuation surfaces in crystals, Letters Journal Technical Physics (SU), Vol. 6, No 6, pp. 589-592 (1980).
1. R. Truell, Ch. Elbaum, B. Chik. Ultrasonic methods in solid state physics. Academic Press, New York and London. (1969).
2. F.R. Akhmedzhanov, J.O. Kurbanov, A.F. Boltabaev. Attenuation of Acoustic Waves in Single-domain and Polydomain LiTaO$_3$ Crystals. Sensors & Transducers. V. **246**. No 7, pp. 43-47 (2020).

STUDY TRAJECTORY SCATTERED IONS FROM SiO$_2$ NANOSTRUCTURES

U.O.Kutliev[1], *A.S.Ashirov*[1], *G.X.Allayarova*[2]

[1]Urgench State University,Urgench, Uzbekistan
[2]Karshi State University, Karshi,Uzbekistan
e-mail: uchkunk@mail.ru

Among different surface methods, the low-energy ion-scattering (LEIS) technique (or ion-scattering spectroscopy, ISS) has been used extensively over the past few decades for analyzing the composition and structure of solid surfaces. In a typical LEIS experiment, a surface is bombarded by noble-gas ions (He$^+$, Ne$^+$, Ar$^+$, Kr$^+$, Xe$^+$) having a primary energy in the range of 1-10 keV. The elemental composition of the surface can be identified by the presence of single-scattering peaks in the energy spectra (the LEIS spectra), while the angular distributions of the scattered ions contain certain information about the surface structures. However, for explaining energy and angular spectrums we have to know the trajectory scattered ions. Therefore in this work we present the LEIS investigations (trajectory scattered ions) from the surface atomic row of SiO$_2$<110> material. Silicon dioxide used as a filler in rubber products, paints, animal feeds, pesticides, insulation materials, and cosmetics. Polycrystalline silicon and silicon dioxide materials are etched in semiconductor manufacturing. In this work was used a method which named binary collision approximation. The binary collision approximation (BCA) has long been used in computer simulations of the interactions of energetic atoms with solid targets, as well as being the basis of most analytical theory in this area. While mainly a high-energy approximation, the BCA retains qualitative significance at low energies. Moreover, computer simulations based on the BCA can achieve good statistics in many situations where those based on full classical dynamical models require the most advanced computer hardware or are even impracticable. On the Figure 1 presents the trajectories scattered ions Ne$^+$(a), Ar$^+$(b) and Xe$^+$(c) from surface atomic row(oxygen atoms) of the SiO$_2$<110> at the angle of incidence $\psi=11^0$ by initial energy 5 keV. We can observe only 2 trajectories on the surface atomic row at bombardment by Ne ions. In the case Ar bombardment, we observe 21 trajectories, but they very close to surface. At the Xe ions bombardment, we also observed 21 trajectory scattered ion from the surface atomic row. But angle of scattering large than in the case Ar ions. So, we can see that by increasing atomic mass bombardment ions we can observe many trajectories scattering ions by the surface atomic row. This method makes it possible to study surface nanostructures by the LEIS.

a   b   c
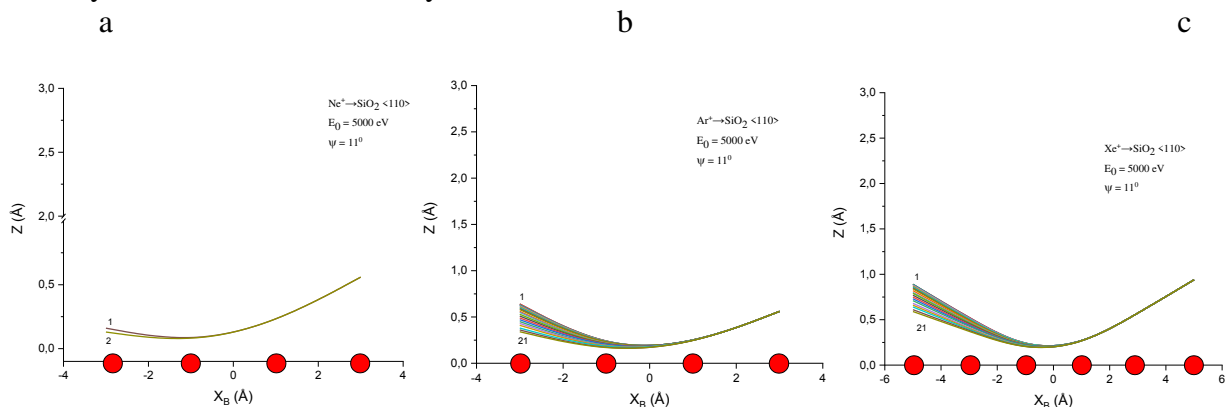
Figure.1. The trajectories scattered ions Ne$^+$(a), Ar$^+$(b) and Xe$^+$(c) from surface atomic row of the SiO$_2$<110> at the angle of incidence $\psi=11^0$ by initial energy 5 keV.

METAL OXIDES AQUEOUS NANOFLUIDS SEDIMENTATION STABILITY

U.A. Yokubov, K.B. Egamberdiev, S.Z. Mirzaev, A.A. Avvalboev, O.V. Trunilina, B.A. Allaev

Academy of Sciences of Uzbekistan, Institute of Ion-Plazma & Lazer Technologies Named after U.A.Arifov, Durmon Yuli str. 33, Tashkent 100125, Uzbekistan
kegamberdiev@yandex.ru

Aqueous nanofluids of metal oxides (TiO_2, SiO_2, Al_2O_3) are widely used in modern nanotechnology: in pharmaceuticals, medicine, food, chemical and manufacturing industries, and the building industry [1,2]. An effective balance of various types of interactions in water, as a polar carrier medium modified with nanoadditives, ensures the appearance of regular nanostructures, and it possible to carry out a controlled process of creating materials with predetermined properties. Low-dimensional molecular aggregates-clusters formation, with they definite structure and stability, is provided by interactions with an energy of 10-30 kJ/mol of hydrogen bonds of water molecules, which are the main structure-forming in aqua [3].

The addition of metal oxide nanoparticles of varying degrees of dispersion changes the structural properties of water as a carrier medium, increasing the stability of clusters. At the same time, the stability of the formed hydrosol is limited by the deposition of nanoparticles and requires additional modification for a significant increase. Such a modifier is usually anionic surfactants, which are amphiphilic molecules consisting of a hydrophobic hydrocarbon chain and a hydrophilic polar group with a pronounced ability to dissolve in polar solvents. The main acting forces in this case are Van der Waals forces, electrostatic forces and hydrophobic interaction forces [4]. The dynamics of the interphase boundary is determined by the overall balance of these forces. The nature of hydrophobic forces, like the van der Waals interaction, extends over distances of several atomic diameters, has an entropic character and is explained by a network structure deformation with hydrogen bonds characteristic. Efficiency of increasing metal oxide nanoparticles hydrosol stability depends not only on their dispersion, but also on the concentration of both nanoparticles and surfactant and can be optimized for each of their types especially.

The particle sedimentation process strongly depends on aqua nanofluid parameters such as particle density, volume, viscosity of the liquid and density of the medium. For spherical particles that do not interact with each other, the sedimentation rate can be expressed according to Stokes' law:

$$\vartheta = \frac{2(\rho - \rho_{\text{ж}})r^2 g}{9\mu}$$

where ϑ - is the particle sedimentation rate; ρ - is the density of the particle; $\rho_{\text{ж}}$ - is the density of the liquid; r - is the radius of the particle; g - is the gravity acceleration; μ - is the dynamic viscosity of the liquid.

Nanoparticles obtained by the method [5] were used as research samples and the control of the size distribution was carried out by the NTA (nanoparticle tracking analysis) using NanoSight LM10 device from Malvern Panalytical with wavelength 405 nm (fig.1). SiO_2 nanoparticles dimension characteristics in silica sample consists of polydisperse size in 50-450 nm range with maximal concentration in 125 nm, as shown in table 1.

Table 1. SiO₂ nanoparticles dimension characteristics in silica sample

Size, нм	55	85	125	210	260	375
Concentration, %	3	9	53	14	13	9

Using anionic surfactant, as dodecylbensolsulfonate Na ($C_{12}H_{25}C_6H_4SO_3Na$), it was possible to increase nanofluid stability with surfactant concentration in the range of values, there is less than the micellization critical concentration (MCC) from 0,2 up to the 1,2 mmol/l.

The stabilizing effect of $C_{12}H_{25}C_6H_4SO_3Na$ at concentrations below MCC is due to the

adsorption of individual surfactant molecules on the surface of metal oxides nanoparticles. The adsorbed molecules increase the charge of the surface and hydrophilize it due to are high hydrophilicity of sulfate groups, what makes it possible to obtain a stable nanofluid. If the surfactant concentration increase to MCC value and above, there is no stabilization effect for such nanoparticles as TiO_2 and SiO_2, since micelles have a negative surface charge, as do this nanoparticles. As a result the dispersed phase precipitates, and at high concentrations of surfactants nanofluid turns into a gel.
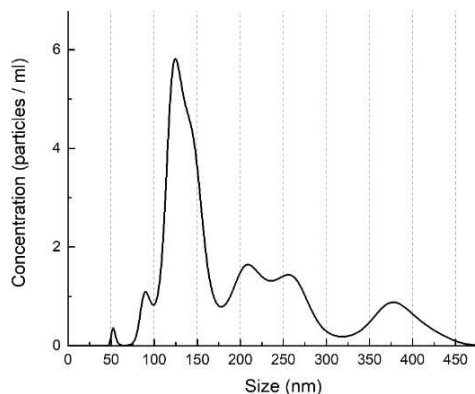
Figure 1. Polydisperse SiO$_2$ nanoparticles range in silica sample

Since water, as a carrier medium, has a high dielectric constant, the ability to exhibit both proton-donor and proton-acceptor properties, hydrate shells are formed around dissolved particles: ions, molecules, and aggregates of various nature according to the hydrophobic hydration model. The dense layer of the hydrate shell consists of hydrogen-bonded water clusters with a structure depending on the nature of the hydrated particle. The loose layer provides a continuous transition from dense layers of hydrate shell around the particle to "free" water. The ratio of the thickness of dense and loose layers, as well as the average lifetime of water molecules in a hydrate shell, depends on the nature of the nanoparticle, the concentration of solutes and temperature. The addition of surfactants makes it possible to change the lyotropic properties and thereby prevent the aggregation (coagulation) of nanoparticles, which can lead either to sedimentation of large aggregates or to the formation of dimensional structures, which culminates in the formation of a gel. Sedimentation occurs when there is a predominance of the direction of motion of particles under the influence of gravity over Brownian motion. Obviously, the anionic surfactant most effective for the stabilize TiO_2 and SiO_2 aqueous nanofluids.

References

1. Kasturee Hajra, Dipak Maity, Sumit Saha «Recent Advancements of Metal Oxide Nanoparticles and their Potential Applications: A Review» *Adv. Mater. Lett.* Issue (January - March) (2024), 24011740 DOI: 10.5185/amlett.2024.011740
2. Yokubov, U., Egamberdiev, K., Allaev, B., Trunilina, O., Telyaev,S., Gafurova, M. «Silica nanoparticles hydrosol for concrete strength increase by adding to mixing water» *Journal of Chemical Technology and Metallurgy*, (2023), 58(5), p. 932–936
3. R.Ludwig, The effect of hydrogen bonding on the thermodynamic and spectroscopic properties of molecular clusters and liquids, *Phys. Chem. Chem. Phys.* **4** ,(2002), 5481-5487
4. Ph. Wernet, D. Nordlund, U. Bergmann, M. Cavalleri, M. Odelius, H. Ogasawara, L. A. Näslund, T. K. Hirsch, L. Ojamäe, P. Glatzel, L. G. M. Pettersson and A. Nilsson, The structure of the first coordination shell in liquid water, *Sciencexpress* 1 April 2004; *Science* 304, (2004), p.995-999.
5. M.Sh. Kurbanov, L.S. Andriyko, J.A. Panjiev, S.A. Tulaganov, V.M. Gun'ko, A.I. Marynin, S. Pikus. Resource-Saving Synthesis of Nanoscaled Silicon Dioxide and Its Textural Characteristics. *Journal of Nanoparticle Research*. 25, 202 (2023), doi.org/10.1007/s11051-023-05852-w.

DFT INVESTIGATION OF REGULATION FILM CRYSTALLIZATION KINETICS WITH THIOUREA ADDITIVE IN PEROVSKITE SOLAR CELLS

I.N. Nurgaliev, M.B. Marasulov, N.R. Ashurov

Institute of polymer chemistry and physics, Academy of sciences of the Republic of Uzbekistan; 7b, A. Kadyri str., 100128, Tashkent, Uzbekistan, tel.: +998-71-241-85-94
e-mail: ilnarvodnik@gmail.com

Perovskite solar cells (PSCs) have recently become one of the most intensively investigated optoelectronic materials due to their merits. A Lewis acid−base adduct approach for high efficiency perovskite solar cell fabrication. Regarding solution-processed perovskite formation, selection of solvents (N,N-dimethyl sulfoxide (DMSO), N,N-dimethylformamide (DMF), and γ-butylolactan(GBL)) to dissolve PbX_2 (X = I, Br, Cl) and organic iodide is important. Most solvents are found to be polar aprotic, which indicates that those solvents can act as Lewis bases. The adduct approach has been found to be adopted generally, where methylammonium or formamidinium lead iodide perovskite with large grain, high crystallinity, and long-lived carrier lifetime is successfully fabricated via an adduct of PbI_2 with thiourea (TU) as sulfur-donor Lewis base. A smooth and large grained perovskite crystal is obtained without the intermediate phase PbI_2–$S=C(NH_2)_2$ using the ideal thiourea amount. Thiourea, through forming MAI-PbI_2-DMSO-thiourea in perovskite precursor solution, significantly impacts the perovskite crystallinity and morphology, as proved using X-ray diffraction patterns and infrared spectroscopy.

In this work, we theoretically investigate the interaction energy between PbI_2 with three solvents to explain an effective method to regulate the crystallization kinetics of perovskite film and is helpful for further development of PSCs. We have carried out quantum theoretical calculations and optimized the model of interaction of PbI_2 with solvents at the B3LYP level (DFT) using DMol3 module of the BIOVIA Materials Studio 2017 program package and calculated its properties, were presented in table.

Table. Interaction characteristics of investigated models

System	Inter. energy, kcal/mol	Band gap, eV	Distance between atoms, Å
PbI_2-DMSO	-0,8144	5,65	-Pb-O= 10.74
PbI_2-DMF	-0,9856	6,01	-Pb-O= 9.22
PbI_2-TU	-13,7276	5,057	-Pb-S= 2.86
PbI_2 DMF DMSO TU	-23,04	5,52	-Pb-DMSO 12.99 -Pb-DMF 15.08 -Pb-TU 6.77

According to the chemical structure of thiourea, its S-donor terminal would interact with Pb terminal of PbI_2 in the perovskite precursor solution, forming intermediate phase of PbI_2·thiourea like DMSO, and such intermediate phase could retard the crystallization process during annealing process contributing to larger grain size. On the other hand, S-donor terminal of thiourea also compensate for the bared Pb defect sites among grain boundaries. These conclusions are consistent with the calculated interaction energies. A possible theoretical mechanism has been presented concerning the perovskite grain growth as thiourea is added.

THE IMPACT OF ELECTRICAL CONDUCTIVITY ON HFO MEMRISTOR PERFORMANCE

A.Khasanov, A.Abdikarimov, E.Khaitbaev, D.Rajapov

Urgench state univesity.
14, KH.Alimdjan str, Urgench city, 220100, Uzbekistan
asrorbekhasanov373@gmail.com

Abstract: In this paper, a two-dimensional HfO memristor is used as a conductive device, and the effect of dielectric conductivity on its I-V graph is studied by modeling. Pt materials were used as the contacts of the memristor, HfO for the dielectric layer, and HfO_{1-x} elements for the conductive filament[1].

Keywords: 2D HfO, I-V curve, memristor conduction filament, ambient temperature, bottom electrode, simulation, conductivity.

1. Introduction: Metal oxide-based RRAM devices are essential devices for future technology. Using it as a permanent memory and logic element in computers, artificial intelligence, and similar future technologies will greatly help to overcome various difficulties and simplify electrical circuits. Many researchers have studied the characteristics of the metal oxide layer of the memristor device using various methods, but the switching mechanism is still unclear[2-3]. This work is aimed at simple modeling of the memristor device using COMSOL Multiphysics 6.2 and studying its IV plot.

2. The structure of the memristor: We used HfO material as a dielectric layer in this memristor. Also, the HfO_{1-x} material is included as an adjacent layer to the dielectric layer to form a current transfer mechanism. In addition, Hf material is added to the top of the dielectric layer to increase the efficiency of the memristor.
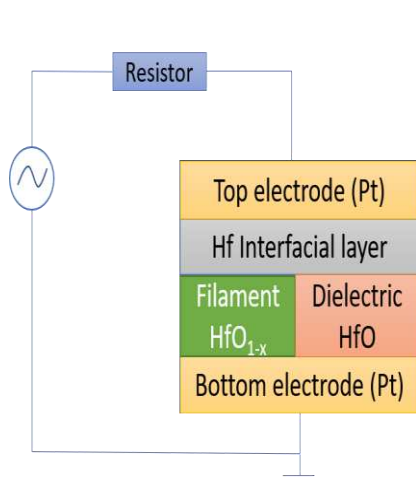
Figure 1. Device schematic circuit

Name	Expression	Value	Description
r_f	3[nm]	3E−9 m	filament radius
r_d	10[nm]	1E−8 m	device radius
h_di	5[nm]	5E−9 m	height of the dielectric
h_te	30[nm]	3E−8 m	top-electrode height
h_be	65[nm]	6.5E−8 m	bottom-electrode height
h_Hf	10[nm]	1E−8 m	height Hf

Table 1. Geometric parameters of the device

3. Process modeling in COMSOL Multiphysics: First, to model the memristor, its geometric dimensions are entered into the COMSOL program. All the parameters we used are in Table 1. The next step is to enter the necessary material parameters for each area. To study the processes we need, Electric Current, Heat transfer, and Electric circuit physics are selected and the necessary settings are made. In addition, the electromagnetic heating submodule is added to take into account the electromagnetic heat occurring in the environment. All these modules calculate the temperature (T) and electric field (E) distribution of the device during execution.
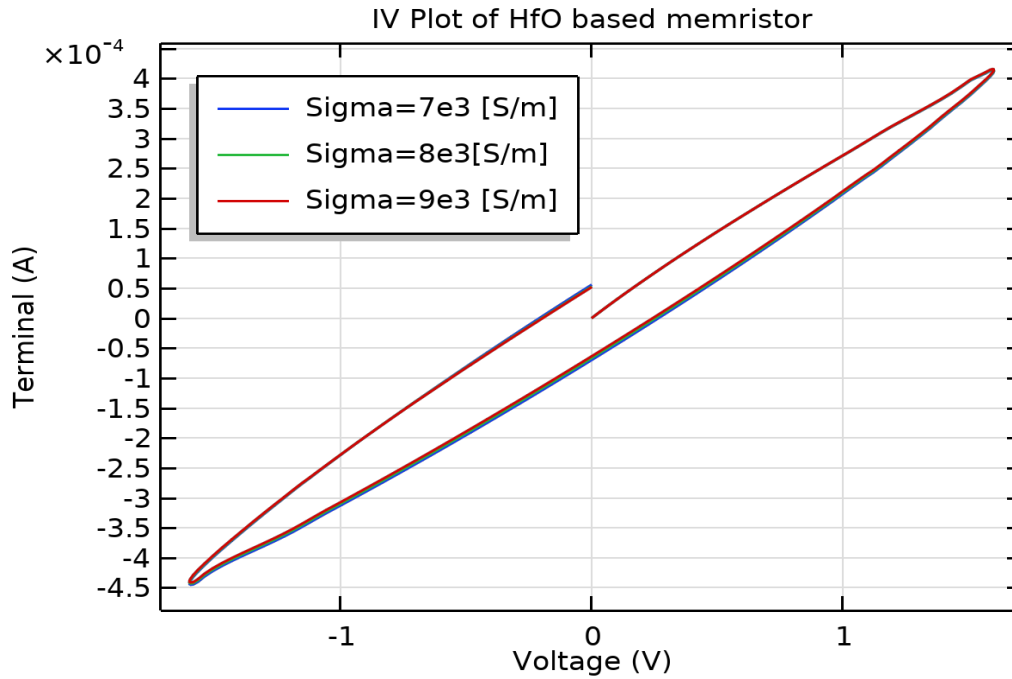
Fig. 2. Effect of electrical conductivity on the I-V curve

4. Simulation results: Memristor operation consists of 2 different state SET and RESET processes. During the SET process, a positive voltage is supplied to the memristor through the circuit, in which the memristor switches from a high resistance state to a low resistance state, that is, CF is formed. During the RESET process, it goes from a low resistance state to a high resistance state. In this process, we considered different values of the conductivity of the dielectric. To study the IV curve, the circuit in Fig. 1 is constructed. Here, the resistance of the resistor is taken as 1000 ohms. The main idea of the simulation was to change the electrical conductivity of the conductive filament material, and we considered the effect of its 3 different values on the IV plot (Fig. 2).

5. Conclusions: The results of 2D modeling show that the change in the electrical conductivity of the conductive filament material in the HfO-based memristor has a significant effect on its IV plot, and it is appropriate to choose materials with a higher electrical conductivity of the conductive filament in the modeling.

References:

1. Zhang, Z.; Wang, F.; Hu, K.; She, Y.; Song, S.; Song, Z.; Zhang, K. Improvement of Resistive Switching Performance in Sulfur Doped HfOx-Based RRAM. Materials 2021, 14, 3330.
2. Jin, S.; Kwon, J.-D.; Kim, Y. Statistical Analysis of Uniform Switching Characteristics of Ta2O5 -Based Memristors by Embedding In-Situ Grown 2D-MoS2 Buffer Layers. Materials 2021, 14, 6275. [CrossRef] [PubMed
3. Usman, I.; Illian, M.; Mohd, H.; Furkan, Z.; Abdullah, S.; Saeed, S.; and Mohd, A. Statistical Simulation of the Switching Mechanism in ZnO-Based RRAM Devices. Materials 2022,15,1205.

MAGNETIC PROPERTIES OF SILICON DOPED WITH IMPURITY ATOMS OF EUROPIUM

G.H. Mavlonov, S.B. Isamov, Y.A. Abduganiev

Tashkent State Technical University, 100095 Tashkent, Uzbekistan
yoldoshaliabduganiyev2@gmail.com

Based on the results of research conducted by scientists and specialists on the formation of compounds of elements belonging to the lanthanides group in single crystalline silicon, the authors have revealed the possibilities of obtaining novel materials that can be used to create modern sensors and magnetic electronic devices [1-4]. The interest in this field is partially motivated not only by the chance to design the technology for obtaining new materials, but also to study their basic physical properties that still remains an urgent issue in the physics of semiconductors. Based on the scientific analysis of the literature, the observation of ferromagnetic state in silicon with dopants of lanthanide series of chemical elements is explained by the parallel arrangement of magnetic moments of dopant atoms in the crystal bulk. Since metals have a high concentration of electrons, it is relatively easy to control their spins. Semiconductor materials, particularly silicon, are diamagnetic materials. It was shown in work [5] that it is possible to change the magnetic properties of initial silicon by introducing the elements belonging to the lanthanides group with high spin ordering to silicon. The obtained results make it possible to apply the semiconductor silicon material in the creation of magnetic sensors for spintronic, for example, in the production of spin transistors There is an increasing interest in controlling its magnetic properties by introducing *4f* group elements into silicon. The spin of $4f^7$ electrons in the outer electron shells of Eu atoms is equal to *S=7/2*. It is of scientific and practical importance to study the magnetic properties of silicon by introducing Eu and dopant atoms. The dopant atoms of 99.999% (product of Hebei Suoyi New Material Technology Co., Ltd.) chemically pure europium (Eu) metallic element selected as dopant atoms were diffused from the gaseous state into the initial n-type silicon. In this case, the relative resistance of the initial silicon ρ= 6; 40; 60 and 80 Ω·cm were selected and prepared with geometric dimensions of $8\times4\times1mm^3$. In an MG17-60/300 electric tube furnace, at a temperature of T=1200˚÷1350˚C and in the interval of t=6÷15 hours, the deposed atoms were diffused into the silicon from the gaseous state. After diffusion, the silicon samples were cooled by steady stepped cooling procedure. Due to the tiny diffusion coefficient of europium atoms, the penetration depth of lead atoms into silicon was small. In this case, it was found that the interstitial atoms are located in the lattice node instead of the reference silicon atoms in the crystal lattice of silicon single crystal [6,7].

Analysis of the research results showed that in samples of silicon diffusion doped with impurity europium atoms at certain temperatures a transition and ferromagnetic state are observed, which are absent in the original silicon. Studies of the magnetic properties of the original silicon and silicon samples doped with impurity europium atoms have shown that magnetic domains are formed in silicon samples doped with europium atoms (Fig. 1)
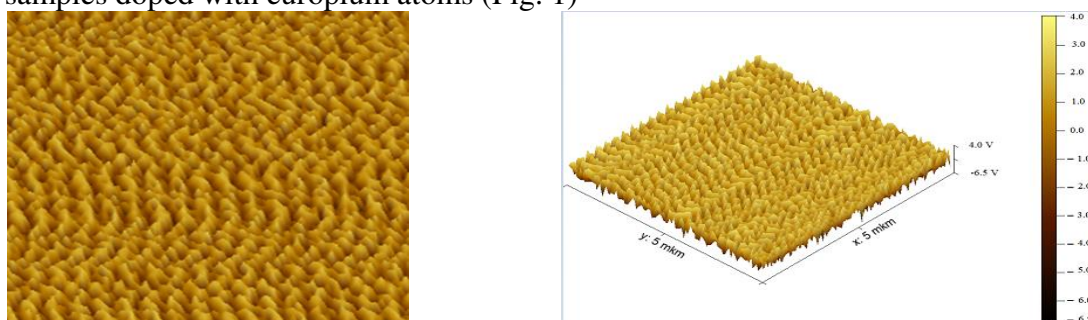
Fig.2. Results of studying magnetic properties on a magnetic-atomic force microscope brand FM-Nanoview1000. when exposed to a magnetic field $B = 250$ mTesla

The results of the study showed that the concentration of impurity europium atoms strongly affects the magnetic properties of the original silicon. As the concentrations of europium impurity atoms increase, the density of the formed magnetic domains increases. This, in turn, leads to an increase in the magnetic sensitivity of the obtained samples. A study of the magnetic properties of silicon doped with europium impurities showed that in the resulting europium samples, europium atoms form magnetic nanoclusters, which lead to the formation of magnetic domains of size. The results of a study of the magnetic properties of silicon doped with impurity atoms make it possible to use them in magnetoelectronics to create magnetically sensitive sensors and magneto-spin transistors.

REFERENCES

1.M.A. Ruderman, C. Kittel. Indirect ex-change coupling of nuclear magnetic mo-ments by conduction electrons//Phys. Rev. 96 pp. 99–102. (1954).
2.Le Breton, J.-C., Sharma, S., Saito, H., Yuasa, S. & Jansen, R. Thermal spin cur-rent from a ferromagnet to silicon by See-beck spin tunneling. Nature 475, 82–85 (2011).
3. G Panayiotakis, D Cavouras, I Kanda-rakis, C Nomicos. Appl Phys. 62: 483. (1996).
4.Arne Brataas, Bart van Wees, Olivier Klein, Grégoire de Loubens, Michel Vi-ret//Spin insulatronics. 885 1-27. (2020).
5.F. Formisanoa, R. Medapallib, Y. Xiaob, H. Renb, E.E. Fullertonb, A.V. Kimela. Jour-nal of Magnetism and Magnetic Materials 502 166429. (2020).
6.M.K. Bahadirkhanov, S.B. Isamov, N.F. Zikrillaev, H.M.Iliev, G.H. Mavlonov, S.V. Koveshnikov, Sh.N.Ibodullaev, Electron. Mater. Proc. 56 No 2, 14 (2020).
7.G. Güntherodt, Phys. Condens. Matter.18 37–78, (1974).

PHOTO RECEIVER ON $Zn_xCd_{1-x}S$ -TYPE SOLID SOLUTION SENSITIVE IN THE UV RANGE (250-550 NM)

Sh.A.Utamuradova, _Kh.S. Daliev, Sh. Kh. Daliev, S.A. Muzafarova, A.S. Achilov, A.Sh. Mavlyanov_

The Institute of Semiconductor Physics and Microelectronics at the National University of Uzbekistan, Yangi Almazar st.20, Tashkent, 100057, Uzbekistan,

e-mail: sh-utamuradova@yandex.ru

Selective photo receivers with maximum sensitivity in various spectral diapasons are applied in various optical electronic devices implemented for environment contamination recording. To monitor water and soil contamination by Bio-Hemi luminescence method, selective photo receivers with maximum spectral sensitivity at 490-500 nm are mostly applied.

Physical and technological basis was developed that would ensure designing of photo receivers (PR) sensitive in the ultra-violet spectrum region based on ZnS-CdS-type compound solid solution. Basing on X-ray structural and phase analysis we have determined that Zn_xCd_{1-x} S-type solid solutions films consist of orientated column-shaped crystallites with dimensions 20-30 A^0 and intercrystalline distance 40-60 A^0. Crystallites are widespread all across the films' thickness [1]. The above UV photo receivers represent a Schottky barrier formed by vacuum deposition of metal (Au) on the solid solution film surface in the temperature range of $500\text{-}100^0$ C.

The UV photo receiver's spectrum range as a function of material composition was investigated within 250—310 nm wavelength. Spectral sensitivity maximum $S_{\lambda\,max}$ is definitely related to Zn in solid solution and varies correspondingly in the 280—480 nm wavelength range. It was revealed that the value of $S_{\lambda\,max}$ and the boundary value of short and long wave spectrum of photo sensitivity characteristics correlate proportionally with the concentration of Zn in the solid solution content and shifts towards smaller wavelengths of solar radiation.

Structure	Zn content in Zn_xCd_{1-x} S	Photo sensibility region	Photo sensibility maximum $S_{\lambda\,max,}$, μ
Au- Zn_xCd_{1-x} S	0,2	0,46+0,5	0,486
	0,3	0,45+0,59	0,47
	0,35	0,43+0,42	0,46
	0,4	0,41+0,45	0,2

One of the significant parameters of these photo receivers is the fact of extension of photo sensitivity toward shorter ranges of wavelengths once a certain voltage is applied in photodiode mode. It has been shown that photo sensitivity spectrum varies linearly on applied voltage, and the integral change is approximately 100-150 nm virtually independently on $Zn_xCd_{1-x}S$-type solid solution's composition.

According to experimental results, the photocurrent (J_p) and integral sensitivity (S_{int}) also strongly depend on V. For example, S_{int} = 3 mA/lm at V=0 V, and in photodiode mode at V = 5 V, S_{int} = 75 mA/lm. For comparison we have taken a multiple of industrial photo receivers PD-7k and PD-11k have, S_{int} = (4-5) mA/lm that are well known for their performance. Photocurrent amplification in PR photodiode mode depends on minority carrier injection from intragrain layers into the volume charge layer of the photosensitive structure. It's shown that the $Zn_{0.7}Cd_{0.3}S$ solid solution is most suited for photo receiver's design in the spectral range λ = 250-400 nm. Current sensitivity at maximum (λ=340-380 nm) is $S_{\lambda\,max}$ =(0.2-0.3) A/W and voltage sensitivity is $S_{\lambda\,max}$ =300 V/W at ambient temperature 100-120°C. The response rate of these RP is =10^{-4} – 10^{-5} seconds, and the angular sensitivity margin is approximately ~120^0. The scanning step of the existing industrial

photo receivers is $15\text{-}20^0$. This parameter of the PR is of great importance when it comes to developing electronic devices for flame control in large industrial gas furnaces.

The major advantage of the developed photo receiver is the ability to scan the photo of EMF, inversion points in the photo diode mode by means of applying voltage.

Further on, to determine accurately the location of light irradiation source, additional complex and extraction mode was applied by using an additional monochromatic irradiation source directed at an angle of the incident light flow. As a result, the background irradiation effect was completely eliminated in the range up to $\lambda = 395$ nm in the UV region and at $\lambda = 470 - 1000$ nm in a long wavelength spectrum. Here the irradiation source tracking accuracy is ~1 nm.

REFERENCES

1. Sh.A.Mirsagatov, B.U.Aitboev, M.A.Makhmudov. "Functional abilities of photo receivers controlled by photo sensitivity spectrum" – UFJ, 2000, No. 5, p.33-37
2. Sh.A.Utamuradova ,Turgunov N.A., Muzafarova S.A., Faizullaev K.M., Norkulov Sh.B. Selective photosensitive photodetectors based on the Schottky barrier The Way of Science. International scientific journal. 2022. No. 10 (104), pp. 13-15.
3. Sh.A.Mirsagatov, P.I.Knigin, M.A.Makhmudov. "Photoconverter based on CdTe-CdO structure" – Geliotechnika, 1991, No1, p.3-7.
4. Sh.A.Mirsagatov, H.Rasykov. "UV photo receivers based on solid solution $Zn_xCd_{1-x}S$" – Gelitechnika, 1993. No2, p.17-23.
5. Sh.A.Utamuradova ,A.S. Achilov, Sh.Kh. Daliev, S.A. Muzafarova Inversion photodetectors for flame monitoring using the radiation spectrum International conference "Fundamental and applied problems of modern physics" Tashkent, Physicotechnical Institute, October 19-21, 2023. pp. 70-77.

X-RAY ANALYSIS OF CARBON NANOTUBES GROWN USING NICKEL OXIDE

I.J. Abdisaidov, S.G. Gulomjanova, Kh.B. Ashurov

Institute of Ion-Plasma and Laser Technologies of Uzbekistan Academy of Sciences, 100125, Durmon yuli st. 33, Tashkent, Uzbekistan.
*e-mail: abdisaidov@iplt.uz

Abstract: The chemical vapor deposition CVD method involves the catalytic decomposition of carbon raw materials using a transition metal catalyst. The X-ray diffractometry device accurately characterizes the properties of carbon nanotubes, including crystal structure, purity, and morphology. To delineate these properties, we conducted an X-ray diffraction analysis of carbon nanotubes synthesized using the CVD method.
Keywords: Nickel oxide, carbon nanotubes, X-ray diffraction, chemical vapor deposition, catalyst, intensity.

Currently, many developing areas of nanotechnology are related to carbon nanotubes (CNTs). CNTs have a very high coefficient of strength, very high thermal and electrical conductivity, fire resistance, and are the best among known materials in terms of mass. CNTs can be synthesized by various methods, such as arc discharge, laser ablation, CVD, etc. CVD is the cheapest, easily controlled, and most widely used method [1].

CVD has many advantages over arc discharge and laser ablation methods in terms of purity, yield, crystallinity, structure control, etc. In the CVD process, the carbon feedstock nucleates and grows from the catalyst nanoparticles.

CNTs were synthesized using the CVD method. This process is described in detail in the literature [2]. Nickel oxide was used as a catalyst in this research. X-ray diffraction (XRD) was conducted to characterize the crystal structure, purity, phase morphology, and other properties of the synthesized CNTs. The XRD graph of CNTs is shown in Fig. 1.
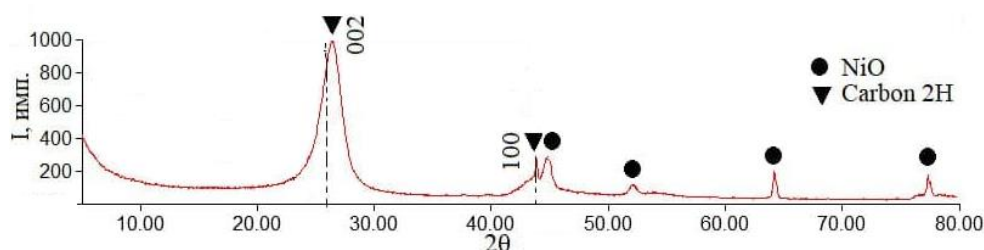
Fig. 1: XRD diffractogram of CNTs synthesized by the CVD method

X-ray diffraction of CNTs synthesized by the CVD method was performed using a Shimadzu XRD-6100 X-ray diffractometer with a Cu-Kα radiation source at a wavelength (λ) of 1.541874 Å, diffraction angle (2θ) ranging from 10° to 80°, with an angular speed of 5°/min. When X-rays are exposed to one wall of the CNTs, certain parallel (hkl) reflected peaks are formed. Fig.1 shows two characteristic peaks of CNTs at 2θ = 25.9° and 43.3°. Among them, the (002) peak observed at 2θ = 25.9° is significant, indicating the crystalline and cylindrical structure of the synthesized CNTs.

All physico-chemical properties of CNTs synthesized by CVD method using nickel oxide, such as lattice structure, purity, light characteristics, crystallinity, etc., can be determined using the intensity and positions of XRD diffraction peaks.

References:

1. Tehrani, M., & Khanbolouki, P. (2018). Carbon nanotubes: synthesis, characterization, and applications. In Advances in Nanomaterials pp. 3-35.
2. Abdisaidov I.J., Gulomjanova S.G., Gaipov B.A., Zaripov A. A., Berdiev U.F., & Ashurov Kh. B., (2022). Virashivanie uglerodnoy nanotrubki metodom ximicheskogo osajdeniya iz parovoy fazi s ispolzovaniyem nikelovogo katalizatora, "Uzbek journal of physics", 24(3), pp. 214-216.

LAYER BY LAYER DEPOSITION OF CONDUCTIVE 2D NANOSTRUCTURES ON TEXTILE SURFACES AS A TOOL TO DESIGN AND MANUFACTURE COMMERCIAL PIEZORESISTIVE MATERIALS

Jamshid Avloni[1], Daminov Rakhimjon[1], Kamil Mukimov[1], [2]Bahodir Abdulahkatov

[1]*Nanotechnology Development Center at the The National University of the Republic of Uzbekistan, Ministry of Higher Education, Science and Innovations of the Republic of Uzbekistan*
[2]*Military Medical Academy of the armed forces of the Republic of Uzbekistan*

Abstract
Wearable electronics incorporating physical, chemical, and biological sensors and actuators have rapidly become an inseparable part of our lives for their use in a wide range of applications, especially for personalized health monitoring, wellness tracking, and early-warning for COVID19 and other infectious viruses. [1–3] Among them, flexible, stretchable, and miniaturized wearable sensors that measure motion, physiological, electrophysiological, and electrochemical signals emanating from the human body present great potential for personalized healthcare applications. [4–5]
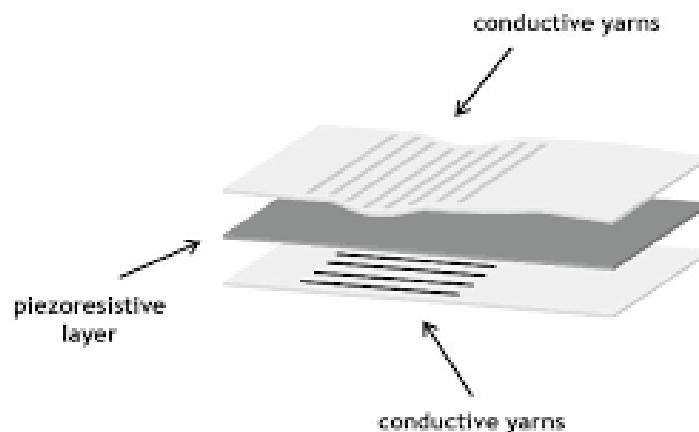
Figure 1. Diagram showing the structure of the pressure mapping sensor
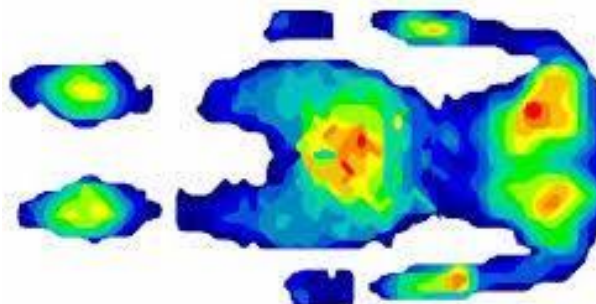
Figure 2. Image from pressure mapping bed sensor

Layer-by-layer (LbL) deposition is a thin film fabrication technique. The films are formed by depositing alternating layers of oppositely charged materials with wash steps in between. This can be accomplished by using various techniques such as immersion, spin, spray, electromagnetism, or fluidics.

The piezoresistive effect describes the change in electrical resistance that occurs when an external force is applied to a semiconductor.

Deposition of alternating layers of oppositely charged conductive carbonaceous nanoparticles and polyelectrolytes on textile surfaces leads to formation of piezoresistive materials with good load sensitivity and fast response times. Easy control over the target electrical resistivity and acceptable uniformity of the electrical resistance of the fabric are the most important parameters for pressure mapping applications. These piezoresistive materials are used in commercial pressure mapping sensors in industrial and biomedical applications, sports, robotics and musical instruments. [6]

The architecture and the number of conductive bilayers allows to control electrical resistance and sensitivity of piezoresitive fabric.

Smart beds built using pressure mapping allow to prevent the bed sores. Pressure mapping shoe insoles are used in sports and hospitals.

Layer-by-layer deposition method also allows to apply antistatic, antibacterial and water repelling treatments onto various textiles.

References:

[1] L. Manjakkal, L. Yin, A. Nathan, J. Wang, R. Dahiya, Adv. Mater. 2021, 33, 2100899.
[2] M. Lin, Z. Zheng, L. Yang, M. Luo, L. Fu, B. Lin, C. Xu, Adv. Mater. 2022, 34, 2107309.
[3] B. Peng, F. Zhao, J. Ping, Y. Ying, Small 2020, 16, 2002681.
[4] R. He, H. Liu, Y. Niu, H. Zhang, G. M. Genin, F. Xu, npj Flexible Electron. 2022, 6, 20.
[5] Y. Lee, J. Kim, H. Joo, M. S. Raj, R. Ghaffari, D.-H. Kim, Adv. Mater. Technol. 2017, 2, 1700053.
[6] Electroconductive woven and non-woven fabric, Jamshid Avloni, US Patent 7468332, 2008.

EPITAXIALLY GROWN CALCIUM FLUORIDE
AS INSULATING MATERIAL IN TWO-DIMENSIONAL SOLID-STATE DEVICES

Banshchikov A.G., Belyakova E.I., Dvortsova P.A., Illarionov Y.Y., Sokolov N.S., Suturin S.M.,
Vexler M.I., Yusupova Sh.A.

Ioffe Institute, 194021 St. Petersburg, Russia,
e-mail: sh.yusupova@mail.ioffe.ru

In the last years, the studies toward the two-dimensional (2D) transistors, or, to be more formal, the transistors with a 2D current-conducting channel, become more and more popular since such devices can offer a way to overcome scaling restriction imposed by the Moore's law. Among the known 2D semiconductor channel materials, there are molybdenum disulfide, graphene, black phosphorus, and their further search is in progress. However, for functioning of the devices, a choice of appropriate insulators is also a challenge. The attempt to fabricate such kind devices with the traditional insulators like SiO_2, high-k dielectrics or hBN were not unsuccessful but elucidated a need for more suitable insulating material [1]. In our recent [2] and present works, we suggest the epitaxial Calcium Fluoride (CaF_2) for this role. Furthermore, CaF_2 can also be exploited as a barrier layer material in other 2D solid-state devices like super-lattices or resonant-tunneling diodes.

Considering an extensive application potential of Calcium Fluoride, careful studies on physical properties, MBE (= molecular beam epitaxy) growth possibilities, manufacturing feasibility and other details with respect to CaF_2 are evidently required. This is what this paper is devoted to. CaF_2 is a crystalline dielectric, perfectly lattice-matched to silicon (Si), with a wide bandgap of 12.1 eV, rather high static permittivity of 8.43, fair conduction band offset to Si of 2.38 eV and large effective carrier mass of $1.0 m_0$ there in [3]. These parameters evidence for the expected good insulating property of the fluoride films, which is especially valuable for the transistor application. The key detail of the epitaxial growth of CaF_2 on Si(111) was a relatively low (250 ^{0}C) temperature; no subsequent annealing procedure was performed. The nominal fluoride thickness d_n ranged from 1–2 to 10–20 nm with the *rms* from 0.1–0.2 nm for the thinnest to approximately 1 nm for the thickest deposited films as measured using the atomic-force microscope.

For studying the electrical characteristics, top gold (Au) round-shaped contacts were deposited through the mask onto the surface of the fluoride creating thereby a metal-insulator-semiconductor (MIS) capacitor $Au/CaF_2/Si(111)$ structure. For the n-Si wafers, an application of positive voltage on the Au electrode rendered the capacitor accumulated and of the negative voltage depleted or inverted. For MIS systems with CaF_2, all the expected features of current-voltage (*I-V*) characteristics were observed – a quasi-exponential increase of the current for the accumulation polarity and, in most cases, also quasi-exponential for the opposite polarity. For a depletion-inversion polarity, instead of a current growth, saturation of current occurred for some samples, indicating a minority carrier deficiency. For the samples showing saturation of *I*, a photosensitivity was observed. All these features are known from the general well-developed theory of MIS tunneling diode structures and in the past were extensively studied for the more conventional capacitors with SiO_2.

A quantitative theory-to-experiment agreement for the *I-V* curves of $Au/CaF_2/Si(111)$ structures was achieved when including a thickness fluctuation into the model. The averaged thickness was set to d_n while the standard deviation σ_d to *rms*. No any artificial fitting factors like e.g. adjustable barrier heights or effective masses, were used. The currents were simulated assuming a dominance of tunneling transport. Both electron and hole components were taken into account considering also a conservation of the transverse wave vector.
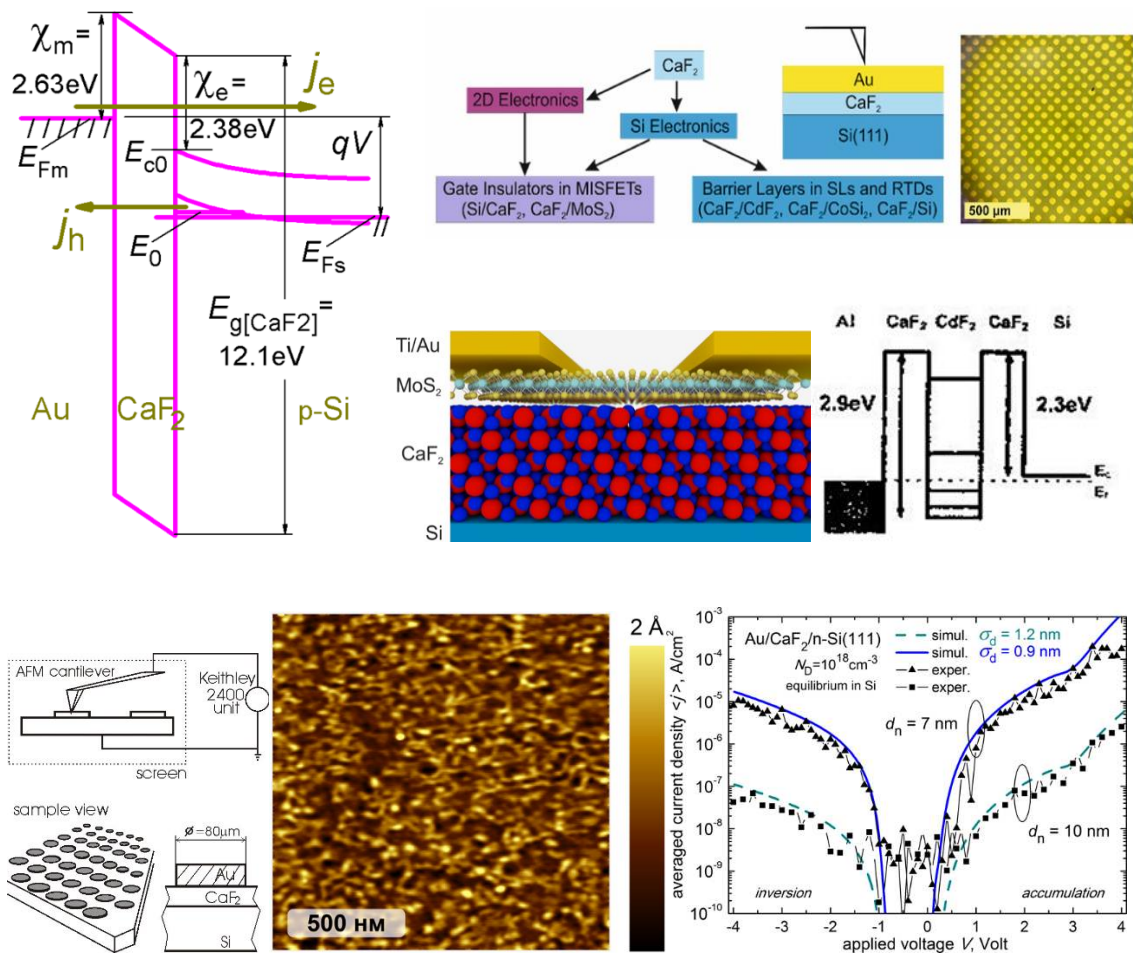
Figure. Top part: Energy band diagram of the Au/CaF$_2$/Si structure; Summary of the possible applications of Calcium Fluoride as a dielectric material, also for the 2D systems; Array of the defined structures with gold electrodes; Drawing of a transistor with a 2D current-conducting MoS$_2$ channel and a fluoride sub-layer; Band diagram of a resonant-tunneling diode with the CaF$_2$ barriers. Bottom part: Measurement schematics; Image of a relief of the grown CaF$_2$ film: Measured vs. simulated current-voltage curves of the MIS structures with Calcium Fluoride (in particular one can see an increase of the standard deviation with increasing nominal thickness). In some cases, in the $V < 0$ branch for the extremely thin ($d_n \sim 2.0$ nm) samples, instead of a monotonous increase, there arose a current plateau (where the current value increased under external irradiation).

The results are summarized in the multipart figure. Commenting to these results, we can conclude that the epitaxially grown fluoride films meet the requirement for the dielectrics in barrier layer for different applications. Further studies should be focused on a reduction of the thickness fluctuations. Also the standard stress tests should be carried out.

References:

[1]Y.Y. Illarionov, T. Knobloch, M. Jech, M. Lanza, D. Akinwande, M.I. Vexler, T. Mueller, M. Lemme, G. Fiori, F. Schwierz, T. Grasser, Nature Communications, 11, 3385 (2020).
[2]T. Knobloch, Y.Y. Illarionov, F. Ducry, C. Schleich, S. Wachter, K. Watanabe, T.Taniguchi, T. Müller, M. Waltl, M. Lanza, M.I. Vexler, M. Luisier, T. Grasser, Nature Electronics, v. 4, pp. 98-108 (2021).
[3]W. Hayes. Crystals with the fluorite structure; Clarendon Press (1974).

OBTAINING Fe NANOCATALYST FOR SYNTHESIS OF CARBON NANOTUBES BY PVD METHOD

Askar Ismatov
Ion-plasm and laser technology institute named after U.A.Aripov

Abstract:
In this study, we explore the use of Physical Vapor Deposition (PVD) methods to obtain iron (Fe) nanostructures, with the primary goal of synthesizing carbon nanotubes (CNTs). The unique properties of CNTs make them valuable in various applications, and the method of synthesis plays a crucial role in determining their quality and characteristics.

Methodology:
The PVD method involves the deposition of Fe nanostructures on a suitable substrate under controlled conditions. Our approach includes a detailed investigation of deposition parameters such as temperature, pressure, and deposition time. Additionally, we explore the influence of substrate type on the growth of Fe nanostructures.

Results:
Successful implementation of the PVD method resulted in the generation of Fe nanostructures, integral for catalyzing carbon nanotube (CNT) synthesis. Microscopic analysis revealed uniform and well-defined structures, with temperature variations impacting size and substrate choice influencing adhesion.

In-depth exploration of deposition parameters indicated that higher temperatures led to the formation of larger nanostructures. Moreover, distinct substrate materials demonstrated varying effects on nanostructure arrangement. This nuanced understanding highlights the adaptability of the PVD process in tailoring Fe nanostructures.

These insights provide a foundation for fine-tuned control in subsequent CNT synthesis, marking significant progress in nanomaterial fabrication..

Discussion:
The discussion focuses on the significance of Fe nanostructures in catalyzing the growth of CNTs. Understanding the relationship between deposition parameters and nanostructure characteristics is crucial for tailoring the synthesis process to achieve desired CNT properties.

Conclusion:
This study contributes to the optimization of PVD methods for obtaining Fe nanostructures, a critical step in the production of high-quality CNTs. The findings offer insights into the control and manipulation of nanostructure growth, providing a foundation for further research in nanomaterial synthesis.

Keywords:
Physical Vapor Deposition, Fe Nanostructures, Carbon Nanotubes, Catalyst, Nanomaterial Synthesis.

PERMEABILITY ASSESSMENT OF A NANOCOMPOSITE MEMBRANE BASED ON POLYVINYL ALCOHOL

U.F. Berdiyev, A.J. Amirova, Kh.B. Ashurov

U.A.Arifov Institute of ion-plasma and laser technologies of the Uzbekistan Academy
E-mail: berdiyev@iplt.uz

Vanadium flow batteries play a crucial role in electrical energy storage, with proton exchange membranes being a key component. The current complexity and high cost of these membranes hinder widespread adoption[1].

To overcome this, an economical proton exchange membrane based on polyvinyl alcohol was synthesized, incorporating silicon oxide nanoparticles. This enhanced membrane exhibits mechanical strength, proton permeability, and vanadium ion prevention properties, meeting the requirements for efficient energy storage systems[2].

The permeability assessment of membranes for vanadium ions V(IV) was conducted within the framework of utilizing a cell consisting of two identical half-cells, with the studied membrane placed between them(Fig.1). A 1M solution of $VOSO_4$ in a 2.5M aqueous solution of sulfuric acid was introduced into one half-cell, while a 1M solution of $MgSO_4$ in a 2.5M H_2SO_4 solution was introduced into the other. The volume of each solution was 5 ml, and the working area of the membrane, in contact with the $VOSO_4$/$MgSO_4$ solutions, was 5 cm2. During the determination of membrane permeability, samples of the solution from the $MgSO_4$ half-cell were collected every hour. The concentration of V(IV) was calculated using the Beer-Lambert-Bouguer law.

Fig.2 Membranes permeability

Fig.1 Membrane permeability test setup.

The synthesized proton exchange membrane based on polyvinyl alcohol with silica nanoparticles has a good barrier function of vanadium ions for VRFB. To assess the permeability of membranes for vanadium V(IV) ions, membranes were compared with the well-known commercial membrane Nafion 117.

Literature

1. Kh. B. Ashurova, *, B. M. Abdurakhmanov, Sh. Ch. Iskandarov, T. K. Turdaliev, A. M. Salimboev, M. M. Adilov and I. J. Abdusaidov. Applied Solar Energy. 2019. 55. 119-125.
2. Berdiev, U. ., Khudaykulov, I. ., Iskandarov, Sh. ., & Turdaliev, T. . (2024). Mechanical properties of a proton exchange composite membrane synthesized on the basis of polyvinyl alcohol. "Uzbek Physical Journal", 25 (4). https://doi.org/10.52304/.v25i4.479

RAMAN SPECTRUM ANALYSIS OF TiO$_2$ DEPOSITED BY THERMAL ALD METHOD ON VARIOUS SUBSTRATES

Kh.B. Ashurov, T.K. Turdaliev*, F.I. Abdurakhmanov, Kh.Kh. Zokhidov

Arifov Institute of Ion-Plasma and Laser Technologies of Uzbekistan Academy of Sciences, Durmon yuli st. 33, Tashkent, Uzbekistan, e-mail: turdaliev@iplt.uz

The investigation and control of the process of depositing thin films of TiO2 onto diverse surfaces present a significant challenge in the contemporary field of science and technology. Thin TiO2 films exhibit unique physical and chemical properties, making them highly sought after in various scientific research and industrial applications [1]. These films are extensively used in solar cells, photocatalysis, sensors, and many other areas. Their distinctive self-cleaning ability, attributed to the simultaneous presence of superhydrophilic and superhydrophobic regions on the surface, is also applied in the development of self-cleaning coatings [2]. Currently, numerous methods exist for depositing thin TiO2 films, each possessing unique advantages and characteristics.

We conducted the deposition process of TiO2 onto diverse substrates, including copper, titanium, silicon, nickel, glass, and aluminum oxide, using the thermal atomic layer deposition (ALD) method. The experiment was performed using the SI PEALD system manufactured by SENTECH Instruments GmbH. In this procedure, titanium tetraisopropoxide (TTIP) and water were employed as the chemical precursors. Nitrogen served as both the carrier gas and the purge gas during the process.

The growth rate per cycle was determined using ellipsometry, yielding a growth of 0.2 nm per cycle. This enabled precise control over the film thickness by specifying the number of deposition cycles. Deposition was carried out for 7500 cycles, resulting in a film thickness of 1.5 micrometers. Sample characterization was conducted using an InVia Raman spectrometer with a resolution of <0.5 cm^{-1} in the visible range. Measurements utilized a 532 nm wavelength laser, a diffraction grating with a period of 1800 lines/mm, an X100 objective, and a standard CCD detector.

Four distinctive Raman active modes of anatase TiO2 with symmetries Eg, B1g, A1g, and Eg were identified at 142, 394, 516, and 637 cm^{-1}, respectively on all samples. These characteristic vibrational frequencies, along with their intensity ratios, confirmed the presence of pure anatase phase in TiO2 [3]. The results demonstrated that irrespective of the substrate, utilizing this method under these deposition conditions led to the growth of titanium oxide with a crystalline Anatase structure.
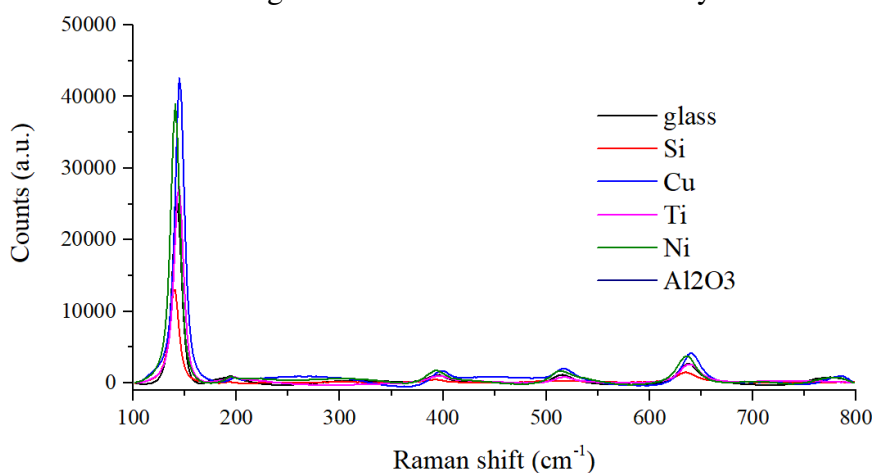
Fig. 1- Raman shift spectrum of TiO2 films deposited on various substrates.

References

[1] Muhaj T. Abdullah et al, J. Phys.: Conf. Ser. 1999 012131 (2021)
[2] Swagata Banerjee, et al, Applied Catalysis B: Environmental, 396, 176 (2015)
[3]Su, W. et al. J. Phy. Chem. C 112, 7710 (2008)

THE INFLUENCE OF REACTANTS RATIO ON THE PROPERTIES OF NICKEL OXIDE NANOPARTICLES

S.G. Gulomjanova, I.J. Abdisaidov, U.B.Rakhmonova, Kh.B. Ashurov

Institute of Ion-Plasma and Laser Technologies, 100125, Durmon yuli st. 33, Tashkent, Uzbekistan.
e-mail: sevara@iplt.uz

Abstract: NiO nanoparticles were obtained by the sol-gel method. NiO nanoparticles were synthesized by sol-gel method. X-ray diffractometry accurately characterized the properties of the synthesized nanoparticles, including crystal structure, purity, and morphology.

Keywords: nickel oxide nanopowder, sol-gel method, calcination temperature, suspension mixing intensity, nanoparticle size

Nickel oxide (NiO) is a chemically stable substance with interesting optical, electrical, and magnetic properties [1]. Thus, it is used in the form of NiO nanoparticles in chroming, as a catalyst, in biomedicine, in gas sensors, in solar energy, in lithium-ion batteries, and in optoelectronic devices, as well as in the composition of solar elements [2].

Various methods are used for the synthesis of NiO nanostructures: coprecipitation, as well as hydrothermal, solvothermal, and chemical precipitation, among which the sol-gel method is the most attractive due to its cost-effectiveness and low energy consumption [3].

As a precursor for the synthesis of NiO using the sol-gel method, a mixture of nickel nitrate ($Ni(NO_3)_2 \cdot 6H_2O$), ammonium hydroxide (NH_4OH), and deionized water was used. The synthesis of NiO nanoparticles is carried out in the following order: $Ni(NO_3)_2 \cdot 6H_2O$ is dissolved in deionized water, to the obtained solution, NH_4OH is added in different proportions and stirred. To age the obtained suspension, it is kept at room temperature for 20 hours. The resulting light-green suspension is then separated on a centrifuge EBA 20S and subjected to calcination in a laboratory furnace SNOL in the temperature range of 400°C for 2 hours.

The crystalline structure, purity, and phase composition of the synthesized nickel oxide nanoparticles were studied using the XRD-6100 Shimadzu diffractometer with a Cu-Kα radiation source at a wavelength (λ) of 1.541874 Å in the angle range of 10°–80° with a step of 0.05°.

In the research work, we studied the influence of changing the ratio of NH_4OH in the reactants at 1:1, 1:2, 1:3 on the properties of nanoparticles. The following conclusions were drawn from the obtained XRD results.
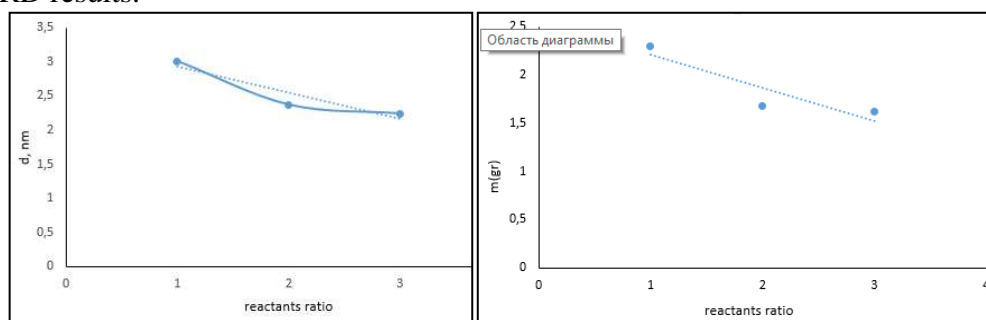
Fig.1 – The impact of NH_4OH content on the size and mass of nanoparticles.

According to the XRD results, the diameter depends on the ratio of NH_4OH in the total mass. As the proportion of NH_4OH increases, the size of the nanoparticles decreases, and the mass of the nanoparticles decreases.

References

1. M. Alagiri, S. Ponnusamy and C. Muthamizhchelvan. Jour-nal of Materials Science: Materials in Electronics 23(3), 728-732 (2012).
2. Shamim, Z. Ahmad, S. Mahmood, U. Ali, T. Mahmood and Z. Ahmad. Open Journal of Chemistry 2(1), 16-20 (2019).
3. N. Prasad, F. Veillon and W. Prellier. Journal of Alloys and Compounds 858, 157639 (2021).

EVALUATING THE INFLUENCE OF TEMPERATURE AND SOLAR IRRADIANCE ON SOLAR I-V CHARACTERISTICS USING MATLAB SIMULINK

Khaitbaev E., Rajapov D., Khasanov A., Jumaboyev B.

14, Kh.Alimdjan Street, Urgench City, Khorezm, 220100, Uzbekistan

eldorkhaitbaev@gmail.com

Abstract

This research scrutinizes the dynamic interplay of temperature and irradiance on the I-V characteristic of a singular solar panel, employing a simulation model within the MATLAB Simulink framework. The simulation spans a spectrum of climatic conditions, simulating temperatures at +25° C, +35° C,   +45° C, and +55° C degrees as in [4], and irradiance levels ranging from 1000 to 100 W/m^2. The study yields comprehensive I-V (current-voltage) characteristics according to [1, 2], providing nuanced insights into the performance of the solar panel under diverse environmental scenarios. The results not only underscore the impact of temperature [3] and irradiance variations but also contribute essential data for the practical design and implementation of solar energy systems, especially in regions prone to extreme weather conditions.

Keywords: solar panel, irradiance, temperature, power output, MATLAB Simulink, STC.

Introduction: The contemporary global energy paradigm is confronted with escalating challenges, necessitating a paradigm shift towards sustainable alternatives. Amidst these challenges, solar photovoltaic (PV) systems offer a promising solution, standing as a beacon for renewable energy. At the forefront of solar energy technology are solar panels, and comprehending their intricacies is crucial for unlocking their full potential. The simulation model employed in this research is anchored in the BYD (Huizhou) Battery BYD 210P6-30, a solar panel esteemed for its efficiency and widespread application [1]. In the depicted figure below, the simulation model is visually represented.
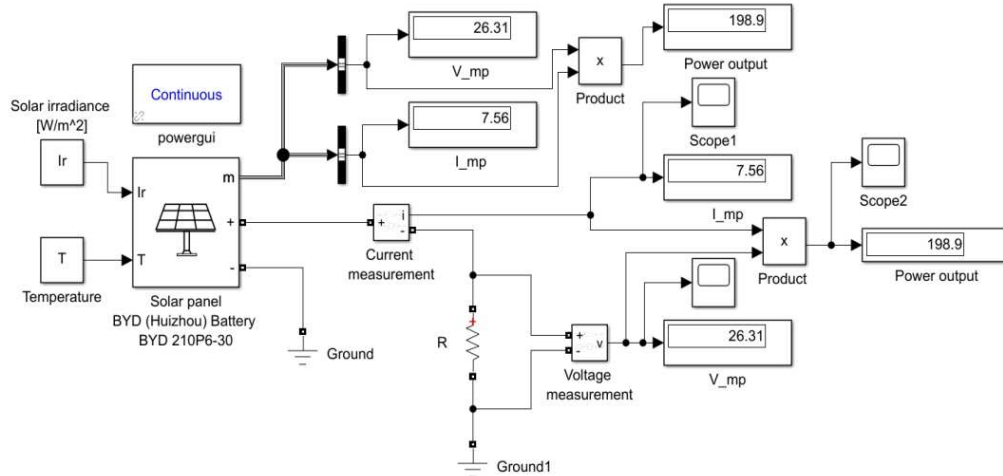
Figure 1: The overall Simulink model of a 200 W solar power system.

Temperature and Irradiance as Influencing Factors: Temperature emerges as a pivotal factor influencing the efficiency of PV modules, with dynamic variations impacting the open circuit voltage (V_{OC}) and, subsequently, the power output. Understanding and incorporating temperature coefficients into system design becomes imperative, aligning projected cell temperatures with data derived under Standard Test Conditions (STC) for precise module output predictions [1].

The general model of PV cell shown in Fig. 1, called as circuit model which includes photocurrent source, diode, parallel resistor expressing the leakage current and series resistor describing the internal resistance to the current flow. The I-V characteristic equation of a PV cell is written as,

$$I = I_{ph} - I_s \left(exp \left[\frac{q(V+IR_s)}{kTA} \right] - 1 \right) - \frac{(V+IR_s)}{R_{sh}}$$ [2].

I_{ph} – Light-generated current or photocurrent
I_s – Cell saturation of dark current
q – Electron charge ($1.6*10^{-19}$C) K Boltzmann constant ($1.38*10^{-23}$ J/K)
A – Ideality factor
R_{sh} – Shunt resistance, R_s – Series resistance
T – Module operating temperature (K)
I_{sc} – PV module short circuit current (8.11 A)
G – PV module illumination W/m^2
G_n – Standard PV module illumination (1000 W/m^2)
E_g – Bandgap for silicon (1.12 eV)
V_{mp} – Output voltage of a PV module at maximum power point (V)
I_{mp} – Output current of a PV module at maximum power point (A)
The provided figures below illustrate the I-V and P-V characteristics of the solar panel under varying solar irradiances [2, 3].
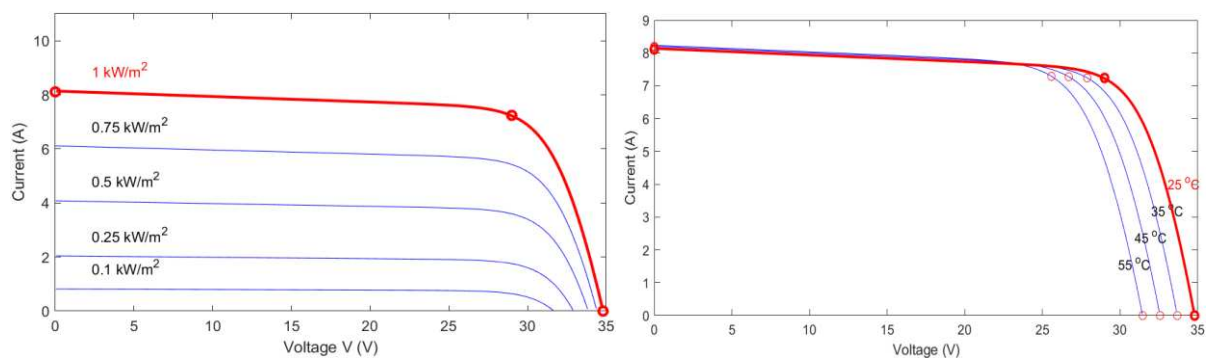
Figure 2: I-V characteristics of the 200 W solar panel under different solar irradiances (left) and in different temperatures (right).

Conclusion: In summary, our research dives deep into understanding how a solar panel's power output responds to temperature and irradiance variations. Through meticulous MATLAB Simulink simulations, we observed the pronounced impact of temperature on open circuit voltage and overall power output. Solar irradiance fluctuations also demonstrated a proportional effect on current and power. These insights, especially relevant in Uzbekistan's climatic context, offer valuable data for designing resilient solar solutions. Our findings contribute to both theoretical understanding and practical applications, shaping informed decisions in solar energy system design and optimization for regions with diverse weather patterns.

REFERENCES

[1] Md.W.Shah, Robert L.Biate, "Design and Simulation of Solar PV Model Using Matlab/Simulink International Journal of Scientific & Engineering Research", Volume 7, Issue 3, (March 2016).
[2] D. Revati, E. Natarajan, "I-V and P-V characteristics analysis of a photovoltaic module by different methods using Matlab software", Materials Today: Proceedings 33, (2020)
[3] Julie C. Ogbulezie, Armstrong O. Njok, Manoj K. Panjwani, Suresh K. Panjwani, "The impact of high temperature and irradiance source on the efficiency of the polycrystalline photovoltaic panel in a controlled environment", International Journal of Electrical and Computer Engineering (IJECE) Vol. 10, No. 4, (August 2020).
[4] A. D. Dhass, E. Natarajan, P. Lakshmi, "An Investigation of Temperature Effects on Solar Photovoltaic Cells and Modules", International Journal of Engineering, Vol. 27, No. 11, (Nov 2014).

ON HOW "SULFUR- MANGANESE" BONDS MIGHT OCCUR IN SILICON

Shoikrom Askarov[1], Бashirulla Sharipov[1], Abdulaziz Mavlyanov[2], Shohista Saliyeva[1], Barnokhon Ibragimova[1]

[1] Tashkent State Technical University, Tashkent, Universitetskaya street 2B, 100095
[2] Semiconductor Physics and Microelectronics Research Institute Tashkent, 100057, Uzbekistan
e-mail: microelectronics74@mail.ru

As multiple studies have previously reported, in the process of thermal treatment of silicon single crystalline samples, that were diffusion doped with sulfur and one of the elements of the transition group, one can reveal in a certain temperature range, the phenomenon of intense interaction between these centers, accompanied by electrical neutralization of both impurity centers[1].

With regards to majority of transition group elements, they appeared to interact with sulfur in the temperature range of intensive decomposition of the "silicon –sulfur" solid solution ($800 \div 950$) ºC, whereas with regard to manganese, such interaction took place directly in the process of diffusion doping of silicon sample (preliminarily doped with sulfur) with manganese.

In order to find out how such complexes appear in the course of such interaction, the authors studied the spectra of EPR of silicon samples successively doped with sulfur and manganese (Si<S,Mn>). For comparison, the EPR spectra of reference Si<S> and Si<Mn> crystals were also studied.

A study of the EPR spectra in reference Si<S> samples showed that they exhibit a single isotropic line with parameters g = 2.064 ± 0.002 and ΔHpp = 8 Gs, due to singly positively charged S^+ centers. In reference Si<Mn> samples, the spectra of non-equivalent exchange-coupled Mn^+ - Mn^+ pairs were observed. The intensity of the lines and the value of the resonant fields of the spectrum in reference Si<Mn> samples changed strongly with temperature. The spectrum had a maximum intensity at T = 4.6 K, and the center of gravity of the spectrum at a given temperature was practically in zero fields, and part of the spectrum was in the region of negative fields. As the temperature decreased, the intensity of the lines of the spectrum decreased, and the center of gravity shifted towards positive fields, and at T = 3.2 K the spectrum was completely registered at positive fields. At this temperature, in the direction of the magnetic field along the <111> axis, the spectrum consisted of four fine structure lines, each of which consisted of 11 hyperfine structure lines with A = 37 G.

In Si<S,Mn> samples, the spectra of the S^+ - center were absent, in addition, in these samples in the weak fields, an EPR spectrum was observed, consisting of several lines, the position and intensity of which varied from sample to sample. In this case, the center of gravity of the lowest field part of the spectrum remained unchanged at 190 G. The results of study of the temperature dependence of the four most intense lines of the spectrum had a maximum at 16 K, in addition, with an increase in temperature ~ 80 K, the lines would shift to the region of stronger fields.

All these facts indicate that the spectrum observed in weak fields differs from the spectra of non-equivalent exchange-coupled Mn^+ - Mn^+ pairs observed in reference Si <Mn> samples. It can be assumed that the observed center is due to exchange-coupled complex based on these atoms, that is, there is an exchange between manganese atoms happens through "sulfur atoms" mechanism.

The absence of a hyperfine structure in the most intense lines and their relatively small width (ΔH = 10–20 G) indicates that the magnetic electrons are on manganese atoms. At the end, it is indicated that the coupling between the centers of sulfur substitution centers and interstitial centers of manganese is carried out through free d - shell.

References

[1] M.K.Bakhadirhanov, Sh.I.Askarov, N.Norkulov. Phys.Stat.Sol.(a), 1994, v.142, p.339

RAMAN SPECTROSCOPIC ANALYSIS OF RECYCLED VANADIUM PENTAOXIDE (V_2O_5)

Sh.Ch.Iskandarov, T.K.Turdaliev, I.Kh.Ashurov, Kh.B.Ashurov

Arifov Institute of Ion-Plasma and Laser Technologies of Uzbekistan Academy of Sciences, Durmon yuli st. 33, Tashkent, Uzbekistan, e-mail: iskandarovshukhrat86@gmail.com

Almost three-quarters of the world's electricity is generated from non-renewable fossil fuel sources, specifically 28.9% from coal, 21.4% from natural gas and 31.1% from oil [1]. The limited and negative consequences of using non-renewable (or fossil) energy sources are well known. While renewable energy sources (hydroelectric, wind, solar, geothermal, thermal and wave energy) are considered as clean energy sources.

Despite numerous chemical energy storage methods, all-vanadium redox flow batteries (VRFBs) are effectively used for large-scale energy storage. These batteries represent a promising technology due to their high charging and discharging rates, environmental friendliness, flexibility and long service life [2]. However, despite efforts to increase the energy density of VRFB electrolytes, this density remains low, which significantly limits the scope of VRFB applications [3]. The solution to this problem is the use of vanadium, which depends on the degree of purity of the oxide (V_2O_5) and additional elements in its composition [4]. In practice, standard electrolytes containing pure vanadium oxide with a purity of 99.99% are most often used [5]. However, this leads to a cost issue since the electrolyte accounts for a significant portion of the cost of a VRFB battery [6]. Considering these problems, recycled vanadium pentoxide can be used as an electrolyte.

Raman spectra of the samples were obtained on an InVia Raman spectrometer (Renishaw, UK) at room temperature. The excitation source was a Cobolt CW 532 nm DPSS laser with a wavelength of 532 nm and a nominal energy of 100 mW.μ, in a diffraction grating with a period of 1800 lines/mm. The recording device used was a standard CCD camera detector. Raman spectroscopy measurements were discussed using the shapes and frequencies of resolved modes located in high and low wavenumber regions ($3Ag+2B_{1g}+B_{2g}+B_{3g}$), corresponding to internal and external modes. Internal modes include elastic (stretching) vibrations of V-O in the wavelength range of 500–1000 cm^{-1}, and external modes contain bending vibrations of V-O-V in the wavelength range of 100-500 cm^{-1}.

Raman spectra of V_2O_5 powder were studied on an InVia Raman spectrometer at room temperature. Raman spectroscopy measurements were discussed using the shapes and frequencies of resolved modes located in high and low wavenumber regions ($3A_g+2B_{1g}+B_{2g}+B_{3g}$), corresponding to internal and external modes. Internal modes include elastic (stretching) vibrations of V-O in the wavelength range of 500–1000 cm^{-1}, and external modes contain bending vibrations of V-O-V in the wavelength range of 100-500 cm^{-1}.

The crystalline powder of V_2O_5 ($3A_g+2B_{1g}+B_{2g}+B_{3g}$) exhibited active Raman modes, which was confirmed by peaks at wavelengths of 145, 195, 284, 303, 406, 481, 527, 700 and 995 cm^{-1} (Figure 1). These peaks were found to match the results obtained for microcrystalline powders of V2O5 in terms of intensity and wavenumber. The Raman spectrum of V_2O_5 crystal powder is presented[7], the peak in the range of 995 cm^{-1} characterizes the elasticity of the V=O bond.

The second peak at 700 cm^{-1} corresponds to the elastic mode of doubly coordinated oxygen (V_2-O_B) arising from corner oxygen. The third peak at 527 cm^{-1} is due to ternary coordination (V_3-O_C). The peak at 406 cm^{-1} indicates bending vibrations of three-coordinate oxygen bonds (V_3-O_C) and V-O_B-V, respectively. The peak at 284 cm^{-1} is attributed to the bending vibration of the O_C-V-O_B bond. Two more Raman peaks are shown at 145 cm^{-1} and 193 cm^{-1}, which correspond to lattice vibrations.
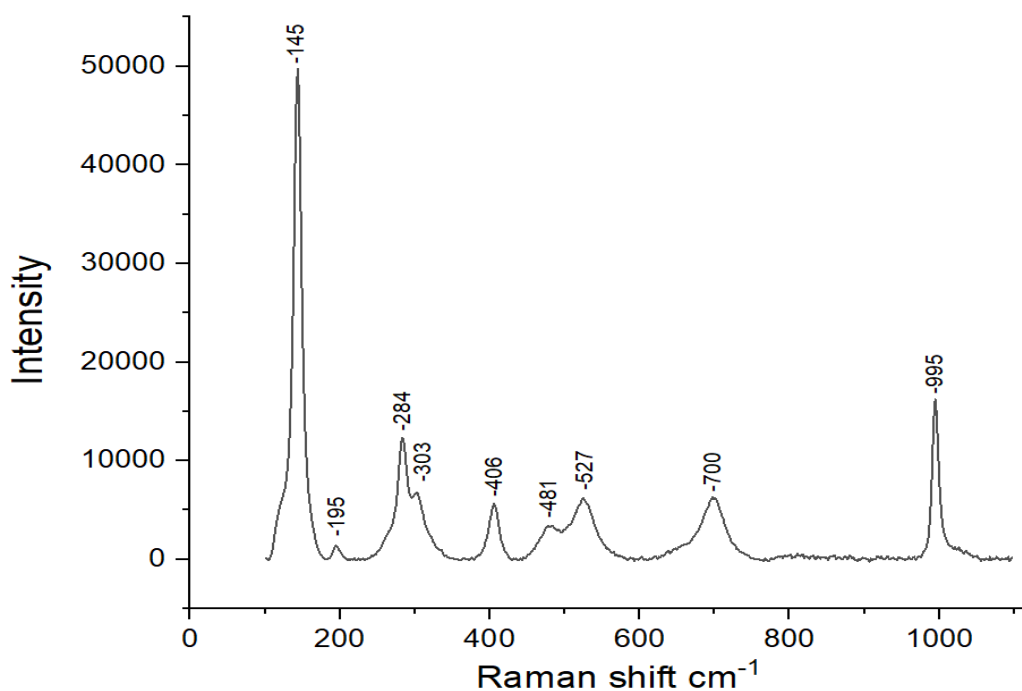
Figure 1. Raman spectrum of V₂O₅ powder.

The results confirm that the recycled vanadium oxide powder exhibits bending vibration with oxygen at 406 cm^{-1} (V_3-O_C) and V-O_B-V. At a wavelength of 995 cm^{-1}, elasticity (stretching) appears, and the connection with oxygen is located at the edges of vanadium.

References

[1] - IEA O. Energy and climate change, world energy outlook special report 2015

[2] - Q. Xu, P. Lan, B. Zhang, Z. Ren, and Y. Yan, ''Energy sources, part A: Recovery, utilization, and environmental effects,'' Energy Sources, vol. 35, pp. 848–858, Mar. 2013

[3] - M. Skyllas-Kazacos, L.Y. Cao, M. Kazacos, N. Kausar, A. Mousa, Vanadium electrolyte studies for the vanadium redox battery-A review, ChemSusChem 9 (2016) 1521–1543.

[4] - Hu, P.; Zhang, Y.; Liu, T.; Huang, J.; Yuan, Y.; Xue, N. Source separation of vanadium over iron from roasted vanadium-bearing shale during acid leaching via ferric fluoride surface coating. J. Clean. Prod. 2018, 181, 399–407.

[5] - Dmello, R.; Milshtein, J.D.; Brushett, F.R.; Smith, K.C. Cost-driven materials selection criteria for redox flow battery electrolytes. J.Power Sources 2016, 330, 261–272.

[6] - Li, M.-J.; Zhao, W.; Chen, X.; Tao, W.-Q. Economic analysis of a new class of vanadium redox-flow battery for medium-and large-scale energy storage in commercial applications with renewable energy. Appl. Therm. Eng. 2017, 114, 802–814.

[7] - M. Benmoussa, E. Ibnouelghazi, A. Bennouna and E. L. Ameziane, Thin Solid Films, 1995, 265, 22; I. Kosacki, M. Massot, M. Balkanski and H. L. Tuller, Mater. Sci. Eng., B, 1992, 12, 345

MEG EFFECT IN LOW DIMENSIONAL NANOSTRUCTURES

[1,2]Turaeva N., [3]Oksengendler B.L., [4*]Marasulov M.

[1]Webster University, USA
[2]Samarkand State University, Uzbekistan
[3]Institute of Material Science, Uzbekistan
[4]Institute of Polymer Chemistry and Physics, Uzbekistan

One of the remarkable nanoeffects occurring in semiconducting nanocrystals is the generation of multiple electron-hole pairs upon the absorption of a single photon. The effect is called Multiple Exciton Generation (MEG) or Carrier Multiplication (CM) and potentially promising to increase the efficiency of solar energy conversion, particularly in photovoltaics and photocatalysis. Fundamental experimental studies of the CM effect have been performed for various semiconductors in different geometries [1-5], including 0D QDs, 1D quantum rods and carbon nanotubes, 2D graphene and nanosheets, and 2D van der Waals-layered materials, core/shell and Janus-like heterostructured nanocrystals. In general, the geometry has a dramatic effect on the CM conversion efficiency. For example, it was shown that the CM in QDs is more efficient than in their bulk counterpart. In PbSe nanorods with the aspect ratio of 6-7, the CM efficiency was 2-fold greater compared to spherical NCs [3]. The highest CM conversion efficiency, 99%, was reported for van der Waals films which is close to the energy conservation limit [4]. Comparison of quantum yields, and the CM conversion efficiencies of various nanostructures was given in fig 1 [4]. To explain the dimensionality effect of CM effect in PbSe nanorods vs QDs established in femtosecond TA and transient PL experiments, we used the Fermi statistical theory based on the assumption of strong Coulomb interaction between excitons [5]. Considering the difference in CM thresholds in nanorods vs QDs, a good agreement between the theory and experimental quantum efficiencies has been received.
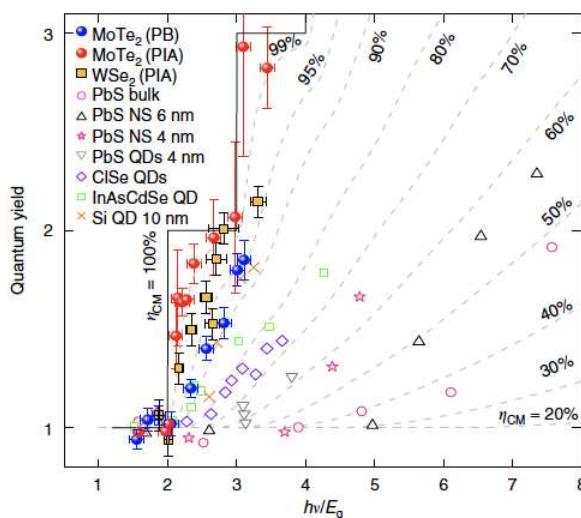
Fig 1. Comparison of the CM efficiencies of various semiconductors [4].

Two important parameters of the CM conversion efficiency are the CM threshold, E_{th}, and the e-h pair creation energy, ε_{e-h}, which is required to generate a new exciton after the CM threshold is reached. Ideally from energy conservation the minimal values of these parameters should be $2E_g$ and E_g, respectfully. However, for bulk and different nanostructures these quantities are considerably larger due to total and partial momentum conservation and fast energy losses of carriers by phonon emission. As the CM conversion efficiency is defined as the bandgap energy divided by the actual energy of electron-hole pair creation, $\eta_{e-h} = E_g/\varepsilon_{e-h}$, then the efficiency

η_{e-h} is less than 1. It is well established that the CM conversion efficiency is defined by the competition between the CM promoted by strong Coulomb interaction and large exciton-binding energies and carrier cooling by phonon scattering and a reduction in ε_{ph} and increase in η_{e-h} can be achieved by increasing the ratio of the time constants of carrier cooling by phonon emission and CM process. In this study, we present a theoretical approach by assumption that these competitive processes define the CM efficiency via exponential function:

$$\eta_{e-h} = exp\left(-\frac{\tau_{e-e}}{\tau_{e-ph}}\right) \tag{1}$$

Here τ_{e-e} is the time constant of electron-electron scattering leading to the CM conversion and τ_{e-ph} is the time constant of carrier cooling by electron-phonon scattering. It was shown [4] that in 2D materials the electron-electron scattering time constant is considerably shorter that for 1D nanowires and 0D QDs. By considering the ratio of time constants of electron-phonon scattering and electron-electron scattering equal to 30 [4] and using Eqn.1, we can receive 97% CM conversion efficiency which is close to the experimental values up to 99% CM conversion efficiency. In general, the analysis of time constants of nanostructures with different dimensionalities shows the tendency of increasing the ratio of time constants of electron-phonon and electron-electron scattering with dimension which results in increasing the CM efficiency. This presented theoretical approach can be used in design of nanomaterials for CM optimization based on their size and dimension.

References

1. M.C. Beard, J. Phys. Chem. Lett. 2, 1282-1288 (2011).
2. D.M. Kroupa, G.F. Pach, M. Voros, et al. ACS Nano, 2018.
3. L.A. Padilha, J.T. Stewart, R.L. Sandberg, et al., Nano Lett.13, 1092-1099 (2013).
4. J.-H. Kim, M.R. Bergren, J.C. Park et.al., Nature Communications, 10, 5488 (2019).
5. Marasulov M., Turaeva N., Oksengendler B.L., Solar Energy, 2020.

MODELING SOME ELECTRONIC AND OPTICAL PROPERTIES OF $Ge_{1-x}Sn_x$ SOLID SOLUTION OBTAINED BY LIQUID PHASE EPITAXY METHOD

Amin Saidov[1], Ritam Chakraborty[2], Umida Asatova[3], <u>Shahzod Masharipov</u>[3], Shukurullo Usmonov[1], Dadajon Saparov[1]

[1]*Physical-Technical Institute, Academy of Sciences of Uzbekistan, Tashkent, 100084 Uzbekistan, e-mail: amin@uzsci.net; sh_usmonov@rambler.ru, dada@uzsci.net, [2]Theoretical Sciences Unit, Jawaharlal Nehru Centre for Advanced Scientific Research, Jakkur, Bangalore-560064, India,* ritamchakraborty@jncasr.ac.in, [3]*Urgench State University, Urgench, 220100 Uzbekistan,* umida72@rambler.ru*,* shahzodbekmasharipov6@gmail.com

At the global level, when growing epitaxial films of narrow-gap semiconductor solid solutions, promising materials are: germanium (Ge) (with a band gap of $E_g = 0.67$ eV) and its solid solution with tin (Sn) (with $E_g < 0.67$ eV). Such materials are of particular importance in the development of thermophotovoltaic generators, thermovoltaic elements, infrared radiation sensors, etc. Therefore, scientific research is being carried out on the growth of epitaxial films of multicomponent semiconductor solid solutions with controlled composition and crystalline perfection, as well as studying their structural, electrophysical and photoelectric properties .

$Ge_{1-x}Sn_x$ solid solutions were grown by liquid phase epitaxy (LPE) from a limited volume of Sn solution-melt in a hydrogen atmosphere. LPE was carried out on a vertically located quartz reactor with horizontally located substrates. Ge washers with crystallographic orientation (111) and a resistivity of 1.0 Ohm cm were used as substrates. The diameter of the substrate was 20 mm, and the thickness was about 400 μm. High-quality films were grown at cooling rates of 0.5÷1.0 deg/min. The content of Sn atoms in the $Ge_{1-x}Sn_x$ solid solution at a temperature of 540°C was 3 at.%.

The crystal lattice constants of the epitaxial film and substrate, and the crystallographic orientation of the epitaxial film were determined using the results of a Dron-UM1 X-ray diffractometer. Analysis of the X-ray diffraction results showed that the lattice constants of the epitaxial film (a_f) and germanium substrate (a_s) were $a_f = 5.6812$ Å and $a_s = 5.6561$ Å, respectively, the crystallographic orientation of the epitaxial film corresponds to the (111) crystallographic plane.

The conductivity type of epitaxial layers of solid solutions was determined by the thermal probe method. The grown epitaxial films had a thickness of 15 μm and hole type conductivity [1-2].

To gain insight into the experimentally synthesized thin film from an atomistic point of view, we performed density functional theory-based calculations. All the calculations were performed using Quantum Espresso [3] Software package using Norm Conserving pseudopotentials and electron's kinetic energy cutoff of 200 Ry and Monkhorst-Pack k-point sampling of 8x8x8. Bulk optimized lattice constant of 5.62 Å was found to be in excellent agreement with the experimentally obtained lattice constant of 5.65 Å.

For simulating the 3% Sn doped Ge structure, we had to consider a 2x2x1 supercell of bulk Ge, with one Ge atom being replaced by one Sn atom. The k-point grid was accordingly scaled to 4x4x8. We performed variable cell relax calculations to minimize the stress and forces in the unit cell. This 2x2x1 supercell is now a tetragonal unit cell. The lattice constant of this unit cell is now 5.64 Å, which tells that it has increased from the previous value of 5.62 Å upon Sn doping. This result is consistent with the experimental XRD result which also points out an increase in the lattice constant from 5.65 Å to 5.68 Å.

We went on to explore the electronic structure of synthesized thin film. The band structure of this $Ge_{1-x}Sn_x$ (with x= 0.03) shows an indirect band gap of 0.37 eV between gamma point and Z point (Fig 1). The projected density of states (PDOS) calculation shows the absence of any state at the fermi level, confirming the semiconducting nature of the synthesized thin film. Sn s-orbitals contribute mainly to the conduction band and Sn p-orbital contributes to the valence and conduction

bands implying that the hybridization of the dopant Sn atom with the host Ge atoms primarily involves Sn-4p orbitals.

Further, we explored the optical properties of the 3% Sn doped system. The first peak in the epsilon (ε_2 imaginary part of the dielectric constant) spectra corresponds to the direct bandgap present at the gamma point in the band structure (Fig 2). The theoretical electron energy loss (EELS) spectrum shows a photon energy peak at around 11 eV.
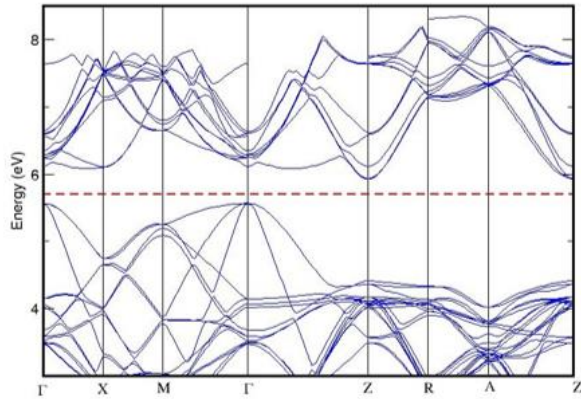
Fig 1. Band structure of $Ge_{1-x}Sn_x$ solid solution with x=3%. DFT calculated band gap = 0.37 eV
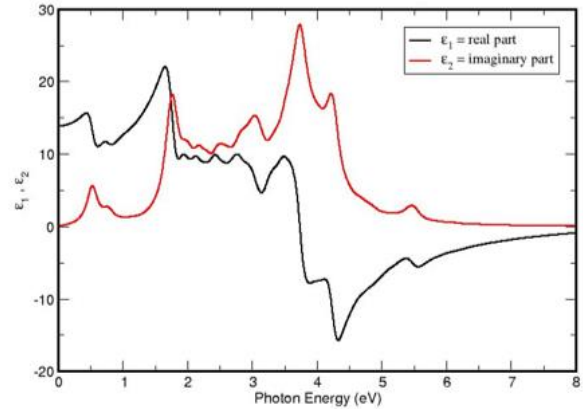
Fig 2. Real and imaginary part of the dielectric constant of $Ge_{1-x}Sn_x$ solid solution with x=3% as a function of incident photon energy

References

[1]   A.S. Saidov, Sh.N. Usmonov, U. P. Asatova, Growth of $Ge_{1-x}Sn_x$ Solid Solution Films and Studu of Their Structural   Properties and Some of Their   Photoelectric Properties. Semiconductors. New York, 2012, Vol. 46, No.8, pp.1088–1095

[2]   A.S Saidov, Sh.K Ismailov, U. P. Asatova. Semiconductor solid solutions $Ge_{1-x}Sn_x$ as a new material for electronics 2021 International Conference on Information Science and Communications Technologies(ICISCT), 2021, pp. 1-3, **DOI:** 10.1109/ICISCT52966.2021.9670382, https://ieeexplore.ieee.org/document/9670382

[3]   https://www.quantum-espresso.org.

POSITIONING OF GERMANIUM ATOMS AT THE SI/SIO$_2$ INTERFACE AND SILICON FILMS DURING ION SYNTHESIS OF NANOMETER-THICK SILICON-GERMANIUM LAYERS

O.O. Mamatkarimov, M.O. Turg'unov, B.H. Kuchkarov

Namangan Institute of Engineering and Technology
Target-based doctoral student of the Scientific Research Institute of Semiconductor Physics and Microelectronics under the National University
Impuls Medical Institute
turgunovmuslimjon4@gmail.com

Structures produced by implantation of Ge$^+$ ions, first at 8×10^{15} cm^{-2} dose at 40 keV and then at 60 energy, to more precisely study the location of germanium atoms at and near the Si/SiO$_2$ interface. At a dose of 1.6×10^{16} cm^{-2} keV and annealing at 850 °C was studied within 20 min. Then, after transferring the silicon film to the implanted oxide, the structures were additionally annealed at 1100°C for 30 minutes to separate the germanium atoms into the bond boundary. At the final stage, the structures were subjected to layer-by-layer anodic oxidation at room temperature, and then the anodic oxidized layers were removed in a solution of HF:H$_2$O=1:100. Thus, the top layer of silicon was thinned to a few nanometers. Then, using the medium-energy ion scattering method, the scattering efficiency spectra of He$^+$ ions with an energy of 150 keV were measured in the range of scattering angles from 110 to 131° relative to the direction of the probe beam.

Diffusion angles at which complete blocking of the emission of scattered particles was observed were determined. This made it possible to determine the magnitude of the angles between the planes inclined to the incoming light. It is possible to estimate the magnitude of tetragonal lattice distortions in intact silicon. Along with the scattering spectra, the Raman spectra excited by the Ar laser line with a wavelength of 514.5 nm and a power of 2-3 MW were studied. The size of the probe spot was 4-6 microns. A T64000 triple monochromator spectrometer manufactured by Horiba Jobin Yvon with a spectral resolution of no more than 2 cm^{-1} was used. A silicon matrix of photodetectors cooled by liquid nitrogen served as a detector. The measurements were performed in a backscattering geometry with the radiation polarization vector directed along the <111> crystallographic direction of silicon. Scattered light is recorded in polarization. The selected geometry allowed for maximum suppression of the Raman signal from the silicon substrate. A cross-sectional electron microscope was also used to analyze the structures.

Figure 1. Raman spectra of Silicon-on-Insulator structures with SiO$_2$ layer implanted with Ge$^+$ ions of 40 keV dose at 8×10^{15} cm^{-2} after annealing at 1100 with 1.6×10^{16} cm^{-2} dose of 60 keV energy. ° C for 30 minutes. The thickness of the cut silicon layer is (a) 3 nm, (b) 60 nm (curve 2), curve 1 - 0 nm. a low-intensity shoulder is also observed, which may be due to localized fluctuations in the nanometer-thick silicon layer. The data in Figure 1. a show that germanium atoms form Ge-Ge and Ge-Si bonds. In this case, both a crystalline phase and an irregular phase are formed on the basis of germanium atoms.Raman spectra of optical phonons were studied in structures compatible with a thicker (60 nm) silicon-on-insulator layer to clarify the positions of germanium atoms.

a)   b)
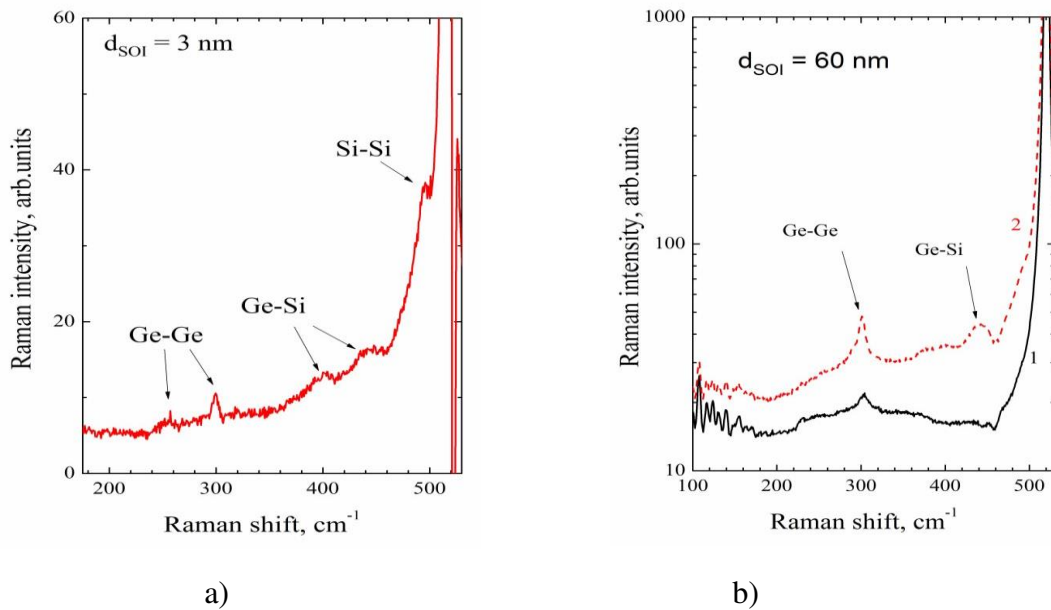
Figure 1 b. shows the Raman spectrum (curve 2) of the corresponding silicon sample with the SiO_2 layer implanted under the same conditions as the Silicon-on-Insulator structure and annealed at the same temperatures. It can be seen that the absence of a silicon layer on SiO_2 leads, firstly, to a decrease in the intensity of the Raman peak at the optical phonon frequency of Ge-Ge bonds, and secondly, to the complete disappearance of the peak. Optical phonon frequency corresponding to vibrations of Ge-Si bonds. This means that the Ge-Si bonds are mainly formed in the truncated silicon layer. The decrease in the peak intensity at the frequency of 300 cm^{-1} can be related to the absence of the Si / SiO_2 boundary and the formation of an intermediate germanium layer.

REFERENCES

1. М.И. Гусева, Б.Г. Александрия. – Влияние плотности ионного тока на структуру и концентрацию изотопных мишеней, приготовленных в электромагнитном сепараторе. ЖТФ. 1961, т. 31, в. 7, с. 867-875
2. M. Watanabe, A. Tooi. – Formation of SiO2 films by oxygen-ion bombardment. Japan J. Appl. Phys.1966, v. 5, n. 12, pp. 737-738.
3. W.J. Kleinfelder. – Properties of ion-implanted boron, nitrogen, and phosphorus   in single-crystal silicon. Technical Report No K701-1 on DARPA Contract SD-87, 1967.
4. А.Е. Городецкий, Г.А. Качурин, Н.Б. Придачин, Л.С. Смирнов. – О возможности получения тонких слоев полупроводниковых соединений методом ионной бомбардировки. ФТП. 1968, т. 2, в. 1, с. 136-137.
5. Е.К. Баранова, К.Д. Демаков, К.В. Старинин, Л.Н. Стрельцов, И.Б. Хайбуллин. – Исследование монокристаллических пленок SiC, полученных при бомбардировке ионами C+ монокристаллов Si. Доклады АН СССР. 1971, т. 200, в. 1, с. 869-870.

INFLUENCE OF RADIATION EXPOSURE ON LUMINESCENT PROPERTIES OF LOW-DIMENSIONAL SiGe/Si (111) HETEROSTRUCTURES

O.O. Mamatkarimov, M.O. Turg'unov, B.H. Kuchkarov

Namangan Institute of Engineering and Technology
Target-based doctoral student of the Scientific Research Institute of Semiconductor Physics and Microelectronics under the National University
Impuls Medical Institute
turgunovmuslimjon4@gmail.com

The world's major scientific centers, great importance is attached to conducting scientific research aimed at obtaining new semiconductor materials, increasing the stability and sensitivity of the electrophysical properties of these materials to external influences such as temperature, light, magnetic field, and radiation. The effect of radiation on the luminescent properties of low-dimensional Si/Ge heterostructures with different levels of spatial localization of charge carriers was studied. It has been shown that the radiation resistance of Si/Ge heterostructures increases with the increase of charge carrier localization efficiency in them. Spatial localization of charge carriers in SiGe nanostructures reduces the probability of their non-radiative recombination in radiative defects created in the Si matrix. Among the studied structures, the highest radiation resistance is manifested by the fluorescent properties of multilayer structures with self-formed Ge (Si) nanodefects. In this case, the most effective spatial localization of charge carriers is realized. considered three-dimensional defects for holes and two-dimensional spatial environments for electrons in Si layers separating adjacent layers.

Low-dimensional semiconductor heterostructures are attracting more and more attention. The spatial localization of charge carriers leads to a significant difference in the electrical and optical properties of low-dimensional structures compared to multilayer semiconductors. Recently, it became known that the radiation resistance of low-dimensional structures based on various heteropyres (InGaAs/GaAs [1], AlAs/GaAs [2] and Si/Ge [3, 4]) is higher than that of layered materials. It is possible to distinguish Si/Ge structures that correspond to the modern technology of semiconductor heterostructures, which make them useful in improving the traditional elements of silicon nano- and microelectronics, and in developing new electronic and optoelectronic devices.

allows use in creation. [5]. In particular, Si/Ge heterostructures with self-generated nanodefects and quantum dots are a promising material for making light and photodiodes on silicon substrates for the wavelength range of 1.3-1.55 μm [6-7]. The effect of radiation exposure on the fluorescent properties of Ge/Si heterostructures was studied.

The studied Si/Ge heterostructures were grown on Si (001) directions by molecular beam epitaxy (diffusion) from solid sources. A SiGe quantum gap (QW), a thin Ge layer, a single layer of self-formed Ge(Si) nanodefects, and a multilayer structure with Ge(Si) nanodefects were studied. Structures with (QW) were grown at 700°C, structures with nanodefects at 600°C. 1010 cm- 2 is formed in structures with defects. The growth conditions for the studied structures are described in more detail in [8,9]. Photoluminescence (PL) spectral measurements were performed at 77 and 300 K using a Bomem DA3-36 Fourier spectrometer. The PL signal was excited by a Nd: YAG laser with a wavelength of L=532 nm. PL spectra were recorded using a cooled Ge photodetector with a low energy limit of 0.7 eV spectral characteristic. The study of the dose effect of ionizing radiation was carried out under pulsed electron radiation with energy of 2 and 4 MeV.

Relatively low intensity of the electron beam. The dose was affected by 0.6 and 20 M rad, respectively. A reactor with a characteristic neutron energy of ~1 MeV and a flux of up to 1015 cm-2 was investigated. Experimental studies on the effect of various radiation effects on the fluorescent properties of low-dimensional GeSi heterostructures showed their higher resistance compared to bulk silicon. The increase in radiation resistance is due to the spatial localization of

charge carriers in SiGe nanostructures, which prevents their diffusion into radiation defects and subsequent non-radiative recombination in them.

REFERENCES

1. М.И. Гусева, Б.Г. Александрия. – Влияние плотности ионного тока на структуру и концентрацию изотопных мишеней, приготовленных в электромагнитном сепараторе. ЖТФ. 1961, т. 31, в. 7, с. 867-875.
2. M. Watanabe, A. Tooi. – Formation of SiO2 films by oxygen-ion bombardment. Japan J. Appl. Phys.1966, v. 5, n. 12, pp. 737-738.
3. W.J. Kleinfelder. – Properties of ion-implanted boron, nitrogen, and phosphorus in single-crystal silicon. Technical Report No K701-1 on DARPA Contract SD-87, 1967.
4. А.Е. Городецкий, Г.А. Качурин, Н.Б. Придачин, Л.С. Смирнов. – О возможности получения тонких слоев полупроводниковых соединений методом ионной бомбардировки. ФТП. 1968, т. 2, в. 1, с. 136-137.
5. Е.К. Баранова, К.Д. Демаков, К.В. Старинин, Л.Н. Стрельцов, И.Б. Хайбуллин. – Исследование монокристаллических пленок SiC, полученных при бомбардировке ионами C+ монокристаллов Si. Доклады АН СССР. 1971, т. 200, в. 1, с. 869-870.
6. J. Dylewski, M.C. Joshi. - Thin SiO_2 films formed by oxygen ion implantation in silicon: electron microscope investigations of the Si- SiO_2 interface structure and their C-V characteristics. Thin Solid Films. 1976, v. 37, n. 2, pp. 241-248.
7. K.J. Reeson. Fabrication of buried layers of SiO2 and Si3N4 a using ion beam synthesis Nucl. Instrum. Meth. Phys. Res. B. 1987, v. 19/20, Pt. 1, p. 269-278.
8. S.I.Vlasov, F.A.Saparov, K.A. Ismailov. Semiconductor Physics, Quantum Electronics and Optoelectronics. 2010, Vol. 13. No. 4, pp.363.
9. B Kuchkarov, O Mamatkarimov, and A Abdulkhayev. «Influence of the ultrasonic irradiation on characteristic of the structures metal-glass-semiconductor». ICECAE 2020 IOP Conf. Series: Earth and Environmental Science 614 (2020) 012027 Conference Series.
10. 10.B.X. Qo'chqarov, A. nishonov, X.O.Qochqarov. The effect of tunneling gurrent on the spedd surface generation of charge garries. *Scientific bulletin of NamSU* 1(7),3-6.

IONIC SYNTHESIS OF INSB NANOCLUSTERS IN SIO$_2$ LAYER FILMS BURIED NEAR THE INTERFACE OF A Si/SiO$_2$ INSULATOR-ON-SILICON STRUCTURE.

O.O. Mamatkarimov, M.O. Turg'unov, B.H. Kuchkarov

Namangan Institute of Engineering and Technology
Target-based doctoral student of the Scientific Research Institute of Semiconductor Physics and
Microelectronics under the National University
Impuls Medical Institute
turgunovmuslimjon4@gmail.com

In our works, the process of ion-beam synthesis of InSb nanocrystals on the SiO2 film near the growth boundary of the Silicon structure on the Si/SiO$_2$ Insulator was studied. According to the information presented in the previous paragraph, the characteristics of the ion-beam synthesis of the InSb phase are that the In and Sb atoms in the silicon oxide matrix have very different diffusion coefficients. In addition, the presence of a truncated silicon layer formed by the hydrogen transfer method indicates the presence of residual hydrogen atoms, which promote the diffusion of In atoms as a result of migration to the SiO$_2$ layer during subsequent annealing. Formation of the InOH complex. These processes can lead to different redistribution of implanted In and Sb atoms and affect the processes of formation and growth of InSb phase nuclei.

Formation of Silicon-on-Insulator structures with a buried layer of silicon oxide placed near the bonding interface with Sb$^+$ and In$^+$ ions was accomplished by a method involving ion-beam synthesis and hydrogen transfer elements. A diagram of structure formation is presented in Figure 1.a. Sb$^+$ and In$^+$ ions were thermally grown on p-type silicon wafers with a diameter of 100 mm (111) (Fig.). The parameters of the used Sb$^+$ and In$^+$ ions ensured the formation of Gaussian-like spatial distributions with a maximum concentration of indium and antimony at a depth of ~110 nm at ~1.2×10^{21} cm^{-3}. Hydrogen ions with an energy of 140 keV were injected into the second silicon plate with a dose of 2×10^{16} cm^{-2} (Fig. 1. b). Then, in a vacuum chamber, the plates are connected to the implanted sides by simultaneously separating the silicon layer along the inner hydrophobic surface formed by the implantation of H$^+$ ions and transferring it from the second plate to the first (1.c- picture).

The processes of connecting wafers, dividing and transferring the silicon layer were carried out in one step at a temperature of 200°C in a vacuum chamber with a pressure of 10^2 Pa. The thickness of the transferred Si layer was about 600 nm. Then the plate is cut into samples. Post-implantation annealing of the samples was carried out in an N$_2$ atmosphere at a temperature of 500-1100°C for 30 minutes. The scattering profiles of embedded atoms and defects were studied using Rutherford Backscattering of 1.7 MeV He+ ions with respect to the probe beam of the substrate in maximum disorder modes and channel mode. The structural properties of the synthesized phase were also studied using HRTEM on a JEM-4000 microscope with a resolution of 0.2 nm at an accelerating voltage of 250 kV. Figure
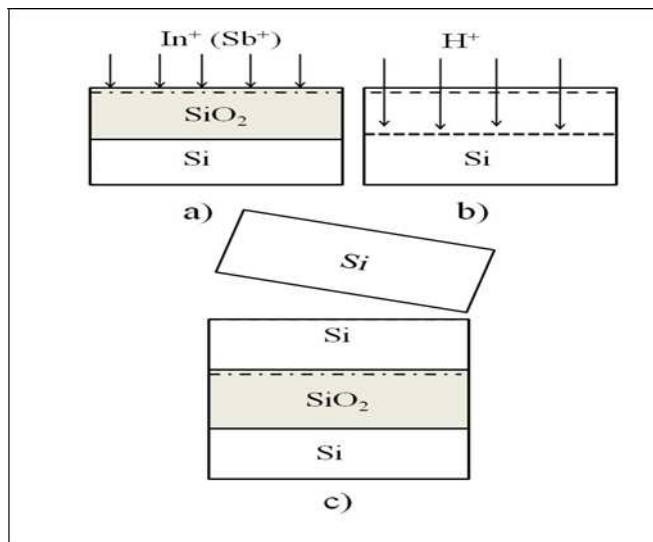
Figure 1. Scheme of formation of Silicon-on-Insulator structures with a buried SiO_2 layer implanted near the bond boundary with Sb_+ and In^+ ions: a) implantation of Sb^+ and In^+ ions on the thermal oxide grown on the first silicon substrate; b) placement of H^+ ions on the second silicon substrate through the protective oxide; c) fusion of the first and second substrates and removal of Si across the implanted layer by H^+ ions.

REFERENCES

1. М.И. Гусева, Б.Г. Александрия. – Влияние плотности ионного тока на структуру и концентрацию изотопных мишеней, приготовленных в электромагнитном сепараторе. ЖТФ. 1961, т. 31, в. 7, с. 867-875.
2. M. Watanabe, A. Tooi. – Formation of SiO2 films by oxygen-ion bombardment. Japan J. Appl. Phys.1966, v. 5, n. 12, pp. 737-738.
3. W.J. Kleinfelder. – Properties of ion-implanted boron, nitrogen, and phosphorus in single-crystal silicon. Technical Report No K701-1 on DARPA Contract SD-87, 1967.
4. А.Е. Городецкий, Г.А. Качурин, Н.Б. Придачин, Л.С. Смирнов. – О возможности получения тонких слоев полупроводниковых соединений методом ионной бомбардировки. ФТП. 1968, т. 2, в. 1, с. 136-137.
5. Е.К. Баранова, К.Д. Демаков, К.В. Старинин, Л.Н. Стрельцов, И.Б. Хайбуллин. – Исследование монокристаллических пленок SiC, полученных при бомбардировке ионами С+ монокристаллов Si. Доклады АН СССР. 1971, т. 200, в. 1, с. 869-870.
6. J. Dylewski, M.C. Joshi. - Thin SiO2 films formed by oxygen ion implantation in silicon: electron microscope investigations of the Si- SiO2 interface structure and their C-V characteristics. Thin Solid Films. 1976, v. 37, n. 2, pp. 241-248
7. K.J. Reeson. Fabrication of buried layers of SiO2 and Si3N4 a using ion beam synthesis Nucl. Instrum. Meth. Phys. Res. B. 1987, v. 19/20, Pt. 1, p. 269-278.

HIGH INDEX SURFACE FOR GRAPHENE SYNTHESIS

T.Juraboev[1,2], N.Esanturdiyeva [2] and U. Khalilov[1,2,3]

[1] *Arifov Institute of Ion-Plasma and Laser Technologies, Tashkent, 100125, Uzbekistan*
[2] *Denau Institute of Entrepreneurship and Pedagogy, Denau, 190507, Uzbekistan*
[3] *University of Antwerp, Antwerp, 2610, Belgium*
Email: tursunpulatjuraboev24@gmail.com

The stability of the catalyst in graphene synthesis depends on surface energy. Catalyst stability is a crucial parameter in controlling graphene nucleation, reducing defects, and minimizing graphene oxide [1]. Generally, low-index surfaces are more commonly used than high-index surfaces in graphene synthesis due to their lower surface energy values. However, there is a growing interest in utilizing high-index surfaces for graphene synthesis. This interest stems from the elevated catalytic activity exhibited by high-index surfaces when compared to low-index surfaces [2]. Consequently, to assess the stability of high-index nickel catalysts with (310), (311), and (331) facets, we determined their respective surface energies using the Molecular Dynamics method. In particular, Fig. 1 shows that the surface energies of Ni(331), Ni(310), and Ni(311) surfaces are 2.05 J/m², 2.10 J/m², and 2.12 J/m², respectively. Among these three high-index surfaces, Ni(331) exhibits more stability than the other two surfaces due to its lower surface energy. Because of its sufficient stability and catalytic activity, the Ni(331) surface can be recommended to experimenters for application in graphene growth.
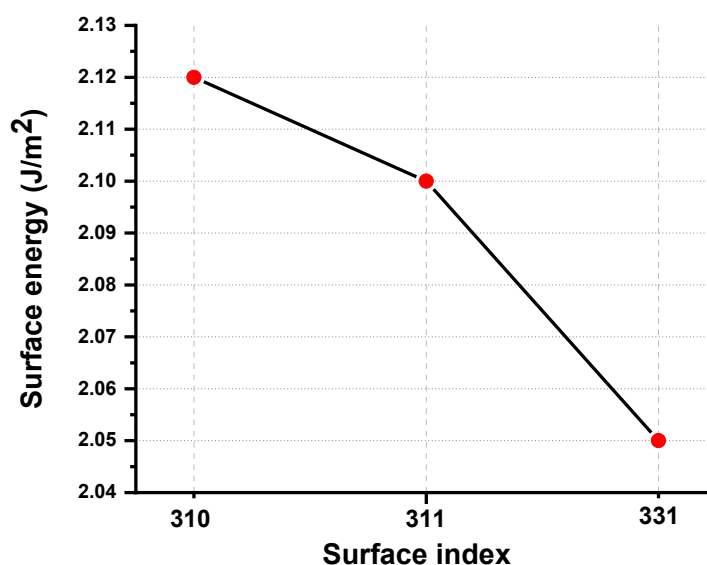
Fig.1 *Surface energy of high index surfaces of nickel crystal.*

Reference

1. Li, M., Li, Y., & Mbengue, J. M. (2015). DFT Investigations on the CVD Growth of Graphene. *Surface Energy*. IntechOpen.
2. Xiao, Chi, et al. High-index-facet-and high-surface-energy nanocrystals of metals and metal oxides as highly efficient catalysts. *Joule* 4.12 (2020): 2562-2598.

THE EFFECT OF VOLUME FRACTION IN THE SYNTHESIS OF LONG ENDOHEDRAL CARBON CHAINS

K. Mehmonov[1], A.Ergasheva[1], and U. Khalilov[1,2]

[1] *Arifov Institute of Ion-Plasma and Laser Technologies, Tashkent, 100125, Uzbekistan*
[2] *University of Antwerp, Antwerp, 2610, Belgium*
kamoliddin.mehmonov@iplt.uz

Endohedral synthesis in a double-walled carbon nanotube (DWNT) is a promising method for safe carbyne growth [1], producing longer carbon chains through catalyzed growth [2,3]. However, the influence of the volume fraction of endohedral catalyst nanoparticles in the synthesis process remains unclear. In this study, we investigate the role of the catalyst (nickel) volume fraction in carbyne synthesis within a DWNT using reactive molecular dynamics (MD) simulations. In particular, we observe that middle nickel atoms with weak bonds can freely move or diffuse along the newly formed longer carbon chain. Eventually, all nickel atoms connect to the terminal atoms of the chain, which is energetically favorable (Fig. 1*a*). Also, the findings reveal an inverse relationship between the growth rate of carbon chains and the filling fraction of nickel clusters. Specifically, at filling fractions of 4.9%, 6.5%, 9.8%, and 19.5%, the formation times for endohedral carbyne are 0.35 ns, 0.49 ns, 0.70 ns, and 0.73 ns, respectively (Fig. 1*b*).
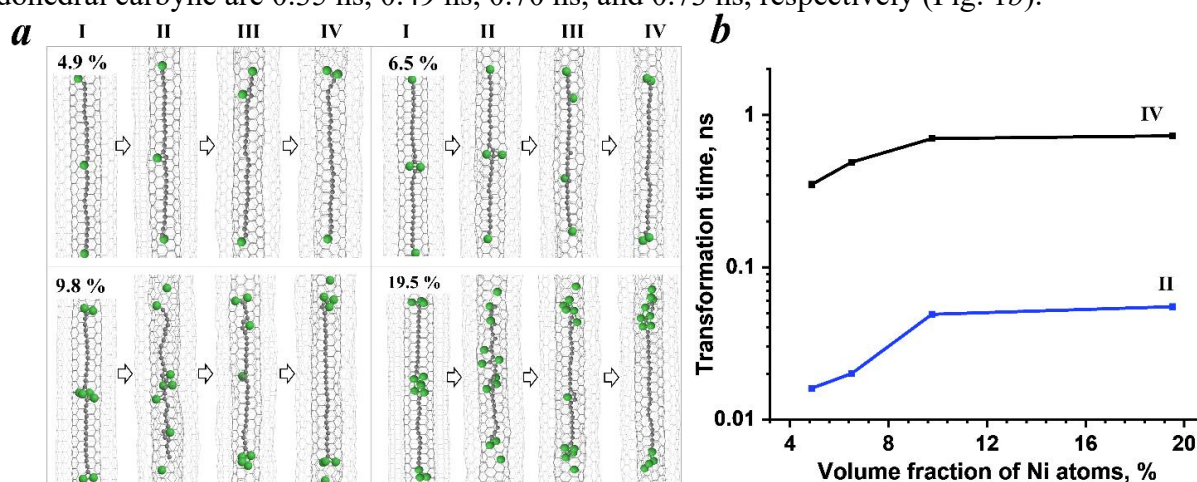
Fig. 1. *a) Transformation of the structure from Ni_{m1}-C_{n1}-Ni_{m2}-C_{n2}-Ni_{m3} to Ni_k-C_{n1+n2}-Ni_l in DWNTs with different volume fraction of Ni atoms. b) Transformation times for cases II and IV as a function of volume fraction of Ni atoms in DWNTs. I, II, III and IV – separate carbon chains, formation of C–C bonds between these two chains, diffusion of Ni atoms along chain and formation of carbyne respectively.*

In overall, these results shed light on the role of the catalyst volume fraction, providing valuable insights for future advancements in carbyne synthesis for the current carbon nanotechnology.

References

[1]   L. Shi et al., Nature Mater **15**, 6 (2016).
[2]   U. Khalilov et al., Carbon **153**, 1 (2019).
[3]   K. Mehmonov et al., Journal of Applied Physics **134**, 144303 (2023).

SYNTHESIS OF FILAMENTOUS NANOWHISKERS OF C_{70} FULLERENE

U.K. Makhmanov, S.A. Bakhramov, A.M. Kokhkharov, B.A. Aslonov, S.A. Esanov,
K.N. Musurmonov, Z. Bekmurodov, A. Shukurov, A. Olimov

Institute of Ion-Plasma and Laser Technologies, Uzbekistan Academy of Sciences, Uzbekistan,
urol_m@mail.ru

Nanowhiskers (NWs) are considered to be filamentous crystals with a transverse size of up to 100 nm and a length that is an order of magnitude or more greater than the transverse size. Carbon nanomaterials (fullerene, carbon nanotube and graphene) are becoming key components of nanotechnologies for the development of complex functional nanostructures [1]. Fullerenes are a hollow sphere/ellipsoid carbon molecule less than 1 nm in diameter, with with semiconductor properties. Semiconductor fullerene nanowhiskers are widely used today to create miniature elements of devices in microelectronics, optoelectronics, nanoengineering, solar energy, biomedicine, nanoelectromechanics and gas sensing [2-5]. To date, there are various methods [6-7] for obtaining nanowhiskers of a wide range of semiconductor materials, such as growth by molecular beam epitaxy, vapor deposition, laser ablation, growth catalysts, magnetron deposition, chemical epitaxy in high vacuum and others. In all cases, the regulation and control of the size and structure of the NWs is of great importance. In particular, when NWs synthesized in solution are transferred to the surface of a solid substrate, changes in their morphology occur due to the process of self-organization. In this regard, there is a need to study the processes occurring in the volume of evaporation of droplets of fullerene solutions.

In this work, we consider the synthesis of nanostructured C_{70} fullerene whiskers (C_{70}NWs) on the surface of a substrate by evaporating a microvolume drop of C_{70} solution. Experimental methods for controlling the geometric dimensions of the synthesized C_{70}NWs are discussed [8]. In our experiments we used the high purity (~99.8%) powders of fullerene C_{70} (Sigma-Aldrich, USA) as well as organic solvent – toluene ($C_6H_5CH_3$, Sigma-Aldrich, USA). Standard K-8 optical glass with a surface roughness of ≤ 7 nm was used as a substrate.
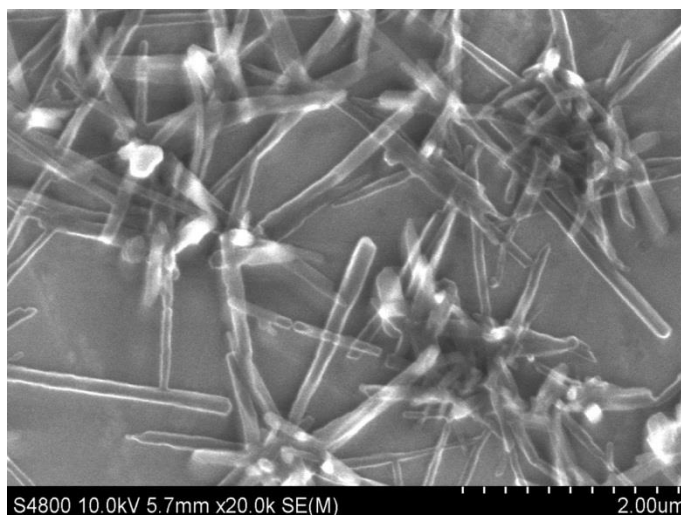
Fig. 1. SEM-image of C_{70}NWs synthesized in the volume of evaporating droplet of C_{70} molecular solution on the flat substrate at T≈36°C. The concentration of fullerene C_{70} in the initial drop of the solution was ~$1.1 \cdot 10^{-3}$ mol·L^{-1}.

UV-visible spectroscopy, electron microscopy, refractometry and dynamic light scattering were used in the experiments. A method has been proposed and implemented for obtaining nano- and microsized whiskers from fullerenes, based on the self-organization of fullerene molecules during the thermal evaporation of a solvent from droplets of fullerene solutions. SEM-image of

C$_{70}$NWs synthesized on a surface of a horizontally located glass substrate, heated to T=36°C presented in Figure 1. In experiments with fixed concentration of C$_{70}$ (~1.1·10^{-3} mol·L^{-1}) in a drop of the working solution, the effect of increasing the temperature of the substrate on the ongoing processes of the evaporation drop was studied. It was established that an increase in the substrate temperature not only led to a more accelerated nucleation and growth of C$_{70}$NWs, but also to a noticeable increase in the final geometric dimensions of the synthesized C$_{70}$NWs. Wherein, the distribution of C$_{70}$NWs on the substrate surface is getting denser. At the same time the average length and width of the resulting C$_{70}$NWs reached the values ~1.8 µm and ~175 nm, respectively. The presented results proved that the size of nanowhiskers can be controlled by changing the substrate temperature at a fixed concentration of C$_{70}$ in the working drop.

Under the same conditions (T≈36°C), we studied the effect of the initial concentration on the size of the synthesized nanoparticles. An increase in the fullerene concentration in the initial droplet led to a noticeable increase in the final C$_{70}$NW size. Thus, it was shown that the geometric dimensions and morphology of the whiskers can be controlled by changing both the initial concentration of the fullerene solution and the temperature of the substrate used.

The experimental results of this work can be used to predict and control the synthesized geometric dimensions of nanostructured whiskers, which will have great potential in nano- and microelectronics, solar cells, third-order nonlinear optics, sensors, and electromechanics.

References

[1] Varadwaj P.R., Varadwaj A., Marques H., Yamashita K. Fullerenes, carbon nanotubes and graphene as tetrel bond donors and acceptors of electrophiles // Cryst. Eng. Comm., Vol. 25, pp. 3417-3438 (2023). DOI: 10.1039/D3CE00184A.

[2] Davis J.J., Coleman K. S., Azamian B.R., Bagshaw C.B., Malcolm L.H. Green. Chemical and biochemical sensing with modified single walled carbon nanotubes // Chemistry: A European Journal, Vol. 9, no. 16, pp. 3732–3739 (2003). DOI: 10.1002/chem.200304872

[3] Kausar A., Ahmad I., Maaza M., Eisa M.H., Bocchetta P. Polymer/Fullerene Nanocomposite for Optoelectronics-Moving toward Green Technology // J. Compos. Sci., Vol. 6, pp. 1-15 (2023). DOI: 10.3390/jcs6120393

[4] Zhang G., Finefrock S., Liang D., Yadav G.G., Yang H., Fang H., Wu Y. Semiconductor nanostructurebased photovoltaic solar cells // Nanoscale, Vol. 3, pp. 2430–2443 (2011). DOI:10.1039/c1nr10152h

[5] Zhang W.D., Zhang W.H. Carbon Nanotubes as Active Components for Gas Sensors // J. Sens., pp. 1-16 (2009). DOI:10.1155/2009/160698

[6] Sathish M., Miyazawa K., Hill J.P., Ariga K. Solvent Engineering for Shape-Shifter Pure Fullerene (C$_{60}$) // J. Am. Chem. Soc., Vol. 131, pp. 6372–6373 (2009). DOI:10.1021/ja902061r

[7] Kahar S.M., Voon C.H., Lee C.C., Hashim U., Mdarshad M.K., Lim B.Y., Gopinath S.C.B., Rahman W. Synthesis of SiC nanowhiskers from graphite and silica by microwave heating // Mater. Sci. Pol., Vol. 34, pp.770–779 (2016). DOI: 10.1109/icobe.2015.7235912

[8] Bakhramov S.A., Makhmanov U.K., Aslonov B.A. The Synthesis of C$_{70}$ Fullerene Nanowhiskers Using the Evaporating Drop Method // Condens. Matter, Vol.8, pp. 62 (2023). DOI: 10.3390/condmat8030062

SYNTHESIS OF VARIOUS DIMENSIONAL NANOSTRUCTURES FROM FULLERENE MOLECULES

U.K. Makhmanov, A.M. Kokhkharov, B.A. Aslonov, S.A. Esanov, K.N. Musurmonov,
Z. Bekmurodov, A. Shukurov, A. Olimov

Institute of Ion-Plasma and Laser Technologies, Uzbekistan Academy of Sciences, Uzbekistan,
urol_m@mail.ru

The nanosized carbon molecules of fullerenes (C_{60}, C_{70}) attract the attention of scientists, primarily due to its unique properties, which allows them to be used in various fields of science, including medicine, modern electronics, materials science and other fields of technology [1-3]. Solutions of mentioned fullerenes in organic solvents can be considered as colloidal systems, since the tendency of the fullerene molecule to form clusters in various solvents is known [4]. In this case, the properties of the synthesized nanoscale clusters become dependent on their geometric dimensions, and differ markedly from the analogous properties of their constituent individual fullerene monomers. The results of the unique physicochemical properties of C_{60}, C_{70} fullerenes in various environments can be extremely important for the creation of new generation nanomaterials with predictable physical properties, as well as for the synthesis of multifunctional micro- and nano-sized electronic devices based on fullerenes. So, the processes of synthesis of various zero-dimensional nanoclusters and one-, two-, and three-dimensional nanostructured materials based on fullerene molecules will attract special attention from a wide range of researchers. At the same time, many questions about intermolecular interactions leading to the clustering of fullerene molecules in solutions, as well as the synthesis of various sized nanostructures based on them, remain controversial.

Thus, the aim of this work is the experimental synthesis of quasi-spherical nanoclusters, one- and two-dimensional nanomaterials of C_{60} and C_{70} fullerenes. Specific physical mechanisms for the synthesis of fullerene-based nanomaterials will be discussed. Crystalline fullerene C_{60} and C_{70} powders with a purity >99.8% were supplied by Sigma Aldrich (USA). Organic solvents used in the experiments – hexane (C_6H_{14}), benzene (C_6H_6), ethylbenzene (C_8H_{10}) and isopropyl alcohol (C_3H_8O) with purities >99% were purchased from Sigma Aldrich (USA). To study the dimensional, structural, and optical features of the synthesized nanosized fullerene materials, we used the methods of transmission and scanning electron microscopy, optical spectroscopy, refractometry, conductometry, and dynamic light scattering.

The experimental results of this work can be used to predict and control the geometric dimensions of synthesized nanostructured materials, which will have great potential in a wide range of practical applications in various branches of science and technology, such as nano- and microelectronics, third-order nonlinear optics, sensors, solar cells, and medicine.

References

[1]. Yin, H.; Lin, H.; Zong, Y.; Wang, X.-D. The Recent Advances in C60 Micro/Nanostructures and Their Optoelectronic Applications // Org. Electron. 93, 106142 (2021). https://doi.org/10.1016/j.orgel.2021.106142

[2]. Kesava, S. V., Fei, Z., Rimshaw, A. D., Wang, C., Hexemer, A., Asbury, J. B., Heeney, M., & Gomez, E. D. Domain compositions and fullerene aggregation govern charge photogeneration in polymer/fullerene solar cells. Advanced Energy Materials, 4(11), [1400116] (2014). https://doi.org/10.1002/aenm.201400116

[3]. Nasir, S.; Hussein, M.Z.; Zainal, Z.; Yusof, N.A. Carbon-Based Nanomaterials/Allotropes: A Glimpse of Their Synthesis, Properties and Some Applications. Materials 2018, 11, 295. https://doi.org/10.3390/ma11020295

[4]. Bakhramov S.A., Makhmanov U.K., Aslonov B.A. The Synthesis of C_{70} Fullerene Nanowhiskers Using the Evaporating Drop Method // Condens. Matter, Vol.8, pp. 62 (2023). DOI: 10.3390/condmat8030062

ADSORPTION OF BORON ATOMS ON CARBON NANOTUBES WITH DIFFERENT TEMPERATURES

Shakhnozakhon Muminova[1], Ishmumin Yadgarov[1,2], Mohinur Choriyeva[1] Utkir Uljayev[1,2]*

[1]Institute of Ion-plasma and laser technologies, 100125, 33 Durmon yuli street, Uzbekistan
[2]Tashkent Institute of Textile and Light Industry
email: shmuminova242526@gmail.com

Due to its unique properties, carbon nanotubes (CNTs) are relevant for research in the fields of physics, chemistry and materials science. Their low weight and chemical stability make them highly sought after, and they find applications in diverse areas such as electronic devices, sensors, and material reinforcement. Additionally, they are employed in fields like adsorbents due to their unique characteristics. Compared to single-walled carbon nanotubes (SWNTs), double-walled carbon nanotubes (DWNTs) exhibit robust mechanical, electrical, and optical properties, along with high chemical stability [1].

In the present work, interactions between DWNTs and boron atoms of (5,5) and (10,10) chirality with metallic conductivity using the LAMMPS software package using the Molecular Dynamics (MD) method at 300 K and 900 K were studied. The ReaxFF potential was employed to compute the processes involving the formation and breaking of bonds between DWNT and boron atoms. The concentration (ρ (%)) of boron atoms adsorbed on the DWNT surface exhibited variation depending on the movement speed (kinetic energy, E_k). As E_k increased, ranging from 1 eV to 32 eV, the ρ (%) value for adsorbed boron atoms changed within the ranges of 2.2%-16.1% and 1.2%-15.7% at 300 K and 900 K, respectively (Fig.1).
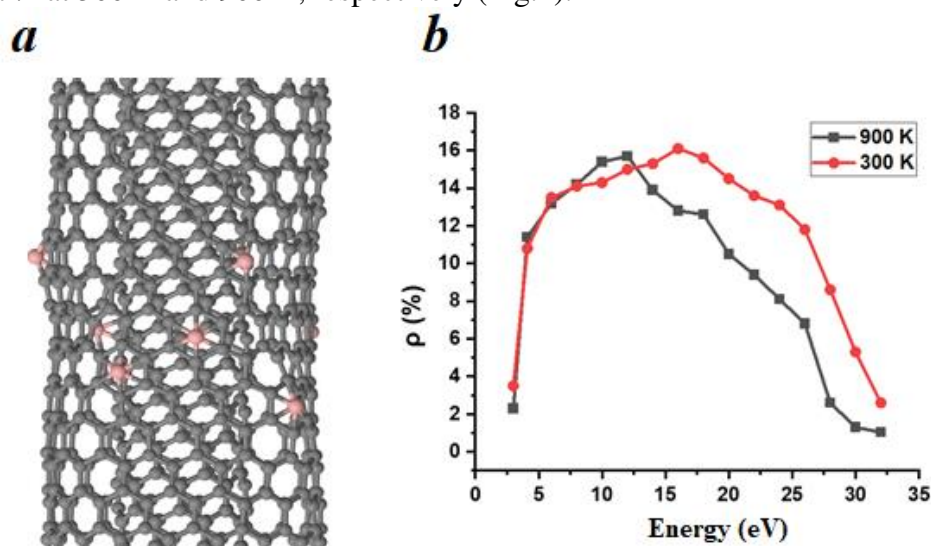
Figure 1. *a*) Boron atoms adsorbed on DWNT. *b*) Boron atoms adsorbed on DWNT as a function of its energy.

The inclusion of boron atoms in nanotubes enhances their reaction capabilities by facilitating charge redistribution within the heterostructure. Introducing boron atoms enables the detection of various crucial chemical compounds and offers control over different concentrations within the nanotubes, thereby regulating the sensitivity of the nanosensors.

[1] G. Speranza, "Carbon Nanomaterials: Synthesis, Functionalization and Sensing Applications", *Nanomaterials*, vol. 11, no. 4, (2021), p. 967.

STRUCTURE AND TRANSPORT PROPERTIES OF THIN ZnO LAYERS ON GaP

P.B. Parchinskiy*, A.A. Nasirov, A.A. Nebesniy, R.A. Nusretov, A.O. Arslanov

Department of Physics, National University of Uzbekistan,
University street, 4th, Tashkent 100174, Uzbekistan
e-mail: pavelphys@mail.ru

Nowadays transparent conductive oxides (TO) have attracted great attention because of their wide application in nano-and optoelectronics and in the field of solar energy. The thin TO layers on wide gape semiconductors, which are also transparent to visible light, are of particular interest due to potential application of such structures for design of devices for transparent electronics and cascade solar cells as well. In this work we present the results of studies of structure and transport properties of thin ZnO layers on p type GaP.

Thin films of ZnO were obtained by ultrasonic spray pyrolysis technique (USP). An aqueous solution of zinc acetate dehydrate ($Zn(C_2H_3O_2) \cdot 2H_2O$, 0.5 mol/L) was used as a source of zinc to obtain ZnO films. We employed an ultrasonic nebulizer with the frequency of 2.5 MHz for atomization of a solution. Oxygen was used as a carrier gas with the flow rate at 500 sccm/min. The GaP substrate temperature was set at 400 ^{0}C and the thickness of films was about 200 nm. Reference ZnO samples on Si substrate were grown simultaneously with ZnO on GaP samples. Fig. 1 shows surface morphology of both, ZnO on GaP and references sample, obtained by JEOL JSM-IT200 scanning electron microscope. It is clearly seen, that for both samples the surface has a pronounced scaly structure, but the scale size for ZnO on Si layer is more homogeneous.
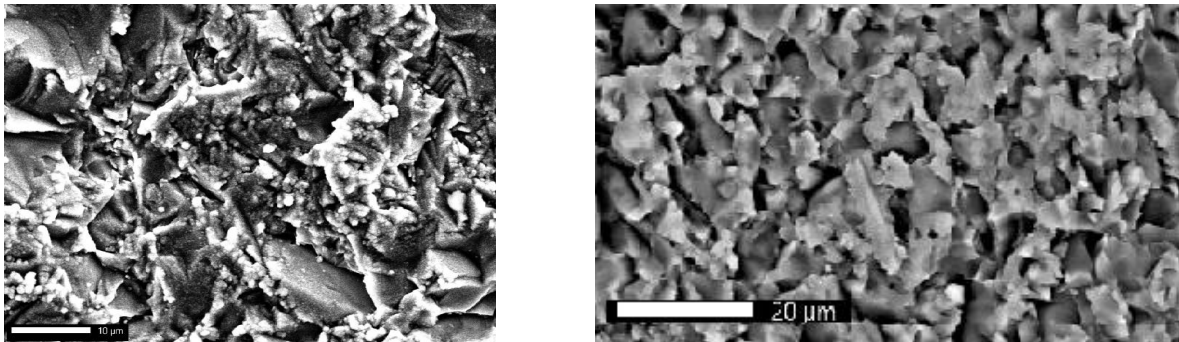
Fig. 1. Surface morphology ZnO on GaP (left side) and ZnO on Si (right side)
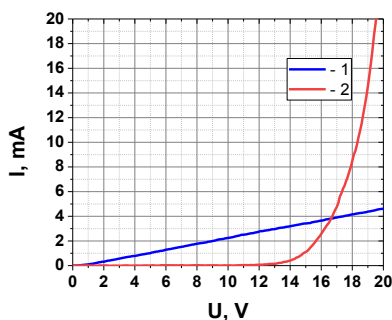
Fig. 2. Conductivity of ZnO on Si (1) and ZnO on GaP (2) layers

Fig. 2 shows the data of resistance measurements of ZnO on GaP and ZnO on Si layers that was performed in the dark at room temperature. One can note, that dependence of I vs V for ZnO on Si layer almost linear and their conductivity obeyed to Ohm law, whereas conductivity of ZnO on GaP layer are strongly depended on bias voltage. More detail investigation reviles that conductivity of ZnO on GaP determined by space charge limited current.

Finaly our investigation demonstrate, that both, structure and conductivity of ZnO layers depend on the type of semiconductor substrates. In more homogeneous ZnO on Si layers current is determined by intrinsic carriers concentration, whereas conductivity of ZnO on GaP can be attributed to the insulating type and is determined by the injection of charge carriers into the volume of the ZnO layer.

USING COMSOL MULTIPHYSICS TO STUDY THE EFFECT OF MOSFET GATE DIELECTRIC THICKNESS AND EXTERNAL TEMPERATURE ON ITS OUTPUT CHARACTERISTICS

Rajapov D., Khasanov A., Khaitbayev E., Khalilloev M.

14, KH.ALIMDJAN STR, URGENCH CITY, 220100, UZBEKISTAN
dilshodbekrajapov5@gmail.com

Abstract: In this article, the dependence of the output characteristics on the dielectric thickness and external temperature in a 3D junctionless MOSFET is studied using Comsol Multiphysics software. The effect of dielectric thicknesses on the output characteristics of the MOSFET surrounded by the gate was examined in three different values. To study the effect of the external temperature under test on the output characteristics of the transistor, the output characteristics at temperatures of 250K, 300K, and 350K were measured and analyzed.

Keywords: MOSFET, Comsol Multiphysics, temperature, dielectric, doping

I.   Introduction: Currently, to increase the level of integration and reduce energy consumption, the sizes of insulated gate field transistors (MOSFET) are getting smaller and smaller. To reduce these sizes, it is necessary to reduce the thickness of the dielectric as much as possible. But if the thickness of the dielectric becomes much smaller than the norm, the output characteristics of the transistor can change a lot[1]. In addition, as the size decreases, self-heating effects appear in MOSFETs, which depends on the thermal conductivity of the dielectric [2]. Therefore, we increase the thickness of the dielectric from 0.5 nm, 1.5 nm, and 3nm. The dependence of the obtained results on the external temperature was studied at three different temperatures and the results were analyzed.

II.   Structure and simulation procedure: COMSOl Multiphysics 6.1 software was used for modeling. In this case, if silicon was selected as the semiconductor material of the channel, the dielectric blank material was formed. In the modeling, the channel length of the transistor was 34 nm, and the gate length was 4 nm, the channel surface was square and its sides were 3.2 nm. An inlet concentration of 10^{20} ($\frac{1}{cm^{-3}}$) of type n was introduced into the channel. The gate voltage of the transistor is 0.8 V, the drain is 0.05 V, and the source is 0 V. The metalwork function on each contact is equal to 4.5 eV[3]. When meshing the model, the same mapped mesh was used for the Drain and Source contacts, and the Sweep mesh was used for the channel. Other parameters are listed in the table below.

T0	300[K]	Temperature
fmx	0.8	"Longitudal DG effective mass"
fmy	0.12	Transverse DG effective mass
mx	fmx*me_const	Longitudinal DG effective mass
my	fmy*me_const	Transverse DG effective mass
mz	my	Transverse DG effective mass
epsOx	3.9	Oxide dielectric constant
mox	0.5*me_const	Oxide DG effective mass
moxstar	0.22*me_const	Oxide DG effective
PhiBox	3.15[V]	Oxide potential barrier
Nd	1e20[cm^-3]	Doping
cp	1	Continuation parameter for doping
Phig	4.5[V]	Gate metal work funktion

(1-table)

III.   Simulation results and discussion: The output characteristics of the transistor are also highly dependent on the temperature of the medium in which it is placed. The following is the result of the simulation carried out to study this relationship.
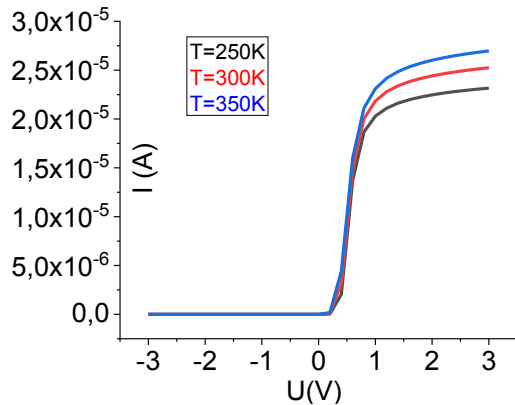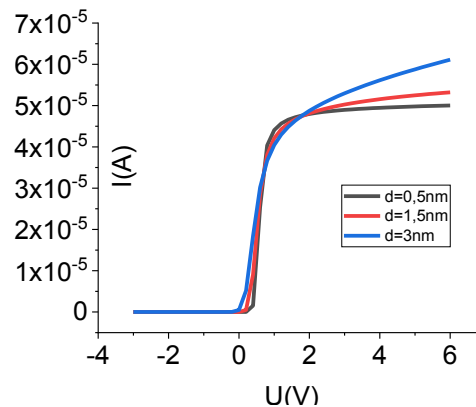
1-Figure   2-Figure

We have learned that when the gate voltage approaches 0.8 V, a large change occurs in the drain current, and this difference increases with increasing voltage until saturation[4](Figure-1).

If we change the thickness of the dielectric, we can observe the change in the output characteristic of the transistor as shown in Figure (2). That is, if the thickness of the dielectric is large, the saturation current will be much larger and will increase as the voltage increases[5]. If the thickness of the dielectric is small if it happens, the saturation current will be smaller and it will be fully saturated even at a lower voltage.

IV.   Conclusions: The modeling results show that if we place the MOSFET in a high-temperature environment, the current passing through it increases, and the current in its output characteristic shifts upwards. If we increase the thickness of the dielectric wrapped in the outer layer, the gate voltage remains unchanged. As the stock and supply voltage increase, the current increases faster.

REFERENCES

[1]. Jiahao Kang, Wei Liu, and Kaustav Banerjee. Appl. Phys. Lett. High-performance MoS2 transistors with low-resistance molybdenum contacts. (2014) 104, pp. 093106 – 1–5.
[2]. Zhansong Geng. Simulation von Grafen-Nanoribbon-und MoS_2 Tranzistoren. Masterarbeit. TU Ilmenau, 2016, pp. 3–84.
[3]. Radisavljevic, B.; Radenovic, A.; Brivio, J.; Giacometti, V.; Kis, A. Single-Layer MoS_2 Tranzistors. *Nat. Nanotechnol.* **2011**, *6*, 147–150.
[4]. Geng, Z. Simulation of Graphen Nanoribbon and MoS_2 Tranzistors. Master's Thesis, TU Ilmenau, Ilmenau, Germany, 2016; pp. 3–17. (In German)
[5]. Liu, H.; Neal, A.T.; Ye, P.D. Channel Length Scaling of MoS_2 MOSFETs. *ACS Nano* **2012**, *6*, 8563–8569. https://doi.org/10.1021/nn303513c.

EFFECT OF PROTON IRRADIATION ON THE PROPERTIES OF n-Si<Pt> SAMPLES

Sh.B. Utamuradova, D.A. Rakhmanov, A.B. Uteniyazova

Institute of Semiconductor Physics and Microelectronics at the National University of Uzbekistan,
20 Yangi Almazar st., Tashkent, 100057, Uzbekistan
e-mail: dilmurod-1991@bk.ru

Modification of semiconductor materials by beams of light ions, in particular protons, is one of the most promising and actively developing physical and technological methods in recent years. Interest in the implantation of silicon crystals by protons is due to a wide and controllable range of processed depths (from 0.1 μm to 1 mm) and the absence of complex radiation complexes with a high annealing temperature after irradiation. The main three factors affecting the change in the properties of semiconductors after proton irradiation are: a change in the electrical properties of semiconductors, radiation defect formation, and accumulation of hydrogen atoms[1].

The aim of this work is to study the effect of radiation to protons on the change in the concentration of optically active oxygen in n-type silicon single crystals doped with platinum (n-Si<Pt>) and to study radiation defect formation after irradiation with hydrogen ions using IR spectroscopy.

The object under study was n-type silicon (n-Si) with a resistivity of 40 Ω cm grown by the Czochralski method. Doping of silicon with platinum was carried out by the diffusion method with deposition of platinum atoms on the silicon surface in evacuated quartz ampoules at temperatures T = 900÷1250 °C for 2÷5 hours. The original (n-Si) and doped (n-Si<Pt>) samples after polishing with diamond paste were irradiated with protons with an energy of 2 MeV, at a current of 0.5 μA, using an electrostatic accelerator "EG-5". The dose rate was 5.1×10^{14} cm^{-2}. The concentration of optically active oxygen and radiation defect formation in silicon samples was determined using an IR spectrometer "Shimadzu IR Affinity-1" in the range of 600 - 3000 cm^{-1} in transmission mode.

Fig.1 shows the IR spectra of single-crystal n-type Si before (curve 1) and after (curve 2) doping with Pt and proton irradiation (curves 3 and 4, respectively). As can be seen from Fig. 1, in all cases, the IR spectra contain peaks in the region of 1280, 1106, 950, 885, 820 and 740 cm^{-1}.

According to[2] , the peaks present in the spectra correspond to different types of chemical bonds: the peak at 1280 cm^{-1} corresponds to the Si-O bond, the peaks at 1106 cm^{-1} and 970 cm^{-1} correspond to the Si-O-Si bonds, the peak at 885 cm^{-1} corresponds to the Si-OH, peak 820 cm^{-1} - silica bond SiO_2 and peak 740 cm^{-1} - metasilicate bond (SiO_3). The peak at the wave number 2360 cm^{-1} corresponds to the C-C bond.

Comparison of the IR absorption spectra of the control and doped samples shows that the introduction of platinum atoms through diffusion leads to a significant decrease (2 times in some samples) in the oxygen concentration. This effect is probably due to the interaction of platinum and oxygen atoms in silicon and confirms the data of various authors on the aggregation of impurity atoms with oxygen.

Irradiation of the original and doped samples with protons leads to an increase in the intensity of the peaks at 1106 cm^{-1} and 885 cm^{-1}. A comparison of the IR absorption spectra of unirradiated and irradiated n-Si<Pt> samples shows that the implantation of hydrogen ions in silicon after irradiation leads to a significant increase in the concentration of optically active oxygen N_O^{opt}. New peaks appear on the IR spectra of the irradiated samples at 1450 cm^{-1}, 1730 cm^{-1} and 2912 cm^{-1} (fig.1), corresponding to the C-O bonds (1450 cm^{-1}, 1730 cm^{-1}) and C- H (2912 cm^{-1}) [3].

The main and most significant changes in the properties of proton-irradiated silicon are radiation defects, the structure of which includes vacancies. These radiation defects include, first of all, the complex interstitial oxygen O_i – V vacancy (A-center), Divacancy (V-V) and the phosphorus complex at the P_S site – vacancy (E-center). In irradiated silicon with a high concentration of oxygen and carbon, the K center is more thermally stable than the E center. This point radiation defect is a complex consisting of an interstitial oxygen atom and an interstitial

110

carbon atom (O_i-C_i). The K-center corresponds to the donor level $E_V + 0.36$ eV near the bottom of the silicon band gap, which has a relatively large charge carrier capture cross section.
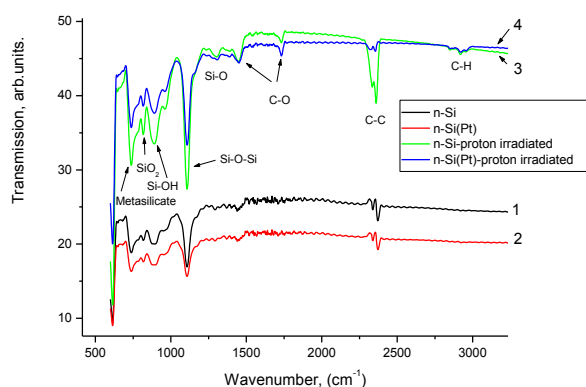
Figure 1. IR spectra of single-crystal n-type Si before (curve 1) and after (curve 2) Pt doping and proton irradiation (curves 3 and 4, respectively).
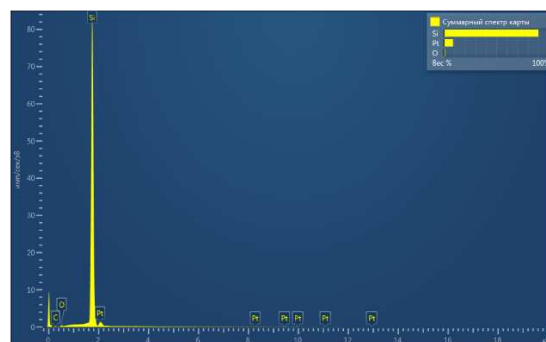
Figure 2. Energy-dispersive spectra of silicon samples doped with platinum.

Relatively close to the A center in the band gap of silicon is the level of the radiation defect, which is a complex of the interstitial carbon atom C_i and the carbon atom at the C_S site. This radiation defect is usually observed in crystals with a relatively low dissolved oxygen concentration and a high C_S concentration, when the C_S carbon atoms themselves become the main traps for C_i atoms. Similar effects with the parameters of the C_i-C_S center are exhibited by the C_i-Si-C_S defects observed in silicon irradiated with protons[4].

The presence of platinum in single crystals is confirmed by X-ray spectral microanalysis, according to which the content of platinum in the samples is 2 at.% or 12 wt.%. The energy dispersive spectra (Fig. 2) indicate the presence in the composition of the studied samples, in addition to platinum atoms, of oxygen and carbon atoms. The content of oxygen atoms in the samples is 0.85 at.% or 1.2 wt.%, carbon atoms 0.7 at.%, respectively.

The irradiation of n-Si and n-Si<Pt> samples with protons, synthesized in this work by protons with an energy of 2 MeV with a dose rate of 5.1×10^{14} cm^{-2}, leads to the formation of radiation defects of the type O_i-C_i, C_i-C_S. Radiation defects characteristic of silicon (proton irradiation) such as the A-center, divacancies, and E-centers could not be explicitly detected by IR spectroscopy.

References

1. Kozlov V.A., Kozlovskiy V.V(2001). Semiconductors. volume 35, issue 7.
2. Utamuradova Sh. B., Stanchik A. V., Rakhmanov D.A., Doroshkevich A.S., Fayzullaev K.M(2022). New materials, compounds and applications., Vol.6, №3. Pp.214-219.
3. Feifel S.C, Lisdat F(2011). Journal of Nanobiotechnology, 9:59.
4. Paulescu M., Vizman D., Lascu M., Negrila R., Stef1 M(2019). Physics Conference AIP Conf. Proc. 1796, 040010-1–040010-4.

EXPERIMENTAL AND THEORETICAL INVESTIGATION OF THE IMPACT OF Fe IMPURITY DOPING AND ITS CONCENTRATION ON THE ELECTRONIC STRUCTURE AND PHOTOCATALYTIC ACTIVITY OF ZnO NANOSTRUCTURES

A. Esbergenova[1,2], Sh. Mamatkulov[3], O. Ruzimuradov[4] and U. Shaislamov [1,2*]

[1]Center for Development of Nanotechnology at the National University of Uzbekistan, University str. 4, 100174 Tashkent, Uzbekistan
[2]Department of Physics, National University of Uzbekistan, Tashkent, Uzbekistan, University str. 4, 100174 Tashkent, Uzbekistan
[3]Institute of Material Sciences of the Academy of Sciences of the Republic of Uzbekistan, Chingiz Aytmatov 2b, 100084 Tashkent, Uzbekistan
[4]Department of Natural and Mathematic Sciences, Turin Polytechnic University in Tashkent, Kichik Halqa Yo'li 17, 100095 Tashkent, Uzbekistan
*e-mail: sulugbek@gmail.com (corresponding author)

Solar energy conversion through photocatalysts technology has become one of the most promising methods in effectively utilizing the renewable and sustainable energy, thereby solving serious environmental and energy problems. Successful implementation of this technology allows production of green hydrogen, conversion of CO_2 into hydrocarbon fuels, water and air purification, etc. Yet, photocatalysis is a complex process that requires highly efficient photocatalyst material combining such properties as suitable band-edge alignment, visible light activity, stability, cost effectiveness and non-toxicity [1].

In this work we investigate effect of the Fe impurity doping and its concentration on the microstructural, morphological, optoelectronic properties, and photocatalytic activity of ZnO nanostructures synthesized by a hydrothermal method. Density functional theory (DFT) calculation was employed to understanding the impact of Fe doping content on the band structure of ZnO.

Figure 1 shows DFT calculated band structure of the ZnO and Fe doped ZnO. Enhanced photocatalytic activity of the Fe doped ZnO was attributed to the as formed shallow donor levels of Fe d orbital below conduction band minimum of the ZnO. Among the different concentrations of Fe dopant, 1% doped ZnO demonstrated highest photocatalytic activity under the visible light illumination.
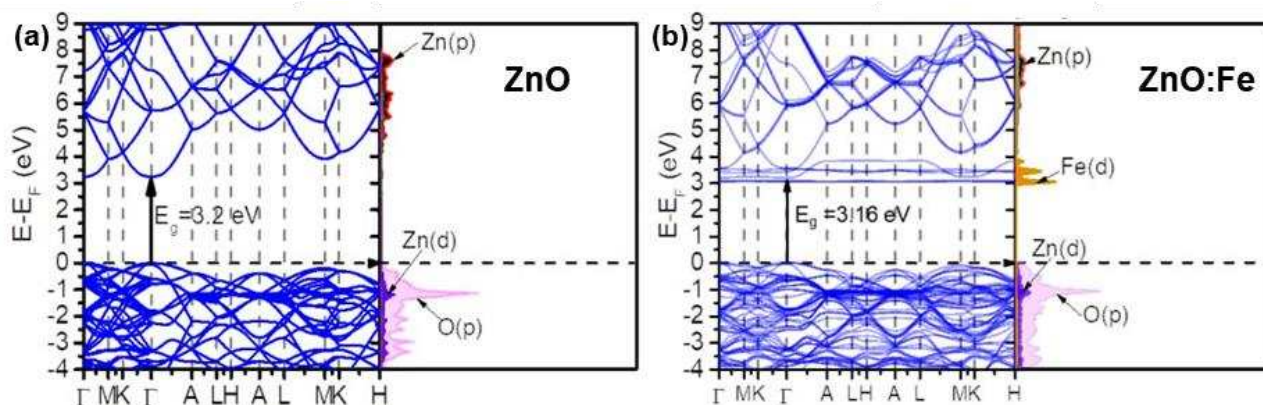
Figure 1. DFT calculated band structure and (PDOS) partial density of states of the (a) pure ZnO and (b) Fe doped ZnO.

Reference

[1] Q. Wang, K. Domen. *Chem. Rev*., 2020, 120(2), 919985

SYNTHESIS AND CHARACTERIZATION OF THE TiO_2 NANOSTRUCTURES FOR ENERGY CONVERSION AND STORAGE DEVICES

U. Shaislamov [1,2], B. Rasulov[2]

[1]Center for Development of Nanotechnology at the National University of Uzbekistan, University str. 4, 100174 Tashkent, Uzbekistan
[2]Department of Physics, National University of Uzbekistan, Tashkent, Uzbekistan, University str. 4, 100174 Tashkent, Uzbekistan
e-mail: sulugbek@gmail.com (corresponding author)

The growing global demand for energy and the limited availability of fossil fuels has has prompted the development of alternative and renewable energy resources. Among these, the effective conversion and storage of solar energy stand out as a promising technology for achieving clean and sustainable energy solutions. While photovoltaics is widely acknowledged as a dependable solar conversion technology, their widespread adoption is hindered by cost considerations and long-term operational challenges. Especially, reliable operation during night-time necessitates high efficiency and durable energy storage devices (such as Li-ion batteries).

Moreover, the effective conversion and storage of solar energy for various applications, such as hydrogen generation, CO_2 conversion, and water/air purification, can be accomplished through photocatalyst technology [1]. Consequently, there is a growing research interest in the development and design of advanced materials that are both suitable and highly efficient for energy storage devices and photocatalysis applications.

TiO_2 is considered as an excellent photocatalyst material due to its suitable band edge position, non-toxicity and stability. Beyond its applications in photocatalysis, the notable high conductivity and stability of TiO_2 make it a valuable candidate for use in lithium-ion batteries. Especially, it can further extend energy density and longevity of the micro/nano sized Si based electrodes for Li-ion batteries. A suitable design of the Si/TiO_2 composite electrode can solve inherent challenges associated with Si-based electrodes, such as cracking and large volume expansion during lithiation cycles [2].

This work presents synthesis and characterization of the TiO_2 nanostructures using hydrothermal synthesis method. Figure 1 shows XRD patterns of the TiO_2 nanostructures.
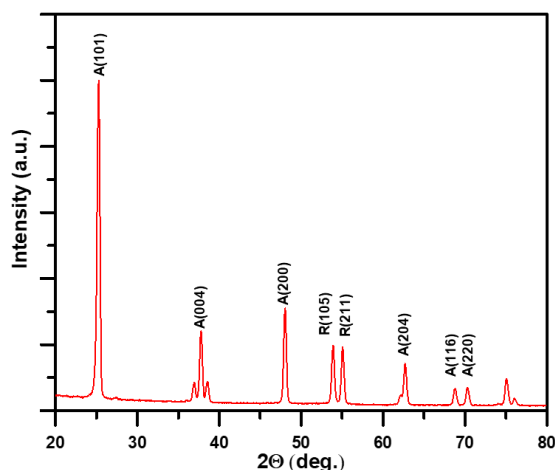
Figure 1. XRD pattern of the TiO_2 nanostructures.

Reference

[1] Q. Wang, K. Domen. *Chem. Rev*., 2020, 120(2), 919985
[2] M. Ko, S. Chae, J. Ma, et al., *Nature Energy*, 2016, 1(9): 16113.

SOLAR-PUMPED THREE-CORE FIBER LASER WITH PARABOLIC TROUGH

A.G. Qakhkhorov, A.A. Sherniyozov, Sh.D. Payziyev

Institute of Ion-plasma and laser technologies AN RUz, Durmon yuli str. 33, 100125, Tashkent, Uzbekistan
114bdulla.gafurovich@gmail.com

In recent years, the conversion of broadband solar radiation into coherent narrow-band laser light has attracted the attention of solar laser researchers. Several types of crystals (Nd:YAG, Ce:Nd:YAG) are used for solar lasers. But recently, scientific works focused on the use of optical fibers as an active medium began to appear [1]. Interest in solar fiber lasers stems from the fact that they may offer advantages such as reduced thermal effects and simple optical cavity design. Since the first solar fiber laser was proposed in 1997, significant improvements have been made in solar-pumped fiber lasers. Transverse solar-pumped fiber lasers are expected to be a better alternative to the above active media. Recently, solar-pumped Nd^{3+}-doped silica fiber lasers have been studied. However, the search for optimal configurations of fiber lasers with high-efficiency is still ongoing. In this work, a parabolic trough concentrator with a length of 30 cm, a width of 23.56 cm and a focal length of 35 cm is considered (Fig 1). In order to evaluate the parameters and study their effect on the overall efficiency, a model of solar-pumped fiber lasers was developed using Monte Carlo photon tracing method [2]. A total of 70.7 W of solar power falls on the surface of this concentrator.
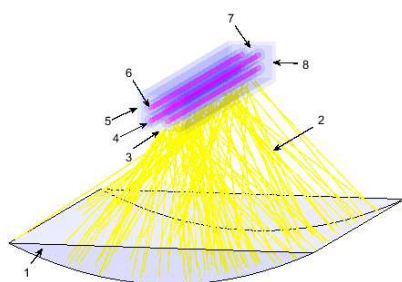
Fig. 1. Overview of the laser system. 1-parabolic-trough, 2-solar light, 3-silica, 4-fiber cladding, 5-left side, 6-fiber core, 7-upper side, 8-right side.
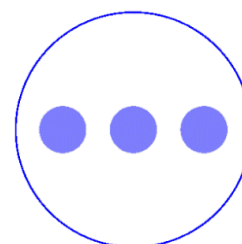
Fig. 2. A cross-section of a silica fiber.

A 28.75 m long three-core optical fiber is placed at the focus of the concentrator as an active medium. A cross-section of a silica fiber is shown in Fig 2. Cladding diameter of 1 mm, core diameter of 200 μm, Nd^{3+}-doped silica fiber is placed inside a parallelepiped-shaped chamber with a width of 2.6 cm and a height of 0.4 cm. In this 3-core fiber, one core is in the center of the cladding, and the other two cores are located 300 μm from the cladding (the distance between the edges of the cores is 100 μm).In the model, the total fiber length is obtained in the form of a row and a column of cylinders. It consists of 3 rows and 25 columns, with a total of 75 cylinders. Absorption efficiency, laser output power and power distribution were calculated using the model. In conclusion, it can be said that the absorption efficiency of the active medium was 9.62%, the absorbed power was equal to 6.8 W. The output power of the laser was 125 mW, and the conversion efficiency from solar radiation to laser beam was 0.18%.

References

1. T. Masuda, M. Iyoda, Y. Yasumatsu, S. Dottermusch, I.A. Howard, B.S. Richards, J.F. Bisson, M. Endo, A fully planar solar pumped laser based on a luminescent solar collector, Commun. Phys. 3 (1) (2020) 60.
2. Sherniyozov A. A., Payziyev Sh. D., "Simulating optical processes: Monte Carlo photon tracing method", Uzbek Journal of Physics, 24(3),157-162. (2022), doi.org/10.52304/.v24i3.357.

COMPUTER MODELING OF C$_{60}$ FULLERENE MOLECULE ADSORPTION ON RECONSTRUCTED DEFECTIVE Si(100) SURFACE

Urolov I[1]., Yadgarov I.[1]

[1]*Institute of Ion-Plasma and Laser Technologies, 33, Do'rmon yo'li Street, 100125 Tashkent, Uzbekistan*
fizik25@mail.ru

Today, calculating the adsorption energy and the length of Si-C bonds of fullerene molecules adsorbed on the surface of silicon monocrystal is one of the most relevant researches in terms of the fact that fullerene-coated surfaces have a promising applied character. In particular, in the presence of defects on the reconstructed Si(100) surface, the adsorption energy of the fullerene molecule and the length of the Si-C bonds become stable due to their high practical importance in the development of molecular devices suitable for semiconductor devices, leading to the intensive development of theoretical research in this field, brought [1].

In this study, the adsorption of C60 fullerene molecule on the reconstructed defective Si(100) surface was studied. Interaction processes between the defective Si(100) surface and C60 were studied using the LAMMPS open package program based on the molecular dynamics (MD) method. Tersoff interatomic potential was used to express the interaction potential energy of Si-Si, Si-C and C-C bonds [2]. The adsorption energy was calculated using the following formula [3]:

$$E_{ads} = E_{ads/sub}^{tot} - (E_{sub}^{tot} + E_{ads}^{tot}).$$
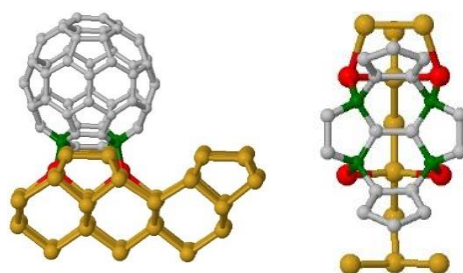
Figure 1. Side and top views of the C60 molecule adsorbed on a reconstructed defective Si(100) surface.

Figure 1 shows the adsorption state of C60 molecule with the hexagon+hexagon configuration on the reconstructed defective silicon surface. In this configuration, the adsorption energy was equal to $E_{ads} = -5.197$ eV, the length of Si-C bonds was equal to $1.92 - 1.99$ Å. Almost no change was observed in the Si-Si bond lengths of the silicon atoms participating in the Si-C bond. It was found that the adsorption energy of C60 molecule on the D2 defect area, which consists of the absence of two side-by-side dimers in the dimer row on the reconstituted Si(100) surface, is significantly higher than the adsorption energies to other types of defect areas. The high energy values can be explained by the increase in the number of bonds that can form bonds with silicon atoms in the secondary layer on the silicon surface of the C60 molecule and the shortness of these bonds compared to the Si-C bonds in the upper layer.

Reference

1. L. Jing, C. Yang, Z. Lin, Arabian Journal of Chemistry, 16, (2023) 104816.
2. P. Erhart and K. Albe, Physical Review B, 71, 035211-1-14, (2005)
3. Y. S. Al-Hamdani, and others, The Journal of Chemical Physics, 144, (2016) 154706

FACTORS OF STABILITY OF CsPbBr3 PEROVSKITE FILMS WITH NANOCRYSTALS

R.R. Kabulov, A. Kutlimratov, M.U. Khazhiev, L.U.Shuxratova

Physical-technical Institute of the Academy of Sciences of the Republic of Uzbekistan, Chingiz Aytmatov street 2B, 100084, Tashkent, Uzbekistan.
e-mail: krr1982@bk.ru

Perovskites of the CsPbX3 type (X-halide anion) are new semiconductor materials that have recently been intensively studied throughout the world [1, 2]. They have unique properties necessary for optoelectronics and photo energy [3-6]. Cesium-lead halide films based on quantum dots have high brightness and a narrow line width and it is possible to select the required color of radiation in the visible range [7]. Thanks to compositional modulations and quantum size effects, band gap energies and emission spectra are easily tuned throughout the visible spectral region 410–700 nm [3]. The photoluminescence of CsPbX3 nanocrystals is characterized by a narrow emission linewidth of 12-42 nm and a wide color gamut, covering up to 140% of the NTSC (National Television System Committee) color standard. The quantum efficiency reaches values of up to 90%, with radiation lifetimes in the range of 1-29 ns [3].

However, despite the excellent optoelectronic properties of CsPbBr3, obtaining structures with high quantum yield and stability under ambient conditions are key issues that require significant attention [7]. Because the impurities used to achieve high luminescence have highly dynamic binding and impair the stability, and therefore the luminescent properties of structures based on them, this limits their widespread use. The authors of [7] claim that to ensure the stability of quantum dots (QDs) based on CsPbBr3 perovskite, oleic acid (OA) and oleylamine (OAm) ligands are used, which play an important role in colloidal support of the integrity of the QD surface. According to the authors of [8], by introducing organic phosphine ligands, the resistance of CsPbBr3 QDs to ethanol, water, and ultraviolet radiation can be significantly improved. Moreover, perovskite films modified with phosphine ligands deposited on glass exhibit high photoluminescence intensity and optical stability compared to films based on pure perovskites.

CsPbX3 layers are known to crystallize in orthorhombic, tetragonal and cubic perovskite lattice polymorphs, with the cubic phase being the high temperature state for all compounds. Interestingly, all colloidally synthesized (NCS) CsPbX3 nanocrystals crystallize in the cubic phase, which can be explained by the combined effect of high synthesis temperature and the contribution of surface energy [3]. The authors of [5] claim that by using controlled anion exchange reactions using a number of different halide precursors, it is possible to precisely tune the chemical composition and optical properties of synthesized cesium-lead halide perovskite colloidal nanocrystals, from CsPbBr3 with green emission to bright emitters in any other region of the visible spectrum and vice versa, by displacing Cl– or I– ions with oxygen ions, as well as by re-introducing Br- ions. This approach provides access to perovskite-based semiconductor nanocrystals with both structural and optical properties comparable to those of directly synthesized nanocrystals. It is also noted that when mixing solutions containing perovskite NCSs emitting in different spectral ranges (due to different compositions of halides), the dynamics of their mutual rapid exchange leads to homogenization of their composition, as a result of which NC emit in a narrow spectral region, intermediate between the original nanoparticles [5].

In general, the resistance to defects in perovskite nanocrystals is due to three distinctive features: their crystal structure, which favors the formation of vacancies but does not contain other point defects; their special electronic structure, which makes vacancies harmless; and their dynamic lattice effects, such as the formation of polarons that prevent carrier capture [9].

The surface morphology and defect density of MHPe play a crucial role in their optical and electronic properties [10]. By controlling surface morphologies and minimizing defect densities, the efficiency and stability of MNR-based structures can be increased. Evidence was provided in [11] that doping the B (Pb) site, especially with Sr2+, can significantly improve the optoelectronic

properties of CsPbX3 (X = Br, Cl). Replacing Pu with Mn2+ in combination with doping with Sr2+ can improve the light output of the structure. This improvement in performance is explained by a decrease in the density of defects and a decrease in microstresses in the local structure of the perovskite. Such results open a promising path to further improve the optoelectronic properties of perovskites.

References

1. Матюшкин Л. Б., Мошников В.А. Фотолюминесценция нанокристаллов перовскитов CsPbY(Y = Cl, Br, I) и твердых растворов на их основе. <u>Физика и техника полупроводников</u>, Выпуск №10, 2017, Том 51. –С. стр. 1387-1392. https://doi.org/10.21883/FTP.2017.10.45018.8575.

2. Гулевич Д.Г., Ткач А.А., Набиев И.Р., Кривенков В.А., Самохвалов П.С. Изменение люминесценции тонких нанокристаллических пленок перовскита $CsPbBr_3$ в ходе реакции анионного обмена *in s itu*. // Журнал технической физики, 2023, том 93, вып. 2. –С. 256-263.

3. Protesescu, L.; Yakunin, S.; Bodnarchuk, M. I.; Krieg, F.; Caputo, R.; Hendon, C. H.; Yang, R. X.; Walsh, A.; Kovalenko, M. V. Nanocrystals of cesium lead halide perovskites ($CsPbX_3$, X = Cl, Br, and I): Novel optoelectronic materials showing bright emission with wide color gamut. // Nano Lett. 2015, 15, 3692–3696. https://doi.org/10.1021/nl5048779

4. Wang, Y.; Li, X. M.; Song, J. Z.; Xiao, L.; Zeng, H. B.; Sun, H. D. Allinorganic colloidal perovskite quantum dots: A new class of lasing materials with favorable characteristics. Adv. Mater. 2015, 27, 7101–7108. https://doi.org/10.1002/adma.201503573

5. Akkerman, Q. A.; D–Innocenzo, V.; Accornero, S.; Scarpellini, A.; Petrozza, A.; Prato, M.; Manna, L. Tuning the optical properties of cesium lead halide perovskite nanocrystals by anion exchange reactions. J. Am. Chem. Soc. 2015, 137, 10276–10281. https://doi.org/10.1021/jacs.5b05602

6. Swarnkar, A.; Marshall, A. R.; Sanehira, E. M.; Chernomordik, B. D.; Moore, D. T.; Christians, J. A.; Chakrabarti, T.; Luther, J. M. Quantum dot–induced phase stabilization of α-CsPbI3 perovskite for high-efficiency photovoltaics. Science 2016, 354, 92–95. https://doi.org/10.1126/science.aag2700

7. Xiaoxia Feng, Jinli Liu, Xiyue Zhao, Pengxiao Xu, Jiacheng Liu. Surface regulation by bifunctional BODIPY to fabricate stable $CsPbBr_3$ for multi-layered optical anti-counterfeiting. Journal of Colloid and Interface Science. Volume 629, Part A, January 2023, Pages 63-72. https://doi.org/10.1016/j.jcis.2022.08.129

7. Xiaoxia Feng, Jinli Liu, Xiyue Zhao, Pengxiao Xu, Jiacheng Liu. Surface regulation by bifunctional BODIPY to fabricate stable $CsPbBr_3$ for multi-layered optical anti-counterfeiting. Journal of Colloid and Interface Science. Volume 629, Part A, January 2023, Pages 63-72. https://doi.org/10.1016/j.jcis.2022.08.129

8. Yan Li, Xiaoyang Wang, Weinan Xue, Wei Wang, Wei Zhu, Lianjing Zhao. Highly luminescent and stable $CsPbBr_3$ perovskite quantum dots modified by phosphine ligands. // Nano Research, 2019, № 4, p. 785-789. https://doi.org/10.1007/s12274-019-2289-8

9. Akkerman, Q. A.; Rainò, G.; Kovalenko, M. V.; Manna L. Genesis, challenges and opportunities for colloidal lead halide perovskite nanocrystals. Nat. Mater. 2018, 17, 394–405. https://doi.org/10.1038/s41563-018-0018-4

10. Y.H. Kim, J.S. Kim, T.W. Lee, Strategies to improve luminescence efficiency of metal-halide perovskites and light-emitting diodes, Adv. Mater. 31 (2019), 1804595.

11. H. Yuce, M. Mandal, Y. Yalcinkaya, D. Andrienko, M.M. Demir, Improvement of photophysical properties of CsPbBr3 and Mn2+: CsPb(Br, Cl)3 perovskite nanocrystals by Sr2+ doping for white light-emitting diodes, J. Phys. Chem. C 126 (2022) 11277–11284.

PHOTOLUMINESCENCE OF NANOSTRUCTURED POROUS SILICON

Kh.B. Ashurov, T.K. Turdaliev*

Arifov Institute of Ion-Plasma and Laser Technologies of Uzbekistan Academy of Sciences, Durmon yuli st. 33, Tashkent, Uzbekistan,
e-mail: turdaliev@iplt.uz

Porous silicon (PS), owing to its unique physical properties arising from a nanoscale structure unattainable in bulk materials, holds significant promise for various applications in science and technology. There are several methods for obtaining PS, and the number of instances of its utilization continues to grow [1]. PS can be employed in the creation of sensitive sensors [2], and, as demonstrated in prior studies, PS with nanocrystalline inclusions shows promise in silicon solar cell (SC) technology [3].

In this study, we employed an electrochemical method described in reference [3] to fabricate porous silicon substrates. The crystallinity of the obtained samples and the recording of photoluminescence spectra were conducted using an InVia Raman spectrometer. The photoluminescence effect in PS samples was evaluated using a He-Cd laser with an emission wavelength of 325 nm as the excitation source.

The obtained Raman spectra confirm the absence of amorphous silicon in the samples, as no lines corresponding to the amorphous phase were observed. It can be inferred that the grown samples exhibit a nanocrystalline structure without an amorphous component. Photoluminescence spectra indicate that the samples exhibit stable and intense photoluminescence in the 700-900 nm range with peaks around ~771 nm. This characteristic feature aligns with the typical photoluminescence of nanocrystalline silicon structures [4], associated with radiative recombination in nanoscale silicon crystals. The peaks at 771 nm suggest the absence of defective silicon oxide in their phase composition. The presence of such oxide in the surface layer of PS is known to diminish photoluminescent properties and shift the photoluminescence peak towards the short-wavelength side.
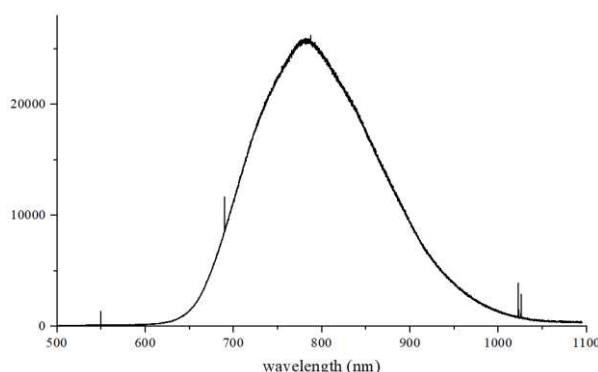
Fig. 1 – Photoluminescence Spectrum of PS Sample

Nanostructured porous silicon samples analysis indicates the formation of layers of nanocrystalline porous silicon, devoid of defective silicon oxide and amorphous silicon. This allows simultaneous utilization of both porous and nanocrystalline silicon properties.

References

[1] Canham, Leigh (Ed.) Handbook of Porous Silicon ISBN 978-3-319-71380-9 (2018)
[2] R.F. Balderas-Valadez, et al, RSC Ad-vances 6(26), 21430. (2016)
[3] T.K. Turdaliev, et al, Applied Solar Energy, Vol. 57, No. 6, (2021)
[4] Y.-J. Jung, et al, Jour-nal of Applied Physics 104(8), 083518 (2008).

THE INFLUENCE OF GRAPHENE DEFECTS ON HYDROGEN STORAGE

U.B. Uljayev[1,2], K.M. Mehmonov[1] and U. Khalilov[1,3]

[1]*Arifov Institute of Ion-Plasma and Laser Technologies, Academy of Sciences of Uzbekistan, Tashkent, 100125, Uzbekistan*
[2]*Tashkent Institute of Textile and Light Industry, 5 Shakhdjakhon Street, Tashkent, 100100, Uzbekistan*
[3]*University of Antwerp, Universiteitsplein 1, 2610, Antwerp, Belgium*
email: utkir.uljayev@iplt.uz

Besides conventional methods, the active investigation of hydrogen storage in carbon nanomaterials, such as graphene, is underway [1]. However, the influence of defects in graphene on hydrogen storage remains unclear. This study focuses on investigating the gravimetric density (wt%) of hydrogen molecules in both pristine and defective graphene using Molecular Dynamics (MD) simulations (Fig. 1*a*). In these simulations, we employed the ReaxFF potential with parameters developed by Zou and colleagues [2] to accurately describe the interactions between atoms in the system. Our preliminary results indicate that the relative mass of H_2 molecules physisorbed around defective graphene (with a maximum concentration of about 3%) is approximately 1.4 times higher compared to its pristine counterpart. Specifically, the gravimetric density of physisorbed H_2 molecules for pristine graphene and graphene structures with defect concentrations of 0.2, 0.5, 0.8, 0.8, 1.9, and 2.9% is 1.56 wt.% and 1.76, 1.88, 2.01, 2.06, 2.08, and 2.12 wt.%, respectively (Fig. 1*b*, red line). This phenomenon can be explained by the appearance of partial charges in graphene, depending on their defect concentrations (Fig. 1*b*, blue line). The results strongly indicate that hydrogen storage can be controlled by tuning the size and concentration of defects in graphene.
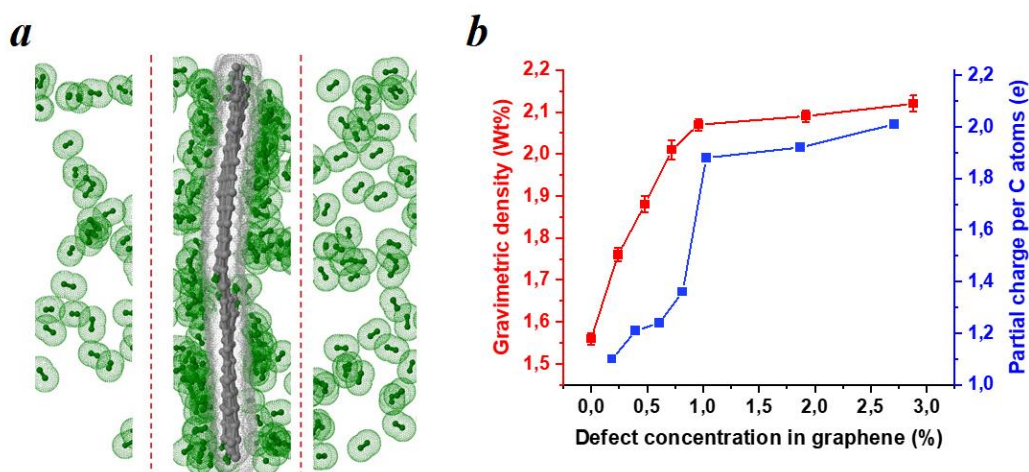
Fig.1. (*a*) H_2 molecules around graphene with a defect concentration of about 3.0%; (*b*) the gravimetric density of hydrogen molecules versus the concentration of defects in graphene.

Literature

1. Shiraz HG et al., Investigation of graphene-based systems for hydrogen storage, *Renew Sustain Energy Rev* 74, 104 (2017).
2. C. Zou et al., Molecular dynamics simulations of the effects of vacancies on nickel self-diffusion, oxygen diffusion and oxidation initiation in nickel, using the ReaxFF reactive force field, *Acta Mater.* 83, 102 (2015).

INFLUENCE OF COMPOSITION AND ANNEALING TEMPERATURE OF ITO FILMS ON THEIR TRANSPARENCY AND RESISTIVITY

A.S. Saidov, Sh.N. Usmonov, A. Kutlimratov, M.U. Khajiev,
D.V. Saparov, Kh.N. Juraev

Physical-Technical Institute Uzbekistan Academy of Sciences Tashkent, Uzbekistan
Hajiev_mardonbek@mail.ru

Conductive transparent indium tin oxide (ITO) films are widely used in various touch screen devices and also in solar cells as current collecting electrodes [1, 2]. There are strict demands on them, both in terms of transparency and current conductivity. Indium tin oxide increases quantum efficiency and reduces photoreflection in the spectral region 310-1048 nm. The enhanced photocurrent is in the spectral peak range around 1033 nm at the edge of the Si band gap. ITO films transmit up to 80-85% of the visible range of light radiation incident on them in the optical range 450-1100 nm [3]. It is known [4] that the ITO material as a semiconductor has a large band gap (E_g ~3.5-3.6 eV), due to which it is transparent in the visible region of the electromagnetic radiation spectrum [1, 3]. However, despite the large band gap, it is a degenerate n-type semiconductor with low resistivity [1, 3].

The change in the resistance of ITO films with increasing concentration of impurity tin atoms does not behave monotonically. At the same time, the work noted that the lowest resistance of ITO was achieved at a SnO_2 concentration of about 10 mol.% and amounted to $3 \cdot 10^{-4}$ $\Omega \cdot$cm. In work [5], at the same doping impurity concentration, a value of $1.77 \cdot 10^{-4}$ $\Omega \cdot$cm was achieved.

There are various methods for producing ITO films, for example, the authors of [3, 6] obtained ITO films by high-frequency magnetron sputtering with simultaneous ion treatment, and in [7] ITO films were obtained by reactive magnetron sputtering. Other researchers prefer to use the sol-gel method to obtain In_2O_3 and SnO_2 films [4]. All these methods require complex and bulky equipment, and the resulting films are small in size; these methods do not allow the production of large-sized ITO films.

Since ITO is a solid solution of indium tin oxide, in which tin atoms replace indium atoms. In order to obtain low resistivity films, the tin oxide (SnO_2) content of the ITO thin film should typically be 6-15 wt.% (4-8 mol.%). If the SnO_2 content in the ITO film exceeds more than 20 wt.% (10.5 mol.%), it is not possible to obtain films with low resistance due to the presence of the SnO_2 phase. It is also not possible to obtain films with low resistance when SnO_2 is less than 5 wt.% (2.8 mol.%) due to the low amount of Sn ions in the solid solution [1].

To obtain ITO films, we used a modified CVD method with a quasi-closed volume, which we presented earlier in [8], where the deposition process of ITO films occurs at normal atmospheric pressure without the participation of a carrier gas. In this method, reagents are applied to the surface of the substrate, where the evaporated molecules of the substances that make up In_2O_3 and SnO_2 thermally decompose and react to synthesize ITO layers consisting of a mixture of In_2O_3 and SnO_2 on the surface of the substrate. The decomposition of the reagents occurs at temperatures above 160 °C and the ITO deposition process is carried out in air, since the deposition product is an oxide, and the oxygen environment does not interfere with the deposition process.

We studied both the electrical and optical properties of the resulting films, the results of which were presented in [8]. As a result of comparing our results with literature data, it was established that the optical properties of transparent conducting oxides are influenced differently by the electron concentration n and their mobility μ [3, 5]. The value of the conduction electron concentration affects the transmittance in both short-wave and long-wave regions. Typically, both of these boundaries shift to shorter wavelengths as n increases. In this case, the change in the transmission edge of an electromagnetic wave of light in the region less than 350 nm (photon energy exceeds the width of the optical band gap) is proportional to $n^{2/3}$ (Burstein-Moss effect), while the transmission edge of a plasma wavelength is proportional to $n^{1/2}$. Mobility μ does not

120

locally affect the short-wavelength transmission cutoff or plasma wavelength. Thus, achieving optimal values of high conductivity and wide bandwidth is possible with a high μ value and a low n value.

Practical application of ITO films requires knowledge of their resistivity. As is known, the resistivity of ITO films depends mainly on the substrate temperature [8], so the dependence of the resistivity of ITO films on the substrate temperature was studied. Hall measurements of the concentration and mobility of the majority charge carriers showed that the observed decrease in ρ with the increasing of the substrate temperature (TS) is mainly due to an increase in the impurity concentration n from $3.9 \cdot 10^{20}$ to $9.1 \cdot 10^{20}$ cm^3. In this case, μ increases from 25 cm^2/(V·s) at T_s = 200 °C to 43 cm^2/(V·s) at T_s = 300°C, and then begins to decrease to 36 cm^2/(V·s) at T_s = 400 °C. Analysis of the obtained results showed that with an increase in the substrate temperature from 170 to 260 °C, a monotonous decrease in resistivity occurs from $6.4 \cdot 10^{-4}$ to $1.9 \cdot 10^{-4}$ Ω·cm. A further increase in the substrate temperature from 400 to 500 °C leads to an increase in resistivity ρ from $1.9 \cdot 10^{-4}$ to $2.9 \cdot 10^{-4}$ Ω·cm, which is associated with a simultaneous decrease in the concentration and mobility of the main charge carriers.

References

1. A. K. Isiyaku, A.H. Ali, S.G. Abdu, M. Tahan, N.A. Raship, A.S. Bakri, N. Nayan. Characterization and Optimization of Transparent and Conductive ITO Films Deposited on n and p-types Silicon Substrates. // *Journal of Theoretical & Applied Physics. / Phys. Memoir* vol. 2, no.1, pp. 15–24, 2020. https://physicsmemoir.online.
2. B Parida, HY Ji, GH Lim, S Park, K. Kim. Enhanced photocurrent of Si solar cell with the inclusion of a transparent indium tin oxide thin film. *J Renew Sustain Energy* vol. 6, no 5, pp.053120, 2014. https://doi.org/10.1063/1.4897656
3. P.N. Krylov, R.M. Zakirova, I.V. Fedotova. Optical properties of ITO films obtained by high-frequency magnetron sputtering with accompanying ion processing. // *Physics and technology of semiconductors*, vol. 47, is. 10, pp. 1421-1424, 2013.
4. Patent No. 201200698 A1 C23C 18/16 (2006.01). Method for producing a transparent conducting film of InSnO. Patrusheva T.N., Snezhko N.Yu., Patrushev V.V. Submission date: 2012.06.04. Published date: 2013.09.30.
5. Untila G.G., Kost T.N., Chebotareva A.B., Timofeev M.A. The influence of tin concentration on the composition, optical and electrical properties of ITO films deposited by ultrasonic spray pyrolysis on silicon and glass // *Physics and semiconductor technology*, 2012. - T. 46, No. 7. - With. 984-990.
6. Nisha M. Growth and characteristion of radio frequency magnetron sputtered indium tin oxide thin films / Ph.D thesis in the field of material science. India – 2006.
7. Balasubramanian N. Subrahmanyam A. Electrical and optical properties of reactively evaporated indium tin oxide (ITO) films dependence on substrate temperature and tin concentration // *Journal of applied physics*,1989. – Vol.22. – p. 206-209.
8. Kutlimuratov A., Zufarov M.A. Kabulov R.R., Khajiev M.U. Morphological, electrophysical and optical properties of ITO films obtained by the modified CVD method. International scientific and technical conference. *Applied Solar Energy*. Vol. 58, No. 4. (2022). (Scopus. Citescore: - 1.3). pp. 497-502.

MECHANISM OF METHANE PLASMA INTERACTION WITH NICKEL SURFACE FOR ETHYLENE PRODUCTION

Khaydarov F.A. [1], Safarov F.M.[1], Khalilov U.B.[1,2]*

[1] *Uz AS, Arifov Institute of Ion-Plasma and Laser Technologies, Uzbekistan*
[2] *PLASMANT Research Group, University of Antwerp, Belgium*
*e-mail: feruzh1987@mail.ru

One of the environmentally friendly technologies - the plasma catalysis method is considered a suitable candidate for the near future in methane reforming, taking into account the absence of emissions of greenhouse gases and the efficiency of energy consumption [1]. Especially, understanding the mechanisms of interaction between the surface of catalysts and methane species in plasma is important in controlling reactions and thereby improving the efficiency of obtaining the desired product, namely, ethylene [2]. Despite the majority of research, these mechanisms have not yet been fully elucidated [3]. In particular, in this simulation-based research, we focused on the analysis of the impact mechanisms of nickel catalysts with different surface facets on the most prevalent radical, methyl radical (CH_3), within methane plasma at a temperature of 1500 K. These simulations were performed using the reactive molecular dynamics (MD) based LAMMPS software package. For accurately representing the interactions between atoms in the simulations, ReaxFF potential parameters developed by Zou et al. were applied [4]. In particular, our results showed that when the CH_3 radical adsorbs on the nickel surface in the case of Ni(111) surface, 37% of the deposited CH_3 radicals do not dissociate, 5% dissociate into CH_2+H, 41% into $CH+H$, and 17% into $C+H$. On the other hand, in the Ni(100) surface case 31% of CH_3 does not dissociate, 4% dissociate into CH_2+H, 42% into $CH+H$, and 23% into $C+H$ (see Fig. 1). These results indicate that the Ni(100) surface exhibits a stronger tendency to dissociate CH_3 radicals owing to its elevated surface energy in comparison to the Ni(111) surface catalyst [6].
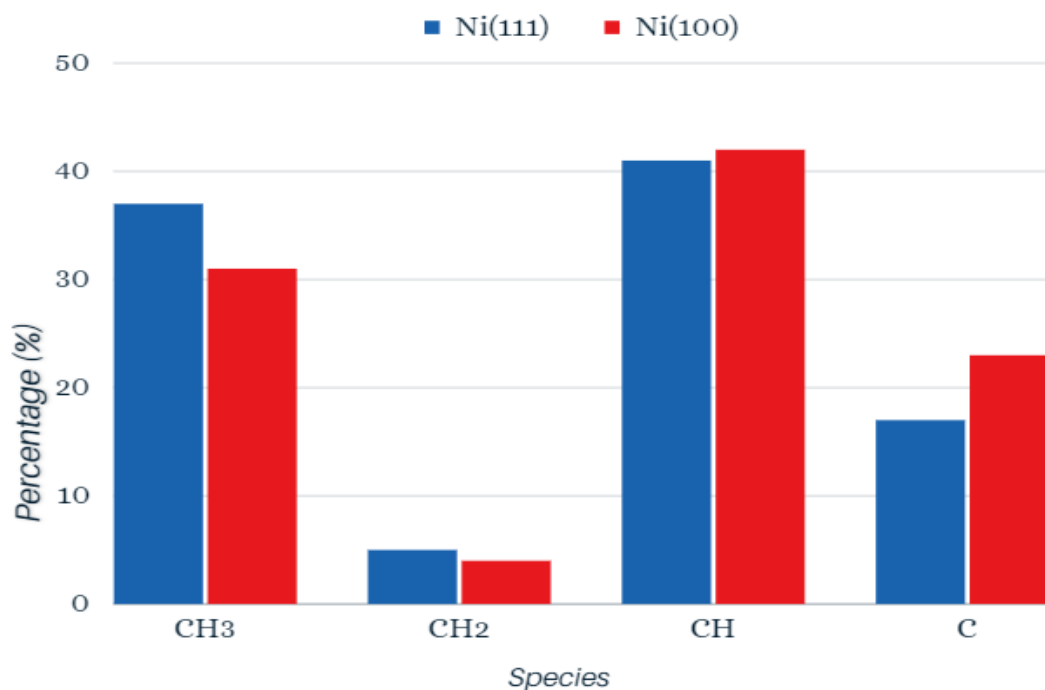
Figure 1. *Percentage distribution of undissociated and dissociated methane species of CH_3 radical on Ni(111) and Ni(100) catalyst surfaces.*

After dissociation, the ethylene formation from methane species is anticipated to occur through reactions such as the following:

$$CH_2 + CH_2 = C_2H_4 \quad (a)$$
$$CH_3 + CH = C_2H_4 \quad (b)$$
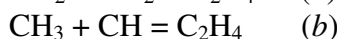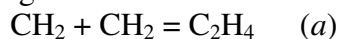
Fig. 1 shows that the formation of CH_2 radicals, which is crucial to the (a) reaction pathway, is deficient quantities for both surfaces. Therefore, attention was given to the abundance and nearness (correlation) of CH and CH_3 species on the surface, which are necessary for the reaction (b). Namely, the figure indicates that the relative abundance of CH_3 (CH) species (i.e., in the least quantity) constituted 37% (41%) and 31% (42%) on the Ni(111) and Ni(100) surfaces, respectively. In summary of these results, it can be concluded that the Ni(111) surface is more advantageous compared to the Ni(100) surface for obtaining ethylene from methane by the plasma catalysis method. These results may serve as a hint for experimentalists in the future.

Literatures

1. J. Feng and et al., Plasma-Assisted Reforming of Methane, *Advanced science*. Vol. 9, 2022, 34
2. E.C. Neyts, Plasma-Surface Interactions in Plasma Catalysis, *Plasma Chem Plasma Process,* 2015
3. E.C. Neyts and et al., Plasma Catalysis: Synergistic Effects at the Nanoscale, *Chem. Rev.* 2015, 115
4. C. Zou et al., Molecular dynamics simulations of the effects of vacancies on nickel self-diffusion, oxygen diffusion and oxidation initiation in nickel, using the ReaxFF reactive force field, *Acta Materialia* Vol 83, 2015, 102
5. J. E. Mueller. Structures, energetics and reactions of hydrocarbons on nickel. PhD dissertation, Pasadena, California, 2010
6. W. Zhang and et al., Equilibrium Crystal Shape of Ni from First Principles, *J. Phys. Chem.* C 2013, 117

BANDGAP OF Si<Zn,S> AND PHOTOCONDUCTIVITY OF Si <S> SAMPLES

Utamuradova Sh.B., A. Sh. Mavlyanov[*], *M.K. Khakkulov*

Institute of Semiconductor Physics and Microelectronics, Tashkent, 100057, Uzbekistan,
*e-mail: microelectronics74@mail.ru

Behavior of sulfur in silicon is characterized by the ionization energy E_i that varies in a large diapason as reported by different authors [1].

The samples of silicon doped with sulfur were investigated under dark conditions in forward connection mode (Fig. 1) and the corresponding photoconductivity spectrum in these samples starts at 0.26 *eV* and increases further to 0.4 *eV*. While reaching the point 0.4 *eV*, the photoconductivity spectrum in dark decreases and its magnitude is less than that of the dark current. Here, we are most likely witnessing what is known as negative photoconductivity while there happens to occur the effect of carrier injection associated with the 0.4 *eV* level. Under constant illumination, the photoconductivity starts at $E_i \approx 0.25$ *eV* and decreases within the 0.4 *eV* range with a sharp downward slope peak at E ≈ 0.52 *eV*, where the phenomenon of infrared quenching of photoconductivity occurs.
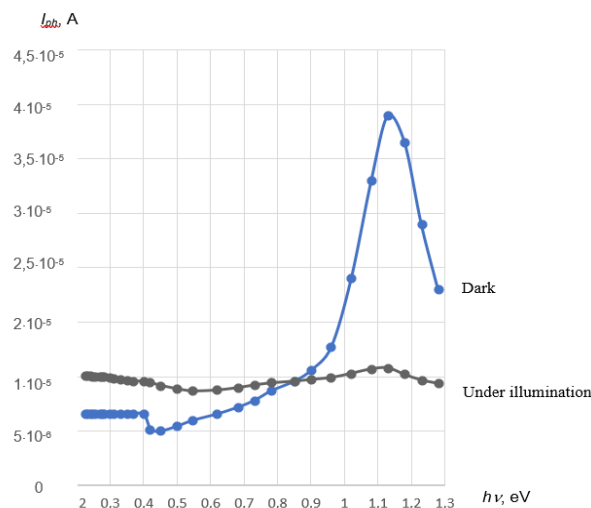
Fig. 1. The spectral dependence curve of photoconductivity of Si <S> sample (initial boron-doped silicon with ρ = 1 Ohm·cm) in dark and under steady illumination at T = 77K in forward connection mode

One can assume that dark current in the forward connection mode, by and large, might be due to the fact that current carriers are possibly being injected from contact points. At voltage "switched-on" mode, electrons are caught at level $E_i = 0.4$ *eV*, since their concentration at level 0.25 *eV* is comparatively low, and at this section the investigated photocurrent is determined by holes.

Having analyzed and summarizing the above experimental data one can tentatively assume that at forward switching mode of the diode structure, we are witnessing the so-called effect of negative photoconductivity due to the process of injection of current carriers associated with level E = 0.4 *eV* [1,2].

The authors also measured the band gap of the *p-n* junction formed on the basis of *n*-type conductivity phosphor-doped silicon samples with resistivity of ρ=100 Ω·cm.

At various temperatures, the authors measured the current-voltage characteristics (CVC) of the samples where *p-n* junction were formed. Their spectral sensitivity was also measured at room temperature by using IKS-12 spectrophotometer in the visible light range. The current-voltage

124

characteristics of the samples were measured using a DC source with a voltage of U=5V and U=12V, a multi-stage potentiometer with a resistance of 10 kOhm, while current measurements were carried out using a Rigol DM3068-type device, voltage measurements were carried out with a Mastech MS8040 device, a thermostat connected to a constant voltage source, digital temperature meter type Espada TPM10 with scale division of $\Delta t=0{,}1^0C$. In order to prevent significant overheating of *p-n* structures, the measurements were carried out by applying short-term impulse voltages. The results of the current-voltage characteristics of samples with a *p-n* junction are shown in Fig. 2.

a)   b)
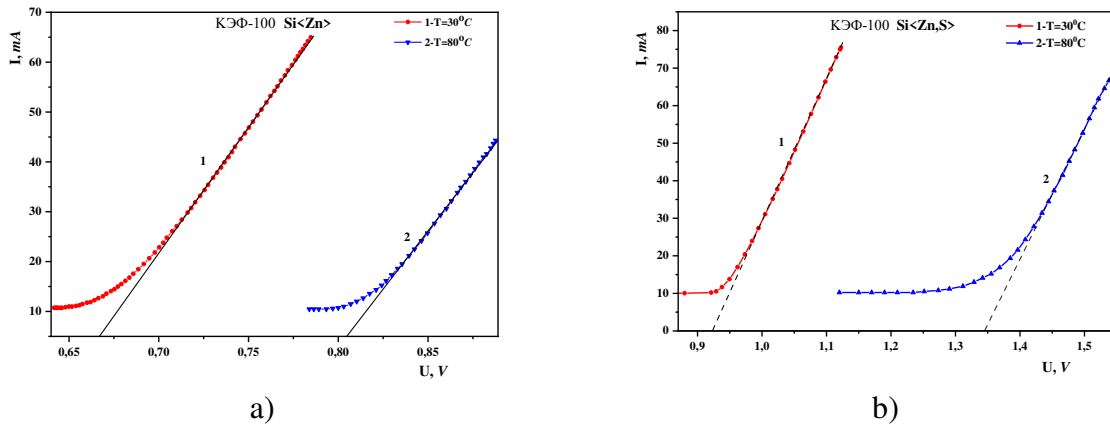
Fig. 2. Current-voltage characteristics (CVC) of silicon samples containing impurity atoms of zinc and sulfur, measured at temperatures: T= 30^{0}C and 2- T= 80^{0}C: a) Si<Zn b) Si<Zn,S>

As a result of measurements and the data reflected on Fig. 2 a) the band gap energies were determined: $E_{gSi_{Zn}} \approx 1{,}14\ eV$ - for silicon samples containing zinc atoms and $E_{gSi_{SZn}} \approx 1{,}38\ eV$ - for silicon samples containing binary compounds of impurity atoms of sulfur and zinc.

Tentative investigations of the short-circuit current and open-circuit voltage of *p-n*-structures, as well as the phase transitions in such structures, together with the analysis of their lux-ampere characteristic previously showed that these structures could in principle be seen as potential photodiodes and/or solar cells. Further calculation of the fill factor and efficiency ratio of these structures would pave the way for prospective application of these structures as solar cells that would allegedly harness the wider solar spectrum thus increasing their economic efficiency. Also, as the band gap (E_g) is a core parameter of a semiconductor material, so, the authors think that an exact knowledge of the band gap in such materials makes it possible to manipulate key performance characteristics of semiconductor devices developed on the basis of such materials.

REFERENCES

1. A. Mavlyanov. *Fotoelektricheskie izmereniya kremniya, legirovannogo margancem i seroj* [Photoelectric measurement of silicon doped with sulfur and manganese]. 2018, P.49. Mauritus, Lambert Academic Publishing.
2. I.M. Vikulin, Sh.D. Kurmashev, V.I. Stafeev. 2008, *Fizika i tehnika poluprovodnikov* [Phys. and Tech of Semicond.], v. 42, Issue. 1, pp. 113-127 (in Russ.)

THE EFFECT OF THE CONCENTRATION OF NATIVE DEFECTS ON THE PHOTOCATALYTIC ACTIVITY OF ZnO MICRORODS

B.N. Rustamova[1], R.R. Jalolov[1,2]

[1]*Arifov Institute of Ion-Plasma and Laser Technologies, Tashkent 100125, Uzbekistan*
[2]*The National University of Uzbekistan, Tashkent 100174, Uzbekistan*
rustamovab777@gmail.com, rr_jalolov@iplt.uz

Nowadays, the demand for drinking water around the world is significantly increasing. But limited water resources and their pollution is a global problem. Also, with the increase in the amount of manufacturing of products, the pollution of water used in industry is increasing. Cleaning the wastewater from various pollutants is very important to ensure environmental sustainability. Traditional technologies of water purification are ineffective for organic compounds or economically require a lot of funds (sedimentation, filtration, adsorption, ozonation biotechnological methods, etc.). For this reason, many researchers have been conducting research on photocatalysis technology, a new and effective method of water purification, in recent years. The use of semiconductor photocatalysts in the formation of free radicals to activate the oxidation of organic compounds is one of the most promising technologies for water purification. Among semiconductor photocatalyst materials, ZnO is of special importance, almost all its parameters show high performance in photocatalytic processes. ZnO is an n-type binary semiconductor material with a wide band gap (3.37 eV) and high exciton binding energy (60 meV). Among ZnO nanostructures, nanorods, nanoribbons, nanocrystals, and porous structures are synthesized in various ways due to their unique crystal structure and morphological properties, and their physicochemical properties are widely studied. Among the technologies for the synthesis of nanostructures, chemical methods are distinguished by their simplicity and low cost. However, nanostructures grown by these methods have different intrinsic defects depending on the synthesis method and conditions. Specific defects observed in nanostructures can affect the fundamental properties of materials and serve to further increase their potential for use in various fields.

In this study, the influence of the native defect concentration on the photocatalytic activity of ZnO microrods synthesized by the hydrothermal method at low temperatures was studied. The growth procedure was designed as follows: 148.7 mg zinc nitrate hexahydrate ($Zn(NO_3)_26H_2O$) and 70.1 mg hexamethylenetetramine ($C_6H_{12}N_4$ (Sigma Aldrich)) was dissolved in a 20 ml deionized (DI) water solution under intense stirring at room temperature, then ultra-sonicated for 1 min. The resulting suspension was transferred into a Teflon-lined stainless-steel autoclave. Quartz substrates were placed in a row in the bottom of the Teflon-lined stainless-steel autoclave with the prepared solution. The stainless-steel autoclave with substrates in it was closed and placed in a thermostabilized reservoir with water at a temperature of 90°C for 5 h. After the synthesis of ZnO nanorods is completed, the autoclave was removed from the bath and cooled at room temperature. After cooling, the samples were taken from the autoclave and dried in open air. The photoluminescence spectra of ZnO microrods were obtained using a photoluminescence set-up coupled to a 0.75 m monochromator with diffraction grating and high sensitive photomultiplier tubes. As excitation source, a longitudinally pumped nanosecond pulse N_2 laser emitting at 337 nm (pulse duration ~6 ns, P~15 kW, repetition rate - 100 Hz) was used. The photoluminescence spectra were recorded using a boxcarintegrator with a gate width of 40 ns. All experimental studies were carried out at room temperature. The photocatalytic activity of samples was performed using the organic dye decay method (Corlon red F3B). In this work, the dye concentration used was 25 ppm and the dye decay was studied by using an ultraviolet-visible spectrophotometer. The dye solution was kept under room conditions for 15 min by stirring and then it was exposed to the light from high pressure DRSh-120 mercury lamp. the intensity of mercury lamp radiation falling on the sample ~ 0.5 W/cm^2.

SEM image of hydrothermally grown ZnO microrods is shown in Figure 1. It can be seen from the image that the nanorods are crystallized in needle-like or star-shaped form, and the diameters of the microrods decrease from the central part towards the tip. The diameters of the central parts of the nanorods are ~800-1200 nm and the length is around 3-5 mm.
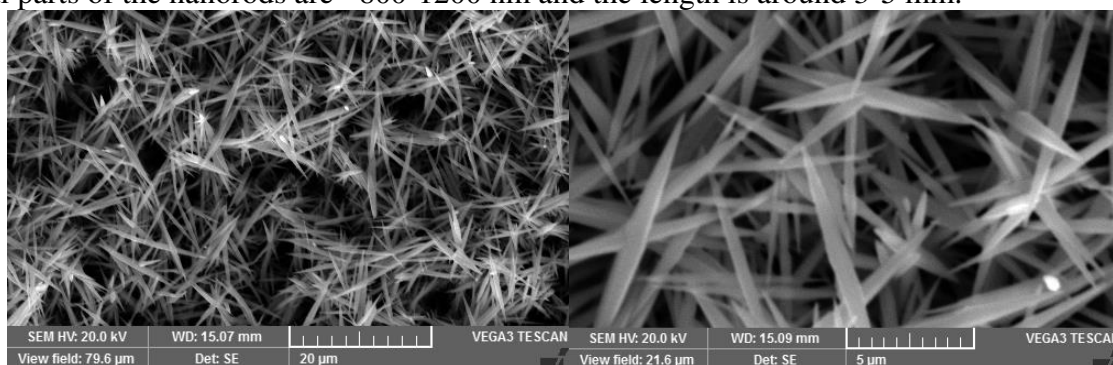
Figure1. SEM image of hydrothermally grown ZnO microrods

The PL spectrum of the as-grown ZnO microrods consisted of a strong and narrow emission band at a wavelength of 387 nm in the UV region, as well as yellow emission bands at a wavelength of ~570 nm in the visible part of the spectrum (Fig2a). The strong and narrow band of emission in the UV region is related to optical transitions or recombination of free excitons near band edge of ZnO [1-3]. The main factor in the appearance of the yellow emission band is the interstitial oxygen atoms or their complexes [3]. In the PL spectrum detected after ZnO microrods were annealed in open air at a temperature of 500 ^{o}C, the intensity of the emission band in the UV region increased by about 3 times, and the yellow emission band attributed to defects was not observed (Fig. 2a).
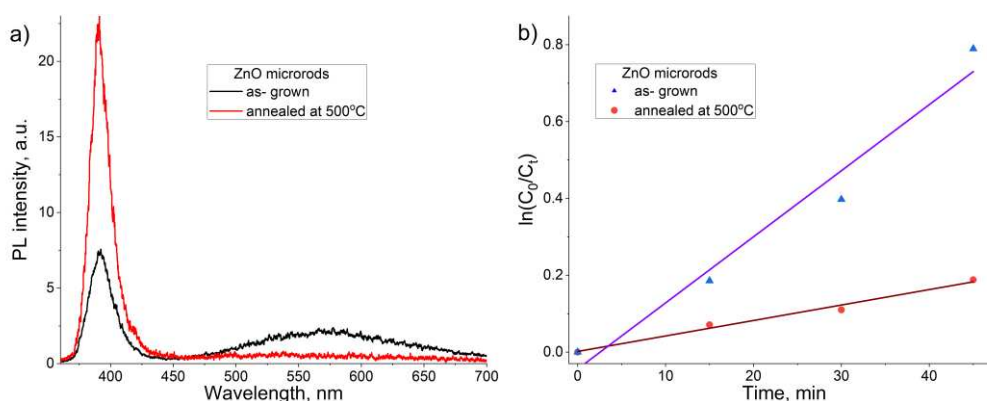
Figure 2. a) PL spectra and b) kinetic properties of Corlon Red F3B organic dye decomposition mechanism of as-grown and annealed ZnO microrods at 500C

The kinetic properties of the degradation mechanism of Corlon Red F3B dye by ZnO microrods are presented in Fig.2b. It can be seen from the graph that the degradation process of Corlon Red F3B dye is almost linear. The value of the organic dye decomposition reaction constant by as-grown ZnO microrods is equal to $17.2 \cdot 10^{-3}$ min^{-1}. ZnO microrods annealed at a temperature of 500°C have 2 times smaller properties of dye decomposition kinetics compared to the as-grown sample, and the decomposition constant of Corlon Red F3B dye is equal to $\sim \cdot 8.7 \cdot 10^{-3}$ min^{-1}.

In conclusion, the photocatalytic properties of ZnO microrods depend on the nature of native defects observed in the microrods, and an increase in the concentration of defects causes an increase in the rate of decomposition of organic dye solutions.

References
1. Ü. Özgür, Ya. I. Alivov, C. Liu, A. Teke, M. A. Reshchikov, S. Doğan, V. Avrutin, S.-J. Cho, and H. Morkoç, J. Appl. Phys. **98** (2005) 041301.
2. Shaymardanov Z Sh, Rustamova B N, Jalolov R R Urolov Sh Z, Physica B 649 414444
3. Sh.Z. Urolov, R.R. Jalolov, Z.Sh. Shaymardanov et al. Optics and Spectroscopy 127, No.6, 1093-1097 (2019).

GLIDING ARC PLASMA APPLICATIONS TO METHANE CRACKING FOR HYDROGEN AND CARBON BLACK PRODUCTION

Nosir Matyakubov[1], Mukhtorjon Karimov[1], Komiljon Yakubov[1], Maksudbek Yusupov[2], Umedjon Khalilov[2]

[1] *Urgench State University, Urgench, Uzbekistan*
[2] *Arifov Institute of Ion-Plasma and Laser Technologies, AS Uz, Tashkent, Uzbekistan*
email: nosirbek0726@gmail.com

Nonthermal plasma (NTP) technology has emerged as a promising and environmentally friendly approach to producing hydrogen and carbon black. In the case of hydrogen production, NTP has demonstrated its efficacy in enhancing the reforming processes of various feedstocks, including methane, ethanol, and ammonia. On the other hand, carbon black, a widely used industrial material, has traditionally been produced through conventional methods with associated environmental concerns. NTP offers an alternative and sustainable approach for carbon black synthesis by providing precise control over particle size, morphology, and surface properties.

This simulation-supported experimental study investigated the application of gliding arc plasma for the decomposition of methane to hydrogen and carbon black production at ambient conditions (i.e., room temperature and atmospheric pressure). The rotational gliding arc plasma was generated by injecting tangential gas flow to the reactor inlet and using a 400 Hz AC power supply. The influence of various process parameters, such as gas composition, discharge power, and reactor design, on the hydrogen generation and characteristics of the resulting carbon black are examined. In addition, the underlying mechanisms, namely, intermediate steps ranging from methane dissociation to the formation of hydrogen and black carbon were investigated using reactive molecular dynamics simulations.

Keywords: *Hydrogen production; gliding arc plasma; methane cracking; carbon black, reactive molecular dynamics simulations.*

CAN ENDOHEDRAL TRANSITION METAL ATOMS INFLUENCE THE HYDROPHILIC PROPERTIES OF CARBON NANOTUBES?

Sh. Matnazarova, U. Khalilov and M. Yusupov

Arifov Institute of Ion-Plasma and Laser Technologies, UzAS, Tashkent, Uzbekistan
shakhrizoda.matnazarova@outlook.com

Carbon nanotubes (CNTs) exhibit excellent physicochemical properties, making them promising candidates for various biomedical applications [1]. Despite notable advancements, off-target side effects, such as cell toxicity due to their hydrophobic nature, limit their utility in this field. To address this issue, the surface of CNTs is modified with hydrophilic functional groups, thereby enhancing their solubility or dispersion in a biocompatible (aqueous) medium and consequently reducing the toxic effects [2].

In this research, we investigated the impact of endohedral transition metal atoms (nickel atoms) in combination with functional groups (carboxylic acid) on the hydrophilicity of single-walled CNTs (SWNTs). Specifically, we created model systems of functionalized SWNTs (or fSWNTs) by attaching one, two, and three carboxylic acid (-COOH) radicals to SWNTs with (5,5) chirality. To explore the influence of endohedral metal atoms, we filled the formed fSWNTs with nickel atoms (Ni@fSWNTs) and conducted reactive molecular dynamics (MD) simulations [3].

The simulation results showed that, in all cases with Ni@fSWNTs, the C-C bond length in the nanotube is slightly larger than the C-C bond length in fSWNTs without Ni atoms. Additionally, the binding energy barrier corresponding to one radical in SWNTs without endohedral Ni atoms remains largely unchanged with an increase in the number of radicals. The introduction of endohedral Ni atoms into SWNTs results in a slight increase in the average energy barrier for binding the functional radical to the surface of SWNTs. Furthermore, endohedral Ni atoms enhance the dipole moment of SWNTs and the energy of interaction with water (Fig. 1), consequently increasing the hydrophilicity of SWNTs and potentially reducing toxicity [3].
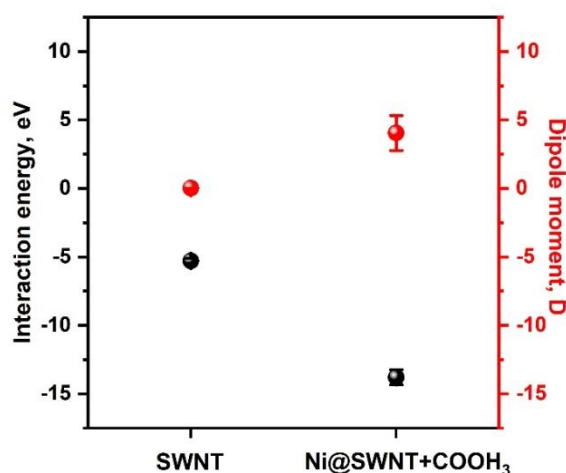
Figure 1. *Average interaction energy (black) of pristine SWNT and SWNT with endohedral Ni atoms functionalized with three -COOH radicals (Ni@SWNT+COOH$_3$) with water molecules, as well as their corresponding dipole moments (red). Associated errors are indicated by the vertical bars.*

References

[1] N.S. Kasálková et al. *J. Nanomater.* 2021, 11(9), 2368.
[2] R. Wang et al. *Mol. Pharm.* 2011, 8(4), 1351.
[3] Sh. Matnazarova et al. *Mol. Simul.* 2023, 49(17), 1575.

PROSPECTS OF CADMIUM TELLURIDE THIN FILM SOLAR CELLS ON ULTRA-THIN FLEXIBLE SUBSTRATES

Nowshad Amin

Department of Electrical and Electronic Engineering, Faculty of Engineering,
Faculty of Engineering,
American International University-Bangladesh (AIUB)
408/1 Kuratoli Road, Kuril, Dhaka 1229, Bangladesh

*e-mail: nowshad@aiub.edu

The so-called first-generation solar cells mainly use crystalline or multi-crystalline silicon as base materials and are still dominating the major market share of over 90%. However, the quest for other materials with better absorption and low manufacturing cost has brought over many other potential candidates such as amorphous silicon (a-Si), cadmium telluride (CdTe), copper-indium-selenide (CIS) as the second-generation solar cell technologies since the early 70s. Some of the thin film photovoltaics are now in the commercialization stage owing to their lab-scale conversion efficiency achievement of over 20%, although the Shockley–Queisser limit shows up to 30%. This talk will show the chronological development of CdTe thin film solar cells since its inception in the '70s. The standard and stable structure of CdTe thin film solar cells entered towards successful commercialization of Giga-Wp scale annual production almost a decade ago, however with some unresolved concerns. Recent advancements in CdTe solar cell technology have introduced the integration of flexible substrates, providing lightweight and adaptable energy solutions for various applications. Our initial studies find that the growth process is to be optimized as the transition from rigid glass substrates to flexible substrates like UTG (ultra-thin glass) possesses some crucial challenges in terms of deposition processes and subsequent layer integration. Issues that can further improve the efficiency as well as the future direction of R&D will be discussed. This will boost the hope for thin film solar photovoltaic technology amid the imminent energy crisis of the world aligning to SDG7.

SIZE-OPTICAL PROPERTIES OF MODIFICATION OF THIOL STABILIZED CdSe/ZnS QUANTUM DOTS

[1]Ishankulov A.F., [1]Islomova Z.R. [2]Shamilov R.R., [1]Khalilov K.F., [1]Galyametdinov Yu.G., [2]Mukhamadiev N.K.

[1]Uzbekistan, Samarkand, Samarkand State University
[2]Russian, Kazan, Kazan National Research Technological University
ishankulov-alisher@mail.ru

Abstract. CdSe quantum dots stabilized with oleic acid were obtained by the colloidal method and their optical properties were studied. By growing a ZnS shell onto the surface of CdSe nanoparticles, CdSe/ZnS core-shell hybrid QDs are synthesized. Ligand exchange reactions were carried out under mild conditions using an excess amount of a thiol stabilizer. The fact of the replacement of stabilizers was established by IR spectroscopy.

Keywords: quantum dots, colloidal synthesis, core-shell nanoparticles.

Quantum dots (QDs) - optically active semiconductor nanoparticles are of interest as components of light-emitting devices, solar cells, luminescent sensors and new-generation biomarkers [1,2].

We have investigated the features of the QD surface modification using various types of stabilizers. The molecules of the initial stabilizer (oleic acid) on the surface of the synthesized CdSe/ZnS QDs were replaced by compounds containing a thiol group: L-cysteine (Cis), mercaptopropionic acid (MPA), dodecanethiol-1 (DT), and dodecyl dihydrolipoate (DDL).

The use of L-cysteine and MPA as a stabilizer made it possible to obtain hydrophilic QDs, while the luminescence intensity slightly decreases. It was determined that the substitution of oleic acid (OA) contributes to a slight shift of the emission peak to longer wavelengths. It was shown that, as a result of surface hydrophilization, the hydrodynamic size of nanoparticles increases due to hydration of the QD surface, due to the presence of charged stabilizer ions.

When the surface is modified with dodecanethiol and dodecyl dihydrolipoate, the QD surface remains hydrophobic. In this case, a high luminescence intensity is maintained and the peak position does not shift. According to IR spectra, a small part of oleic acid molecules on the QD surface remains unsubstituted. The hydrodynamic particle size is slightly reduced as a result of the modification, due to the smaller length of the stabilizer molecules in comparison with oleic acid.

References
1. Chaudhuri R. G., Paria S. Chem. Rev., 112, 4, 2012, 2373-433.
2. Medintz I.L. Nature Materials, 4, 2005, 435-446.

Contents

Contributed Talks